Room temperature single-photon source based on semiconductor quantum-dot nanowire for integrated photonics

Saransh Raj Gosain

THÈSE

Pour obtenir le grade de

DOCTEUR DE L'UNIVERSITÉ GRENOBLE ALPES

Spécialité : PHYSIQUE

Arrêté ministériel : 25 mai 2016

Présentée par

SARANSH RAJ GOSAIN

Thèse dirigée par **Kuntheak KHENG**, Université Grenoble Alpes
et codirigée par **Edith BELLET-AMALRIC**, CEA

préparée au sein du **Laboratoire PHotonique ELectronique et Ingénierie QuantiqueS**
dans **l'École Doctorale Physique**

Source de photons uniques à température ambiante utilisant des nanofils semi-conducteurs à boîtes quantiques pour la photonique intégrée.

Room temperature single-photon source based on semiconductor quantum-dot nanowire for integrated photonics.

Thèse soutenue publiquement le **13 décembre 2021**,
devant le jury composé de:

Monsieur Nicolas CHAUVIN
CHARGE DE RECHERCHE, INL (Institut des Nanotechnologies de Lyon), Université de Lyon,
Rapporteur
Monsieur Vincent SALLET
CHARGE DE RECHERCHE, GEMAC (Groupe d'étude de la matière condensée), Université Paris-Saclay,
Rapporteur
Monsieur Thierry BARON
DIRECTEUR DE RECHERCHE, LTM (Laboratoire des Technologies de la Microélectronique), Université Grenoble Alpes,
Président
Madame Valia VOLIOTIS
PROFESSEUR DES UNIVERSITES, INSP (Institut des NanoSciences de Paris), Sorbonne Université,
Examinatrice

This thesis is dedicated to my parents

For their endless love, support, encouragement, and for always believing in me.

Acknowledgement

This dissertation represents the culmination of a long-held dream and would not have been possible without the contribution of a long list of people.

Foremost, I would like to express my deepest gratitude to my advisor Kuntheak Kheng and co-advisor Edith-Bellet Amalric for giving me the opportunity to work on this ambitious project in this beautiful city (Grenoble), and for their continuous support during my Ph.D. and research. Without their continuous optimism concerning this work, encouragement, enthusiasm and moral support this study would hardly have been completed. They were always available for guidance and rich discussions.

Then, I would like to convey my warmest gratitude to Joël Cibert. It was an absolute pleasure to work with Joël. He was present in all the meetings, and has guided me throughout at very step of this PhD work and this manuscript. His advise has been invaluable and this work would not have been possible without his immense contribution.

This thesis presents MBE growth, quantum optics measurements, simulation and nanofabrication of semiconductor materials. For the MBE growth part, I would specially like to thank Régis Andre for fruitful discussions and feedback, and a big thanks to Yann Genuist and Yoann Cure for their technical support. All the quantum optics measurements presented in this work were performed with David Ferrand. My sincerest gratitude to him for working long hours with me, and for all the rich discussions. Simulations and nanofabrication were performed in collaboration with Gilles Nogues. A big thanks to Martien den Hertog and Eric Robin for all the TEM measurements.

I would also like to thank all the researchers and PhD students at the Nanophysique et Semiconducteurs team for making it a fun experience. Thank you to all the nice people I met in the team, specially Alberto Artioli with whom I shared office for 3 years.

Lastly I would like to thank my family and friends, without there constant moral support this work would not have been possible.

Contents

List of Acronyms

Introduction

Translation of quantum mechanics to real world technologies offers extreme advantages in the field of communication, computation and metrology. At the core of quantum technologies is a quantum bit (or qubit), an extension of classical bit. Polarization of a single-photon can be used to encode a qubit [1]. In fact, polarization of a photon is quite convenient as it is possible to manipulate and separate two orthogonal states with the help of very simple components such as beam splitters, polarizers, etc. On one hand, single-photons are decoherence free systems which can be used in quantum computing [2, 3] and quantum metrology [4], and on the other hand they can be used as flying-qubits for exchanging quantum information over long distances. In 2009, quantum-key distribution over a 144 km free-space link was demonstrated using single-photons at wavelength of 850 nm [5].

In the past, single-photon sources were realized using a variety of quantum systems, for example through spontaneous parametric downconversion of a laser beam [6], single atoms, trapped ions [7], color centers [8, 9]. However, such systems show either poor light extraction or lack any possibility for scalability and integration.

Another single-emitter system which shows potential for high scalability with integrated photonics is based on a semiconductor epitaxial quantum dot (QD). QDs can be used to generate single or entangled photons, can be scaled up to realize multi-qubit quantum networks and can also be embedded in an optical waveguide to realize photonic devices. After careful designing of the QD surroundings, their extraction efficiency can also be optimized. For example, when embedded in a nanowire (NW), the light from the QD can be guided and collected efficiently in free space (as we will see in this manuscript). Moreover, a QD-NW is a single unit that can be easily picked-up and transferred from one substrate to another, and to a photonic circuit [10]. However, as is the case with most single-photon emitters, QD's single-photon demonstrations usually require cryogenic temperatures.

In 2012, our group demonstrated single-photon emission in the visible range (~550 nm) at room temperatures using a CdSe QD embedded in a ZnSe NW [11]. Single-photons in the visible range are particularly interesting for quantum-information technologies since visible light is not absorbed by earth's atmosphere. However, these QD-NWs had a low quantum yield, showed poor light extraction and were not vertically oriented since the NWs with the [111] axis were grown using molecular beam epitaxy (MBE) on a [001] substrate. Moreover, out of 100s of NWs, only one demonstrated single-photon emission at room temperature. Still, this study proved the possibility of realizing a visible light single-photon emitter at room temperature using CdSe QDs in ZnSe NWs.

In 2016, Thibault Cremel [12], also from our group, realized vertically oriented CdSe-ZnSe QD-NWs along the [111] crystal direction. But the MBE growth process was not optimized, with a low reproducibility, and involved a very thin shell: we will see in this manuscript how important is the shell for efficient light guiding and collection along the NW axis.

In this context, the goal of this PhD work is four-fold: 1. to design the shape of the NW for efficient light collection along the NW axis, 2. to develop and control the MBE growth process in order to realize CdSe QD in vertically oriented and low density ZnSe NWs of desired design, 3. to study these QD-NW luminescence for single-photon emission at cryogenic and room temperatures, 4. to show prospects for coupling of photon emission from these QD-NWs with photonic devices (waveguides).

Keeping the above goals in mind, this manuscript is organized as follows:

1 Chapter 1 introduces the reader with the fundamentals necessary to understand the results of this manuscript and provide references for further reading: the methods used to realize a CdSe-QD in ZnSe-NW using MBE, the tools and techniques used to characterize the QD-NW heterostructure, and for the detection of single-photons.

2 Chapter 2 calculates the NW shape for an efficient light extraction in free space along the NW axis using finite-element method numerical calculations.

3 Chapter 3 presents the MBE growth of ZnSe NWs. The effect of different growth parameters (such as fluxes, sample temperature and sample tilt) on the radial and axial growth of the core and shell of NWs is discussed. One of the points that we also had to study is the simultaneous growth of a 2D layer in between the NWs, that buries the bottom of the NW. The best conditions to grow vertically oriented, low density, tapered ZnSe core-shell NWs are determined. Then, insertion of CdSe QD in ZnSe NWs is also presented.

4 Chapter 4 is dedicated to the optical and single-photon emission properties of CdSe-Zn(Mg)Se QD-NWs. This chapter is divided into three parts: Part A discusses the emission properties of QD-NWs when excited with a continuous wave laser from cryogenic to room temperatures. Part B discusses the emission properties of QD-NWs when excited with a pulsed laser. Here, we compare anti-bunching measurements performed under continuous and pulsed excitation and see how decay time of the excited states in the QD affects them differently. In part C, we will show characterization of QDs for single-photon emission at room temperature.

5 Chapter 5 provides future prospects for the integration of QD-NW with photonic devices (waveguides). Finite-difference time-domain simulations were performed to show the evanescent coupling of light from the QD-NW to silicon-nitride waveguides. Also will be shown nano-fabrication of a simple design for performing photon anti-bunching measurements on-chip.

Finally, a global conclusion and prospects for future studies are given in the end.

Chapter 1

Quantum dot in a nanowire as single-photon source

Contents

The aim of this chapter is to introduce the reader with the fundamentals necessary to understand the results of this manuscript and provide references for further reading. The first part of this chapter starts with a short review on single-photon emitters for quantum technologies in section 1.1. In section 1.2 we discuss the prospects of semiconductor quantum dot (QD) as single-photon emitters, various types of self-assembled QDs available today for single-photon emission and advantages of QD in a nanowire (NW) design in section 1.2.2. In section 1.3, we discuss the general properties of II-VI group semiconductors, the catalyst assisted growth mechanism for NWs and the state of the art. The second part of this chapter deals with the methods used in this work to realize a CdSe-QD in ZnSe-NW using MBE along with the the tools and techniques used to characterize the QD-NW hetrostructure and for the detection of single-photons.

1.1 Single-photons for quantum technologies

A single-photon source is a non-classical light source that ideally generates spatially separated and indistinguishable photons one at a time. These single-photons generated one after another are usually triggered with an electrical or optical input.

At the core of all quantum technologies is a qubit. Using polarization of single-photons, qubit operations with high fidelity can be realized for applications such as in quantum computing and quantum metrology. Already entangled photons [13] were realized and CNOT gate (analogous to universal NAND gate for classical computers) operations were implemented using single-photons [3]. One of the most important and direct application of single-photons in quantum technologies is quantum key distribution (QKD) for long distance encrypted communication [14, 15] where single photons acts as flying-qubits. QKD is a cryptographic communication protocol which generates a shared secret key between two groups, who can then use this key to encrypt or decrypt information. The information is stored in the polarization of the single-photons. QKD provides unconditional encryption of information based on the laws of quantum mechanics. In 2009, QKD over a 144 km free-space link was demonstrated using weak coherent laser pulses at wavelength of 850 nm [5].

Single-photon sources are indispensable to quantum technologies given that they meet a few basic requirements [16]: 1) high single-photon purity (auto-correlation function $g^2(0) = 0$, described later in 1.4.3.3), 2) high indistinguishability ([17]) and 3) high brightness. Other useful properties for practical applications are: 4) high repetition rate (less than 1 ns decay-time), and 5) single-photon emission at high temperatures.

1.1.1 Single-photon emitters

The most common and convenient process for generating single photons so far was the spontaneous parametric downconversion of a laser beam [6]. However, it's a stochastic process and thus generate single photons at random.

The simplest process with which single-photons of high purity, indistinguishability and high efficiency can be generated is with single quantum system with two (or more) discrete energy levels. In a two-level system, an electron can get excited from the ground state through an electrical or optical trigger (laser excitation). When this electron relaxes back to the ground state it will release a photon (or not if it relaxes non-radiatively) within its radiative lifetime. This two-level system cannot generate another photon before the excited electron has completely decayed to its ground state. Such a system, called a single-photon emitter, therefore guarantees single-photon emission only with no multi-photon component.

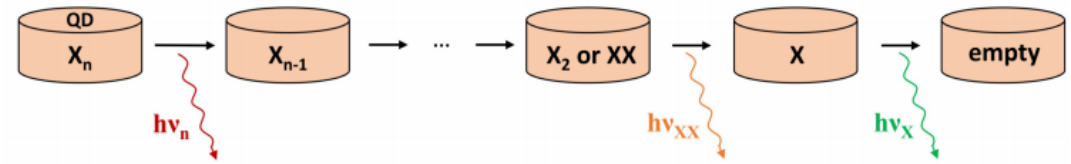

Figure 1.1: Scheme for emission of mutli-exciton (X) state in a QD in a radiative cascade. Each transition releases a single photon. Taken from [12].

However, emission mechanism from a single-photon emitter is not as straight forward as described above. A single-photon emitter emits photon in a radiative cascade. The electron-hole pair generated is called an exciton (X). An X recombines emitting a photon of energy which depends on the band gap of the emitter. If the emitter is excited very strongly multi-Xs are formed which recombines progressively

i.e. $X_n \rightarrow X_{n-1}$ ..... $XX \rightarrow X \rightarrow 0$. This process is explained in Fig 1.1 and is called a radiative cascade [18]. A combination of spatial confinement and Coulomb interaction results in emission of a photon of different emission energy in each step, and therefore, by spectral filtering of any of these photons a single-photon source can be realized. Usually either the X or bi-exciton (XX) states are considered for a single-photon source.

Similar to a XX, when three Xs exists in a QD it is called a tri-X, and so on. But charged carriers are not always formed in pairs of an electron and a hole. An unequal combination of charges can be formed as shown in Fig 1.2 (a). When an extra charge carrier (electron or hole) is present along with the X, it's called a charged exciton (CX). And if it is present along the XX, it's called a charged bi-exciton (CXX).

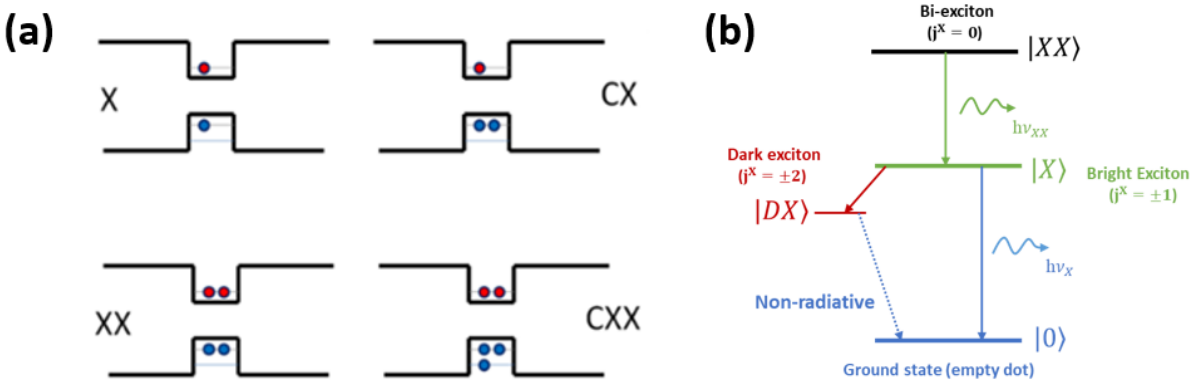

Figure 1.2: (a) Different states of a QD. The X level corresponds to one electron and one hole in their lowest excited states. The XX with two Xs. The charge-X(XX) with an extra hole or electron along with an already existing X(XX). (b) Radiative cascade decay path from XX to the ground state. The X state is split into Dark-X and Bright-X. Recombination from the Dark-X is only through non-radiative channels.

Moreover, an X can be further split into a bright-X which corresponds to an electron-hole pair with antiparallel spins (total angular momentum $J_z = \pm 1$), or a dark-X corresponding to an electron-hole pair with parallel spins ($J_z = \pm 2$) [19]. Since, photons have a ± 1 total angular momentum, bright-X recombines radiatively and a dark-X non- radiatively. For the XX state where two Xs with opposite-spin carriers are present $J_z = 0$. And therefore, there is no dark state which exists for the XX.

1.1.2 Available single-photon emitters

Single atoms, ions or molecules have discrete energy levels and therefore are by nature single-photon emitters. Early studies in 1997 by Kimble *et al.* for generating single photons using discrete energy level systems were based on single sodium atoms where they are captured atoms in a Magneto-optical trap [7]. However, there is always a high probability of trapping more than one atom in such cavities. The complexity involved with such systems makes it very difficult to integrate with photonic devices for practical applications.

In addition to atoms, ion and molecules, color center in diamonds were extensively studied as single-photon emitters. Pure diamonds are transparent but they can get color due to defects in the diamond

crystal called color centers. There are more than 500 known color centers in diamonds. One such and very famous color defect is the Nitrogen-Vacancy (NV) color centre [8] which gives a pink color. It is a point defect where one of the carbon atoms in diamond crystal is replaced by a nitrogen atom and an adjacent atom is left empty (vacancy). There are other color centers in diamonds that were used as single-photon emitters such as silicon centers [9] and nickel-nitrogen complex center [20]. And these are just two others out of hundreds of color centers explored. However, most NV centers have a broad fluorescence spectrum of about 100 nm linewidth at room temperatures making them very challenging to be used as a source of indistinguishable single photons.

Another type of single-photon emitter is a semiconductor QD which is discussed in the following section

1.2 Semiconductor quantum dots

A QD is a semiconductor nanostructure surrounded by another semiconductor material with a larger band gap which is either a 3D or 1D-material (e.g., NWs). All the dimensions of the QD are reduced (less than twice the radius of its exciton Bohr radius) to induce quantum confinement which results in discrete energy levels in the valence and conduction band. The band structure of a QD and its surrounding material are explained in Fig 1.3. Due to the discrete energy levels in a QD just like an atom, they are sometimes referred to as artificial atoms. A QD is thus inherently a single-photon emitter. The energy of the emitted photon is mostly determined by the band gap of the QD and its size, and therefore can be tailored according to application needs. The most important advantage of a QD based single-photon emitter is that it is a solid-state system which offers high scalability and integration over other sources.

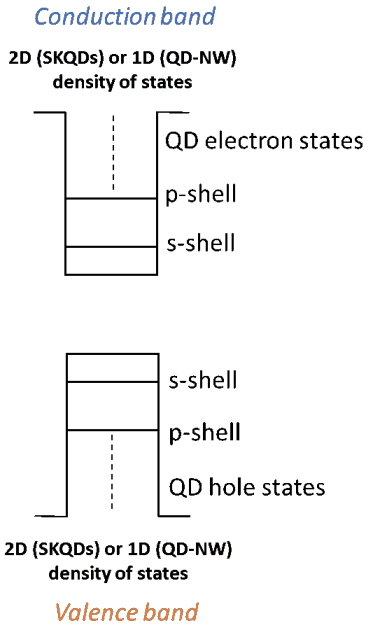

Figure 1.3: Band diagram for a QD confined by another material. The QD have discrete states in the CB and VB.

Semiconductor QDs are typically realized through epitaxial growth techniques: molecular beam epitaxy (MBE) (techniques used is this thesis) or metal-organic chemical vapor deposition (MOCVD). While these two are the most widely used techniques, other techniques include plasma synthesis or fabrication techniques such as lithography and wet/dry etching.

1.2.1 Stranki-Krastanov quantum dots

Two principle ways to realize epitaxial quantum dots can be distinguished: first is the growth of a 2-dimensional layered structure (quantum well) which is followed by etching process to further lower the dimensions [21], and second an epitaxial growth technique (modeled by Stranski and Krastanow in 1939) which exploits the lattice mismatch between the layers. The SK growth of QDs [22] generally initiates with deposition of a thin film of a material lattice-mismatched with respect to the substrate, leading to formation of strained monolayers (ML). This layer-by-layer growth continues until a critical thickness is beyond which it undergoes a transition with the formation of 3D relaxed islands.

There are several Stranki-Krastanov quantum dots (SKQDs) systems explored so far which emit single-photons from the UV to IR region. However, most systems emit single-photon under 200 K. In Fig 1.4 is shown a summary of epitaxial grown QDs single photon emitters selected from literature as a function of temperature (with a $g^2(0)$ value well below 0.5). The IR region is covered by InAs/InP [23], InAs/GaAs [24], GaAs/AlGaAs [25] SKQDs. However, in the IR region, none show above 200 K single-photon emission. The UV region is currently dominated by the III-nitride and III-arsenide based QDs and currently GaN based SKQDs show room temperature single-photon emission. Holmes *et al.* [26] showed single-photon emission around 290 nm from GaN/AlGaN SKQDs at very high temperatures of 350 K (with $g^2(0)$ value of 0.34).

Single-photon emitters in the visible range

Single-photon sources emitting in the visible range are very important for quantum information application since visible light is transparent to the earth's atmosphere. For visible a few promising QD systems are available which emit above 200 K. Deshpande *et al.* [29] reported anti-bunching upto 280 K ($g^2(0)$ of 0.37 under pulse excitation and 0.32 under continuous excitation) with an InGaN/GaN SKQDs emitting at 620 nm. Similarly, Wang *et al.* [30] used InGaN QDs grown on a non-polar crystal to show anti-bunching upto 220 K ($g^2(0) = 0.47$).

Single-photon emission in the visible using II-VI QDs was shown using CdSe QDs. Although, CdSe QDs are often prepared in colloidal (solution) form [24], a handful of studies were reported on single-photon emission based on epitaxial CdSe QDs system (including this work). Rakhlin *et al.* [31] reported anti-bunching ($g^2(0) = 0.15$ at 80 K using CdSe/ZnSe SKQDs with a ZnSSe/ZnMgSSe barrier. Sebald *et al.* [32] reported anti-bunching ($g^2(0) = 0.4$) at 100 K with CdSe/ZnSe SKQDs grown by MBE. Fedorych *et al.* showed [33] room temperature single-photon emission ($g^2(0) = 0.16$, with CW excitation) around 550 nm from CdSe/ZnSSe SKQDs embedded in a MgS barrier.

Drawbacks of SKQDs

Although, SKQDs are inherently single-photon emitters, there are a few major drawbacks of SKQDs which makes it difficult to use them for practical applications:

- Shape, size and density depends strongly on the lattice mismatch between the QD material and

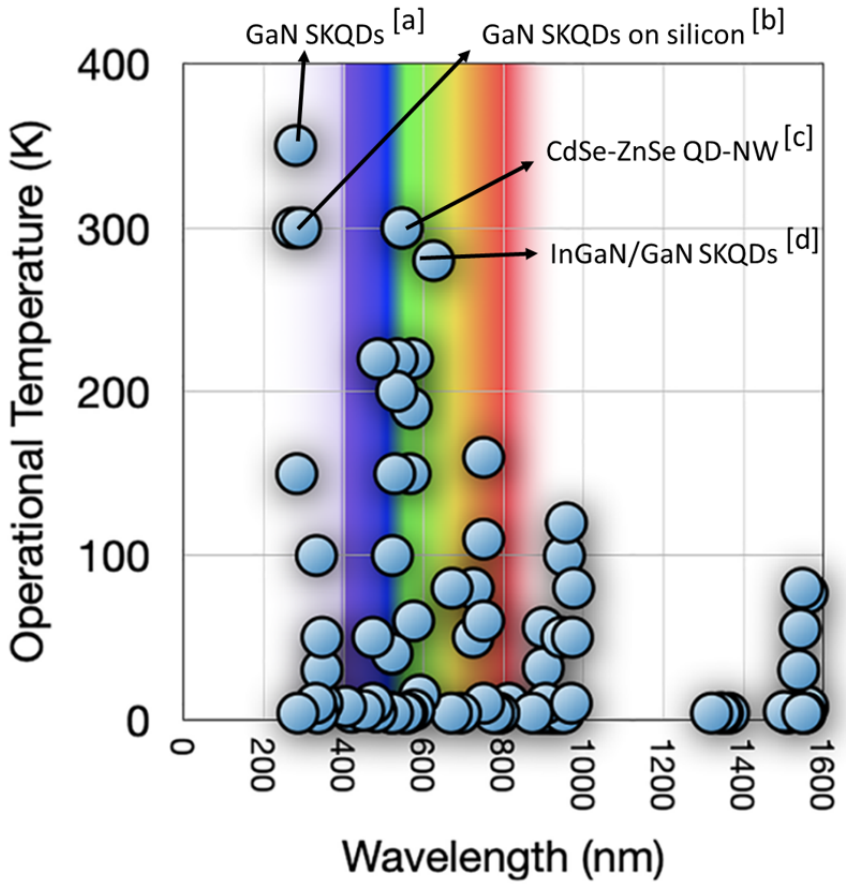

Figure 1.4: Summary of single-photon based on epitaxial grown QDs selected from literature as a function of temperature with a $g^2(0)$ well value below 0.5. Highest temperature at which single-photon emission was reported is at 350 K using GaN QDs. In the visible range, only CdSe-ZnSe QD-NW (from our group) was reported to emit single photons upto 300 K using II-VI semiconductors. Image taken from [27]. Refereces are taken from: a [26], b [28], c [11], and d [29].

the wetting layer material and is very difficult to control independently. The density of the QDs is usually very high. Attempts were made to control the randomness in location, density and size of SKQDs [34, 35].

- Size is not just difficult to control from one sample to another but also varies a lot on the same sample. A distribution in size means a broad spectral distribution.
- QD growth is random and exact location is not at all predetermined. There were some efforts to first identify QDs using photo-luminescence (PL) measurements and then localize those QDs using lithography and etching [36]. But such processes are time consuming and only beneficial for studying the properties of a single QD. This is a huge drawback of SKQDs as it makes scaling and integrating with quantum devices very difficult.
- In fact, the SKQDs are surrounded by 2D materials which acts as a pathway for charge carriers to escape. This is the reason why single-photon properties for most SKQDs degrade at room

temperatures.

- Efficient extraction of light from SKQDs is generally an issue due to total internal reflection from the 2D layer above it. Various techniques were employed to improve the light extraction efficiency from SKQDs and generally consists of etching the material around the QD to give a nanopillar structure around the QD [37]. But such a technique is not very useful for scaling and integration unless the exact position of the SKQDs can be predetermined and controlled.

- Finally, SKQDs growth requires a lattice mismatch between the QD and the substrate material. Growth of SKQDs is in fact a result of the strain applied due to the lattice mismatch. Therefore, growth of SKQDs cannot be done on any substrate, which makes it even more difficult for integration with other devices.

1.2.2 Quantum dot in nanowire

Some drawbacks of SKQDs can be removed using a QD in NW design. Unlike in SKQDs where a QD is surrounded by a higher band gap 2-dimensional material (wetting layer at the bottom and a barrier layer on top), in a QD-NW system, a thin slice of QD material is embedded in a higher band gap 1-dimensional nanowire structure (QD-NW). QD-NWs structure are usually realized with Vapor-Liquid-Solid (VLS) and Vapor-Solid-Solid (VSS) bottom-top epitaxial growth techniques. The QD-NW system has also been used to realize a single-photon source. Dalacu *et al.* [38] realized InAsP QD in InP NWs. The QDs emitted at ~950 nm with a g^2 (0) of less than 0.005 at 4 K. Bounouar *et al.* in 2012 from our group [11] reported single-photon emission at 300 K with a g^2 (0) value of 0.48 (with pulsed excitation).
The QD-NW design offers various advantages over the SKQDs design:

- The QD confinement is controlled by the NW. The radius of the QD is controlled by the catalyst and the NW radius. The height of the QD (along the NW-axis) is then controlled by the amount of QD material sent on the substrate. Control over QD size has shown to control its emission profile (discussed later in section 2.2.1).

- With NW design, there is no strict lattice mismatch condition that applies between the NW and the substrate material. This is because the strain applied by the substrate on the NW can be easily relaxed on the sides of the NW. Which means that different material combination can be tried with control over the QD shape and size over a broad range. Moreover, NWs can be grown on different substrates allowing easy integration.

- A QD-NW is a single object that can be easily manipulated, removed from one place and transferred to another. It is a single-photon emitter that can be easily integrated with any device.

- The density of the NWs (and therefore of QDs) is controlled by the catalyst density on the substrate. Not only is it possible to control the random density of the catalyst but it can be deposited at predetermined locations on the substrate using lithography techniques. Organized arrays of NWs can be realized with control over density and position. This feature allows easy integrating and scaling.

- Electrical injection of the carriers in the QD is also possible with metallic contacts which can be deposited at both ends of the NW or on the sides of the NW.

- The extraction of light from the QD in a NW design can be very efficient. The NW can act as a waveguide with HE_{11} as the principle mode of propagation for light. But the size and shape of the NW has to be optimized and tailored to the wavelength of light emitted as in the case of an optical fiber.

As far as we know, only CdSe QDs from the II-VI group have shown to emit single-photons in the visible range at high temperatures (above 200 K). And for all the above-mentioned reasons, we considered a NW design (ZnSe NWs) for the confinement of CdSe QDs.

1.3 II-VI group semiconductor nanowires

In this section, we discuss the basic properties of II-VI semiconductor materials, techniques widely used for the growth of II-VI NWs and state of the art for the growth of ZnSe NWs.

1.3.1 Properties of II-VI semiconductors

II-VI semiconductors materials are a group of alloys where II refers to Mg, Zn, Cd, Pb or Mg and VI to either Se or Te. Group-II elements have two valence electrons in the outer most *s* shell and group-VI elements have six valence electrons- two in *s* shell and four in *p* shell. Group-II element gives (cation) its two electrons to group-VI element (anion) to covalently bond through $sp3$ hybridization of molecular orbitals to form II-VI semiconductor materials.

II-VI materials crystal structure are usually observed in either Zinc Blende (ZB) or Wurtzite (WZ) phase. The ZB phase consists of two faced centered cubic lattices (one from II and one from VI) separated by 1/4th the length of the cubic lattice along the [111] direction (*i.e.* the diagonal length of the cube). The atomic layer sequence in the ZB phase is ABCABC with C plane rotated by 60° with respect to A plane. The WZ consists of tetrahedrally arranged atoms stacked in ABABAB sequence.

In the bulk form, ZnSe, CdTe and ZnTe are usually observed in ZB phase, and CdSe in the WZ phase. For ZnSe NWs, both WZ and ZB phases were observed to exist in the same NW [39]. For CdSe QDs it is difficult to determine the structure. Both ZB and WZ structures were obtained for CdSe QD [40]. Since, the electronic band structure is dependent on the crystal phase of the material, control over growth of crystal phases of a NW is very important, but is very difficult to control and not fully understood.

For ZB phase, along the [111] or [-1-1-1] direction, one side of the ZB lattice have cations (group-VI) and one side anions (group-II). This is same for WZ along the [0001] or [000-1] direction. By convention, if the [111] surface of the substrate ends group-II elements it is called a (111)A surface and if it ends with group VI elements it is called (111)B surface. Therefore, ZnSe(111)A substrate surface ends with Zn atoms and ZnSe(111)B with Se atoms. This convention is followed for III-V materials also. For example, GaAs(111)A surface ends with Ga atoms and GaAs(111)B with As atoms. Previously, we have observed that the polarity of the substrates becomes important when growing ZnSe NWs. We will talk about this in the following section.

There are two parameters to consider when trying to realize a QD-NW semiconductor heterostructure for their optical properties: their band gaps and their lattice mismatch. QD and NW lattice mismatch result in strain either on the QD or on the NW. And for a QD to be confined in a NW geometry, the band gap of the QD should be smaller than the NW. In table 1.1 is given lattice parameters and band gap for Se based semiconductors used in this work.

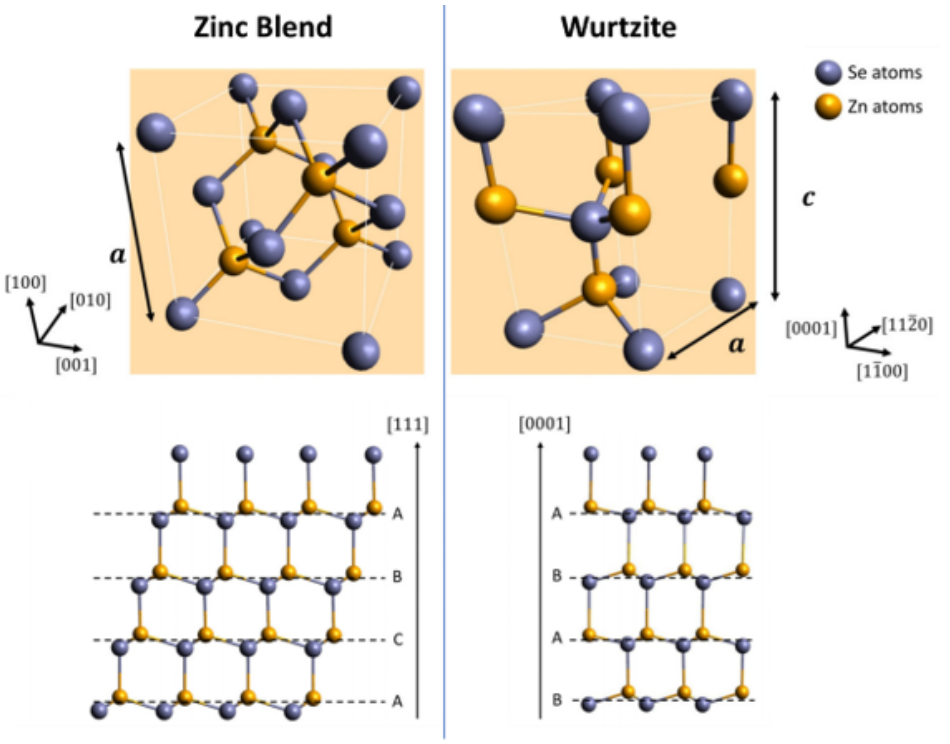

Figure 1.5: ZB and WZ crystal structure along with their stacking sequence of atoms along the [111] and [0001] directions respectively. Taken from [12]

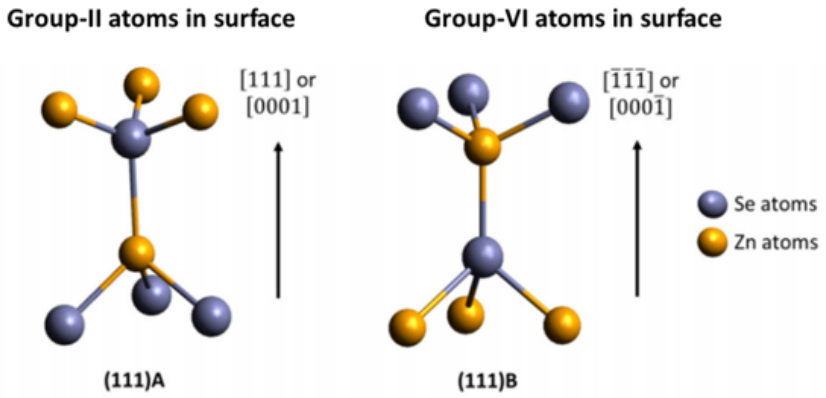

Figure 1.6: Scheme to show (111)A and (111)B directions. Taken from [12]

The band gap of CdSe in any phase is well below the ZnSe bandgap. After the CdSe-ZnSe QD-NW growth, we can grow an even higher band gap ZnMgSe shell around the ZnSe core. This is done to further confine the carriers in the NW-core and then the QD, but to also protect the QD in the NW-core from dangling bonds and defects which can act as traps for carriers.

During the growth of QD-NW or core/shell NW, ternary alloys can also form such as $Cd_XZn_{1-X}Se$ (or

	ZnSe (ZB)	ZnSe (WZ)	CdSe (ZB)	CdSe (WZ)	MgSe (ZB)	MgSe (WZ)
$a\ (nm)$	0.566	0.398	0.604	0.430	0.589	0.414
$c\ (nm)$		0.653		0.701		0.672
$E_G\ (eV)$	2.800	2.851	1.77	1.82	2.47 to 5.6	2.44 to 3.6

Table 1.1: Band gap and lattice parameters of materials that will be used in this thesis [12].

$Zn_XMg_{1-X}Se$). The lattice parameter of such ternary alloys is given by the Vegard´s law [41] which for example for $Cd_XZn_{1-X}Se$ is given as:

$$a_{Cd_XZn_{1-X}Se} = xa_{CdSe} + (1-x)a_{ZnSe} \tag{1.1}$$

And the band gap can be calculated with the quadratic formula [42]:

$$E_G^{Cd_XZn_{1-X}Se}(x) = xE_G^{CdSe} + (1-x)E_G^{ZnSe} - b_{Cd_XZn_{1-X}Se}x(1-x) \tag{1.2}$$

where $b_{Cd_XZn_{1-X}Se}$ is the bowing parameter.

1.3.2 VLS and VSS nanowire growth mechanism

Most well-known semiconductor NW growth mechanisms reported in literature are either catalyst free or catalyst assisted. Catalyst driven growth uses a metallic nanoparticle (NP) to facilitate growth of NWs along a particular crystal orientation of the semiconductor material. Catalyst assisted techniques include vapor-liquid-solid (VLS), vapor-solid-solid (VSS) or solution-liquid-solution (SLS) growth.

Vapor-liquid-solid growth

VLS is the most well-known and refined catalyst assisted NW growth mechanism and was first proposed by Wagner and Ellis in 1964 in Bell Labs for the growth of Si-NWs using Au-droplet. In a typical VLS growth process for the growth of semiconductor NWs, metal NPs (Au, Ag, Cu, Al, etc) are used as catalyst to initiate nucleation. The schematic of NW growth under VLS mechanism is shown in Fig 1.7. During the growth process, the metal NPs are first heated above the metal-semiconductor eutectic temperature to form liquid metal-semiconductor alloy. For *e.g.*, the melting temperature of Au is 1064° C. The growth of Si and Ge NWs with Au-NPs as catalyst under VLS scheme takes place around 360° C, which is around the eutectic temperature for Au-Si and Au-Ge. Similarly, for Au-NP catalyzed growth on GaAs, the eutectic of Au-Ga with 34 % Ga is formed at 339.4 °C [43]. Solubility of As in Au is very low [44].

The semiconductor source material in vapor phase impinges on the NP and on the sides of the NW. It diffuses diffuse into the liquid alloy and this quickly results in a supersaturation of the semiconductor material in the liquid alloy. Any further diffusion of the semiconductor material results in a liquid/solid interface with the formation of a nuclei. The newly generated nuclei propagates along the liquid/solid interface to form a new layer (a ledge) of the semiconductor crystal. This process is repeated leading to continued growth of NW in a layer by layer fashion. Growth of NW is therefore achieved through a transfer of the semiconconductor material from the vapor phase into the liquid alloy at the vapor/liquid

interface, followed by continuous solid addition at the liquid/solid interface. The ledge formation and layer-by-layer growth was confirmed through in-situ TEM obervation for the growth of Si NWs using Pd as catalyst [45].

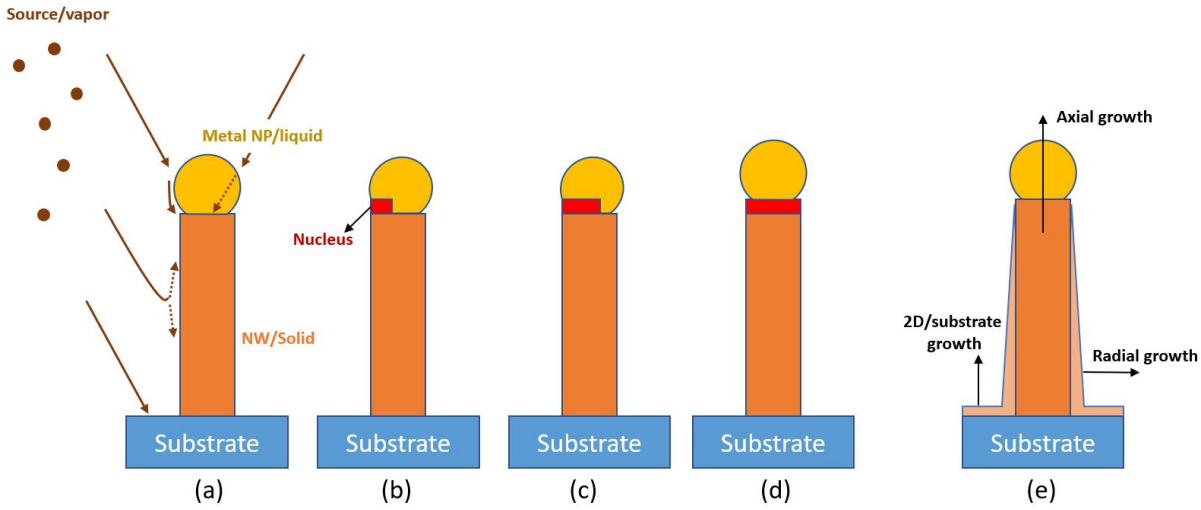

Figure 1.7: Schematic of the VLS NW growth process. (a) Different phases of the semiconductor material i.e in vapor phase (as source), in liquid phase (in metal NP) and in solid phase (NW). (b) Formation of a nuclei at the liquid/solid (metal NP/NW) interface. (c) Ledge propagation and nucleation. (d) Formation of a completely new layer of the NW. (e) Different growth process during the VLS growth of NWs. NW axial growth via metal catalyst, NW radial and substrate growth via direct deposition.

During the NW growth, the metal NP sits at the top of the NW. The role of the metal NP is two fold: first to act as catalyst for the growth of NWs and second, to partially control the radius of the NW [46].

Alongside the catalyst-mediated growth that results in the axial growth of the NW, direct vapor deposition on the sidewalls of the NW and on the substrate surface also exists. This leads to radial growth of the NW, and eventually tapering of the NW as the length increases. This process is illustrated in Fig 1.7 (e).

Although VLS mechanism is widely used for the growth of NWs, growth of CdSe-ZnSe QD-NW in VLS mode may not be the most suitable. During VLS growth, the solubility of the atoms in the liquid NP is high. The NP therefore depletes progressively during growth. This is a problem for the growth of heterostructures along the NW as it is necessary to deplete the NP of one type of atoms before inserting the other type.

Vapor-solid-solid growth

If the NP-semiconductor eutectic temperature is above the NW growth temperatures then the NP remains crystalline even during growth. Due to the crystalline nature of the NP during growth, the percentage of semiconductor material that diffuses in the NP is very small. This growth mechanism is called the Vapor-Solid-Solid (VSS) growth mode because the NP (catalyst) and the NW both are in solid phase. Rest of the growth process for VSS is similar to VLS.

We grow our ZnSe NWs on ZnSe buffer layers using Au-NPs. The lowest eutectic temperature of

Au-Zn and Au-Se which is 684° C with 34.5% of Zn and 760°C with 52% of Se respectively [47]. Buffat *et al.* [48] studied the melting point of Au-NPs as a function of their radius, and for an Au NP of about 2.5 nm radius, the eutectic temperature could be reduced by about 200° C. We use growth temperatures for ZnSe NWs between 300-400° C and Au-NP of about 4 nm radius. This modified eutectic for the Au-NPs. Therefore, our NW growth takes place in VSS growth mode.

The main advantage of VSS over VLS growth mode for growing a QD-NW system is the possibility of having abrupt interfaces between the QD and the NW. In VSS mode, the solubility of catalyst is low (so growth rates are also low), therefore, the catalyst depletes the semiconductor atoms very fast and consequently abrupt interfaces can be achieved. Moreover, VSS growth of ZnSe NWs on ZnSe buffer layers prevents incorporation of impurities like Si or Ga in the ZnSe NWs (if grown directly on Si or GaAs substrates).

1.3.3 State of the art

Growth of semiconductor materials with MBE is like cooking. With years of experience with the growth of II-VI and III-V semiconductors within our group, over the last few years we have developed a base recipe for the growth of ZnSe NWs which needs further optimization and improvements.

ZnSe NWs can be grown by metal organic chemical vapor deposition [49] and MBE. MBE offers the possibility of precise control over growth parameters and in-situ monitoring of the growth process. For epitaxial ZnSe 2D-layers, it is known that optimum MBE growth temperatures are close to 300° C, as higher temperatures degrade optical properties [50]. The ZnSe NWs MBE growth temperatures are also usually in the 300-400 °C range. In 2005, A. Colli *et al.* [51] were able to grow very dense ZnSe NWs by MBE, catalyzed by Au NPs, at growth temperatures between 300-400° C on SiO_2/Si(001) substrate. The NWs were as thin as 10 nm in diameter but had a very high density, a lot of defects, kinks and were not vertically aligned. S. K. Chan *et al.* in 2005 [52] also reported growth of ZnSe NWs on (110), (100) and (111) oriented GaAs substrates by MBE using Au catalyst at a high temperature of 520° C. For both studies, the NW growth was reported to follow VLS growth mechanism. Only the NWs grown on (111) surface were vertically aligned. The NWs had a diameter of more than 30 nm with high density. Y. Ohno *et al.* [53] realized growth of ZnSe NWs on ZnSe(001) buffer layer on GaAs substrate at 250-300° C by MBE. The diameter at the top of NWs was reported to be in the range of 8 to 20 nm. Most NWs were tilted and kinked. The NWs were reported to have zinc blend structure. In 2010, C. H. Hsiao *et al.* [54] realized growth of high density ZnSe/ZnCdSe NWs by MBE on oxidized Si(100) substrate at a growth temperature of 280 °C. The NWs were reported to have a tapered shape ($\sim$1.8 μm length and $\sim$42 nm diameter) with a mixture of Zinc Blende and Wurtzite structure. More recently, in 2017, Y. Kim *et al.* [55] reported Au and Ni-catalyzed growth of ZnSe and CdSe NWs on Si(100) substrate under VLS mechanism. The ZnSe NWs were grown at 750 or 800 °C and CdSe NWs were grown at 550-600 °C. The ZnSe NWs were reported to have both Zinc Blende and Wurtzite structure, while CdSe NWs only had Wurtzite phase when Au was used as catalyst. However, Zinc Blende phase was also reported for CdSe NWs when Ni was used as catalyst. In 2018, D. Wisniewski *et al.* [56], reported single ZnSe NWs based field effect transistor. The NWs were grown on Si(111) substrate, catalyzed by Au-droplets, at 650 °C. Single NWs were isolated by suspension in a solution of isopropyl alcohol and drop-cast onto a thermally oxidized (100 nm SiO_2) silicon substrate.

Within our group, in 2009, first studies of growth of ZnSe NWs included growth on SiO_2/Si(001) substrates where the NWs had no epitaxial relations with the substrate [57]. As a result, there was no control over the orientation of the NWs. To control the orientation of the NWs, an epitaxial relation be-

tween the NWs and the substrate was necessary. However, one problem faced during the growth of ZnSe is the unavailability of commercial ZnSe substrates. Since, the lattice parameter of bulk GaAs (0.565 nm) and bulk ZnSe (0.567 nm) at 300 K are very similar, ZnSe NWs were then grown on ZnSe(100) buffer layers on GaAs(100) substrates [58] (see Fig 1.8 (a)). The ZnSe buffer layer acts as a pseudo-substrate and prevents Ga and As contamination in the ZnSe NWs. But the problem with these NWs was that most of the NWs were tilted at an angle as the growth of the NWs is along the (111) direction. Thibault Cremel from our group then tried growing ZnSe NWs on ZnSe(111)A and ZnSe(111)B surfaces [12]. On ZnSe(111)A surface, NWs were mainly bent during the growth, which suggested that they are composed of a lot of defects. On ZnSe(111)B, NWs were mainly vertically oriented. It was also observed that the ratio of Zn:Se sent onto to the sample had a profound impact on the yield of the NWs. Under Zn excess and stochiometric conditions, the NWs growth was inhibited (see Fig 1.8 (b)). The NWs were tilted and had a rough lateral surface. However, under Se-rich conditions, NWs were mainly vertical with a smooth lateral surface.

In 2009, A. Tribu characterized the CdSe-ZnSe QD-NWs grown on SiO_2/Si(001) substrates and showed single-photon emission up to 220 K [57]. However, the emission was weak and since the NWs density was very high, single photon emission was not possible on as-grown sample. Single-photon emission could only be shown on a single QD-NW dispersed on a silicon substrate. Then in 2012, Samir Bounouar [11] characterized CdSe-ZnSe QD-NWs grown on ZnSe(100) buffer and showed for the first time anti-bunching at 300 K (Fig 1.9) using the biexciton state with a short lifetime of 300 ps. As far as we know, no other system other than CdSe QDs has shown room temperature single-photon emission in the visible range. However, the emission from these NWs was very weak as they had no shell (NW radius about 5 nm and no shell) to guide the light and also to protect the QDs from carrier traps in the form of defects and dangling bonds at the surface. Only a handful of NWs could emit at high temperatures, and only one could show single photon emission at 300 K out of the hundreds of NW that were checked. Also, emission was collected from NWs dispersed (lying flat) on another substrate with a bottom mirror to enhance light extraction.

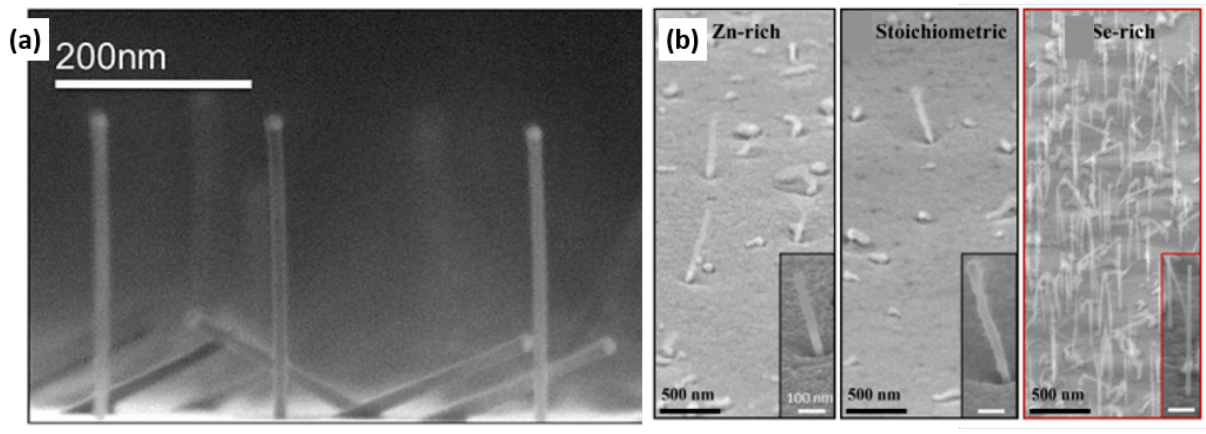

Figure 1.8: (a) Cross-section SEM image of ZnSe NWs grown on ZnSe(100)-GaAs(100) surface. Taken from [11]. (b) Side view SEM image (65 angle) of ZnSe NWs grown on ZnSe(111)B-GaAs(111)B surface under Zn-rich, stochiometric and Se-rich conditions. Taken from [12].

Although the NWs grown by Thibault Cremel were as per expectations (straight on ZnSe(111)B

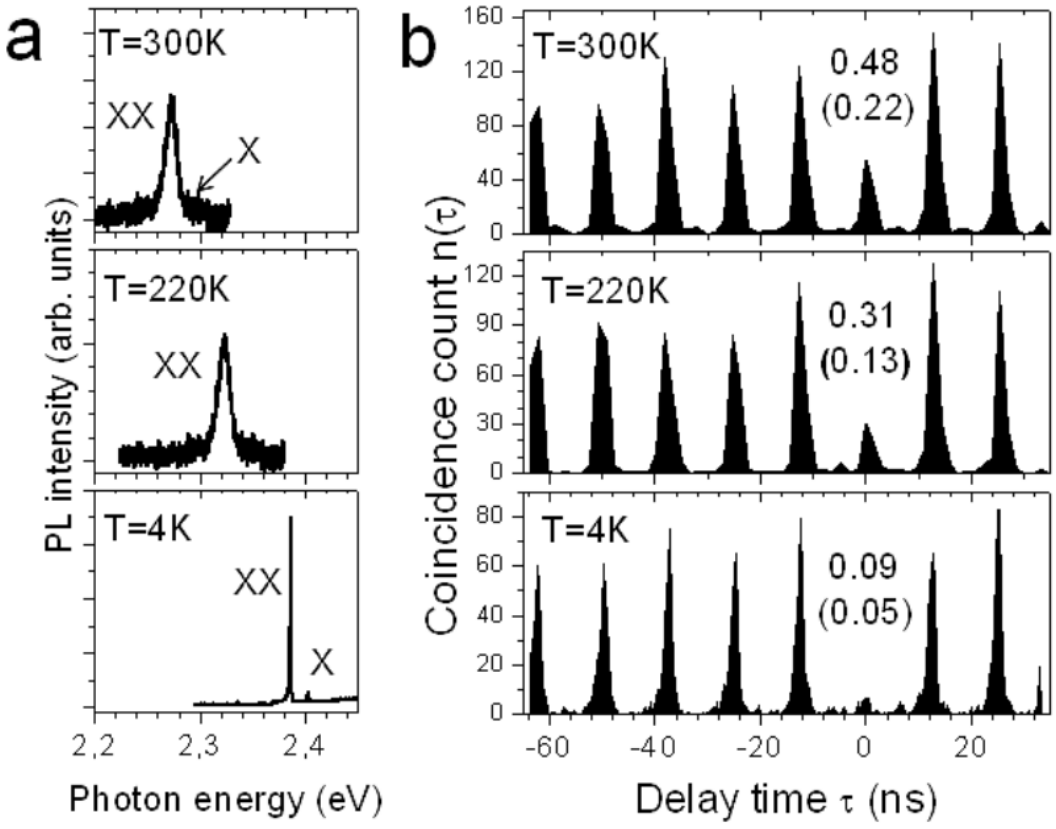

Figure 1.9: Single photon emission from a CdSe QD in ZnSe NW from our group. (a) μ-PL measurements at different temperatures and (b) anti-bunching measurements on the XX -peak at 4, 220 and 300 K. Image taken from [11].

buffer), we had very little understanding of the growth parameters and were struggling to have a complete control over the growth process. For example, NWs density was too high to probe a single NW from the top on an as grown sample. CdSe-QD insertion in these NWs was mostly laterally and not in the center. Also due to lack of an epitaxial shell, these QD-NWs had a very weak emission intensity with no control over the emission profile.

The knowledge gained over the years in our group for the growth of ZnSe NWs on ZnSe(111)B buffer layers is used in this work to further improve and optimize the growth process.

1.4 Experimental techniques

In this section, we discuss the main tools and techniques that we used to realize and characterize the CdSe QD in ZnSe/Zn(Mg)Se NW based single-photon emitter. We will start with the growth technique-MBE, that was used to grow QD-NW heterostructure. And then we discuss the techniques used to study the structural morphology of the QD-NWs in section 1.4.2. Finally, will be discussed the optical characterization techniques used to study the single photon emission of the QDs in section 1.4.3.

1.4.1 Molecular beam epitaxy

All thin film deposition techniques can be generally divided into two categories: chemical vapor deposition (CVD) and Physical Vapor Deposition (PVD). In CVD technique, a heated substrate is exposed to one or more volatile precursors (mostly halides or hydrides) which interact and/or break down and are deposited on the substrate through the process of diffusion. Atomic Layer Deposition (ALD) is a subset of CVD. In PVD technique, no decomposition of source material takes place. The source material goes from a condensed phase to gaseous phase which then enters a chamber with the substrate in high (or ultra-high) vacuum. The source material atoms then physically stick onto the substrate forming chemical bonds with the substrate material. Most common type of PVD processes are sputtering and evaporation.

MBE is a subset of PVD wherein epitaxial growth of materials takes place on a heated substrate under ultra high vacuum (UHV) conditions. Due to UHV conditions the atomic or molecular fluxes are in ballistic mode which means that their mean free path (distance traveled before collision) is longer than the source-substrate distance. The growth of new material is a kinetic driven process. First, atoms physically adsorb on the surface through Van der Waals interaction after which they can either adsorb on the substrate or get desorbed from the substrate. Two or more different types of atoms (for e.g., one from group-II and another from group-VI) can also interact with each other on the surface. Incorporation usually takes place near a ledge vacancy or a surface vacant site. For the first case, a step-propagation growth mode is followed and for the latter nucleation takes place. Both leads to a 2D-layer formation. For further reading on MBE, step growth and nucleation growth mechanism refer to [59], [60].

There are several advantages of MBE over other techniques: 1) extremely low growth (deposition) rates below monolayer (ML)/per second. This permits high quality growth of extremely thin films in a very precise and controlled way. 2) In-situ characterization such as Reflection High Energy Electron Diffraction (RHEED) is possible due to UHV environment. 3)Very high quality growth without defects and impurities can be realized. 4) Unlike CVD, deposition temperatures can be relatively low- 300-400° C for our CdSe-ZnSe QD-NWs. Unfortunately, it has some disadvantage too. It's a slow technique which means its more suited to scientific research than high volume production. Moreover, its an expensive and complex techniques (partly because of the requirement for UHV environments).

An image of the MBE setup used in this thesis is shown in Fig 1.10. The MBE setup consists of one introduction module to introduce the samples, two growth chambers and one metal deposition chamber. A Riber 32P growth chamber is used for the deposition of II-VI materials (tellurides and selenides) and other is MECA2000 growth chamber for the deposition of III-V materials (GaAs, InAs) as well as Au. The introduction module and the growth chambers are connected with each other and the sample remains in high vacuum while transferring from one chamber to another. Both growth chambers are fitted with the following:

- Knudsen effusion cells made of boron nitride, which stores and sublimates the source materials from the solid to gaseous state using high-powered electric current. II-VI chamber has 8 effusion cells for Se, Cd, Zn, Te, Mn, Mg, ZnTe and CdTe. The III-V chamber has effusion cells for Ga, As, In and Au. In front of each cell is a mechanical shutter which provides rapid opening or closing of the effusion cells. The fluxes from the effusion cells can be measured using a beam flux sensor.

- The chambers are fitted with a pumping system consisting of a cryopump operating at 10 K, an ionic pump and a tungsten sublimation pump. Together they create UHV in the range of 10^{-11}

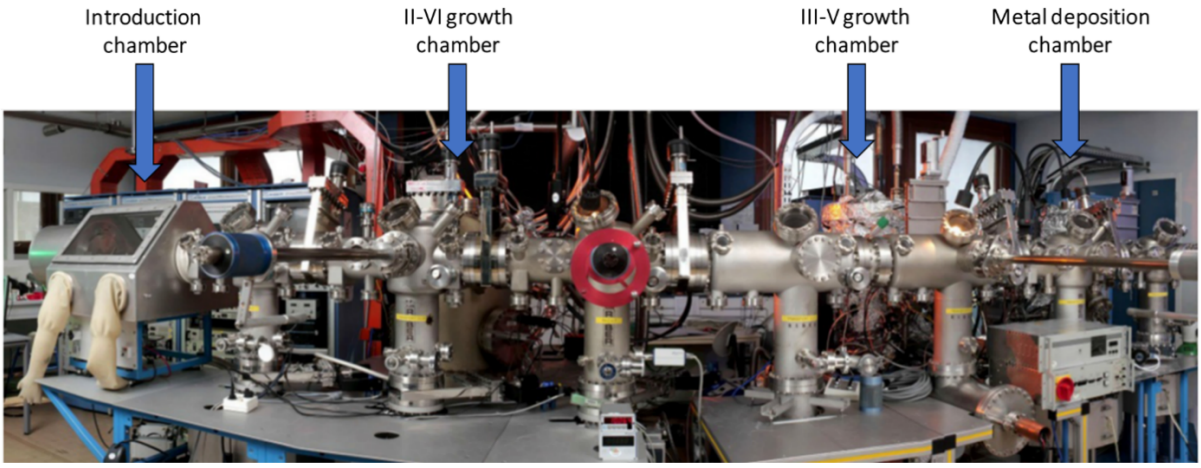

Figure 1.10: MBE growth system used for the epitaxial growth of the samples presented in this work.

Torr.

- Mass spectrometer which measures the chamber background composition during vacuum.
- RHEED module which measures the growth rate and the quality of thin film growth.
- Finally, the substrate is glued on a Molybdenum-block with liquid Indium through surface tension. Indium provides an excellent heat transfer between the block and the substrate. The Molybdenum-block is heated by radiation. The temperature of the substrate is measured with a thermocouple which is in direct contact with the Molybdenum-block. For good control over the growth of the NWs, ideally uniform and reproducible heating across the substrate surface is needed. Temperature variations from one Molybdenum-block to another are to be taken in account. The holder and also rotation of the block rotation on its plane.

For high reproducibility, sometimes samples were glued to a silicon wafer which was then attached on a ring shaped molybdenum holder. In this case the silicon wafer is directly heated. With this configuration we expect more uniformity of the samples.
Top and side (vertical) view scheme of the II-VI and III-V chambers in our MBE setup is shown in Fig 1.11. From the side view, it can be seen that the effusion cells make a certain angle with the substrate normal which can result in uneven distribution of fluxes on the sides of the NWs. To minimize its effect, we rotate the sample during NW growth.

1.4.1.1 Reflection High Energy Electron Diffraction

The MBE chambers are fitted with a RHEED system to precisely monitor the MBE growth in-situ. It helps us in determining the nature and quality of the crystalline material that is grown and also its growth rate. RHEED consists of an electron gun that sends a collimated electron beam (size $\sim$1mm^2, accelerated at 30 KV) that hit the substrate surface at a grazing incident angle of 2-3°. Due to such low incidence angle and due to small wavelength of electrons, the penetration depth of electrons is just a few mono-layers (ML) layers. The beam is scattered by the sample surface before hitting a phosphor screen

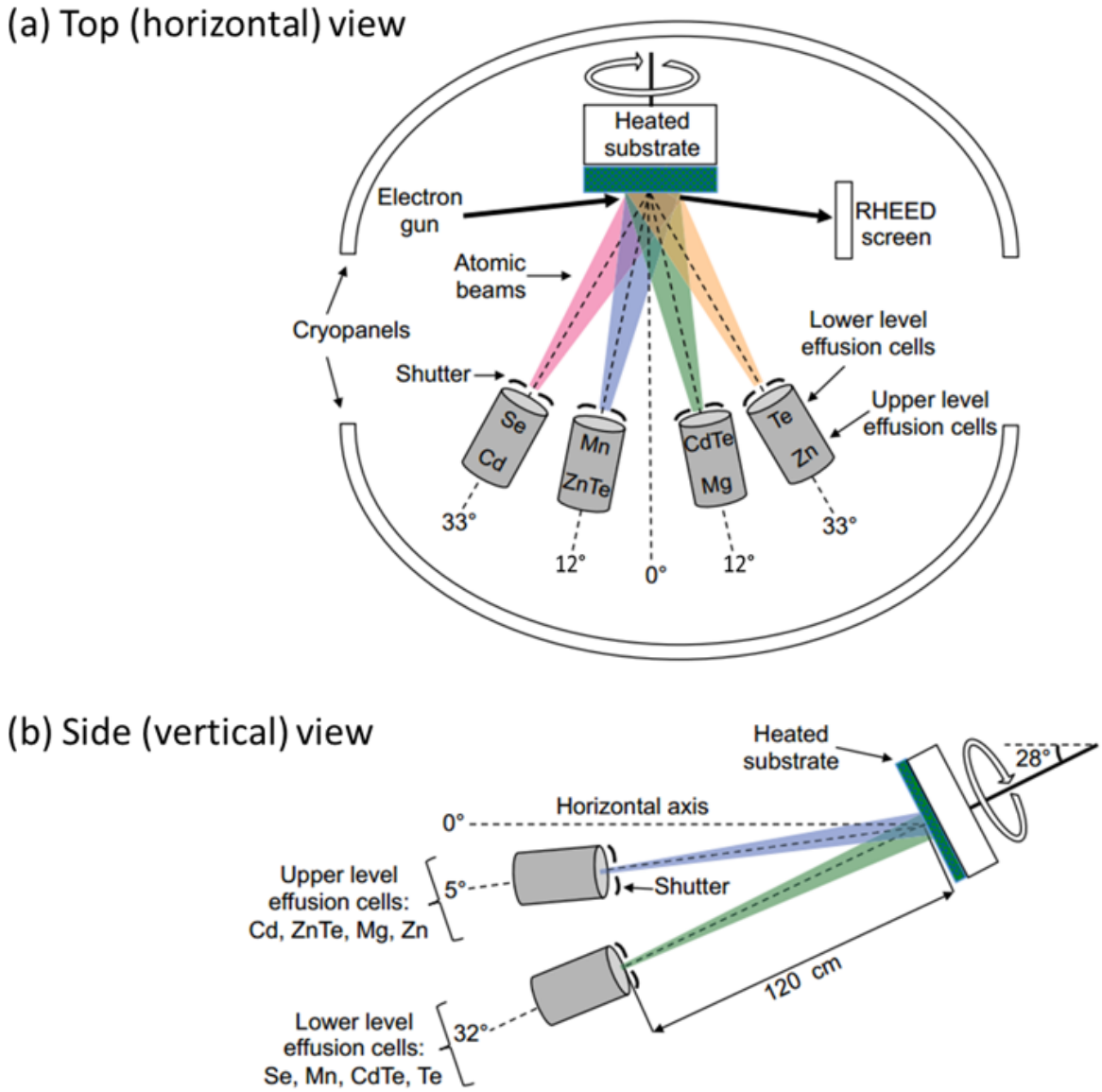

Figure 1.11: Scheme for the top and side view of the II-VI growth chamber in our MBE system. The angles of the effusion cells are indicated with respect to the horizontal axis of the chamber.

resulting in a diffraction pattern which corresponds to the reciprocal lattice of the substrate surface. In addition to the crystalline structure of the grown material, RHEED patterns can help us identify morphology of the substrate surface:

- a perfect 2-D crystalline surface result in vertical long streaks perpendicular to the sample surface (Fig 1.12 (a)).
- An incomplete 2D surface or rough surface gives vertical streaks with breaks in between (Fig 1.12 (b)).

- A polycrystalline surface (powder) results in concentric circular pattern (1.12 (c)).

- If the surface has nano objects on top such as SKQDs or NWs, a diffraction pattern with dots will be observed (1.12 (d)).

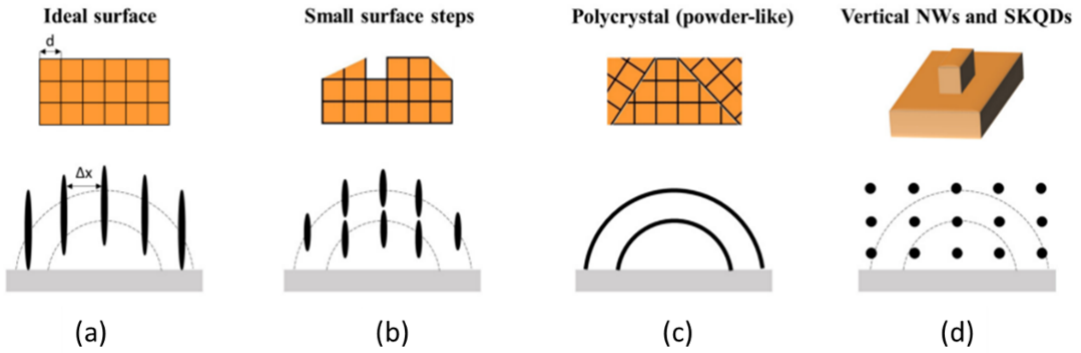

Figure 1.12: Scheme for the RHEED pattern observed for different surface morphologies. Image taken [12].

Real time 2D growth rates and information about in-plane lattice can be obtained by following the modifications in RHEED pattern. In Fig 1.13 is shown how a 2D layer formation takes place. At first, when a perfect 2D surface exists, the RHEED pattern has the maximum intensity. After some growth time, the 2D surface is covered with islands but a second 2D layer has not yet completely formed. The RHEED intensity therefore decreases due to diffraction from a rough surface. This goes on till half of the surface is covered with islands and the intensity reaches a minimum. Any growth from this point increases the RHEED pattern intensity and reaches a maximum when a second 2D layer is complete *i.e.* when one ML is deposited. This fluctuation in RHEED intensity is called RHEED oscillations and can be used to measure growth rates. One RHEED oscillation corresponds to 1 ML growth on the surface.

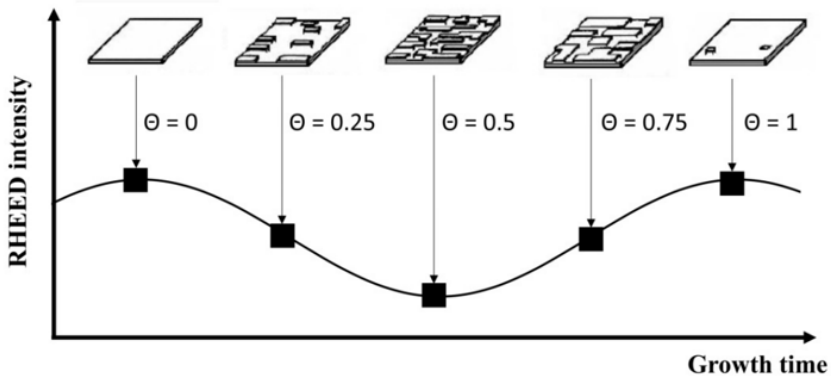

Figure 1.13: Scheme showing the idea behind the RHEED oscillations.

1.4.1.2 Growth rate calibration

Since we have separate Zn, Se, Cd and Mg effusion cells for the growth of CdSe QD in ZnSe/Zn(Mg)Se NWs, to be reproducible and accurate, we do not rely on measured beam equivalent pressure (BEP) fluxes. Before every growth, we calibrate the Zn and Se cell fluxes for a required growth rate using RHEED oscillations.

For this we use reference samples: ZnTe(001) for calibration of Zn flux, CdSe(001) for Se and CdTe(001) for Cd and Mg. Calibrations on these reference samples are done at growth temperatures optimal for depositing these materials and are 340° C, 380° and 300° C for ZnTe(001), CdSe(001) and CdTe(001) respectively. These temperatures are also close to NW optimal growth temperatures – between 300 to 400° C. For calibration of Zn on ZnTe(001), Te is in excess. Similarly for Se calibrations on CdSe(001), Cd is in excess and for calibration of Cd and Mg on CdTe(001), Te is in excess.

1.4.1.3 Total flux sent onto the sample

Throughout this thesis work, more than 60 samples were prepared. To compare different samples grown at different growth rates and growth time, what is convenient is to compare the total amount of material sent onto the sample. For our system, we grow ZnSe NWs with Se in excess, therefore Zn limits and controls the growth of ZnSe NWs. For different growth times and different flux (ϕ) amounts of Zn in ML/s, we can calculate the Zn amount sent onto the substrate in nm. This makes it easier to compare different samples.

As said in the previous section, Zn flux in ML/s is measured using RHEED oscillations on a ZnTe (001) reference substrate (ϕ_{ZnTe}). But flux in ML/s depends on the crystal lattice and its orientation. The ϕ_{ZnTe} in ML per unit time per unit area is $\frac{\phi_{ZnTe}}{2(a_{ZnTe})^2}$. Where a_{ZnTe} is the lattice constant for ZnTe ZB crystal with value of 0.610 nm. If the same Zn amount is sent onto the ZnSe surface, the ϕ_{ZnTe} in ML per unit time per unit area must be changed to $\phi_{ZnTe}\frac{(a_{ZnSe})^2}{(a_{ZnTe})^2}$ in ML/s to take into account the difference in lattice parameter of the 2 materials. Now, the Zn flux in nm/s ([Zn]) on a ZnSe surface can be given as:

$$[Zn] = \phi_{ZnTe}\frac{1}{2}\frac{(a_{ZnSe})^3}{(a_{ZnTe})^2} \tag{1.3}$$

where a_{ZnSe} is the lattice constants for ZnSe ZB crystal with value 0.567 nm. Equation 1.3 gives the flux impinging on the 2D surface of ZnSe in nm/s.

1.4.1.4 Sample tilt

During NW growth, we sometimes tilt the sample by 10° towards the Zn cell to change the ratio of flux onto the sides of the NWs to the flux onto the substrate. To understand this, we have to look again at the scheme for the position of effusion cells in our II-VI growth chamber. The incident angle (α) from the effusion cells with respect to the sample normal (also the NW axis) in the horizontal plane (α_h) are as shown in Fig 1.11 (a). In the vertical plane, α_v is 23° for the upper level (Zn, Mg, ZnTe, Cd) and -4° for the lower level (Se, Mn CdTe, Te) effusion cells (see Fig 1.14 (a)).

In the "standard" position, flux ϕ on the axis of the cells is at the center of the moly-block (hence the sample). Therefore, the flux normal to the NW sides is then given as: $\frac{\phi}{\pi}\sin\alpha$ (averaged over NW's circumference, hence the factor $1/\pi$). And the flux normal to the substrate is: $\phi\cos\alpha$. Therefore, the tangent of α gives the ratio of fluxes arriving at the sides of the NW to the substrate. The $\tan\alpha$

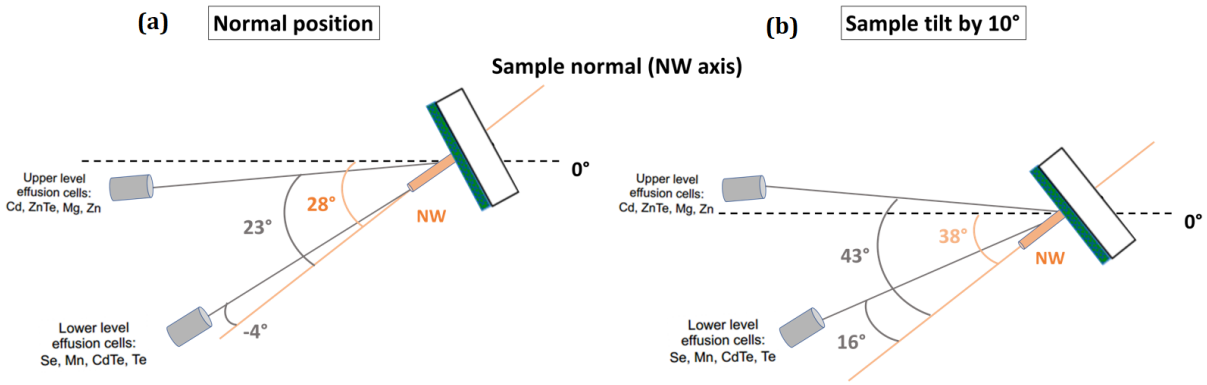

Figure 1.14: Scheme for the position of effusion cells at (a)normal and (b) tilted(10°) position of the sample. In blue are given the angles which the effusion cells makes with the sample normal.

is calculated as: $\tan\alpha = \sqrt{\tan^2\alpha_H + \tan^2\alpha_V}$, and is given in 1.2 for all the cells in our II-VI MBE chamber.

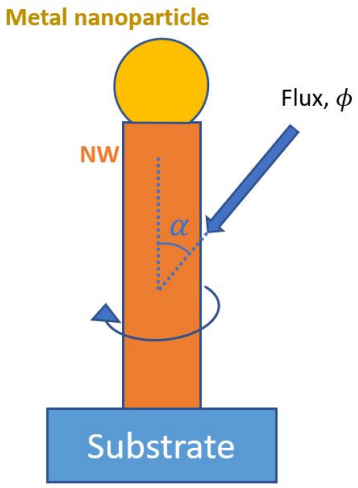

Figure 1.15: Flux ϕ arriving on the substrate and on the NW sidewalls in our MBE setup. Flux on the NW sidewalls is averaged over the circumference of the NW.

Effusion cells	$tan(\alpha)$ – normal position	$tan(\alpha)$ – 10° sample tilt
Cd, Zn	0.78	1.14
Se, Te	0.65	0.71
ZnTe, Mg	0.47	0.96
Mn, CdTe	0.22	0.36

Table 1.2: $\tan\alpha$ values for normal and tilted position for all effusion cells in the II.VI chamber. $\tan\alpha$ is the ratio of flux arriving on the sides of the NWs to the flux arriving on the surface of the sample.

When, the sample is "tilted" by 10° towards the Zn effusion cell, the new values for α_v are 43° and 16° for the upper and lower level cells respectively. The $\tan\alpha$ values in the 10° tilted position are also given in table 1.2. It can be seen that $\tan\alpha$ values for Zn changes from 0.78 to 1.14 (a factor of 1.46) when sample is tilted. Therefore, by tilting sample by 10°, we send more Zn flux on the sides of the NWs compared to the substrate surface.

1.4.2 Morphology and composition characterization techniques

The main characterization tool used to study the morphology and composition of the QD-NWs is electron microscopy- scanning electron microscope (SEM), transmission electron microscope (TEM) and energy-dispersive X-ray (EDX) spectroscopy.

1.4.2.1 Scanning electron microscope

SEM imaging was performed on a Zeiss Ultra 55 (field emission gun) microscope at 5-15 kV with typical beam currents of 0.1-2.5 nA. Standard secondary electron imaging using in-lens detector were used to characterize the sample. With SEM we can measure the size of the NWs and the density of the NWs on the substrate.

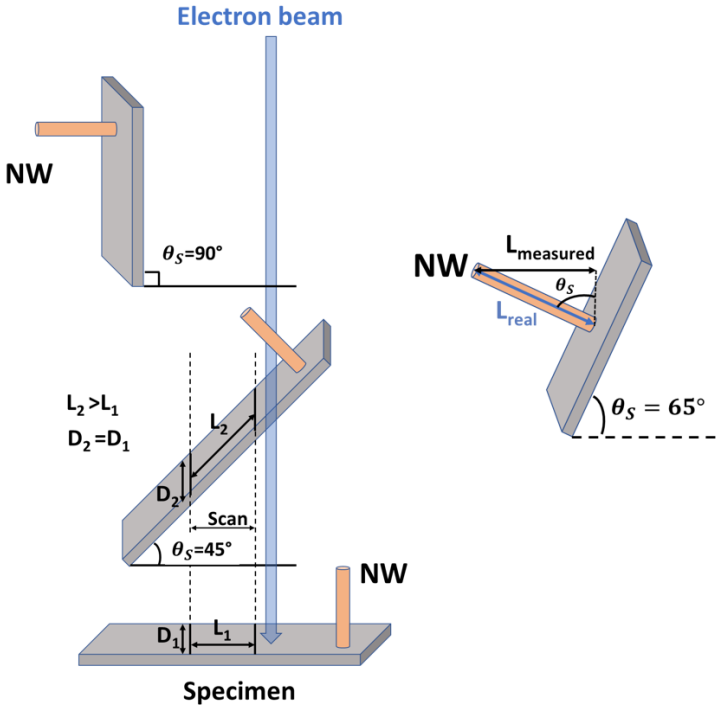

Figure 1.16: Scheme to show the affect of SEM measurements with different SEM-angle (θ_S) values.

The samples were cleaved from the center and imaged at different θ_S values (see Fig 1.16). The θ_S of 65° was used to study the surface of the sample, NW density, and length and diameter of the NWs. An θ_S of 90° was used mostly to measure the thickness of the 2D-layer that was formed during NW growth. It should be noted that because of sample tilt, projection effects should be considered (see Fig 1.16).

We measure the size (diameter and length) of the NWs using SEM images taken at θ_S of 65°. While the measurement of the diameter of the NWs remains unchanged, the real length of the NWs is given by:

$$L_{real} = \frac{L_{measured}}{\sin(\theta_S)} \tag{1.4}$$

where $L_{measured}$ is the SEM measured length and θ_S is in radians. Similarly, to calculate the density of the NWs on the substrate, the lateral length on the substrate in the SEM image remain unchanged, whereas the vertical length in the image is given by:

$$Real\ vertical\ length = \frac{length\ measured}{\cos(\theta_S)} \tag{1.5}$$

1.4.2.2 Transmission electron microscope

Crystallographic information about the NWs, the QDs and the NPs can be obtained by transmission electron microscope (TEM). All TEM measurements were performed by Dr. Martien Den Hertog with the Philips CM300 high resolution TEM (HRTEM).

The samples for TEM measurements were prepared in two different ways- in one method a thin piece of the sample is cleaved from edge of the sample. It is described in [61]. In another method, NWs are dispersed on a carbon grid by direct contact with the surface. Sometimes a thin carbon layer (5-10 nm) was deposited on the NWs to protect them from electron beam damage and to also reduce their movement.

1.4.2.3 Energy dispersive X-ray spectroscopy

Energy-dispersive X-ray (EDX) spectroscopy allows to analyze the elemental composition of a sample. When an electron beam hits the inner shell of an atom, it knocks off an electron from the shell, while leaving a positively charged electron hole. When the electron is displaced, it attracts another electron from an outer shell to fill the vacancy. As the electron moves from the outer higher-energy to the inner lower-energy shell of the atom, this energy difference can be released in the form of an X-ray. The energy of this X-ray is unique to the specific element and transition [62]. In the end, a spectrum is generated which is a histogram of the number of photons collected as a function of their energy. To analyze the concentration of an element in the sample, the background needs to be subtracted and the intensity of each element line is calibrated to a standard sample with known thickness and concentration. EDX is particularly useful to detect the presence and location of the QD and to map the chemical distribution of elements in the QD and in the NW [63].

All EDX measurements were performed by Dr. Eric Robin using an EDX spectrometer coupled to a TEM (FEI Tecnai Osiris TEM equipped with four silicon drift detectors and operated at 200 kV).

1.4.3 Single-photon detection

Detection of single photons from a QD-NW is a very challenging task. In this section, we discuss the optical setups and techniques that were used to characterize single QD-NWs for their optical properties.

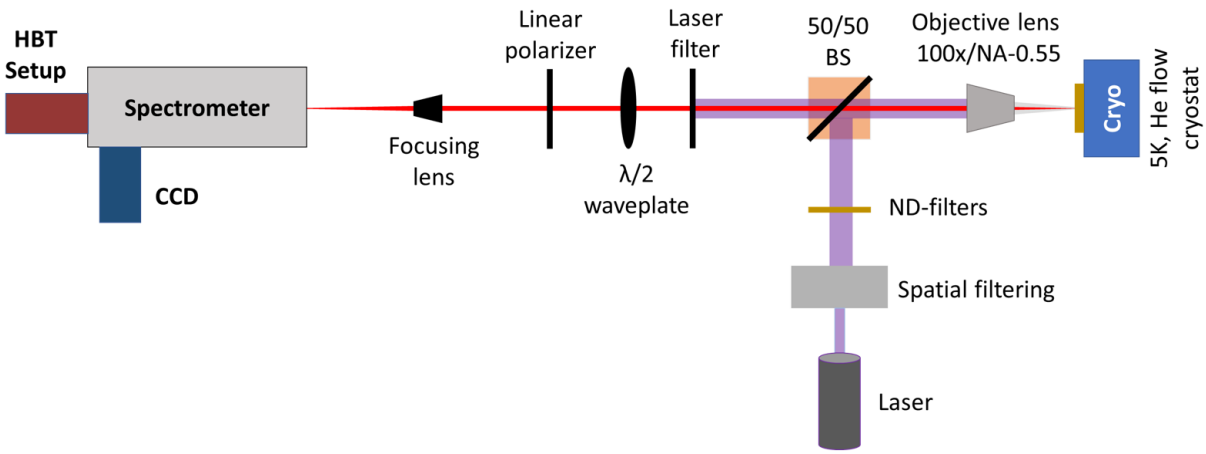

Figure 1.17: Schematic representation of the μ-PL setup we used for the basic optical characterization of the QD-NW.

1.4.3.1 Micro-photoluminescence setup

The main method used in this thesis to characterize the optical properties of the QDs and NWs is μ-PL (micro-photoluminescence) spectroscopy. A schematic of the setup used is given in Fig 1.17.
Two lasers are available to excite the QD in continuous wave (CW) excitation: a 405 nm (3.06 eV) and a 488 nm (2.54 eV) diode laser. ZnSe NW emit around 2.82 eV (440 nm) [39] and CdSe QD within the range of 500-600 nm (2.48-2.07 eV). The CdSe-QD in the NW can be excited indirectly with the 405 nm laser where charge carriers created in the ZnSe NW relax to the QD. The 488 nm laser (excitation below the barrier bandgap) allows exciting directly the QD through 0D-1D transitions (with relaxation of the 1D-carrier, electron, or hole). This transition is described in Fig 1.18.

The laser beam is first spatially filtered using beam expanders, objectives, and pinholes for a better-focused beam. Laser excitation power is then tuned with the help of a rotating density filter after which it is passed through a 50/50 beam splitter and then focused on the sample using a long working distance microscope objective of numerical aperture NA=0.55 and 100x magnification. This results in a laser spot of about 1 μm diameter on the sample. The sample is mounted on a cold finger cryostat cooled with He and the sample can be cooled down to 5-6 K. The cryostat itself is mounted on a piezoelectric stage for nm adjustments of the laser spot on the sample. The emission light is analyzed by a 0.46 m spectrometer equipped with 600 gr/mm and 1800 gr/mm gratings. The spectrometer then sends the emission light to a Peltier charge-coupled device (CCD) of 1024×256 pixels.

To study the PL intensity with respect to the polarization angle, we used a rotating $\lambda/2$ waveplate placed in front of a linear polarizer which acts as a polarization analyser. The axis of the polarization analyser is aligned parallel to the axis of the spectrometer slits (for maximum transmission). For linearly polarized light the $\lambda/2$ waveplate rotates the angle of the electric field of the emitted light with respect to the polarizer axis. The intensity of emitted light as a function of angle follows Malus's law.

1.4.3.2 Time-resolved spectroscopy setup

Lifetimes of carriers in the QD were recorded using a time-correlated single-photon counting (TCSPC) module [64]. The schematic of the setup used is shown in Fig 1.19. The TCSPC module measures

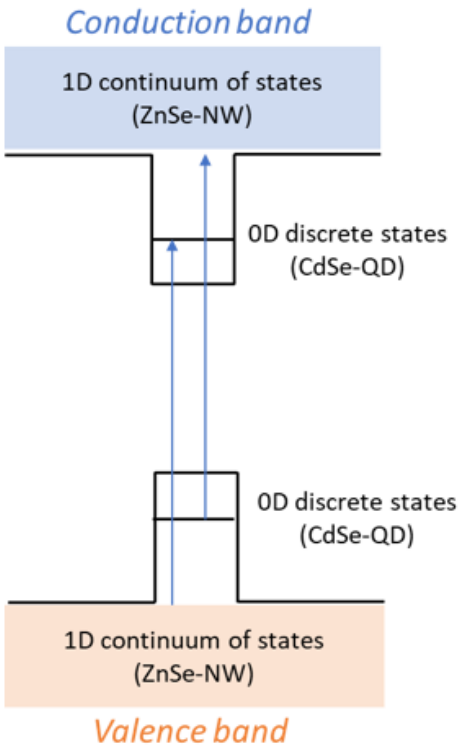

Figure 1.18: Scheme for 0D to 1D transitions in CdSe QD in a ZnSe NW. An electron can jump from the ZnSe NW valence band with 1D density of states to the CdSe QD conduction band, or an electron can jump from the QD valence band to the ZnSe NW 1D density of states (relaxing further into the QD conduction band).

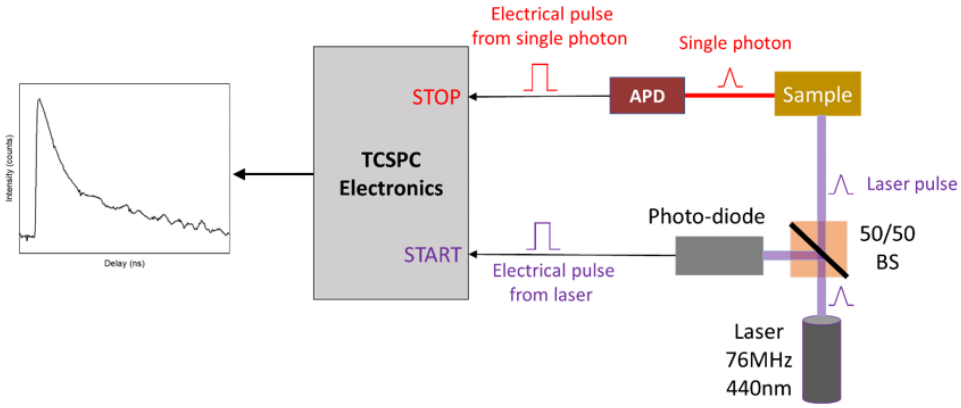

Figure 1.19: Schematic representation of the working principle of the time-resolved spectroscopy setup used in this thesis to characterize the lifetime of carriers in the QD.

the arrival time of single-photons with respect to a reference signal. A laser pulse starts the clock and the detected single-photon stops the clock. The laser first passes through a 50/50 beam splitter which

splits it into two paths, one-half towards the photo-diode and the other-half towards the sample. The photo-diode provides the start signal to the TCSPC module. And after excitation of the sample with the other half of the laser pulse, emission from the sample is detected by an avalanche photo-diode (APD), which provides the stop signal.

The time measured between the start and stop signal is collected for hundred-thousands or millions of photons. This results in a histogram, where the x-axis is the time measured and the y-axis is the number of photons counts. The temporal resolution of the setup is limited by the response time of the fast APD used here, which is 50 ps [65].

The laser used is a near infra-red Titanium-Sapphire laser which is doubled in frequency to 440 nm (2.82 eV) using a frequency doubling crystal, β-BaB_2O_4. The pulse frequency of the laser is 76 MHz (13.1 ns repetition time).

1.4.3.3 Anti-bunching experiment setup

Single-photon emission can be confirmed using the Hanbury Brown Twiss (HBT) experiment setup, which was originally designed to measure the angular diameter of stars [66]. The HBT experiment can be used to measure the second-order intensity correlation function ($g^2(\triangle t)$) of the emitted photons. $g^2(\triangle t = 0)$ then gives the purity of the single-photon source. Nowadays, the HBT experiment setup is commonly employed in the field of quantum optics.

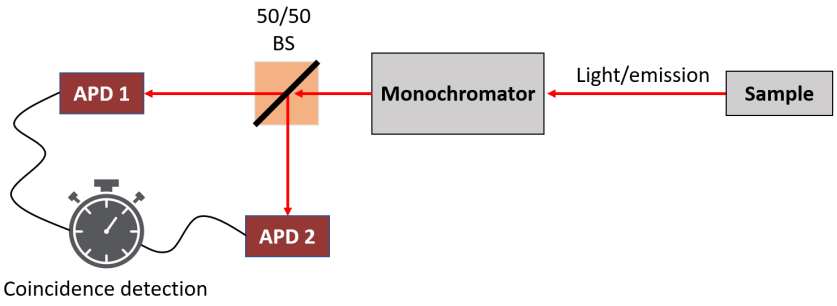

Figure 1.20: Schematic representation of the working principle of the HBT setup.

A schematic of the HBT setup used in this thesis is shown in Fig 1.20, where a beam of photons from a light source is split into two beams by a 50/50 beam splitter. Each beam is sent to an APD. These two APDs produce signal pulses when they are triggered by the incoming photons. In a start-stop auto-correlation method, a signal pulse from one of the APDs starts a time counter (t) until the counter receives a signal pulse from the other APD(stop) at time $t+\triangle t$. The counter then records one coincidence at the time delay ($\triangle t$) between these two signal pulses. This process results in a histogram showing the number of photon pairs with arrival time separation of $\triangle t$. If the probability of detecting one photon in a one-time interval is much smaller than 1, this histogram (normalized by the averaged histogram value for much longer delay times than the correlation time) can be approximated as the second-order correlation function $g^2(\triangle t)$, which can be expressed in quantum mechanics as [67]:

$$g^2(\Delta t) = \frac{\left\langle \Psi \left| \hat{a}^\dagger(t)\, \hat{a}^\dagger(t+\Delta t)\, \hat{a}(t+\Delta t)\, \hat{a}(t) \right| \Psi \right\rangle}{\left\langle \Psi \left| \hat{a}^\dagger(t)\, \hat{a}(t) \right| \Psi \right\rangle^2} \tag{1.6}$$

where $\hat{a}$ and $\hat{a}^{\dagger}$ represent the annihilation and creation operators for the photon number states in an electromagnetic field Ψ. If a stream of perfect single-photons is measured by the HBT setup, since a single-photon cannot be detected by both APDs at the same time, the two APDs will never produce signal pulses at the same time. As a result, there will be no coincidence occurring at time delay $\triangle t = 0$. Hence, a perfect single-photon source should exhibit $g^2(0) = 0$. On the other hand, in a coherent light source, like lasers, the emitted quantum states have no well-defined photon number and give $g^2(0) = 1$.

However, an actual single-photon source, produced by periodic excitations, can emit single-photons most of the time, but also has a small probability of emitting multiple photons, then $g^2(0)$ will be greater than, but close to, 0. A quantum light source, which can produce photon number states, will give a $g^2(0) < 1$, indicating that photon anti-bunching is occurring. A common criterion for a quantum light source to be considered as a "good" single-photon source (usable for quantum cryptography) is $g^2(0) < 0.5$. However, for practical applications in quantum optics and quantum information a $g^2(0)$ close to ideal zero should be aimed for.

Continuous and pulse excitation

To measure the g^2 function we have two options for the excitation of the QD: continuous wave (CW) or pulse excitation. In Fig 1.21, are shown typical autocorrelation histograms for CW and pulse excitation at 5 K for a pure two-level system.

For CW excitation, antibunching is observed through a characteristic dip at zero delay, confirming that no two photons are detected at the same time by the two APDs. The correlation tip of the characteristic dip is such that:

$$\frac{1}{\tau_d} = \gamma_{rad} + \gamma_{pump} \tag{1.7}$$

where γ_{rad} is the radiative and γ_{pump} the pump rate. Therefore, the correlation time is at best the radiative lifetime. In pulse mode, each peak represents the coincidences recorded after excitation with laser pulses. The zero-delay peak here represents the probability of two photons detected at the same time by the two APDs. And therefore, the anti-bunching signature for pulse excitation is the absence of a peak. However, this is (as we will see in chapter 4) true only if the lifetime of the excited state is much lower than the repetition time of the laser pulses.

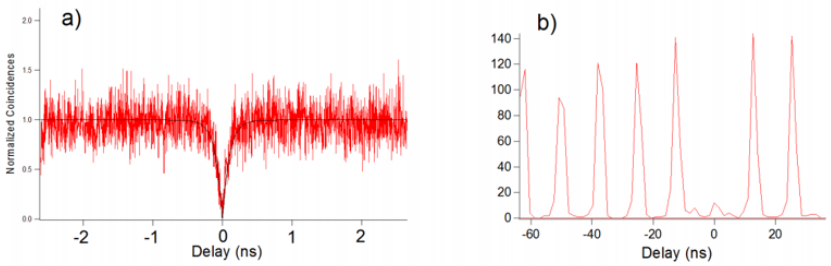

Figure 1.21: Auto-correlation histogram for (a) CW and (b) pulse mode excitation. Taken from [8]. A good single-photon source is identified with a dip in the auto correlation histogram at zero delay time for CW excitation whereas it is identified with an absence of a peak for pulse excitation.

Chapter 2

Extraction of light from a quantum dot in a nanowire

Contents

Although generating a pure, bright, coherent and highly deterministic single photon is now possible with QDs, there is a major challenge we still face: the efficient extraction of light from the QD either in free space (vacuum) or in photonic circuits. And therefore a QD-based single-photon source with high extraction efficiency in a single optical mode is highly desirable. The goal of this chapter is to provide quantitative data on the shape and size of our CdSe-ZnSe QD-NW system for efficient extraction of light along the NW axis in free space. Extraction of light from our QD-NW system in photonic circuits is discussed in chapter 5.

In this chapter, we will first start with a short review of single-photon extraction strategies that were employed in the past to efficiently extract single photons from a QD. Then in section 2.3 we will discuss the finite element method (FEM) numerical calculations that we performed to optimize the shape and size of our ZnSe NWs to efficiently extract light from CdSe QD along the NW direction. This shape and size of the QD-NW was targeted using molecular beam epitaxy (MBE) as reported in chapter 3.

2.1 Single photon extraction strategies

The most studied QDs for single photon emission are usually grown by self-assembly using MBE and are buried in a high refractive index matrix (n~3.5 for InP, GaAs and 2.6 for ZnSe). Collection of

photons outside of this matrix thus becomes difficult due to total internal reflection at the semiconductor matrix-air interface (Fig 2.1 (a)). At incident angle of light = 0°, the effective reflectivity of light is given by the Fresnel equation: $R_{eff} = |\frac{n-n_2}{n+n_2}|^2$, which gives a transmission into air ($n_2 = 1$) of 96% from glass, ~69% from InP and GaAs, and ~80% from ZnSe. Above 0° incident angles, the transmission of light decreases till the Brewster angle ($\theta_B = \tan^{-1}\left(\frac{n_2}{n}\right)$), beyond which the transmission is zero. The θ_B for InP and GaAs is ~ 16° and ~ 21° for ZnSe.

And so, the light extraction efficiency for such a system is very low as most of the light is back-reflected into the substrate. Therefore, several strategies were suggested for high photon extraction from a QD.

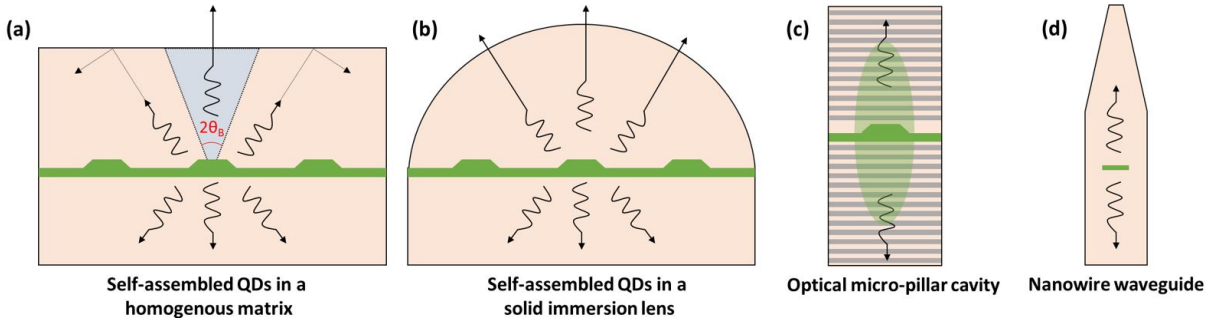

Figure 2.1: Single photon collection strategies. (a) Self assembled QDs in a homogeneous high refractive index material. Photons emitted at an angle larger than the Brewster angle (θ_B), are trapped inside due to total internal reflection. (b) A solid immersion lens on top of QDs used to avoid total internal reflection. (c) A single QD in a micro-pillar cavity sandwiched between Bragg reflectors. (d) A single QD in a NW waveguide. Photons are collected along the NW axis.

2.1.1 Solid immersion lens

Zwiller *et al.* [68] for the first time gave a solution to the total internal reflection problem by positioning a hemispherical solid-immersion lens on top of an ensemble of QDs (Fig 2.1 (b)). It means that light from the QD reaches the lens/air interface at normal incidence at all angles above the QD and therefore there is no more total internal reflection of light emitted above the QD. More recently, a solid immersion lens fabricated on top of a pre-selected single QD with localization accuracy better than 2 nm has shown to increase the PL intensity (collected in a numerical aperture (NA) of 0.8) by a factor of 2 with respect to the bare sample [69].

There are a few major caveats to this strategy though. Since the immersion lens is only on the top, light is still lost at the bottom and on the side directions of the QD. Also, such QDs are grown at random positions on the substrate. It is therefore necessary, using μ-PL to scan the QD position one by one and then an immersion lens is fabricated on top. This process is therefore difficult to scale up for large-scale production.

2.1.2 Optical micro-cavity

Another strategy is to embed a QD in an optical cavity sandwiched between two mirrors, usually Bragg reflectors, facing each other at distance d. Such a system is called a micro-cavity with only one mode

which must be put in resonance with the optical transition of the QD and therefore photons are emitted only in this particular mode. The cavity mode photons can then be further coupled to waveguides. At the core of this system is the Fabry-Perot resonator which results in resonant standing waves at multiples of frequency $f = c/d$, where c is the speed of light. This results in enhancement of QDs spontaneous emission rate into the resonant cavity mode (Purcell effect) and is quantified by Purcell factor [70]:

$$F_P = \frac{3}{4\pi^2}\left(\frac{\lambda_{vacuum}}{n}\right)^3 (\frac{Q}{V}) \tag{2.1}$$

where (λ_{vacuum}/n) is the wavelength in the microcavity material of index n. Also, $Q = f/\triangle f$, is the quality factor and V is mode volume. The Q value is related to the bandwidth, $\triangle f$, of this resonator and also to the lifetime of a photon inside the cavity. For high Q values, the photon spends more time inside the cavity due to internal reflection, and therefore, the enhancement of the emission rate of the QD in the single (cavity) mode is high. For extraction of these cavity mode photons, a cylindrical micro-cavity can also be fabricated around the QD to provide confinement in all three dimensions with its radiation pattern being highly directional (Fig 2.1 (c)). Such a structure is called a micro-pillar resonator. J. M. Gérard *et al.* [71] were the first to show Purcell enhancement of InAs QDs in GaAs/AlAs micro-pillars. Such micro-pillars confine light in the axial direction as in a Fabry-Perot resonator and in the radial direction due to total internal reflection from the interface of high refractive index micro-pillar material and air. This ensures high quality factor Q and emission directionality along the NW axis.

But a disadvantage of micro-cavity systems is that a high quality factor Q also means narrow operation bandwidth $\triangle f$ which requires precise matching of QD-emission energy with the cavity mode, either through tuning of cavity resonance or QD size. This also forces the QD system to operate at cryogenic temperatures to have QD emission linewidth narrower than the cavity linewidth.

2.1.3 Nanowire waveguide

A NW waveguide can be used to enhance both light emission properties and light extraction efficiency without the stringent frequency matching of the QD's emission and the cavity mode, as in the case of a micro-cavity. Unlike a micro-pillar resonator, a NW waveguide is not based on periodic variation of the refractive index but is rather composed of a high refractive index material surrounded by a low refractive index material (air), just like an optical fiber. In an optical fiber, the core refractive index n_1, and the cladding refractive index n_2, are chosen such that $n_1 > n_2$. Light is confined in the high refractive index core material due to total internal reflection.

A waveguide may support several guided modes which can be a combination of Transverse Electric (no electric field in direction of propagation) and Transverse Magnetic (no magnetic field in direction of propagation) modes. For an optical fiber, the preferred guided mode is the HE_{11} mode which has a Gaussian electric field distribution profile without any cut-off (Fig 2.2 (a)). And unlike Gaussian beams in vacuum, HE_{11} guided mode inside the optical fiber (of constant diameter) maintains a Gaussian profile without spreading to transverse directions.

When a QD is embedded in an ideal NW waveguide, its spontaneous emission is mostly guided in the HE_{11} mode. This is quantified using β-factor which is the ratio of the spontaneous emission rate in the HE_{11} mode (P_M) compared to the spontaneous emission rate in all the modes including.

$$\beta = \frac{P_M}{P_M + \gamma} \tag{2.2}$$

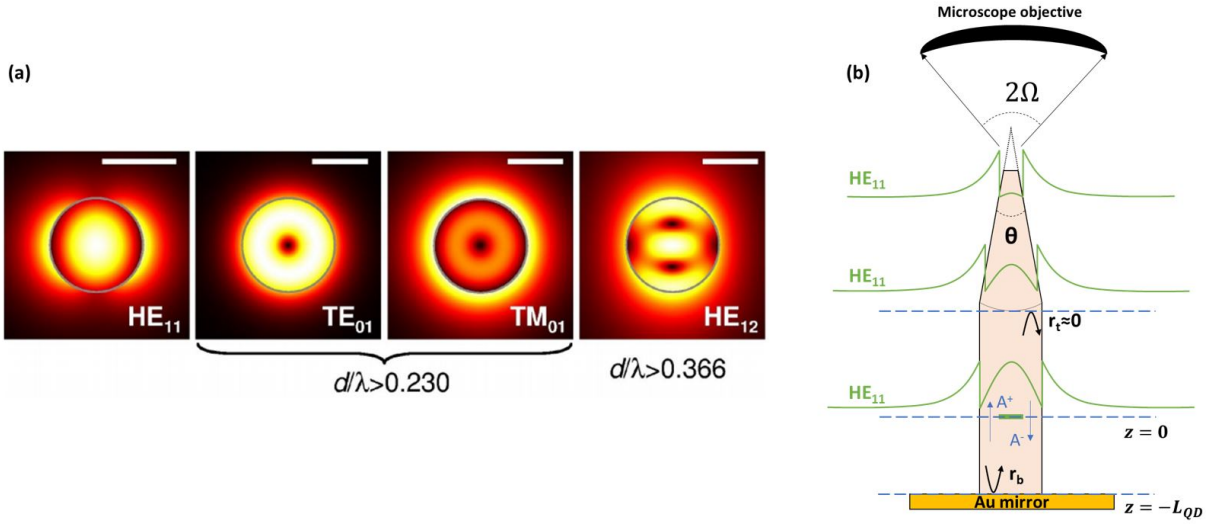

Figure 2.2: (a) In-plane electric field amplitude map of the first guided modes for an infinitely long GaAs (n=3.45) circular wire (diameter d) with an on-axis radial dipole (emitting with vacuum wavelength $\lambda = 950$ nm). The profile of HE_{11} mode shown for different d/λ values. The scale bar is 200 nm. For NW remains in mono-mode regime for $d/\lambda < 0.366$ and in HE_{11} mode for $d/\lambda < 0.230$. Figure extracted from [72]. (b) Scheme for tapered NW waveguide on a planar gold-mirror for efficient light extraction from the top of the NW in an solid cone of angle 2Ω. The HE_{11} mode adiabatically expands which leads to directive far field emission.

The emission rate is proportional to the power emitted. The γ modes comprise the other excited modes except HE_{11}, such as HE_{12}, and the transverse leaky modes, such as TE_{01} and TM_{01}. A β-factor greater than 0.9 for a broad bandwidth of $\triangle\lambda/\lambda = 0.26$ was theoretically predicted for infinitely long circular waveguides with a dipole perpendicular to the wire axis [73]. Confinement of light along the HE_{11} mode in a NW waveguide of refractive index n, can be achieved by controlling the NW radius r. An analytical calculation of guided modes in an infinitely long circular waveguide has shown that high transverse confinement (radial dipole) is obtained for $r.n/\lambda = 0.405$ for single-mode regime [74]. This gives a radius of 86 nm for optimum light guiding in ZnSe circular waveguides (n=2.6) with a radial dipole emitting at 550 nm.

An infinite circular photonic wire is ideal for guiding single photons. But in practical scenarios, two big challenges are faced. First, half of the emission is lost in the NW waveguide in the opposite direction of detection. And second, emission from the quantum dot is scattered and reflected by the wire ends. The first problem can be solved using a metal mirror or Braggs mirror to reflect the emission of the emitter from the opposite direction towards the detector´s direction [75]. For the second problem, I. Friedler *et al.* proposed an elegant solution *i.e.* tapering of top facet of the wire [76] (Fig 2.2 (b)).
They start with an assumption that a NW (cylindrical, no tapering or bottom mirror) behaves like a Fabry-Perot resonator where the top and bottom facets of the NW partially reflect light. A dipole emitter, just like a QD, is placed at position z-axis (NW axis) with the QD at the origin of z. The modal amplitudes of HE_{11} in the forward (A^+) and in the backward (A^-) directions are then given as:

- $A^+ = 0$, for $z < 0$

- $A^+ = A_s \exp\left(2i\pi\frac{z}{\lambda_{NW}}\right)$, for $z > 0$, wave propagating with $k = \frac{2\pi}{\lambda_{NW}}$
- $A^- = 0$, for $z > 0$
- $A^- = A_s \exp\left(-2i\pi\frac{z}{\lambda_{NW}}\right)$, for $z < 0$, wave propagating with $k = -\frac{2\pi}{\lambda_{NW}}$

where the phase $\phi = 2\pi\frac{z}{\lambda_{NW}}$ is due to the propagation of the electromagnetic wave. And A_s is the amplitude discontinuity induced by the dipole source. For a radial dipole, A_s is directly related to P_M (power in HE_{11} mode), and is given as $P_M = (A^+)^2 + (A^-)^2 = 2A_s^2$.

Tapered nanowire

Now we introduce the effects of the NW shape with the possible reflections at the 2 ends of the NW. At the top facet, if the NW is tapered , it will result in a gradual shift from high refractive index NW material to low refractive index air. And by doing so we introduce an adiabatic expansion of the HE_{11} mode until it's mostly supported in air (Fig 2.2 (b)). This means that there are negligible reflection of the forward propagating wave A^+ from the top facets. Therefore, A^- remains the same.

At the bottom facet, however, the backward propagating wave A^- is partially transmitted and partially reflected at the base of the NW ($z = -L_{QD}$) with amplitude $A_s \exp\left(2i\pi\frac{L_{QD}}{\lambda_{NW}}\right)|r_B|\exp(i\phi_B)$. Where r_B is the bottom reflection coefficient. The reflected beam propagates upwards with an additional phase due to propagation with $k = \frac{2\pi}{\lambda_{NW}}$ and contributes to the forward propagating wave A^+. Therefore,

- for $z < 0$,
  $A^+ = A_s \exp\left(2i\pi\frac{L_{QD}}{\lambda_{NW}}\right)|r_B|\exp(i\phi_B)\exp\left(2i\pi\frac{z+L_{QD}}{\lambda_{NW}}\right)$, and
- for $z > 0$,
  $A^+ = A_s \exp\left(2i\pi\frac{z}{\lambda_{NW}}\right) + A_s \exp\left(2i\pi\frac{L_{QD}}{\lambda_{NW}}\right)|r_B|\exp(i\phi_B)\exp\left(2i\pi\frac{z+L_{QD}}{\lambda_{NW}}\right)$
  $A^+ = A_s \exp\left(2i\pi\frac{z}{\lambda_{NW}}\right)\left[1 + \exp\left(2i\pi\frac{2L_{QD}}{\lambda_{NW}}\right)|r_B|\exp(i\phi_B)\right]$

Now, just below the QD ($z = 0$), $A^- = A_s$ and $A^+ = A_s|r_B|\exp(i\phi)$, with $\phi = 2\pi\frac{2L_{QD}}{\lambda_{NW}} + \phi_B$. Therefore, the power emitted downwards is given as:

$$P_d = A_s^2(1 - |r_B|^2) \tag{2.3}$$

Similarly, just above the QD, $A^- = 0$ and $A^+ = A_s[1 + |r_B|\exp(i\phi)]$. Therefore, the power emitted in the upwards direction in the HE_{11} mode is given as:

$$\begin{aligned} P_u &= |A^+|^2 \\ &= A_s^2|1 + |r_B|\exp(i\phi)|^2 \\ &= A_s^2[(1 + |r_B|\cos\phi)^2 + |r_B|^2\sin^2\phi] \\ &= A_s^2[1 + 2|r_B|\cos\phi + |r_B|^2] \end{aligned} \tag{2.4}$$

From this upwards emitted power, a part $T(\theta)P_u$ is transmitted outside of the NW (tapering half-angle $\theta/2$) in the HE_{11} mode. A $T(\theta)$ value close to 1 can be achieved by controlling the $\theta/2$. Smaller the $\theta/2$, more gradual the change in refractive index and more relaxed expansion of the HE_{11} mode. A part of the upward emitted power, $T(\theta, \Omega)P_u$, is collected by the microscope objective in a solid cone of numerical aperture NA=$\sin\Omega$, and therefore depends not only on the tapering half-angle $\theta/2$ of the NW but also on the collection angle Ω.

The total power emitted by the dipole is now given as:

$$\begin{aligned} P_T &= P_M + \gamma = P_u + P_d + \gamma \\ &= A_s^2[1 + 2|r_B|\cos\phi + |r_B|^2 + 1 - |r_B|^2] + \gamma \\ &= 2A_s^2[1 + |r_B|\cos\phi] + \gamma \end{aligned} \tag{2.5}$$

And the power collected in a solid cone of angle Ω above the NW is given as:

$$T(\theta,\Omega)P_u = T(\theta,\Omega)A_s^2|1 + |r_B|\exp(i\phi)|^2 \tag{2.6}$$

And therefore, the efficiency with which photons are extracted from the NW and collected in a solid cone of angle Ω is given as:

$$\begin{aligned} \eta &= \frac{T(\theta,\Omega)P_u}{P_T} \\ &= T(\theta,\Omega)\frac{A_s^2|1 + |r_B|\exp(i\phi)|^2}{2A_s^2[1 + |r_B|\cos\phi] + \gamma} \\ &= \frac{T(\theta,\Omega)}{2}\frac{P_M|1 + |r_B|\exp(i\phi)|^2}{P_M[1 + |r_B|\cos\phi] + \gamma} \\ &= \frac{T(\theta,\Omega)}{2}\frac{P_M|1 + |r_B|\exp(i\phi)|^2}{P_M|r_B|\cos\phi + P_M + \gamma} \end{aligned} \tag{2.7}$$

and with $\beta = \frac{P_M}{P_M+\gamma}$, extraction efficiency becomes:

$$\eta = \frac{T(\theta,\Omega)}{2}\frac{\beta|1 + |r_B|\exp(i\phi)|^2}{1 + \beta|r_B|\cos\phi} \tag{2.8}$$

From eq. (2.8), we can say that the ability to collect photons from the NW is dependent on four parameters: (1) the β-factor (extraction in HE_{11} mode) and hence the radius of the NW, (2) the bottom reflection coefficient $|r_b|$, with a mirror at the base of the NW $|r_b| \sim 1$ (3) the phase ϕ and hence the QD position taking also into account the phase at the reflection, and finally (4) the $T(\theta,\Omega)$, therefore the tapering angle of the NW and the collection angle Ω.

Note that P_u is maximum for $\phi = 2\pi$ or a multiple of 2π, due to constructive interference. And minimum for $\phi = \pi, 3\pi, ..$ due to destructive interference. This explain the importance of QD position. For constructive interference: $P_u = A_s^2 * (1 + r_B)^2$ is max for $r_B = 1$ (bottom mirror).

It is clear that the radius, the tapering half-angle ($\theta/2$) and the position of the QD from the bottom 2D-surface (or mirror) are three key parameters that will determine the shape and the size of the NW and the position of the QD for efficient light extraction in the top direction of the NW-axis. And these parameters will be optimized using FEM simulations in section 2.3. But to understand the results of simulations we have to first understand key concepts which are significant for NWs: the emission profile of a QD and the dielectric screening of the electric field.

2.2 Emission profile of CdSe quantum-dot

As discussed in the previous section, the preferred guided mode in a NW, just like an optical fiber, is the HE_{11} mode and has a Gaussian profile. For maximum light extraction, emission from a QD in a NW should be coupled to this mode. The emission of a QD can be described as the contribution of dipoles with their axis along the axis of the NW or perpendicular to it. To have a simple insight on how to couple the QD emission with the HE_{11} mode, we have to look at the emission pattern of a dipole in vacuum.

2.2.1 Dipole in free space

In an empty space, electromagnetic fields from a dipole oscillating along the z-axis can be completely defined by the vector field $\vec{E}(x, y, z, t)$ and $\vec{B}(x, y, z, t)$. The Poynting vector for this dipole, which is defined as the density of the energy flow for an electromagnetic field, is given as:

$$S = \frac{1}{\mu_0}(E \times B) \tag{2.9}$$

And its time-averaged poynting vector reads [77]:

$$<S> = \frac{\mu_0 p_0^2 \omega^4}{32\pi^2 c} \frac{sin^2\theta_d}{r^2}\hat{r} \tag{2.10}$$

where μ_0 is the vacuum permeability, p_0 is the dipole moment, ω is the dipole´s angular frequency, c is the speed of light in vacuum, θ_d is the angle with respect to the z-axis, r is the distance from dipole and $\hat{r}$ is a unit vector.

From (2.10) we can see that the direction of energy flux of a dipole is fixed by $\sin^2\theta_d$, which has a toroidal shape. Therefore, the radiation pattern of a dipole in empty space has a toroidal shape with its maximum emission orthogonal to its oscillating axis (Fig 2.3). This is also true for a dipole in a homogeneous environment.

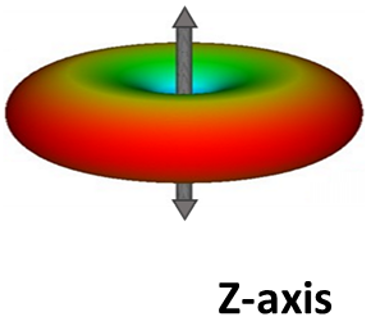

Figure 2.3: Radiation pattern (red toroid) of a dipole oscillating along the vertical axis.

To couple maximum light from a NW, we therefore, need a dipole with its polarization axis orthogonal to the NW axis and hence the maximum emission is along the NW axis. This is called a radial dipole. A radial dipole can be realized with a QD in wurtzite structure, or with a flat QD in the zinc-blende structure [12] and this is relevant for the present study. When the dipole is along the NW axis, its maximum emission is orthogal to the NW axis. This is called a longitudinal dipole. This dipole can be realized with an elongated QD in the zinc-blende structure [12]. Experimentally, we do not consider such QDs but it is interesting to introduce the longitudinal dipole in order to discuss dielectric screening in the following section.

2.2.2 Dielectric screening in a nanowire

While designing a NW waveguide, an important phenomenon that requires attention is the dielectric screening effect. For very small NW diameters ($d \ll \lambda/n$), electric field ($E_{external}$) orthogonal to the NW axis generates charges at the surface of the wire. As a consequence of this, an electric field $E_{induced}$, is generated opposite to $E_{external}$ (Fig 2.5). The total electric field ($E_{external} + E_{induced}$) is thus strongly reduced and this effect inhibits the spontaneous emission of a radial emitter in the NW.

For smaller diameters, the charge separation is small, and therefore $E_{induced}$ is strong. $E_{induced}$ can be minimized by increasing the charge separation with a large enough NW diameter. Therefore, we not only need a radial dipole for maximum light extraction, but also a NW diameter large enough to guide the HE_{11} mode and minimize the dielectric screening effect. But it should be noted that NW diameters

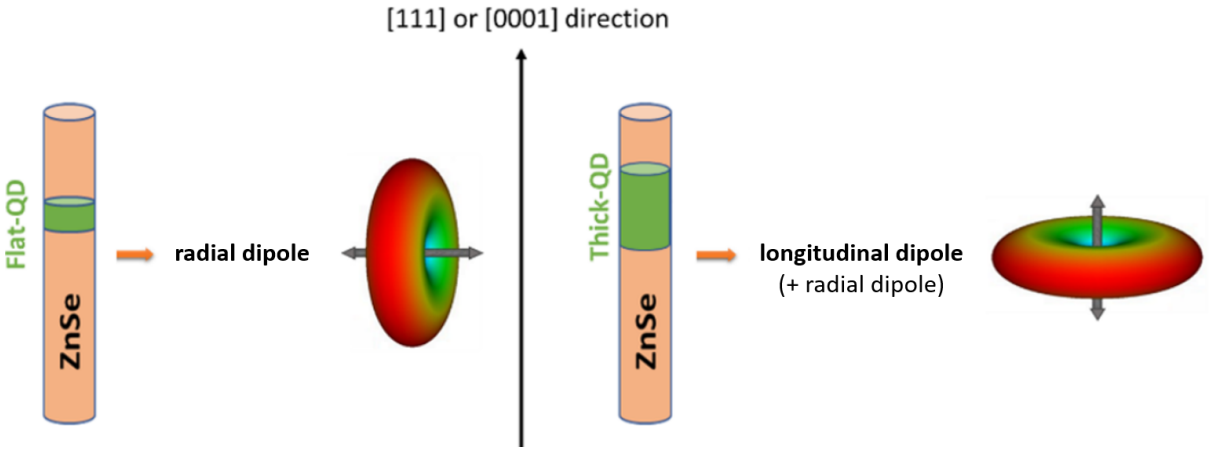

Figure 2.4: Radiation pattern of a flat or thick QD in a NW in the ZB structure. A flat QD behaves like radial dipole and a thick QD like a longitudinal dipole with their maximum emission along and perpendicular to the NW-axis respectively.

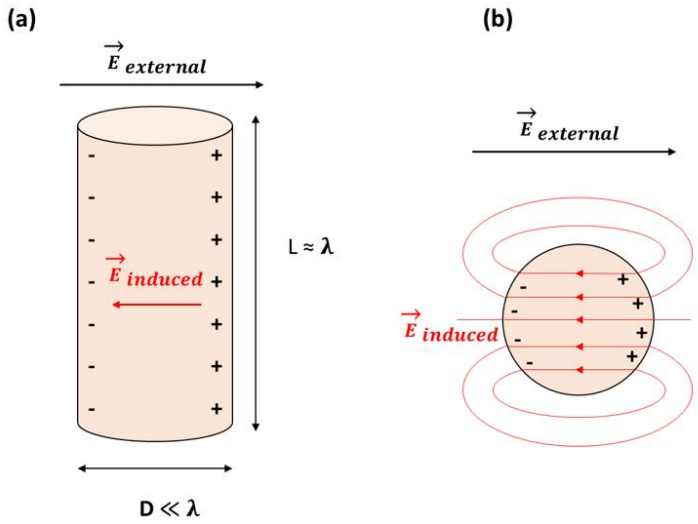

Figure 2.5: (a) Side view and (b) top view of a NW showing dielectric screening effect in the electrostatic approximation. Dipoles polarized orthogonal to the NW axis (small dimension) are screened. Dipoles polarized along the NW axis (large dimension) are not affected by dielectric screening effect.

should not be too large as this will result in appearance of other non-guided modes (such as HE_{12}, TE_{01} and TM_{01}) in which QD's emission can propagate.

In the electrostatic approximation ($D \ll \lambda/n$), the dielectric screening effect of a NW (refractive index n_{NW}) embedded in a medium (n_{medium}) can be estimated using the ratio of emitter decay time in a NW (τ_{NW}) and in bulk material (τ_{bulk}), derived from [78]:

$$\frac{\tau_{NW}}{\tau_{bulk}} = \frac{1}{4}\frac{n_{NW}}{n_{medium}}\left[\left(\frac{n_{NW}}{n_{medium}}\right)^2 + 1\right]^2 \tag{2.11}$$

This ratio corresponds to the modification of the NW decay time with respect to the bulk. For $n_{NW}/n_{medium} > 1$, NW decay time is longer than the bulk. For an electric field parallel to the NW axis, the electric field inside the NW is not attenuated and it behaves like in the bulk case.

In conclusion, for maximum light extraction from our NW-waveguide along the NW-axis, we need a QD with radial polarization, an optimal NW diameter to guide HE_{11} mode and prevent dielectric screening, and a tapered design for maximum photon transmission from the top facet. Since the design of the NW waveguide now is quite complex, we optimized all these parameters numerically.

In the following sections, are discussed the numerical calculations performed using FEM to optimize the ZnSe photonic wire radius and tapering half-angle $\theta/2$ for maximum light extraction along the wire axis for an emitter located at the center of the wire. At the end, are provide the optimum dimensions for the geometry of the ZnSe photonic wire and this ideal geometry will be aimed for during the growth of CdSe -ZnSe QD-NW using MBE in chapter 3.

2.3 Numerical calculations

We used the COMSOL Multiphysics simulation tool, which uses finite element method (FEM) technique [79], to optimize the shape and size of our tapered ZnSe photonic wire. In the following sub-section, the 3D model of the NW that was simulated in COMSOL is defined.

2.3.1 3D design

Our photonic wires are realized using MBE in two steps. The growth process is discussed in chapter 3, but in short, first, growth of ZnSe NW-core ($n = 2.66$) and insertion of CdSe QD in the core takes place. The second step involves the growth of the tapered ZnSe or ZnMgSe shell ($n = 2.63$). The ZnSe core can be represented by a cylinder with a base radius of about 10 nm and top radius of about 5 nm, which is also the radius of Au catalyst on top of the NW. The shell consists of a cylindrical (of the same length as the core) and a conical section (above the core).

Since the refractive index of the core and shell (even if ZnMgSe) material are very similar, we approximate the ZnSe/ZnMgSe wire by a single NW material of n=2.66 (ZnSe) in the COMSOL 3D model to save computational time. In Fig 2.6 (a) is shown a 2D view of the 3D model. The 3D model is designed as follows:

- Since, we grow ZnSe NWs on a ZnSe buffer layer, an 800 nm ZnSe buffer layer is introduced in the model.
- The cylindrical part of the NW is fixed at 500 nm in height (H_1).
- The height (H_2) of the conical section of the NW is related to the tapering half-angle $\theta/2$ and to the radius of the wire (R_2) by: $H_2 = R_2/\tan(\theta/2)$.
- The tip radius (R_1) of the photonic wire is fixed at 5 nm, which is close to the observed Au catalyst radius of 4 nm.

- A dipole representing the QD emitter is placed at the center of the wire. The dipole emission wavelength is fixed at 550 nm and its position will be varied from 10 to 300 nm from the bottom of the wire. An emission wavelength of 550 nm was chosen as our CdSe QDs have an experimentally observed emission around this wavelength.

- To observe the guiding effect of the NW, we integrate power (time-averaged Poynting vector described in eq. (2.10)) emitted by the dipole over a surface of numerical aperture NA of 0.6 (black area in Fig. 1) in the upwards direction. The distance between this surface and the NW tip is always kept more than 1 μm to be in the far-field regime.

- The entire NW is enclosed in a half-sphere with $n = 1$ (vacuum, air, nitrogen helium, etc) of radius 5.1 μm.

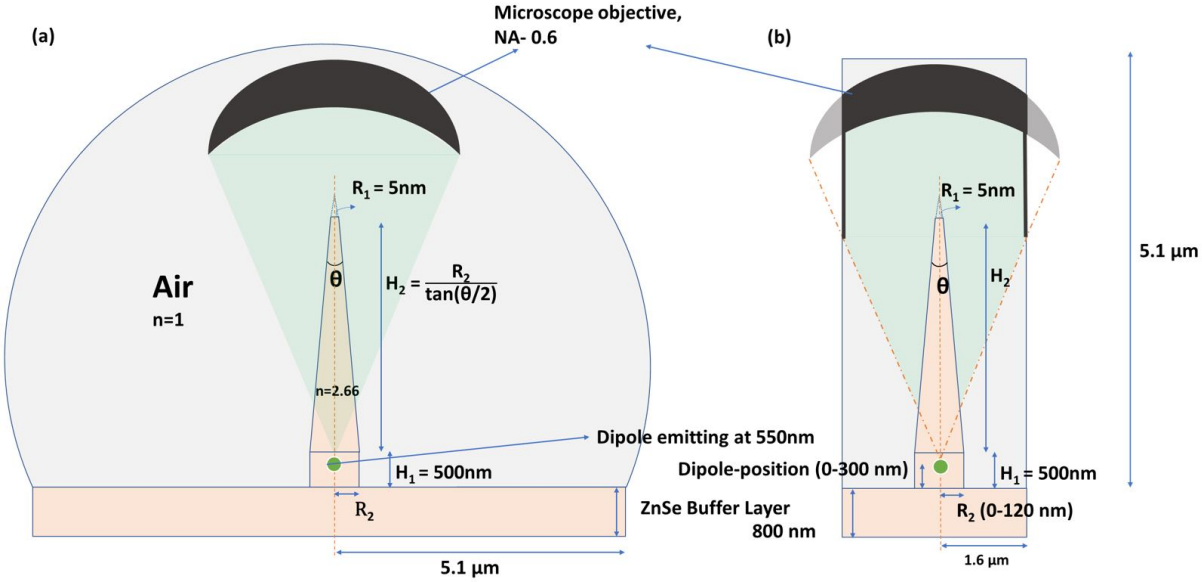

Figure 2.6: (a) 2D view of the 3D photonic wire design used to run COMSOL simulation. In (b) is shown a 2D view of the reduced model which was used to save time and resources on numerical simulations.

The computing time and memory requirement of the hardware to compute a COMSOL model is strongly related to the number of degrees of freedom. For physics interfaces like COMSOL, there are dependent variables present in all the nodes of the mesh created to solve such geometries. And therefore, degrees of freedom are given by the number of nodes multiplied by the number of dependent variables.

For very large R_2 (> 100 nm) and very small $\theta/2$ ($< 2°$) values, the entire length of the photonic wire exceeds 4 μm. And the mesh size was chosen to have 5-6 nodes for calculation per effective wavelength of light. For such large structures, the number of degrees of freedom to solve for were between 6-8 million and simulation time exceeded 2-3 days with the hardware we use. To reduce the simulation time, instead of using a spherical design (Fig 2.6 (a)), a reduced cylindrical design was thus used (Fig 2.6 (b)). By doing so the number of degrees of freedom were reduced to 1-1.5 million and simulation times were significantly reduced for a given set of parameters.

This 3D cylindrical model can be further truncated by dividing it into 4 equal parts and then applying

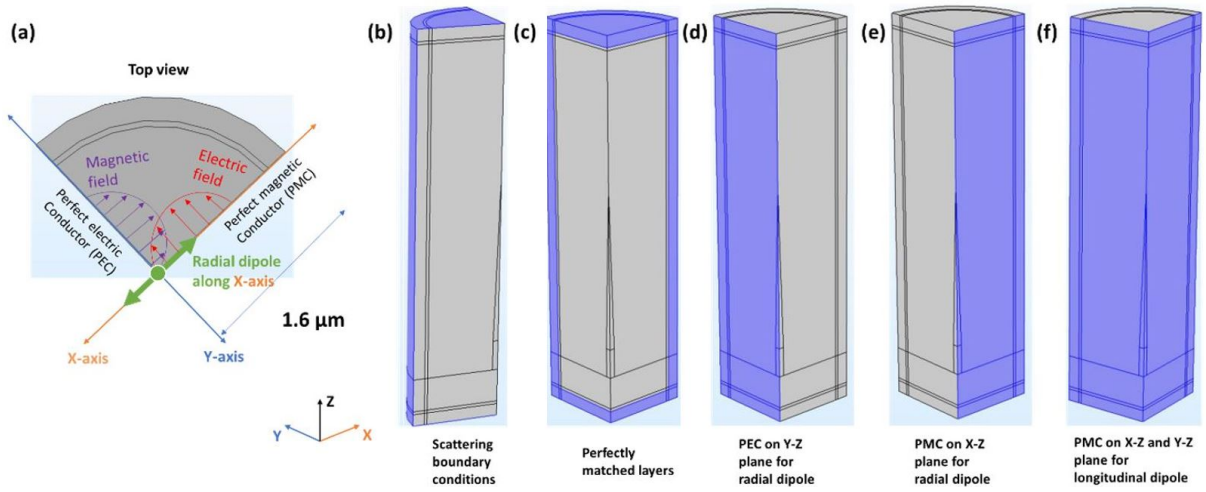

Figure 2.7: (a) Top view of the reduced COMSOL model. For a radial dipole (in green) oscillating along the X-axis, its magnetic fields and electric fields are aligned along the Y and X-axis respectively. Light emitted from a radial dipole thus propagates along the Z-axis. Longitudinal dipole (not shown here) is oscillating along the Z-axis. Since we are simulating only quarter of the photonic wire, necessary boundary conditions are applied: (b) scattering boundary conditions, (c) perfectly matched layers (PML) to avoid any scattering and reflection from the edges of the model. For a radial dipole (d) perfect electric conductor (PEC) on Y-Z plane and (e) perfect magnetic conductor (PMC) on X-Z plane are applied to provide symmetry for the magnetic and electric fields respectively. For a longitudinal dipole, only (f) PMC is applied on X-Z and Y-Z plane. The conical structure at the center of the 3D model is the tapered NW.

the following boundary conditions. These boundary conditions are also required for our open boundary problem (light emitted in infinitely large free space).

- Scattering boundary conditions [80] at the outer surface of the geometry (blue color in Fig 2.7 (b)). It is used to avoid the back reflection of the outgoing wave from the exterior boundary of the computational domain. This boundary condition is completely transparent for the wave which are normal to the incident boundary. Therefore, some waves will still be reflected when they hit the boundaries of the model.

- To avoid these remaining reflections, in addition to scattering boundary conditions we use another boundary condition: perfectly matched layers (PML) [81] at the outer layers of the geometry (blue color in Fig 2.7 (c)). PML is an artificial absorbing layer for wave equations. PMLs absorb all the scattered light from the edges of the geometry with almost no reflections.

- For a radial dipole oscillating along the X-axis, perfect electric conductor (PEC) boundary conditions are applied on the Y-Z plane (Fig 2.7 (a) and (d)). PEC sets the tangential component of an electric field to zero and imposes symmetry for magnetic fields. Y-Z plane thus acts as a mirror to the magnetic field component of the dipole emission. Similarly, perfect magnetic conductor (PMC) boundary conditions were imposed on the X-Z plane (Fig 2.7 (a) and (e)) which imposes symmetry for electric fields.

- For a longitudinal dipole oscillating along the Z-axis, PMC boundary conditions were imposed on both X-Z and Y-Z plane (Fig 2.7 (f)).

2.3.2 Radial emitter in vacuum

At the first step, we simulate a radial dipole in vacuum (no NW, $n = 1$) to see the emission of a dipole in free space above a ZnSe buffer layer (Fig 2.8 (a)). The position of the dipole from the buffer layer is varied from 10 to 300 nm (steps of 10 nm) and the power is calculated in the black region of NA 0.6.

In Fig 2.8 (b) is plotted the power collected in NA 0.6 above the NW (distance more than 4 μm) as a function of dipole distance from the 2D buffer layer. The Power collected is minimum at 10 nm, gradually increases to a maximum at around 140 nm, and then decreases again till 280-290 nm.

This observation can be explained as follows. The light reflected from the air/ZnSe interface should be shifted by an integer multiple of wavelength to interfere constructively with the light emitted in the upward direction. When light travels from a lower refractive index material to a higher refractive index material, the reflected light undergoes a phase shift of π which is equivalent to light traveling a distance of half a wavelength. Therefore, for a dipole position at $\frac{\lambda}{4}, \frac{3\lambda}{4}, \frac{5\lambda}{4}, \ldots$ nm, the light going up constructively interferes with the light reflected from the bottom 2D surface, and for a dipole position at $\frac{\lambda}{2}, \lambda, \frac{3\lambda}{2}, \ldots$ nm it will result in destructive interference. This is what we observe in Fig 2.8 (b). For $\lambda = 550$ nm, maximum power due to constructive interference is collected for a dipole position of around 140 nm $\sim \lambda/4$. Whereas the lowest power is observed around 280 nm $\sim \lambda/2$ which results in destructive interference.

Not that this result corresponds to the situation of a radial dipole in a NW of radius- 0 nm and it will be used in the following section.

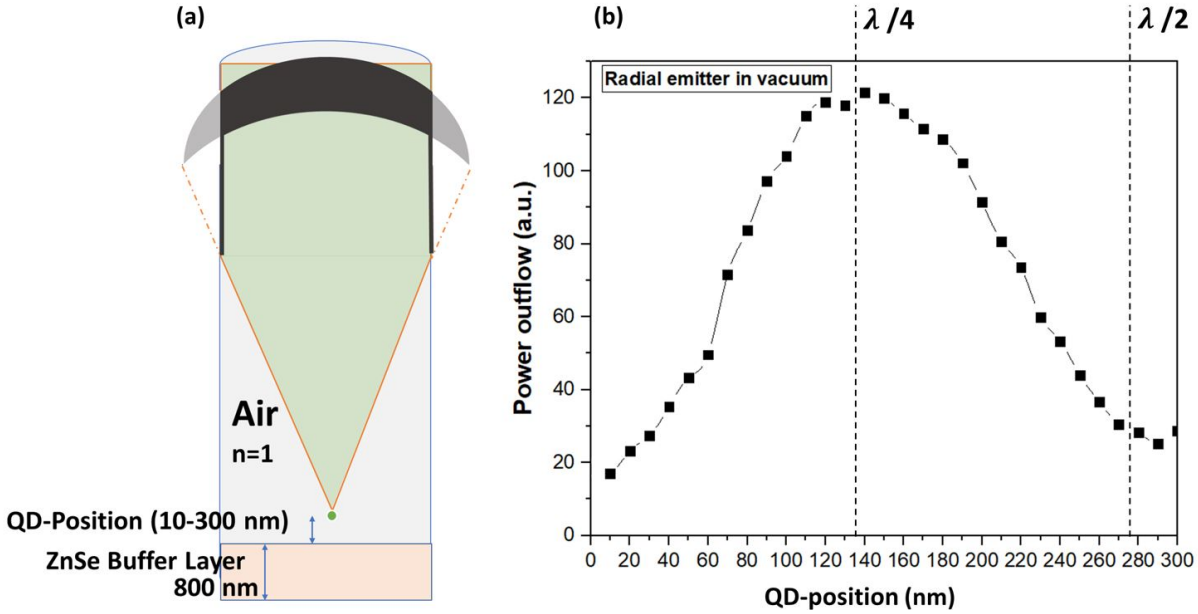

Figure 2.8: (a) Reduced model for a radial dipole in air without a photonic wire above a ZnSe buffer layer. Power emitted by the dipole is collected in the black region with NA of 0.6. (b) Power collected for such a dipole in NA 0.6 as a function of dipole position from 10 to 300 nm (steps of 10 nm).

2.3.3 Radial emitter in ZnSe photonic wire

The 3D-NW model, described in Fig 2.6 (b) with boundary conditions described in Fig 2.7, is used to simulate a radial dipole along the X-direction in a ZnSe photonic wire. The effect of a longitudinal dipole and of a tapering half-angle $\theta/2$ will be studied in section 2.3.4 and 2.3.5 respectively. To start with, we fix $\theta/2$ value to 2°. J. Claudon *et al.* [72] have predicted above 90% transmission efficiency for $\theta/2 < 4°$ for GaAs ($n = 3.45$) photonic wires. Since we are interested in maximizing the extraction efficiency of the wire, which depends on the β-factor (and therefore on the radius of the NW), the radius of the NW is varied from 10-120 nm (by steps of 10 nm) in order to find the optimal radius necessary to collect the maximum light from the dipole along the NW axis (*i.e.* coupled light to the HE_{11} mode). Note, that the effective wavelength in the NW changes with radius. Therefore, the dipole position is also varied from 10 to 300 nm (by steps of 10 nm) for each radius value with a dipole emitting at 550 nm. The power is again collected in a NA of 0.6. The region of the collection is always more than 1 μm above the tip of the NW to remain in the far-field.

In Fig 2.9 is shown the electric field map of its X component $E_X(X = 0, y, z)$ for four different radius values and a fixed emitter position at 100 nm. The height H_2 of the NW is dependent on the tapering half-angle $\theta/2$ and on the radius R_2. Since, $\theta/2$ is fixed to 2°, the length of the NW (shown in light pink color) changes with R_2. On the right side of the figure is the strength of E_X in log scale, with dark blue being the least and red for the highest.

For a very small NW radius, $R_2 = 10$ nm, the NW region, and nearby region is dark-blue *i.e.* the power radiated by the emitter is low and equal in all directions- no guiding effect is seen. Once R_2 of 50 nm is reached, guiding of light along the NW direction can be seen (coupling to HE_{11}) but is very weak. Around 80-90 nm radius, we are mostly in the single-mode regime, where the strong coupling of light from the dipole to the HE_{11} mode can be seen with red spots all along the NW. With further increase in radius, introduction of others modes of propagation can be seen.

Power collected in NA 0.6 above the NW for different radius and dipole position is shown in Fig 2.10, for a fixed $\theta/2$ of 2°. In Fig 2.9 (a) is shown power collected for QD position from 10 to 140 nm and in (b) from 150 to 300 nm. A general trend is seen for all dipole positions. For low R_2 values, the power collected remains low till about 50-60 nm. Further increase in radius results in a decrease in power collection which is due to the introduction of others modes of propagation. For dipole positions 100 and 270 nm, the power collected is maximum out of all dipole positions. For these two positions, the power collected when the dipole is in vacuum *i.e.* no NW, is also marked at 0 nm radius in the two plots.

To appreciate in more detail the effect of the dipole position, in Fig 2.11 is plotted the power collected in NA 0.6 for dipole positions of 10 to 300 nm for a radius of 80, 90 and 100 nm (radius range for which maximum power collection is observed). For a given radius, the change in power in NA 0.6 for different dipole positions is weak. The power collection remains similar for all positions for R_2 of 90 and 100 nm; while for R_2 of 80 nm, a maxima and minima of power can be appreciated but the difference is still not very pronounced.

In Fig 2.12 is plotted the power collected in NA 0.6 (P) normalized with the total power emitted by the dipole in all directions *i.e.* P_T, as a function of NW radius R_2 for a fixed dipole position of 100 nm. The ratio P/P_T is very similar to the the β-factor (eq. (2.2)) as the P comprises mostly of light guided in the HE_{11} mode, collected in the direction of the NW in NA 0.6.

P/P_T is only 0.24 for a radius of 10 nm and remains low till 50 nm radius (0.39). This is because we see almost no guiding effect till 50 nm (see Fig 2.9). Beyond 50 nm radius, P/P_T increases. The ratio

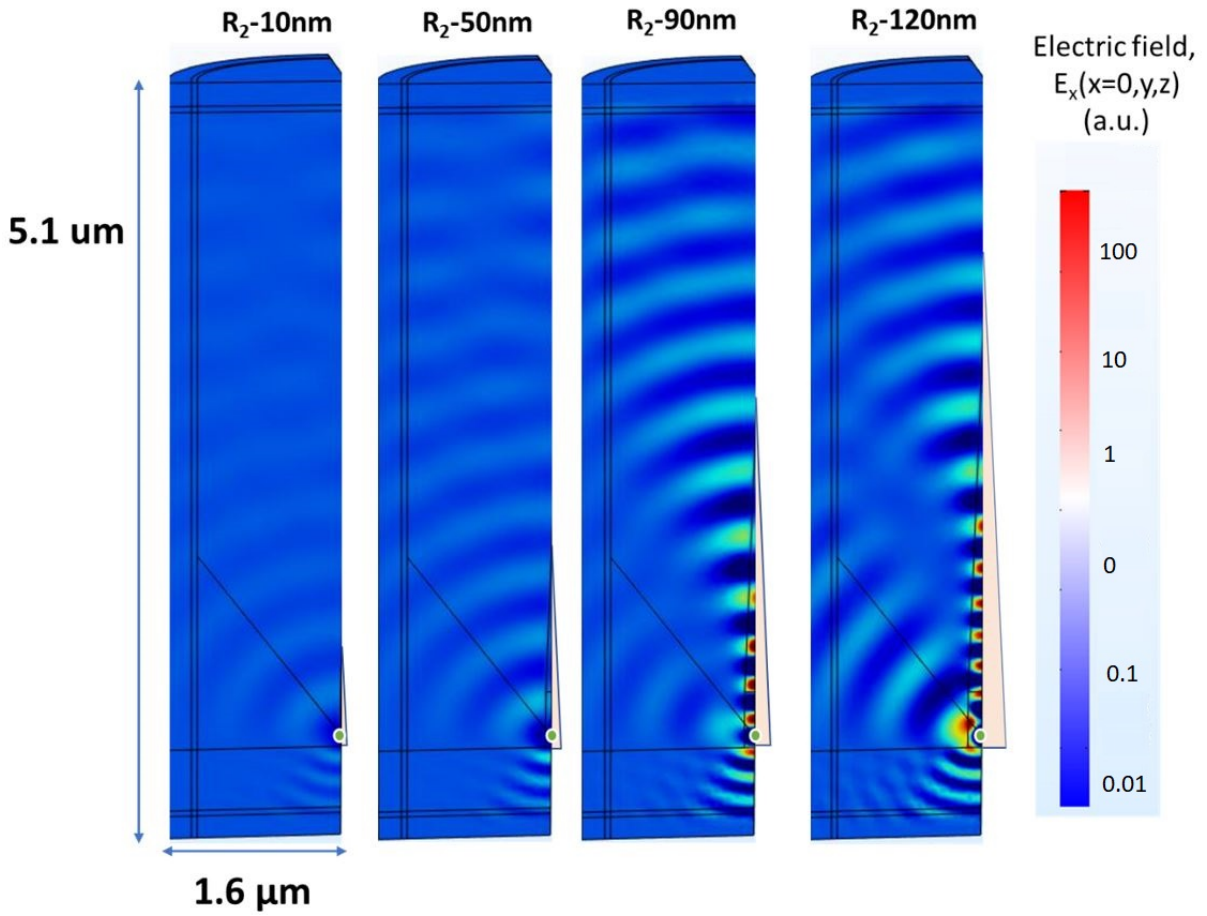

Figure 2.9: X-component of the electric field for different NW radius R_2 (10, 50, 90 and 120 nm) and fixed radial dipole position at 100 nm from the bottom 2D-surface. The green circular dot represents the dipole. The NW height is related to the $\theta/2$ and is shown in light pink color.

P/P_T remains high for a wide radius range, in other words, the NW remains in a single-mode regime for radius in the 70-100 nm range and decreases with a further increase in radius due to the addition of other modes (for example HE_{12}). The maximum P/P_T value of 0.64 is reached for a radius of 90 nm. This low P/P_T is due to the loss of half of the emission in the direction of the 2D surface. But the ratio is still more than 0.5 since some light is reflected from the 2D surface. To increase the collection in the upward direction, a mirror to reflect this lost emission will certainly increase P/P_T.

Optimal coupling to light from dipole to the principal mode of the NW is reached at R_2 values around 80-100 nm, where the power collected in NA 0.6 is maximum. An 80-90 nm radius is also in good agreement with theoretical value [74] of 86 nm ($R_2.n/\lambda = 0.405$) for a radial dipole emitting at 550 nm in an infinite ZnSe cylindrical waveguide. *The most optimized radius and emitter configurations to effectively couple the photons to the principle mode of NW are- NW radius of around 90 nm with emitter position around 100 nm or radius of 80 nm with emitter position around 270 nm.*

The power collected in NA 0.6 for 0 nm radius (case of no photonic wire) is higher than the power collected for the initial radius values of the photonic wire. This indeed is a direct result of the dielectric

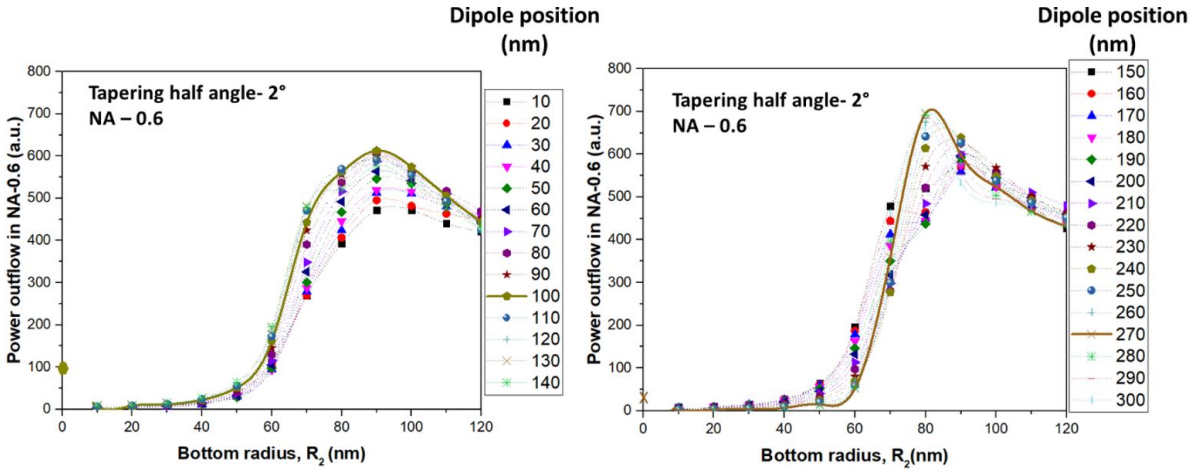

Figure 2.10: Power collected in NA 0.6 for NW radius from 10 to 120 nm (steps of 10 nm) and for dipole position from 10 to 140 nm (steps of 10 nm) in (a) and from 150 to 300 nm in (b).

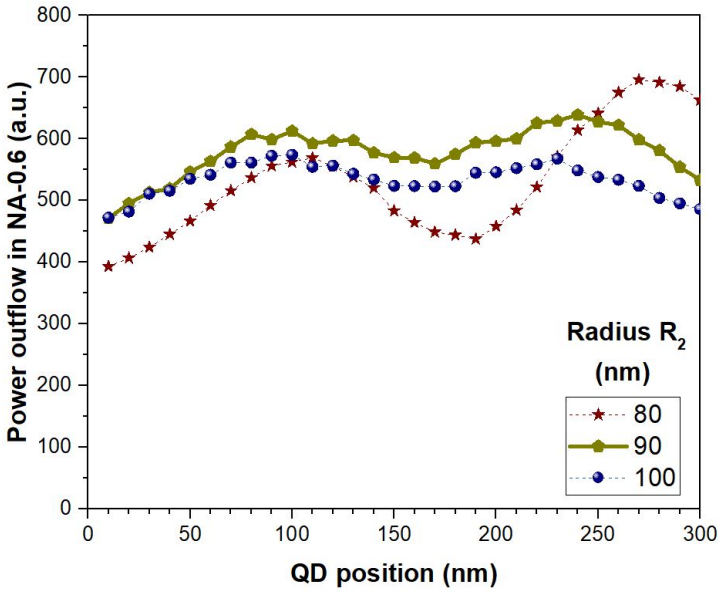

Figure 2.11: Power collected in NA 0.6 for NW dipole position of 10 to 300 nm (steps of 10 nm) and radius R_2 of 80, 90 and 100 nm

screening effect (discussed in section 2.2.2). And this effect remains strong till 50 nm of radius is reached in most cases. From this radius onwards dielectric screening starts to become weak and coupling to principal mode of the NW starts to become strong. It should be noted that for a given radius, the change of power in NA 0.6 for different dipole positions is not as pronounced as for different radius. Also, the increase in power for increasing radius follows a very steep curve from 50 nm in most cases. This points towards the fact that dielectric screening is a major barrier to overcome for an efficient photonic wire with a radial dipole. To confirm this hypothesis, a longitudinal dipole in ZnSe photonic wire is studied

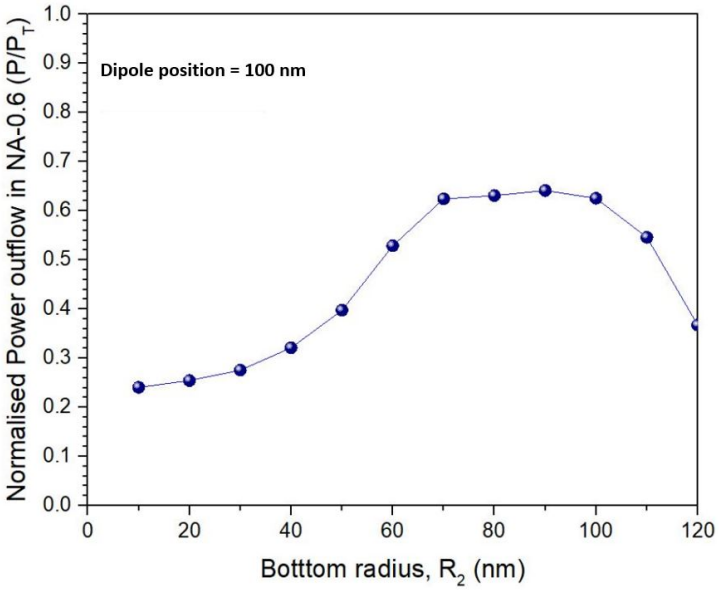

Figure 2.12: Power collected in NA 0.6 normalized by the total power collected in all directions (P_T), as a function of radius R_2 for a fixed dipole position of 100 nm.

in the following section, since dielectric screening does not affect a longitudinal dipole.

2.3.4 Longitudinal emitter in a ZnSe photonic wire

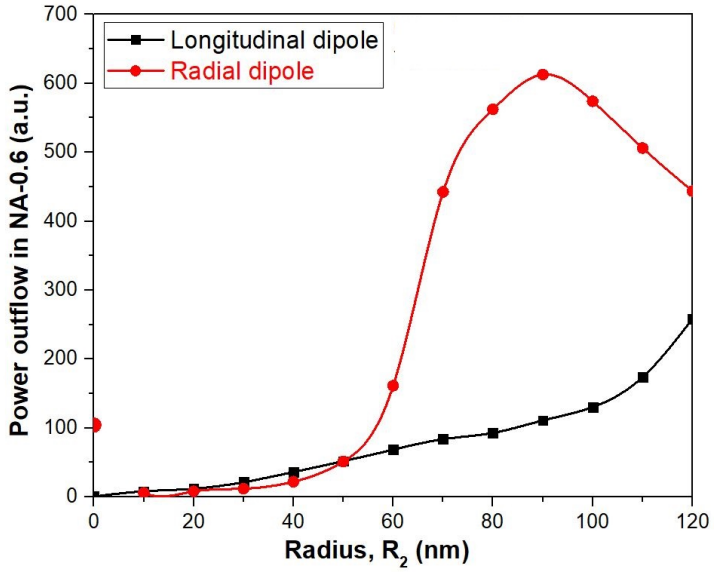

Figure 2.13: Comparison between the effect of NW radius on the power collected in NA 0.6 for a radial (red)) and longitudinal dipole (black). The dipole position and tapering half-angle $\theta/2$ are fixed at 100 nm and 2° respectively.

In Fig 2.13 is plotted power collected in NA 0.6 for a longitudinal and radial dipole at 100 nm from the 2D surface in a NW of radius R_2 = 90 nm with a tapering half-angle $\theta/2$ of 2°.

Two observations can be made: first, the power collected for a longitudinal dipole is almost five times less than that collected for a radial dipole for the optimum R_2 range of 80-100 nm. Indeed, a radial dipole is more efficient since its emission is naturally directed along the NW axis in contrast with a longitudinal dipole. Second, the increase in power for a longitudinal dipole is gradual, unlike for a radial dipole, which is steep after 50 nm. Here gradual increase is due to the guiding effect of the NW with no effect of dielectric screening. Indeed, a longitudinal dipole is protected by the length of the NW from dielectric screening, similar to a radial dipole protected by a thick NW.

Similar trends were observed by Henderson *et al.* [74] who studied a dipole emitting at 700 nm in a telluride core fiber in air cladding. They studied the total electric field emitted by a radial and longitudinal dipole at the center of the wire. They observed that for a radial dipole, the emission is 60% guided, while it is 45% guided when a longitudinal dipole is used. Clearly, a radial dipole is favorable for efficient light extraction in the guided modes of our NW with optimum radius.

2.3.5 Tapering effect on transmission efficiency

So far we have discussed the dipole orientation, the dipole position, and most importantly the radius of the NW to maximize the coupling of light from a dipole to the principle mode of propagation along the NW axis. Now we will discuss how this guided light can be coupled to the far-field without scattering/reflection effects at the top facets of the NW i.e the effect of the tapering half-angle ($\theta/2$) to maximize the transmission of photons from the NW in the solid angle of NA.

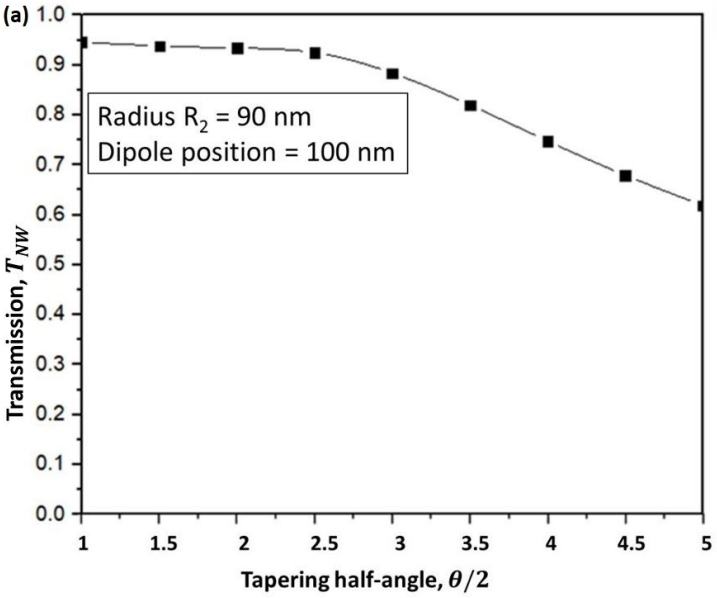

(b)

$\theta/2$ (degree)	Total height of NW, $H_1 + H_2$ (nm)
1	5650
1.5	3900
2	3100
2.5	2550
3	2220
3.5	1980
4	1790
4.5	1650
5	1530

Figure 2.14: (a) Effect of tapering half-angle $\theta/2$ on transmission efficiency of photons. Transmission efficiency T_{NW} is the power collected in NA 0.6 above the NW divided by the total power collected in the region everywhere above the dipole. (b) Total height of NW for corresponding $\theta/2$ values, where H_1 and H_2 are the heights of the cylindrical and tapered section of the NW respectively (see Fig 2.6).

Optimized R_2 and dipole position are 90 and 100 nm respectively. In Fig 2.14, is plotted the transmission T_{NW}, which is the power collected in NA 0.6 above the NW divided by the total power collected in the region everywhere above the dipole.
The T_{NW} is above 90% for $\theta/2 \leq 3°$ and decreases for $\theta/2$ above 3°. Indeed, small values of $\theta/2$ favors progressive deconfinement of the HE_{11} mode and leads to directed far field emission. However, very small $\theta/2$ values means very large heights for the NW. For $\theta/2 = 1°$, a very long NW with total height $(H_1 + H_2)$ above 5500 nm is required. And for $\theta/2 = 2.5°$, this height is half at around 2500 nm. But the T_{NW} is similar and above 90 % for both heights.

These results are similar to what I. Friedler *et al.* observed for GaAs NWs (n=3.45) [76]. They performed 3D fully-vectorial calculations on a GaAs NW of finite length with a radial dipole at the center emitting at 950 nm. With an optimized 104.5 nm NW radius at the dipole level and a tapered NW height of 2 μm ($\theta/2$ =2.9°), they observed 99 % HE_{11} mode transmission and 96% collection efficiency for a NA of 0.75.

2.4 Conclusion

In summary, we have optimized the shape and size of a ZnSe NW with a light emitter emitting at 550 nm using FEM based numerical calculations in COMSOL.

Although a longitudinal dipole is not prone to dielectric screening, a QD insertion with a radial dipole is required for maximum light extraction along the NW axis. The radius of the NW is the key parameter for effective guiding of the light along the NW axis and to decrease the dielectric screening effect. For maximum light extraction, NW radius at the level of the QD should be in the range of 80-100 nm.

The transmission efficiency of the NW is improved with a tapered design which provides an adiabatic expansion of the HE_{11} mode. A tapering half-angle $\theta/2$ of less than 3° is required for high transmission of light from the NW in the far-field.

The shape of the ZnSe NW defined by the radius and tapering half-angle $\theta/2$, optimized in this chapter, and also a QD with a radial dipole, will now be targeted using MBE growth technique in the following chapter.

Chapter 3

Growth of ZnSe nanowires and CdSe dots by molecular beam epitaxy

Contents

3.1 Introduction

This chapter is devoted to the growth of ZnSe NWs and then CdSe QDs embedded in ZnSe NWs using molecular beam epitaxy (MBE). Understanding and controlling the mechanisms involved for the growth of ZnSe NWs is important if we want to control both the properties of the CdSe QD inserted in the core and the light-guiding effect of the shell. The main objective of the work presented here is to gain insights on how to determine and control the parameters that play a crucial role in the growth process of ZnSe NWs.

The first step of the growth concerns the substrate surface preparation and gold deposition (section 3.2). The characteristic sizes of the NWs that we have to measure range from 3 nm in diameter to 5 μm in length. To this purpose we set up a procedure described in section 3.3. The growth of the ZnSe NWs is analyzed in detail for a growth temperature of 350°C (section 3.4): we study the effect of Zn and Se flux as well as the ratio Zn/Se, and then the evolution with time of the radius and the length. Then, the effect of growth temperature and sample tilt on the axial and radial growth of NWs, and the 2D growth of the substrate, are studied in section 3.5 and section 3.6 respectively. Our QD-NW follows a core-shell growth scheme which is presented in section 3.7. A model to describe the radial, axial and 2D growth is discussed in section 3.8. Finally, insertion of CdSe QDs in ZnSe NWs is presented in section 3.9.

3.2 Substrate preparation

Before the growth of ZnSe NWs, several steps are involved in the preparation of the substrate. These steps are the same for all samples. As shown in Fig 3.1, ZnSe NWs are grown on a ZnSe(111)B buffer layer grown on GaAs(111)B substrates. A thin (under 1 monolayer (ML) thick) Au layer is then deposited and heated to give rise to Au nanoparticles (NPs) that act as a catalyst for the growth of NWs.

As discussed in section 3.2.2, the presence of the ZnSe buffer layer prevents Ga or As incorporation into the NWs. Moreover (see section 1.3.2), the low growth temperatures imply that the growth is in the Vapor-Solid-Solid (VSS) growth mode.

Before starting the growth of each sample, the fluxes from effusion cells are calibrated. Calibration of fluxes is explained in section 1.4.1.2.

3.2.1 Deoxidation

Commercial GaAs(111)B substrates are epitaxy-ready, still there is a thin layer of GaAs amorphous oxide present on their surface that must be removed before starting any growth.

The substrates are first out-gassed in a low-pressure environment outside the growth chambers. This is done to get rid of surface impurities before entering the substrates into the high-vacuum (1×10^{-9} Torr) III-V growth chamber. The substrates are then heated above 580 °C under a strong As flux (calibrated to 1×10^{-5} Torr) above 400 °C. This is very important as above 400 °C, As starts to desorb from the GaAs surface. A strong As flux ensures the surface is saturated with As and avoids the formation of vacancies. The whole process is monitored using the RHEED diffraction pattern. At the start, the RHEED pattern is barely visible due to the oxide layer. When the sample temperature is raised to about 580 °C, a 2D RHEED pattern starts to appear which becomes clearer with a further increase in temperature. For most samples, a clear RHEED pattern indicating complete deoxidation was usually observed around 620 °C.

For a smooth ZnSe buffer layer, a smooth GaAs layer is required and for this reason, just after the deoxidation step, we grow a high-quality GaAs buffer layer on top of the deoxidized GaAs surface.

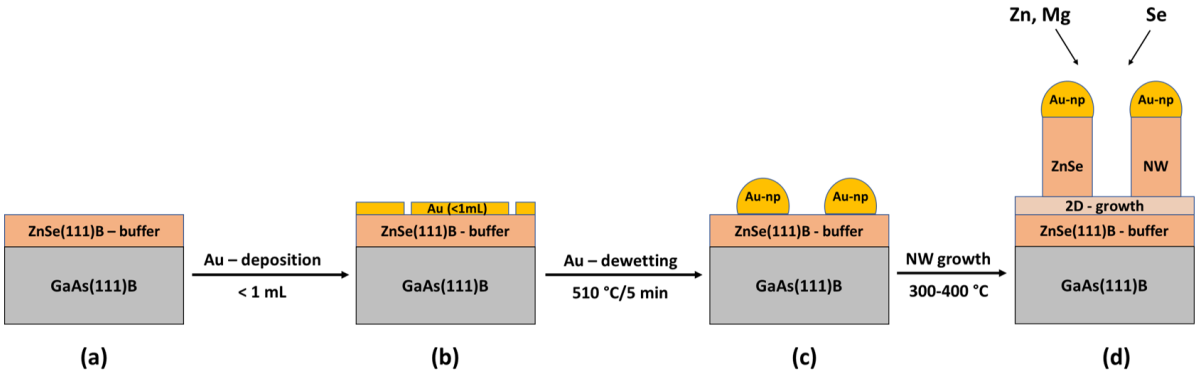

Figure 3.1: Scheme for the growth of ZnSe NWs on GaAs(111)B surface. First, (a) a thin (~8 nm) ZnSe(111)B buffer layer is deposited on GaAs(111)B substrate followed by (b)deposition of less than 1 ML of Au. (c) Dewetting of Au-ML at 510 °C for 5 min results in Au-NPs of radius 3.7±0.8 nm (average for 9 NWs measured with TEM images, Fig 3.7). Au-NPs then act as catalyst for the (d) growth of ZnSe NWs in VSS mode using Zn and Se effusion cells.

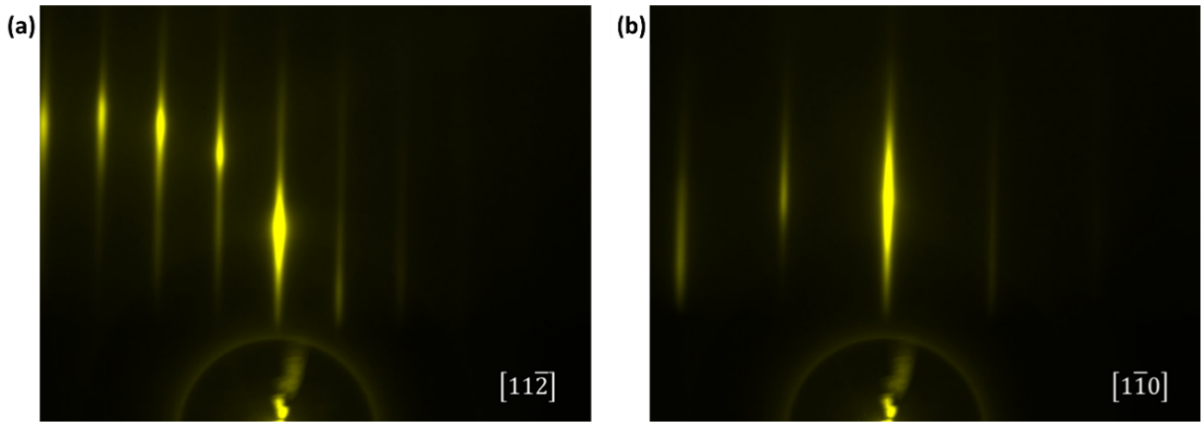

Figure 3.2: Typical RHEED diffraction pattern for a GaAs(111)B substrate after deoxidation along the (a) $\left[11\bar{2}\right]$ and (b) $\left[1\bar{1}0\right]$ azimuths. Bright, straight streaks (in yellow here) are indicative of a smooth 2D-surface *i.e.* complete deoxidation of the GaAs surface.

For this Ga beam flux was calibrated to 8×10^{-7} Torr (10 to 12 times lower than As flux). GaAs is then deposited for 3 minutes (~45 nm) followed by 5 s under vacuum and then under As flux till the substrate temperature is lowered to 400 °C. Following this step, vertical streaks along the $\left[1\bar{1}0\right]$ and $\left[11\bar{2}\right]$ azimuths were clearly visible (Fig 3.2).

3.2.2 ZnSe buffer

The substrate in transferred to the II-VI chamber where we deposit thin layers (a few nm) of ZnSe (111)B. Best conditions for the growth of ZnSe(111)B layers on GaAs(111)B surface was found by Thibault Cremel [12]: growth at low temperature (280 °C) with a Zn:Se growth rate ratio of 1:2 and

avoid the presence of Ga_3Se_2 at the interface.

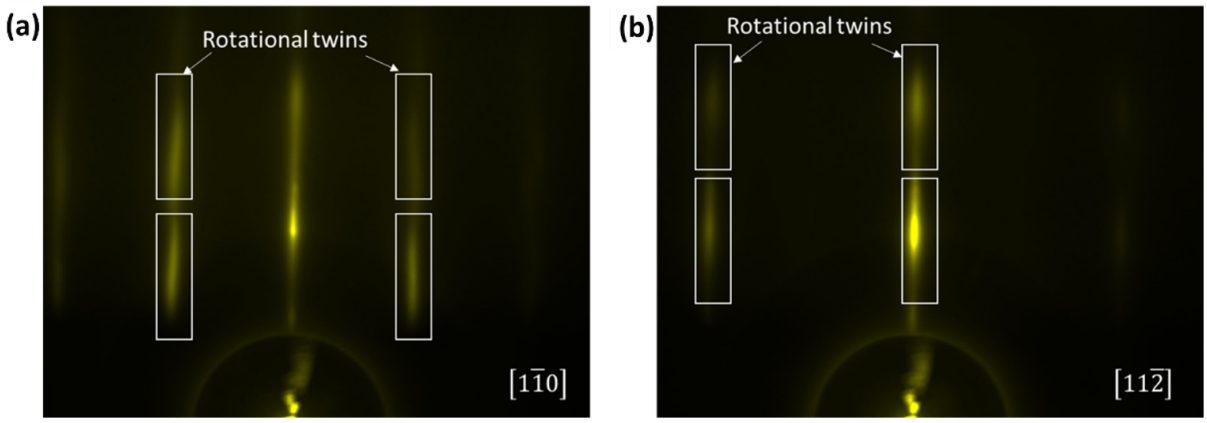

Figure 3.3: Typical RHEED pattern for a thin (8 nm) ZnSe(111)B buffer layer grown on top of GaAs(111)B substrate along the (a) $\left[1\bar{1}0\right]$ and (b) $\left[11\bar{2}\right]$ azimuths. The rectangles indicate the presence of rotational twin defects characterized by slightly inclined brighter segments along the ZnSe surface vertical streaks.

In our case, we exposed the deoxidized GaAs(111)B surface to Zn while increasing temperature from 100 to 280 °C followed by a 2 min deposition of ZnSe with Zn and Se growth rates of 0.25 and 0.5 ML/s. Often RHEED oscillations were observed for the first layers and a ZnSe buffer layer of about 8 nm was deposited. In Fig 3.3, rotational twins along the vertical streaks of $\left[11\bar{2}\right]$ azimuths of the ZnSe(111)B are visible on the RHEED patterns. They correspond to 180° rotation of the ZnSe surface of the [111] direction [58]. Such defects are quite common and were observed in ZnTe(111)B [63] and GaAs(111)B [82].

3.2.3 Deposition and dewetting of Au

In a catalyzed MBE growth of semiconductor NWs, the catalyst determines the size and location of NWs on the substrate. And therefore, control over gold deposition and dewetting steps is very critical for the control over the shape, size, and density of the NWs and thus the QDs. And by controlling the size (radius below 5.4 nm: CdSe Bohr exciton radius [83, 84, 85]) of the QD we control the emission properties of the QDs. To achieve this, we aim to deposit only a fraction of a ML of Au on the ZnSe buffer layer at room temperature in an UHV environment, followed by dewetting of this thin-film to realize Au NPs.

Miryam Elouneg-Jamroz from our group [58] studied the effect of dewetting temperature on the radius of the Au-NPs and the effect of the amount of Au deposited on the density of Au-NPs for ZnSe(111)B surface in our setup. Following this work, we deposited Au with Au effusion cell at 1080 °C for 15 s followed by dewetting at 510 °C for 5 min. The nucleation of Au-NPs at 510 °C was confirmed by observing the RHEED pattern. From room temperature to about 350 °C, only vertical streaks of ZnSe are observed. After 380 °C, diffraction spots corresponding to Au-NPs start to appear. At first, these spots are broad and weak. With an increase in temperature up to 510 °C, they become brighter. Reduction in diffraction spot size indicates that the real size of the NPs has increased, as the RHEED diffraction pattern is in reciprocal space. Fig 3.4 shows a typical RHEED pattern of ZnSe(111)B surface

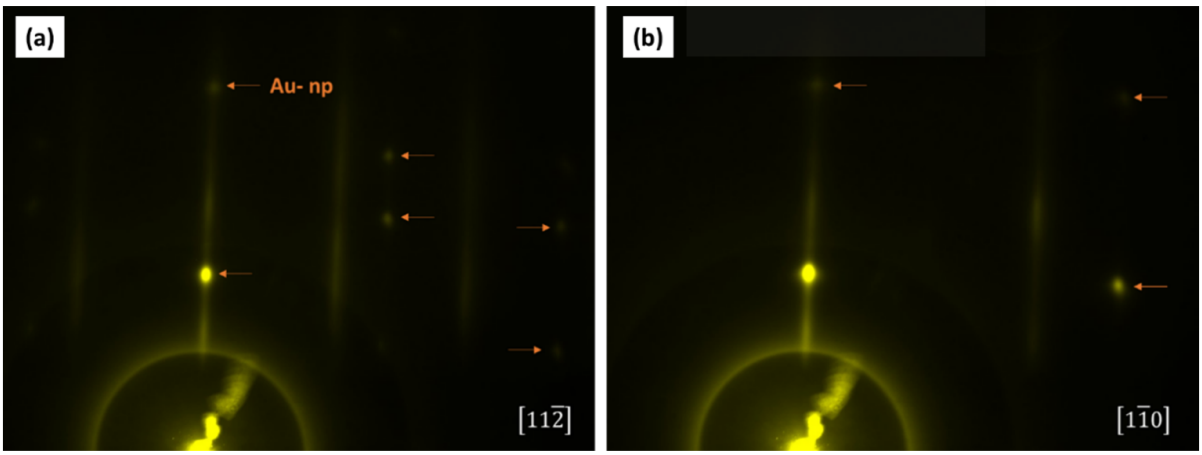

Figure 3.4: Typical RHEED pattern of ZnSe(111)B surface covered with Au-NPs dewetted at 510 °C for 5 min along (a) $\left[11\bar{2}\right]$ and (b) $\left[1\bar{1}0\right]$ azimuths. The yellow streaks corresponds to the bulk ZnSe 2D-surface The spots (indicated with orange arrows) confirms the presence of solid crystalline Au-NPs.

after Au-NP dewetting. This process mostly resulted in low (<1 NW/μm^2) Au-NP density. But this process is not totally optimized and we often had difficulty in reproducing the same Au-NP density.

Before presenting the results on the growth of NWs, methods used to analyze the morphology of the samples are discussed in the following section.

3.3 Analysis of the sample morphologies

In this section is explained how we measure the density, the Au-NP size, the 2D layer thickness, and the shape of the NWs mostly using SEM and occasionally with TEM imaging.

3.3.1 Density measurement

The density of the NWs is an important feature for probing a single NW during optical measurements. Density was measured using low-resolution SEM images with a wide-angle view of the sample surface. In Fig 3.5, are shown two side view SEM images of different samples with low and high densities of NWs. The black box represents an area of 1 μm^2 on the sample surface. The vertical dimensions of the box are corrected for the SEM-angle using the formula:

$$Real\ vertical\ length = \frac{SEM\ measured\ length}{\cos(65°)} = \frac{SEM\ measured\ length}{0.42} \tag{3.1}$$

Once the 1 μm^2 box is defined on the SEM image, NWs are manually counted within the box. This is repeated for several images from different parts of the sample to get an average value of the density of NWs on the whole sample.

3.3.2 Nanoparticle size measurement

Au-NP size was measured using both SEM and TEM images. In Fig 3.6 (a), is shown a side view SEM image of two NWs with the Au-NP at the tip. Accurate measurement of the Au-NP from SEM

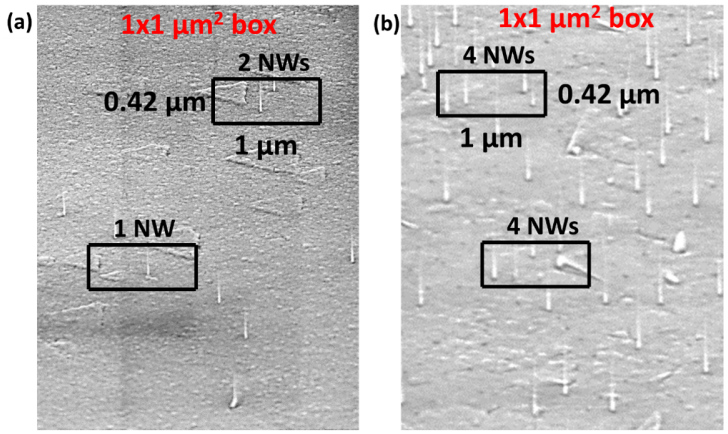

Figure 3.5: Side view SEM image (angle of 65°) of two samples with (a) low (<1-2 NWs/μm^2) and (b) high (>4 NWs/μm^2) NW density. The NWs are manually counted inside the black boxes which have an area of 1 μm2 on the surface. The vertical axis of the box was corrected for the SEM viewing angle of 65° using equation 4.1 (1 μm on the surface = 0.42 μm on the image).

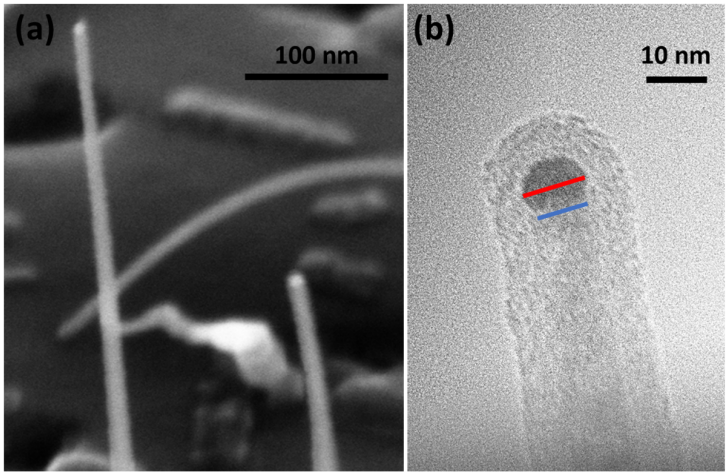

Figure 3.6: (a) Side view SEM (angle of 65°) and (b) TEM image of a NW showing the Au-NP at the tip of the NW. In the TEM image, the red line is where the radius of the NP (5.3±0.2 nm) is measured and the blue line is where the radius at the interface of the Au-NP and the NW is measured (4.7±0.5 nm).

images was very difficult mainly because of the low resolution of the SEM images. Moreover, in SEM measurements the Au-NP vibrates under the electron beam, increasing the apparent NP radius. A precise measurement is obtained only from high resolution TEM images of an NW such as shown in Fig 3.6 (b). TEM samples were prepared after cleaving a small piece from the edge of the sample as described in [61]. The NW shown in the TEM image has a carbon coating to protect the NW from charging and damage from the electron beam.

In the TEM image, the Au-NP radius measured at the red line is 5.3±0.2 nm. Whereas the radius at the interface of the Au-NP and nanowire is 4.7±0.5 nm. The error bars on the measurement come from

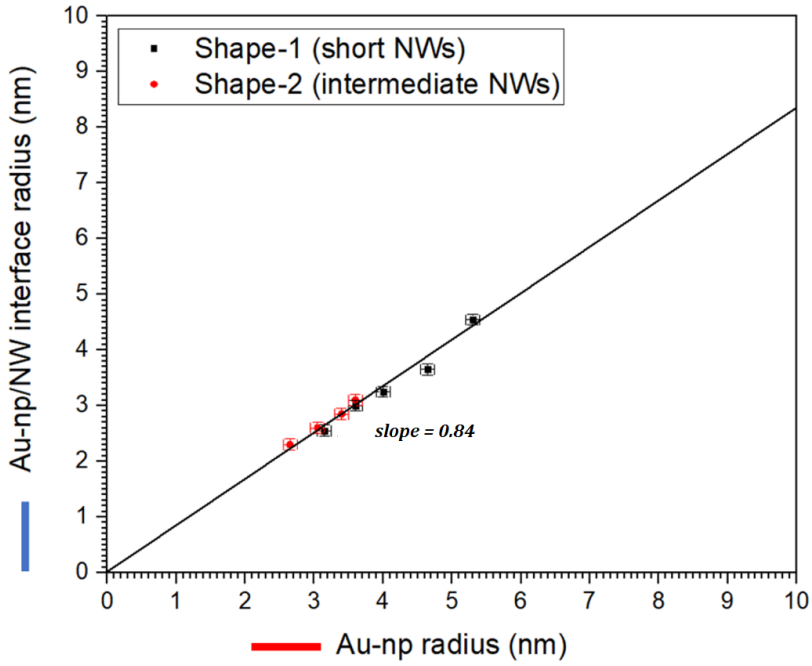

Figure 3.7: The NP-NW interface radius *vs.* the Au-NP radius measured from TEM images of 5 NWs from sample M3595 (black points) and 4 NWs from sample M3587 (red points) shown in Fig 3.10 and Fig 3.11 respectively. The error bars for the NP radius is 0.2 nm and for the interface radius is 0.5 nm since the NP-NW interface was difficult to visualize. The slope of the fit shown (of NWs with both samples) is 0.84.

repeated measurements of the radius on the TEM image. The Au-NP/NW interface is not very clearly observed in the TEM images and therefore a larger error bar is obtained for interface radius compared to the error bar for the NP size. The NP shape is somewhere between a half-sphere and a full-sphere, unlike the case for ZnTe NWs where the NP is found to be either a half-sphere or very close to a full-sphere [86].

We measured Au-NP size from TEM images of 9 NWs. In Fig 3.7 is shown Au-NP radius and NP-NW interface radius measured from TEM images for these 9 NWs of which 5 NWs (black) belong to sample M3595 and 4 (red) belong to sample M3587 (section 3.3.4). Average Au-NP radius and NP/NW interface radius were found to be 3.7±0.8 nm and 3.0±0.6 nm (avg.±SD). The NP/interface radius is equal to 84 % (from the linear fit presented with black line) of the radius of Au-NP radius.

3.3.3 2D-layer measurement

During the MBE growth atoms impinging the 2D surface contribute to the growth of a 2D-layer. This takes place at the same time as the NW growth, and therefore with time the base of the NW is buried in this 2D layer. To measure the total length of the NW L_{NW} it is then also necessary to measure the thickness of this layer. The 2D-layer measurements are made with SEM where the sample is first cleaved from the middle and observed in the SEM at 90° angle at the cross-section of the sample (Fig 3.8) at different places on the sample, and an average is taken. Error bars on the 2D measurements come from these multiple measurements on different places of the same sample.

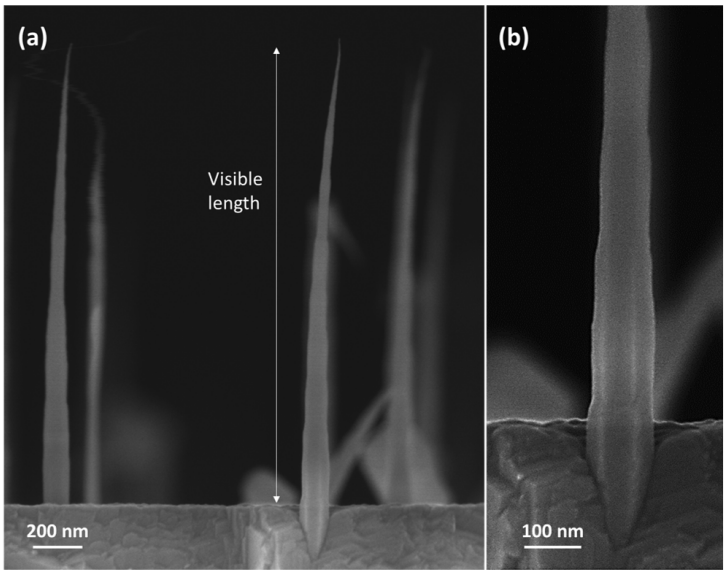

Figure 3.8: (a) Cross-sectional SEM view of a NW sample grown at 350 °C for 20 min followed by a Zn(Mg)Se shell grown for 120 min at 320 °C. (b) Image magnified at the base of the NW. The base of the NW is buried in the 2D layer.

3.3.4 Different nanowire shapes

Depending on the length of the NWs, we observed three different types of shapes. These shapes were observed from SEM images (Fig 3.9) and confirmed with TEM images: shape-1, observed for short NWs, shape-3 for very long NWs, and shape-2 for intermediate NWs. The three shape types observed are as follows:

Shape-1 (short NWs)

These are NWs with length L<150 nm, shown in Fig 3.9 (a) and Fig 3.10. These NWs consist of a long thin cylinder that often sits on top of a small pedestal. Although 3D objects and a few NWs crawling on the 2D surface were observed, they don't coalesce to form a 2D layer.

In Fig 3.10 are shown TEM images of 5 NWs from a sample (M3595). Average NWs length was observed to be 110±17 nm (avg.±SD) from SEM images. For each NW a second image is provided with blue lines to help visualize the NWs.

From SEM images (shown in Fig 3.9 (a)) shows clearly the base of the NWs. In the TEM images, the NWs appear to have a cylindrical shape. However, the base of the NWs in the TEM images is masked by the substrate and is not visible. Therefore, the entire length of the NWs can only be measured with SEM images.

On SEM images, it seems that the NP radius is smaller than the radius at the NP/NW interface (Fig 3.6 (a)). But from TEM images of several NWs, it is confirmed that the NP size is slightly bigger than the NP/NW interface radius. The reason for this is the more pronounced charging effect of the electron beam on the NW surface than the metal Au-NP in the SEM.

Shape-2 (Intermediate NWs)

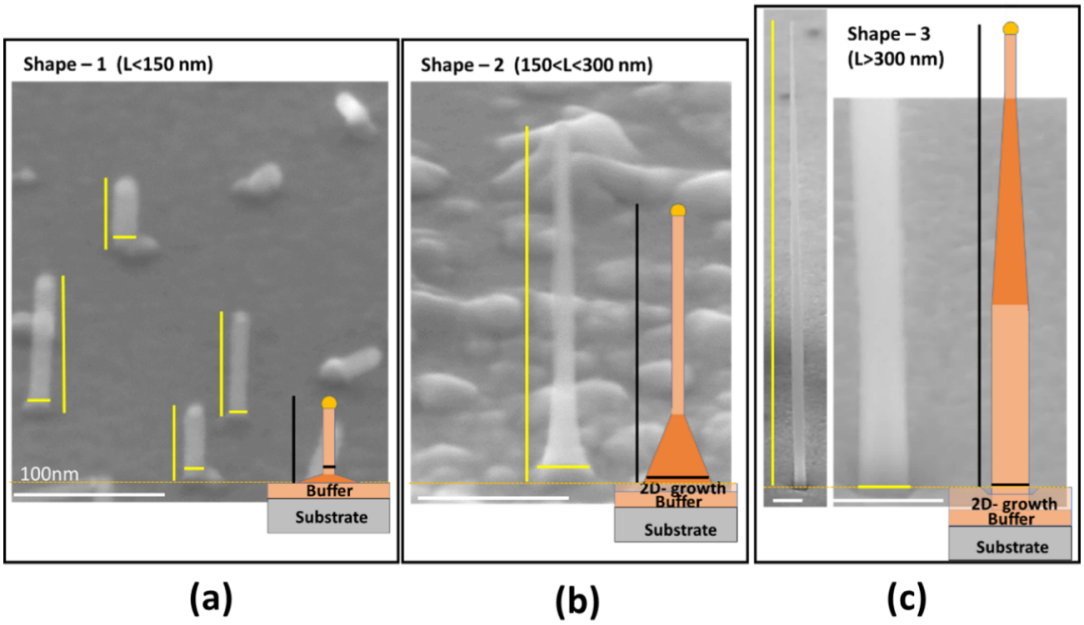

Figure 3.9: Side view SEM images (angle of 65°) of NWs from different samples representing the different shapes of NWs observed. The schemes represent the shapes of these NWs. (a) Short NWs (shape-1) are made up of a cylindrical section with or without a small pedestal at the base. (b) Intermediate NWs (shape-2) consist of a wide top-angle conical section at the base of the NW with a cylindrical section on top. (c) Long NWs (shape-3) consist of three sections- a cylindrical section (facets observed sometimes) at the base with a long conical section in the middle with a narrow top-angle and a short cylinder section at the top of the NWs. The yellow lines are where the visible length and base radius of the NW are measured. All scale bars in white are 100 nm.

These are intermediate NWs with 150<L<300 nm, shown in Fig 3.9 (b) and Fig 3.11. These NWs consist of a short conical section at the bottom of the NWs with a wide top angle followed by a thin cylindrical section at the top. Shape-1 NWs evolve into shape-2 NWs over time.

In Fig 3.11 are shown TEM images of 4 NWs and SEM images of 3 NWs from a single sample M3587. Average length measured from SEM images was 230±22nm (avg. ±SD).

Again these NWs have a carbon coating for TEM, and the base of the NWs is masked by the substrate. From the SEM images, the 2D surface is full of 3D-objects which still do not fully coalesce.

In Fig 3.12 is shown the radius as a function of position from NP/NW interface for the NW M3587-NW1, over the length visible in TEM. The shape of the NW is that of type 2 (see the scheme of Fig 3.9 (c)) *i.e.* a short cylindrical section on top of a conical section. The cylindrical section is roughly 60-70 nm in length while the conical section extends to at least 100 nm in length.

In Fig 3.13 are shown the same measurement of NW radius as a function of position from NP/NW interface for all NWs from sample M3587. Base radius values of several NWs from SEM (open black circles) are added to Fig 3.13. The average SEM base radius of 9±2 nm (avg. ±SD), as closed black circle, matches with the extrapolated conical section radius (solid black line) from the TEM images.

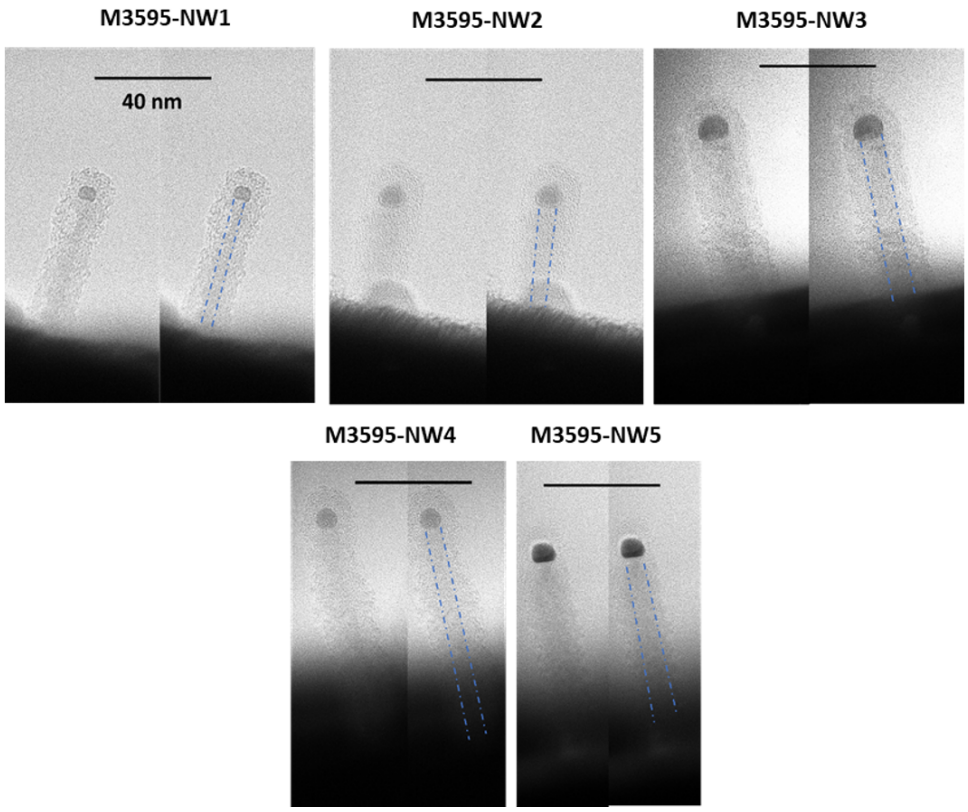

Figure 3.10: TEM images of 5 NWs representing shape-1 from sample M3595 grown at 350 °C for 8 min with Zn and Se fluxes of 0.165 and 1 ML/s respectively. The NWs have a carbon coating to prevent them from charging the effects of the electron beam. For each NW two TEM images are shown. The second image is a copy of the first image but with blue lines to help visualize the NW. The scale bar for all images is the same (40 nm). The dark regions at the top of each NWs are the Au-NP. The real length of the NWs is impossible to estimate from the TEM images as the base of the NWs is masked by the substrate.

Shape-3 (Long NWs)

These are NW with L>300 nm, shown in Fig 3.9 (c): For these NWs, a cylindrical section with facets is observed at the bottom of each NW followed by a conical section in the middle with a narrow top angle, followed by a small cylindrical section at the very top. A crater (hole) in the 2D surface was usually observed around the NW. For shape-3 NWs, SEM images are enough to confirm the shape. Shape-2 NWs evolve into shape-3 NWs over time.

3.3.5 Measurement determination (error bars)

As shown in the previous sections, we have different shapes of NWs and 2D layers in which the NWs are buried. Therefore, how we measure the dimensions of the NWs becomes important if we want to compare different samples. In this section, is explained the procedure we followed to determine the shape of the NWs as accurately as possible.

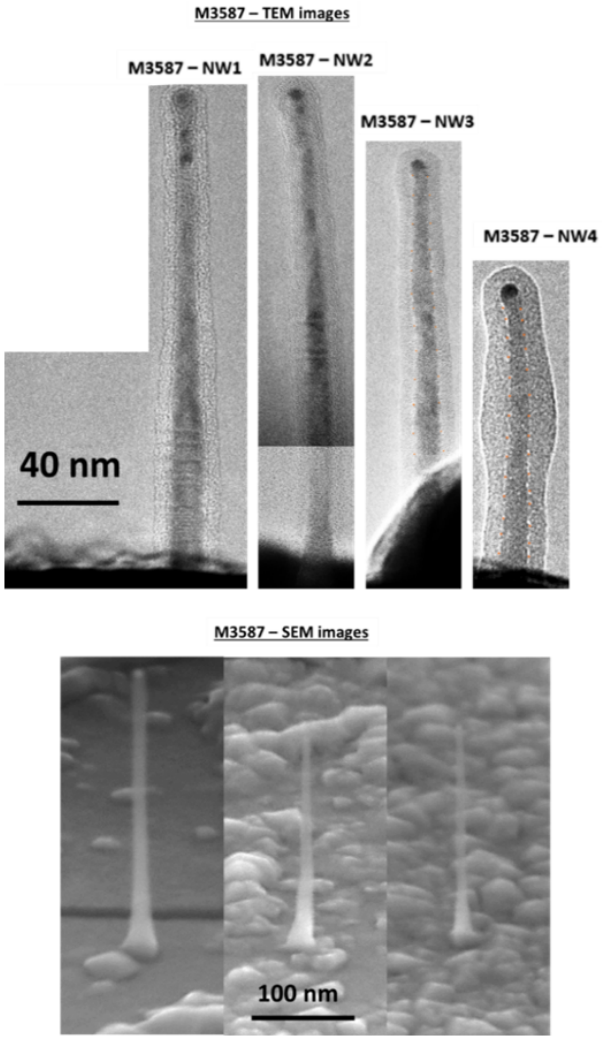

Figure 3.11: TEM images of 4 NWs and side view SEM images (angle of 65°) of 3 NWs representing shape-2 from sample M3587 grown at 350 °C for 20 min with Zn and Se fluxes of 0.165 and 1 ML/s. The scale bar is same for all TEM images (40 nm) and for all SEM images (100 nm). The NWs in the TEM images have a carbon coating to prevent them from charging effects of the electron beam.

Radius and length are the two important parameters that we use in identifying the shape of the NWs and therefore the axial and radial growth of the NWs. They were measured mostly from SEM images taken at an SEM-angle of 65° and occasionally at 90° to the sample normal. The lengths for the SEM images taken at 65° angle were corrected as:

$$Corrected\ NW\ length = \frac{SEM\ measured\ NW\ length}{\sin(65°)} = \frac{SEM\ measured\ NW\ length}{0.906} \tag{3.2}$$

From the SEM images, we can directly measure the base radius and visible length of the NWs. In Fig 3.14 is shown scheme for shape-2 and shape-3 NWs. The length l_{NW} is the visible NW length measured with SEM just above the 2D surface. The total length L_{NW} of the NW includes the length buried in the

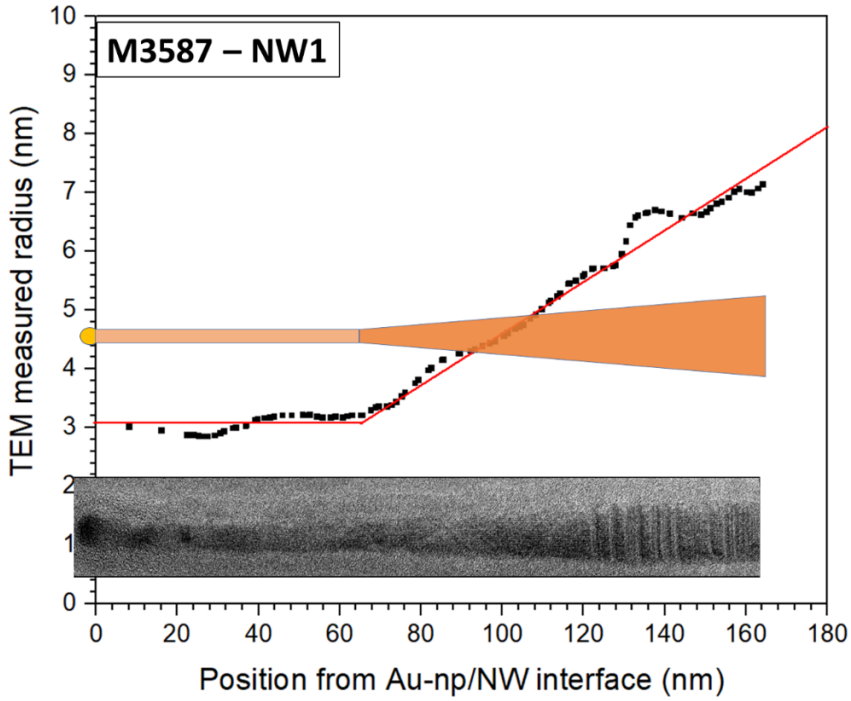

Figure 3.12: Radius measured for M3587-NW1 at different position from the Au-NP/NW interface. Radius is measured from TEM image of M3587-NW1 superimposed on the plot with the same scale. The schemes of shape-2, with a cylindrical section that sits on a broad-angle conical section, is also superposed. The red line is a guide for the evolution of radius along the NW length.

2D and is given as:

$$L_{NW} = l_{NW} + 2D_{NW} \tag{3.3}$$

where the $2D_{NW}$ is the 2D-layer thickness related to just the NW growth and is given as:

$$2D_{NW} = (2D_{Total}) - (2D_{Buffer}) \tag{3.4}$$

where the $2D_{Total}$ is the total 2D thickness measured with SEM. The $2D_{Buffer}$ is estimated to be about 8 nm (from RHEED oscillations). Since the error bars in measurement of $2D_{Total}$ are or orders of $2D_{Buffer}$ or more, SEM measured $2D_{Total}$ is kept for $2D_{NW}$.

The visible radius measured with SEM at the base of the NW (close to the 2D surface) is r_{NW}. However, the real NW radius (R_{NW}) is buried in the 2D. For shape-3 (long) NWs with a cylindrical section at the base, R_{NW} is essentially the same as r_{NW}. For shape-1 (short) and shape-2 (intermediate) NWs, the 2D thickness could not be observed in SEM, and again R_{NW} is essentially r_{NW}. Therefore, for the rest of the thesis, only r_{NW} is presented.

While measuring the radius and length of the NWs, importance was given to maximizing the magnification of the SEM images. For the length, images are taken so that the entire length of the NW is visible in a single image while maximizing the magnification. While for short NWs (Shape – 1), both length and radius could be measured from a single high magnification image, for intermediate and long NWs (Shape 2 and 3), at least two images were taken on each NW with different magnification, one with low magnification for measuring the entire visible length and another one at higher magnification

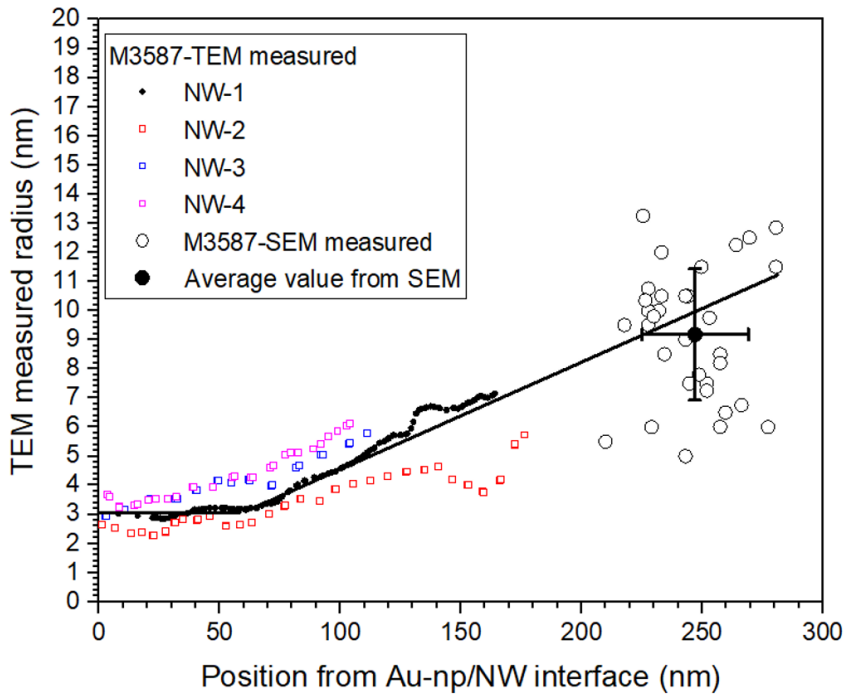

Figure 3.13: Radius measured for different NWs as a function of position from the Au-NP/NW interface for sample M3587. Square symbols represent radius measured for NW1, NW2, NW3 and NW4 using TEM images (Fig 3.11). The SEM data measured for individual NWs (open circles) and the average values (closed circle) is also represented on the graph. The solid black line representing the scheme in Fig 3.12 is also added. The error bars on the SEM measured radius and length for each NW are according to table 3.1

to measure the base or tip radius of the NW.

Error bars

For each NW the error bars on length and radius are defined after repeated manual measurement of length and radius on the same image. Therefore, error bars for SEM images are defined by the magnification of the image. For a NW with a high magnification such as shown in Fig 3.9 (a and b), the error bar for radius and length are taken as ±0.5 nm and ±5 nm. The error bar for length is higher because sometimes the bottom and tip of the NWs are not clearly defined. For long NWs, the length is calculated from a low magnification image such as in Fig 3.9(c) while the radius from a high magnification image such as the image on the right in Fig 3.9 (c). Here the error bar for length is ±15 nm and ±2 nm for radius.

Throughout this thesis, the length and radius of an individual NW are reported with their error bars defined according to the table 3.1. The average length and average radius for a sample are reported as the average of at least 30 NWs measured at different regions on the sample, along with the standard deviation *i.e.* average length and radius ± standard deviation (avg. ±SD).

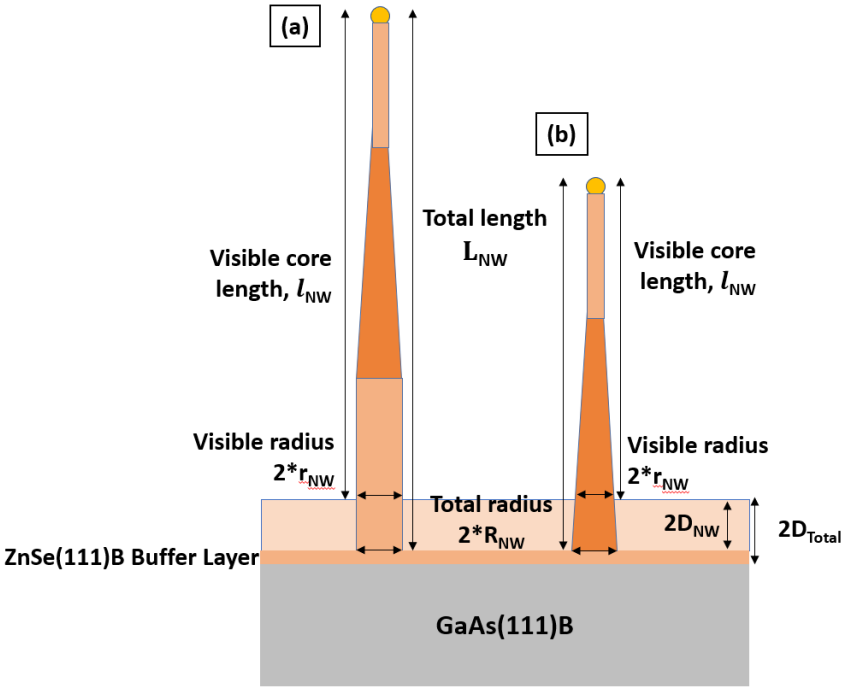

Figure 3.14: Scheme for the growth of NWs defining all the measured and calculated parameters. (a) Shape 3 and (b) shape 2 NWs are presented. The visible NW length is measured from the tip of the NW to the 2D surface (l_{NW}). And the total NW-core length (L_{NW}) takes into account the $2D_{NW}$ thickness in which the NW is buried. Similarly, R_{NW} is the radius of the NW buried in the $2D_{NW}$. $2D_{Total}$, l_{NW} and r_{NW} are measured directly from SEM images, while $2D_{NW}$, R_{NW} and L_{NW} are calculated.

SEM image magnification	Error bar in measured radius (nm)	Error bar in measured length (nm)
Shape-1 NWs	±0.5	±5
Shape-2 NWs	±1	±10
Shape-3 NWs	±2	±15

Table 3.1: Error bars for base radius and length of NWs measured from SEM images for the three different shapes. Error bars are related to the magnification of the SEM images, with high magnification images giving low error bars

3.3.6 Summary

In summary, three shape types for NWs were observed with SEM and TEM: 1. short NWs with a thin cylinder, sitting or not on a small pedestal, 2. intermediate NWs with a broad-angle conical section with a thin cylinder on top, and 3. long NWs with a thick cylindrical section at the bottom with a long narrow-angle conical section in the middle and a thin cylindrical section on top. The average Au-NP size determined from TEM images was 3.7±0.8 nm (avg. ±SD). With NW growth, is associated a 2D-growth. This 2D layer thickness has to be taken into account while calculating the real NW length and radius.

In the following section, we discuss the effect of parameters such as Zn and Se flux, and growth time, for the growth of ZnSe NWs at one fixed temperature.

3.4 ZnSe nanowires growth at 350°C

In this section, is presented NWs growth at 350 °C. We studied the effect of Se and Zn fluxes, and then the evolution with time.

3.4.1 Effect of Se and Zn amount on nanowire growth

Se and Zn amounts and the ratio of Zn/Se sent onto the sample to grow ZnSe NWs affect the shape, size and crystal quality of the ZnSe NWs. From previous studies [12] done in our group, we know that excess of Zn inhibits ZnSe NWs growth and that Se amount twice higher than Zn results in vertical NWs with smooth lateral NW surfaces.

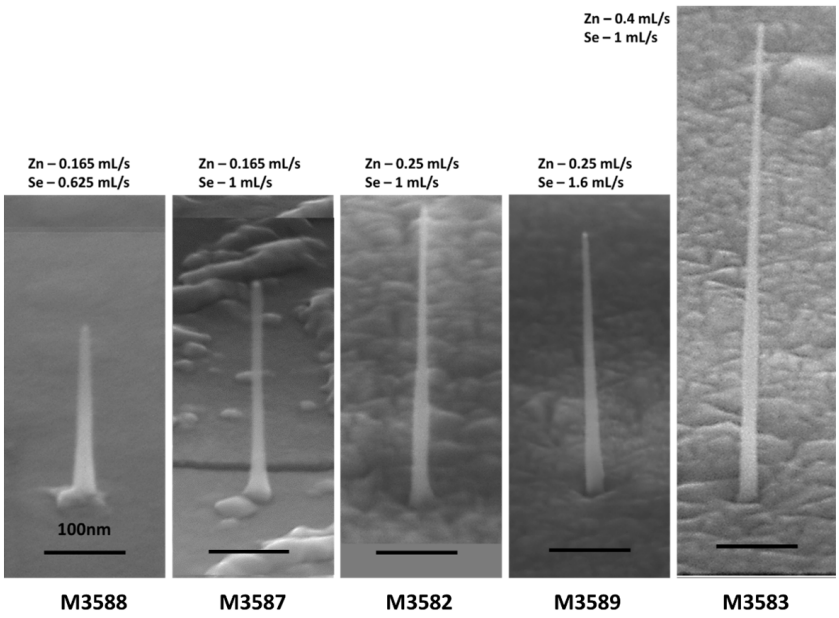

Figure 3.15: Side view SEM images (angle of 65°) of typical NWs grown at 350 °C for 20 min with varying amount of Se and Zn as given in table 3.2. The scale bar is same for all images (100 nm).

To check the dependence on Se and Zn flux, 5 samples (M3588, M3587, M3582, M3589, and M3583) were prepared. The Se and Zn fluxes (in ML/s) for these samples are given in table 3.2 and in Fig 3.16. Since excess of Se is required for vertical and smooth surface NWs, Se was always kept at least twice the Zn amount. All samples were grown at 350 °C for 20 min.

SEM images of these 5 samples are shown in Fig 3.15. In Fig 3.16, r_{NW} is plotted as a function of L_{NW} for all 5 samples with at least 30 NWs per sample. Error bars on each NW are according to table 3.1 and the average length, radius with their standard deviation (SD), and 2D layer thickness for these samples are mentioned in table 3.2.

For the same Zn flux rate (comparison of samples M358-M3587 and samples M3582-M3589), an increase in Se flux have almost no effect on the size of the NWs. Whereas, for an increase of Zn flux with

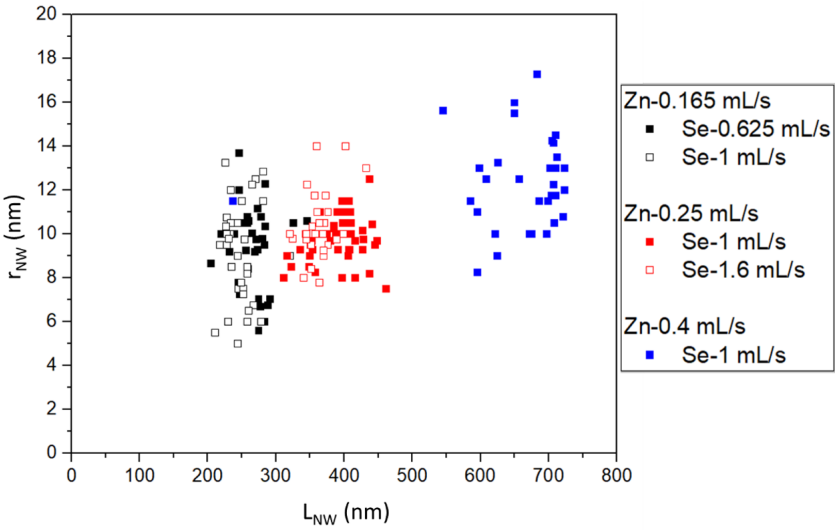

Figure 3.16: Visible base radius r_{NW} *vs.* total length L_{NW} for samples grown with varying amounts of Zn and Se at 350 °C for 20 min. Open symbols represent higher Se amounts for same Zn amounts. The average values of r_{NW} and L_{NW} are given in table 3.2. The error bars of each measurement are given in table 3.1

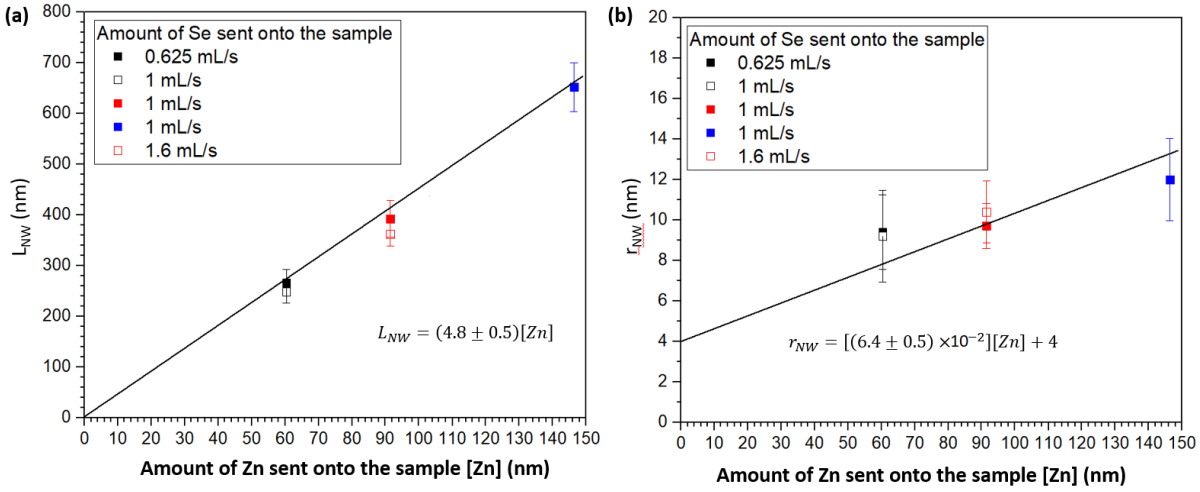

Figure 3.17: Average values of (a) total length L_{NW} and (b) visible base radius r_{NW} of NWs grown at 350 °C as a function of the amount of Zn and Se sent onto the sample surface with Se always at least twice the amount of Zn. Open symbols represent higher Se amounts for same Zn amount. The SD in average values of more than 30 NWs is taken as the error bars. The linear fit (black line) is also presented.

the same Se flux (samples M3587-M3582-M3583), both L_{NW} and r_{NW} increase. This is quite evident if we plot the average values (SD as error bars) of L_{NW} and r_{NW} as a function of the amount of Zn sent onto the sample surface in Fig 3.17, where a linear fit is also presented. For the r_{NW} the fit starts from 4 nm which is the Au-NP radius as measured by TEM. Note that the radius measured by SEM is

systematically larger by 1 or 2 nm. Both L_{NW} and r_{NW} increase linearly with Zn amount. The slope for the increase in L_{NW} and r_{NW} with increasing Zn amount is 4.8±0.5, and 6.4±0.5 × 10^{-2}, respectively. No effect on the shape and size of NWs is seen with a change in Se flux.

3.4.2 Evolution of nanowires with amount of Zn

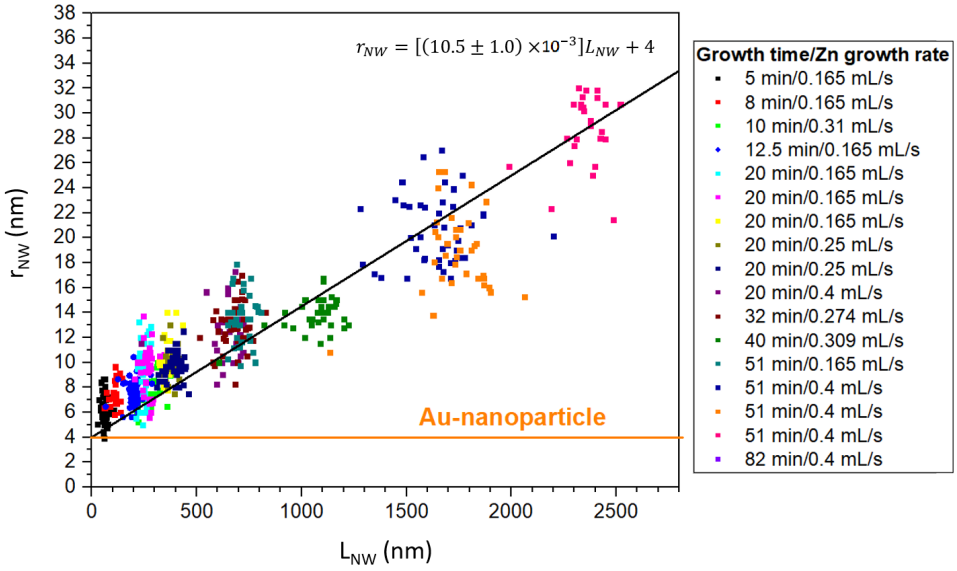

Figure 3.18: Visible base radius r_{NW} *vs.* total length L_{NW} for all the samples presented in table 3.2. For each sample all the measured NWs are represented. All samples were grown at a temperature of 350 °C. Linear fit starts from the average radius of Au-NPs (4 nm).

In this section we discuss how the shape and size of the NWs is affected by the total amount of Zn sent onto the sample (whatever the way we change it: by changing either the growth time or by changing the flux).

Different samples were grown, all at 350 °C, for a range of growth time and different Zn fluxes. These samples are described in table 3.2. Rows with light blue, light green, and orange colors are samples grown with 0.165, 0.25, and 0.4 ML/s respectively. Some samples were repeated to evaluate reproducibility. As seen in the previous section, the effect of different Se fluxes can be neglected since Se flux was always at least twice the Zn flux. In table 3.2, also mentioned are the L_{NW} and r_{NW} values averaged over for at least 30 NWs for each sample.

The evolution r_{NW} *vs.* L_{NW} for all samples in table 3.2 is presented in Fig 3.18. The black solid line is the linear fit to these NWs which starts from 4 nm (i.e Au-NP radius).

Samples with same Zn amount: M3589 and M3582 with Zn-77.87 nm and samples M3600, M3607 and M3608 with Zn-295.9 nm, all have similar L_{NW}, r_{NW}, and $2D_{Total}$ with variation within the SD for L_{NW} and r_{NW}, and within the error bar for $2D_{Total}$. Therefore, the reproducibility of our samples is quite good.

In Fig 3.19 is shown (a) L_{NW} and (b) r_{NW} as a function of Zn amount sent onto the sample surface for all samples in table 3.2. Both L_{NW} and r_{NW} increase linearly with Zn amount (fit is presented with solid black line). While the increase in L_{NW} is very fast (almost 5 times), the r_{NW} increase is rather slow

Sample Number	Growth time (min)	Growth rate (mL/s)		Zn amount sent onto the sample (nm)	Visible base radius r_{NW} (nm) (avg.±SD)	Total length L_{NW} (nm) (avg.±SD)	Total 2D $2D_{NW}$ (nm)
		Zn	Se				
M3593	5	0.165	1	18.76	6.2±1.2	60±14	10±5
M3595	8	0.165	1	29.31	7.5±0.9	110±18	20±5
M3467	10	0.31	1	52.64	7.6±1.2	280±45	45±5
M3592	12.5	0.165	1	36.28	7.7±0.9	200±25	25±5
M3587	20	0.165	1	53.8	9.2±2.2	245±22	35±5
M3588	20	0.165	0.625	52.64	9.4±1.9	265±27	45±5
M3589	20	0.25	1.6	77.87	10.4±1.5	360±23	75±5
M3590	20	0.165	1	81.84	10.0±1.2	385±23	82±5
M3582	20	0.25	1	77.87	9.7±1.1	390±35	55±5
M3583	20	0.4	1	120.35	12.4±2.0	710±50	92±5
M3435	20	0.274	1	85.55	12.9±1.8	675±60	0
M3470	40	0.309	1	183.75	14.0±1.3	1070±110	130±10
M3591	51	0.165	1	126.23	13.5±2.0	715±45	105±10
M3600	51	0.4	1	295.9	20.6±2.7	1640±165	175±10
M3607	51	0.4	1	295.9	18.9±3.2	1740±145	295±15
M3608	51	0.4	1	295.9	22.1±3.8	1920±150	245±15
M3602	82	0.4	1	471.5	28.6±2.8	2350±105	470±15

Table 3.2: Growth parameters used to study the effect of the amount of Zn sent onto the sample surface on NW shape and size. Samples are listed here with increasing growth time. All samples were grown at 350 °C with different amounts of Zn and Se. Se was always at least twice the Zn amount. Rows with blue, green, white and orange colors represents sample with Zn-0.165, 0.25, 0.3 and 0.4 ML/s. The avg. ±SD for the visible base radius r_{NW}, the total length L_{NW} and the total 2D thickness $2D_{Total}$ is indicated for each sample.

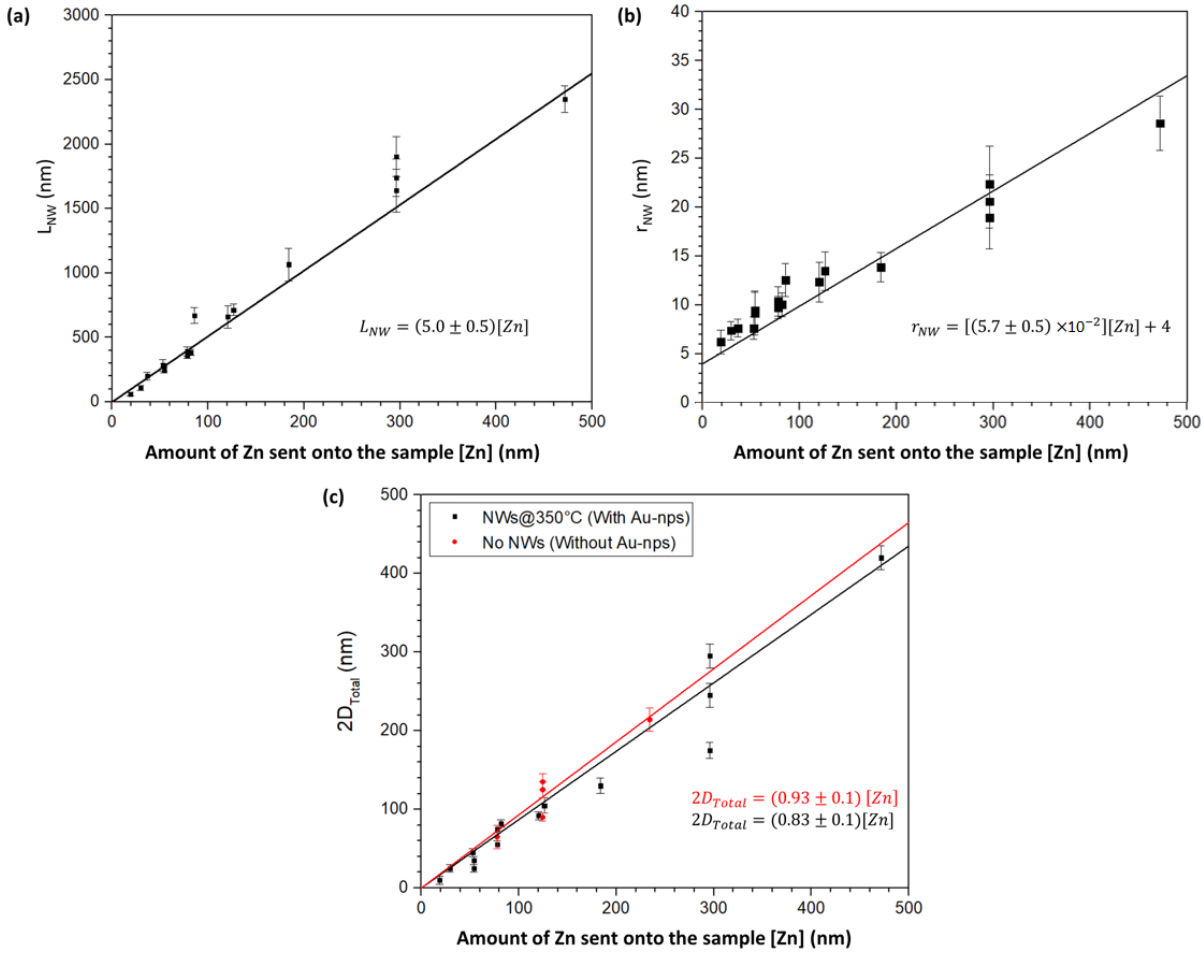

Figure 3.19: Effect of amount of Zn sent onto the sample on the size of the NWs. Average values of (a) total length L_{NW}, (b) visible base radius r_{NW}, and (c) total 2D thickness $2D_{Total}$ for samples listed in table 3.2. For $2D_{Total}$ are also mentioned (in red) samples with no Au-NP on the surface (therefore, no NW growth). The error bars are the SD in average values. The slopes of the linear fits are indicated

(about 5.7±0.5 × 10^{-2} times) with increasing in Zn amounts. From the slopes of the fit, it can be said that axial growth is about 100 times faster than radial growth, as also revealed by the linear fit in Fig 3.18. The fit for L_{NW} starts from zero. This suggests that there is no incubation time observed for the growth of ZnSe NWs.

In Fig 3.19 (c) is shown $2D_{Total}$ as a function of Zn amount sent onto the sample surface with (all NW samples in table 3.2) and without Au-NP on the surface of the samples (therefore, no NW growth), also grown at 350 °C. Their linear fits are presented as black and red solid lines. 2D growth for samples with no NW growth (without Au-NP) is slightly higher than samples with NWs growth (with Au-NPs). The slope of the fits gives us the percentage of Zn adatoms that contribute towards the 2D layer thickness. Without Au-NP, 93 % of Zn adatoms contribute towards 2D layer growth, and with Au-NPs (NWs growth) about 83%. This means that only a very small 10 % of Zn atoms sent onto the sample surface may contribute towards the growth of ZnSe NWs, but the error bar is large.

3.4.3 Summary

In summary, we studied the effect of Zn and Se amounts on the growth of ZnSe NWs at 350 °C and how they evolve with time. We have observed that as long as Se flux is twice the Zn flux, the amount of Zn sent onto the sample surface controls the NW growth. The L_{NW} and r_{NW} both increases linearly with Zn amount. The L_{NW} increases 100 times faster than r_{NW}. There is no evidence of an incubation time during the initial growth of NWs.

3.5 Effect of growth temperature (300-400 °C) on ZnSe nanowires

In this section we discuss the effect of temperature on the axial and radial growth of NWs, and 2D growth of the sample. The range of growth temperature that we studied is 350±50 °C (400, 350, 320 and 300 °C). In the following section is detailed the NWs grown at 320 °C, before presenting the growth at other temperatures (300 and 400 °C in section 3.5.2 and section 3.5.3).

3.5.1 Growth at 320°C

Four samples were grown at 320 °C. These samples had Zn and Se fluxes of 0.4 and 1 ML/s respectively and were grown for different times (table 3.3). Fig 3.20 (a) shows an SEM image of a NW from sample M3611 (longest sample of the series), grown at 320 °C for 130 min. The average L_{NW} and r_{NW} for this sample is 3700±70 and 59±5 nm. The NW surface looks very smooth and a crater (hole) is present around the NW in the 2D surface. A thick $2D_{Total}$ of 830±40 nm was measured which means about 2870 nm of L_{NW} was visible with SEM.

Sample Number	Growth time (min)	Growth rate (mL/s)		Zn amount sent onto the sample (nm)	Visible base radius r_{NW} (nm) (avg.±SD)	Total length L_{NW} (nm) (avg.±SD)	Total 2D $2D_{Total}$ (nm)
		Zn	Se				
M3596	20	0.4	1	120.35	12.3±1.2	655±62	113±10
M3601	51	0.4	1	295.9	22.8±1.7	1450±123	215±10
M3612	82	0.4	1	471.5	45.5±5.5	2335±87	480±15
M3611	150	0.4	1	743	59±5.1	3700±72	830±15

Table 3.3: Growth parameters used to study the effect of time (or amount of Zn sent onto the sample surface) on NW shape and size for samples grown at 320°C. Samples are listed with increasing growth time. All samples were grown with same flux of Zn and Se. The avg. ±SD for the visible base radius r_{NW}, the total length L_{NW} and the total 2D thickness $2D_{Total}$ is indicated for each sample.

In Fig 3.20 (b) is shown a plot of r_{NW} *vs.* L_{NW} for all samples grown at 320 °C as well as the linear fit (red line). For comparison linear fit for NWs at 350 °C (black dashed line) is also provided.

To analyze in more detail the effect on axial and radial growth rates, the evolution of L_{NW} (total NW length) and r_{NW} (Visible NW length) as a function of the amount of Zn sent onto the sample surface in nm is shown in Fig 3.21. Again, linear fits for the sample at 350 °C are shown in black dashed lines. Both radial and axial growths of the NWs are linear with Zn amounts. While there is almost no change

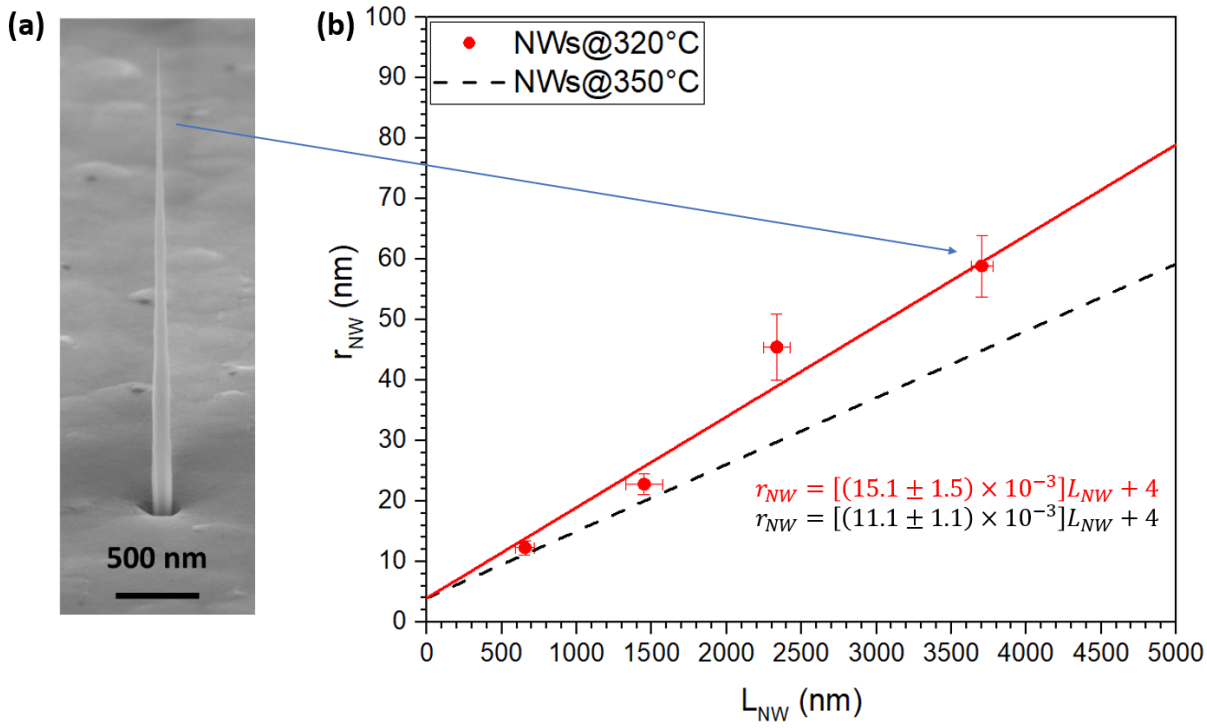

Figure 3.20: (a) Side view SEM image (angle of 65°) of a NW from sample M3611, grown at 320 °C. (b) Visible base radius r_{NW} *vs.* total length L_{NW} for all the samples grown at 320 °C (red circles with red line as fit). The fit for samples at 350° is presented in dashed black line (obtained from Fig 3.18). For each sample the average with SD as the error bar is represented. Linear fit starts with 4nm for r_{NW}. The blue arrow points towards the sample to which the NW in the SEM image belongs to.

in axial growth with a decrease in temperature from 350 to 320 °C, about 33 % increase in radial growth is observed. This is in agreement with the change of slope *i.e.* tapering angle, observed in Fig 3.20.

The $2D_{Total}$ also increases linearly with Zn amount sent onto the sample (Fig 3.21 (c)). From the linear fits, a 20 % increase in 2D growth is observed with a decrease in temperature from 350 to 320 °C.

The crystal quality was characterized with TEM for a NW grown at 320 °C. The NW was found to be defect free (Fig 3.34, introduced later).

3.5.2 Growth at 300°C

Although, increase in radial growth of NWs is observed at 320 °C, even with 130 min of NW growth, a r_{NW} of 80-100 nm (required for efficient light guiding) is not achieved. Therefore, ZnSe NWs growth was also investigated for an even lower growth temperature of 300 °C. In Fig 3.22, is shown SEM images of 2 NWs from two different samples: one grown for 20 min and other for 130 min. The Se and Zn fluxes were calibrated to 0.4 and 1 ML/s for both samples, similar to all samples grown at 320 °C. Contrary to the NWs grown at 320 °C showing a smooth conical surface, here the NW's surface have several segments of different orientations. As shown later in the TEM image of a core-shell NW in Fig 3.36, the NWs (shell in the image) grown at 300 °C were full of defects all along the NW length.

The average L_{NW}, r_{NW} and $2D_{Total}$ for the 20 min sample are 600±15 nm, 20±2 nm, and 170±10

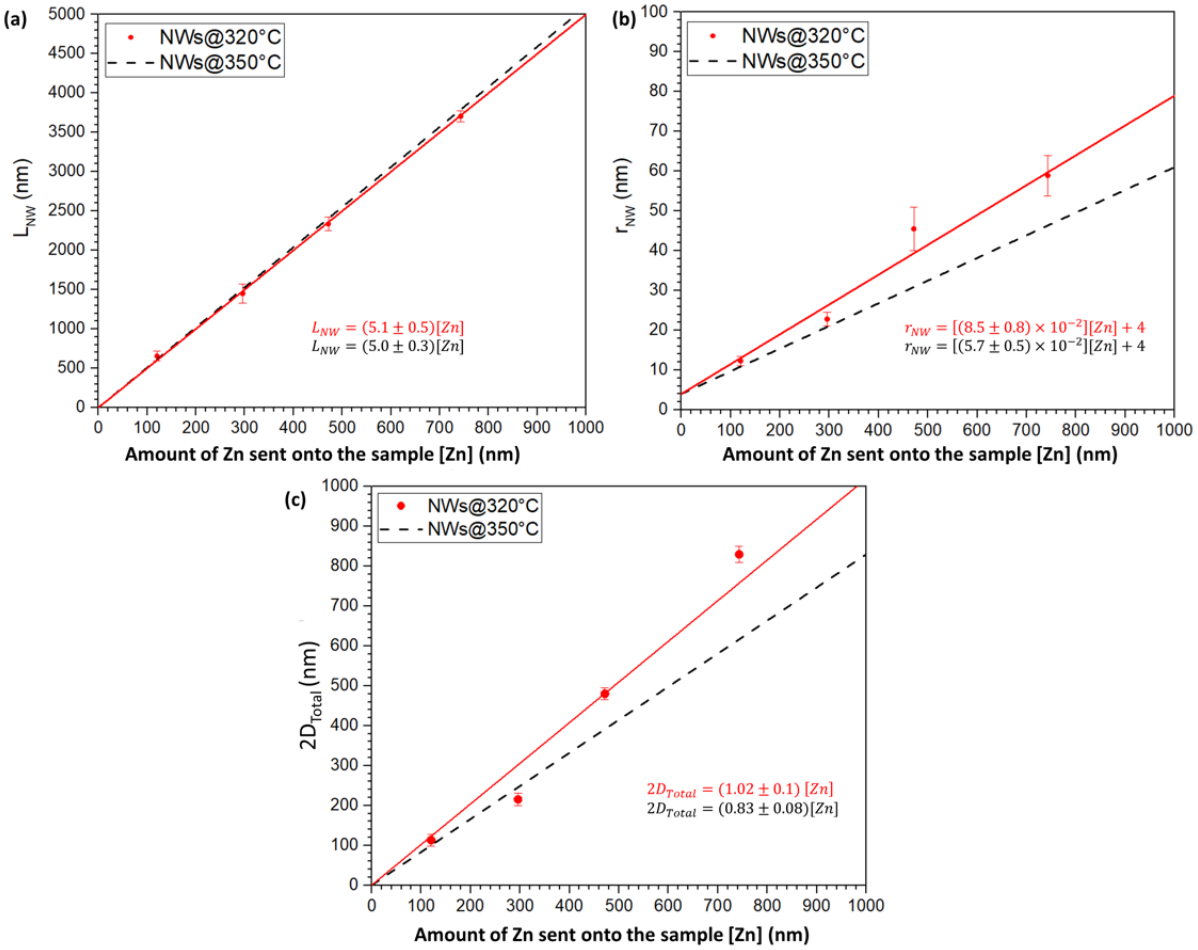

Figure 3.21: Effect of temperature on average values of (a) total length L_{NW}, (b) visible base radius r_{NW}, and (c) total 2D thickness $2D_{Total}$ with varying amounts of Zn sent onto the sample. Samples at 320 °C (in red) are listed in table 3.3. The dashed black lines present fit for samples at 350 °C obtained from Fig 3.19. The error bars are the SD in average values.

nm respectively, and for 130 min sample are 4200±165 nm, 75±10 nm, and 745±30 nm respectively.

In Fig 3.23 is plotted (a) L_{NW}, (b) r_{NW} and (c) $2D_{Total}$ as a function of Zn amount sent onto the sample surface for the two sample grown at 300 °C (in pink). Linear fits for the samples at 320 and 350 °C are also shown for comparison. Although the slope of the fit for L_{NW} is similar and within error bars for the three temperatures, the slope for r_{NW} and $2D_{Total}$ increases with decreasing temperatures from 350 to 300 °C. There is about 46 % and 37 % increase in radial growth and 2D growth respectively with decrease in temperature from 350 to 300 °C.

The further decrease in temperature to 300 °C confirms the previous trend of increase in radial and 2D growth. And for 130 min of NW growth, a r_{NW} of 75±10 nm is observed which is close to required 80-100 nm values for efficient light guiding. However, as mentioned before, NWs are full of defects with a surface with several segments of different orientations, as confirmed with TEM images (Fig 3.36, introduced later).

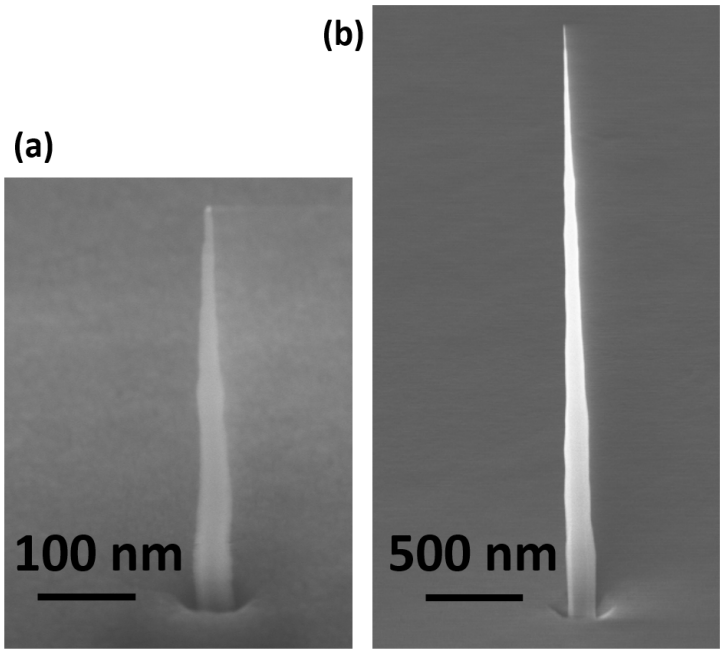

Figure 3.22: Side view SEM image (angle of 65°) of two NWs from samples grown at 300 °C for (a) 20 min and (b) 130 min.

The change in 2D growth rate (on only 2 points) suggests that there is an effect of temperature not only on the ZnSe layer growth, but even on the ZnTe which serves as a calibration of the Zn flux. However, growth at 300 °C is highly defective and we did not go further.

3.5.3 ZnSe NWs@ 400 °C

Above 350 °C, we investigated only growth temperature of 400 °C. In Fig 3.24, is shown SEM images of two nanowires grown at 400°C for (a) 20 and (b) 40 min with Zn-0.288 ML/s and Se-1.65 ML/s. Zn amounts sent onto these sample's surface was about 82 and 164 nm respectively.

The r_{NW} for both NWs in the SEM images is about 7±0.5 nm, close to radius of the Au-NP, while the L_{NW} is about 620±10 and 875±10 nm for the 20 and 40 min growth sample respectively. Both NWs have a very high aspect ratio with minimal radial growth. Such NWs are very fragile and it was not possible to perform a complete study including NWs of longer lengths. No measurable 2D layer could be detected for these samples.

3.5.4 Summary

Growing ZnSe NWs (at 350 °C) we can see that the radial growth is very slow and we aim to obtain a NW with a radius in the range 80-100 nm. One possible solution is to decrease growth temperature. Indeed we do increase the radial growth but if we go too low (300 °C) we start to introduce defects in the NW. Another problem we face is the 2D growth during NW growth. To reach a radius of 80-100 nm implies having a 2D layer of about 1 μm. Therefore is it possible to be in a growth configuration where we keep (or increase) the radial growth but keep the thickness of the 2D layer smaller.

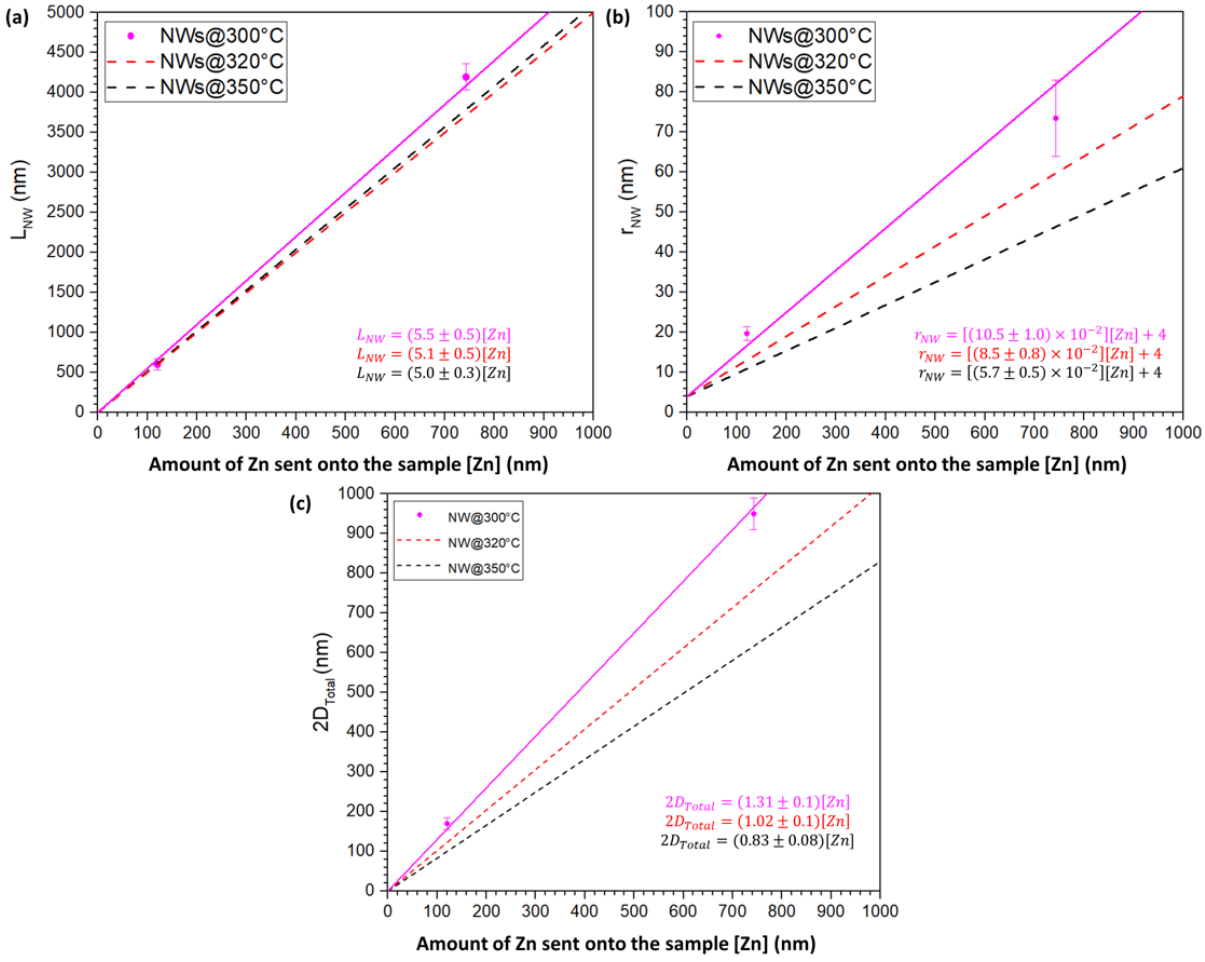

Figure 3.23: (a) total length L_{NW}, (b) visible base radius r_{NW}, and (c) total 2D thickness $2D_{Total}$ for samples grown at 300 °C (magenta) as a function of Zn amount sent onto the sample surface. In solid magenta line is linear fit to the sample at 300 °C. For comparison linear fit of samples at 320 (red) and 350 °C (black) are also shown.

3.6 Effect of sample tilt

With a sample tilt of 10° towards the Zn cell, we expect a decrease in Zn flux on the substrate compared with that on the sides of the NW (see Fig 3.25) by a factor from 1.28 in the normal position to 0.87 in the 10° tilted position (see section 1.4.1.4 for more details). Note that the sample is no more centered on the axis of the Zn cell, so that flux can be smaller than in the standard position, particularly if the cell is only partly filled. To check it two samples were prepared with a 10° sample tilt towards the Zn cell (hereafter called OFF-AXIS).

In Fig 3.26 is presented (a) L_{NW}, (b) r_{NW} and (c) $2D_{Total}$ *vs.* Zn amount sent onto the sample surface for two samples (20 and 184 min) grown at 320° C - OFF AXIS (in blue). The Zn and Se fluxes of 0.4 and 1 ML/s respectively are similar to samples grown at 320 °C. For comparison, the linear fit for samples grown at 320 °C without a sample tilt is also shown in red dashed line.

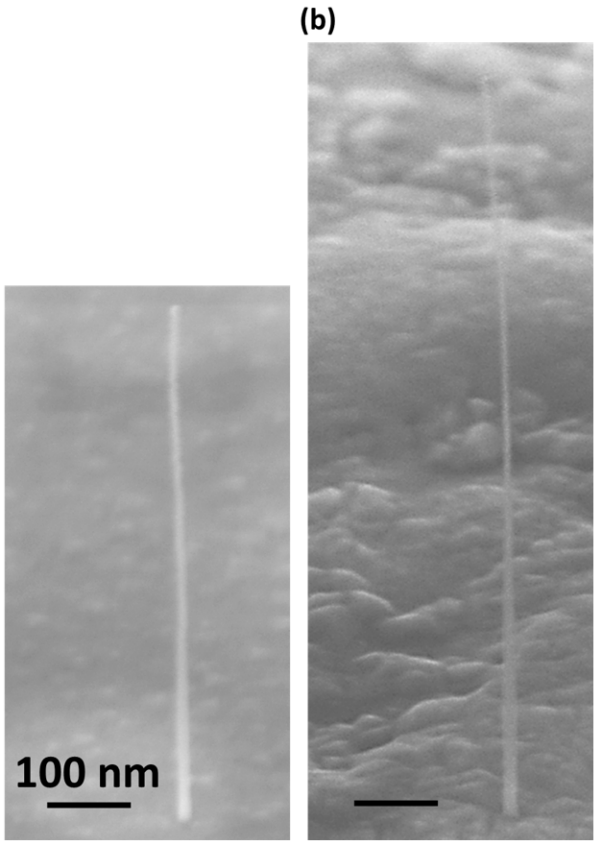

Figure 3.24: Side view SEM images (angle of 65°) of NWs grown at 400 °C for (a) 20 min and 40 min.

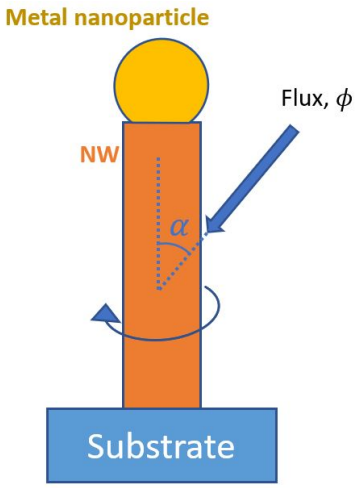

Figure 3.25: Flux ϕ arriving on the substrate and on the NW sidewalls in our MBE setup. Flux on the NW sidewalls is averaged over the circumference of the NW. Repeated from Fig 2.3.

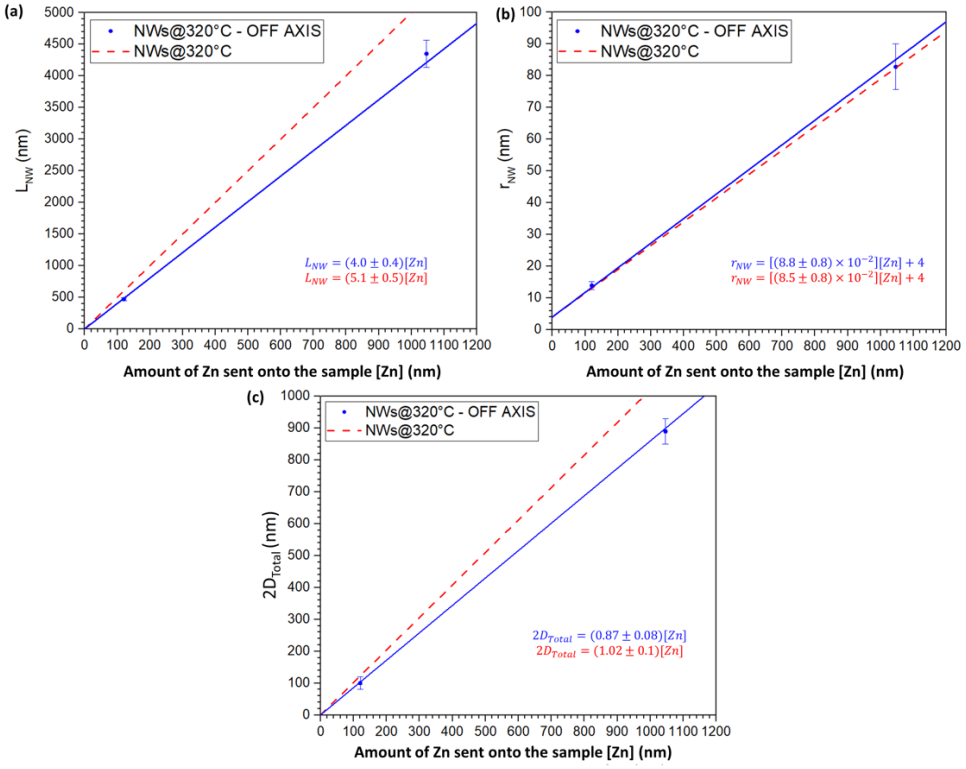

Figure 3.26: (a) Total length L_{NW}, (b) visible base radius r_{NW}, and (c) total 2D thickness $2D_{Total}$ for samples grown at 320 °C - OFF AXIS (blue) as a function of Zn amount sent onto the sample surface. In solid blue line is the linear fit to the sample at 320 °C - OFF AXIS. These sample were tilted by 10° during growth. For comparison linear fit of samples at 320 °C without sample tilt (red) is also shown.

With a 10° sample tilt, the slope of the linear fit for L_{NW} decreases by more than 15 %, whereas the slope for the r_{NW} is almost unaffected. The slope for the $2D_{Total}$ is also decreased by almost 15 %. For the sample grown for 184 min, the r_{NW} is 82±7 nm, L_{NW} is 4350±215 nm and the $2D_{Total}$ is 890±40 nm.

In conclusion, with a sample tilt of 10° at 320 °C, the axial growth of NWs and 2D-surface growth are decreased but the radial growth of the NWs is unchanged. We will come back to the tilt effect in section 3.8.

3.7 Core-Shell NWs

The concept of core-shell NWs is important for the growth of our QD-NWs. We want to grow a NW first, which acts as a core for the insertion of QD, and then, grow a thick and tapered shell for the guiding of light from the QD. The NW core controls the size of the QD and therefore its optical properties. The NWs grown at 350 °C (section 3.4) are promising for the insertion of QD. Therefore, samples were grown where a core was first grown at 350 °C to initiate the NW growth, and then a shell was grown.

To compare these shell samples with NW samples studied so far, it is important to separate the axial and radial growth of the shell from that of the core. The scheme for the growth of a shell on a core is

given in Fig 3.27. We grow a shell on a core whose average r_{NW}, L_{NW}, and $2D_{Total}$ values are previously known from a sample with just core growth.

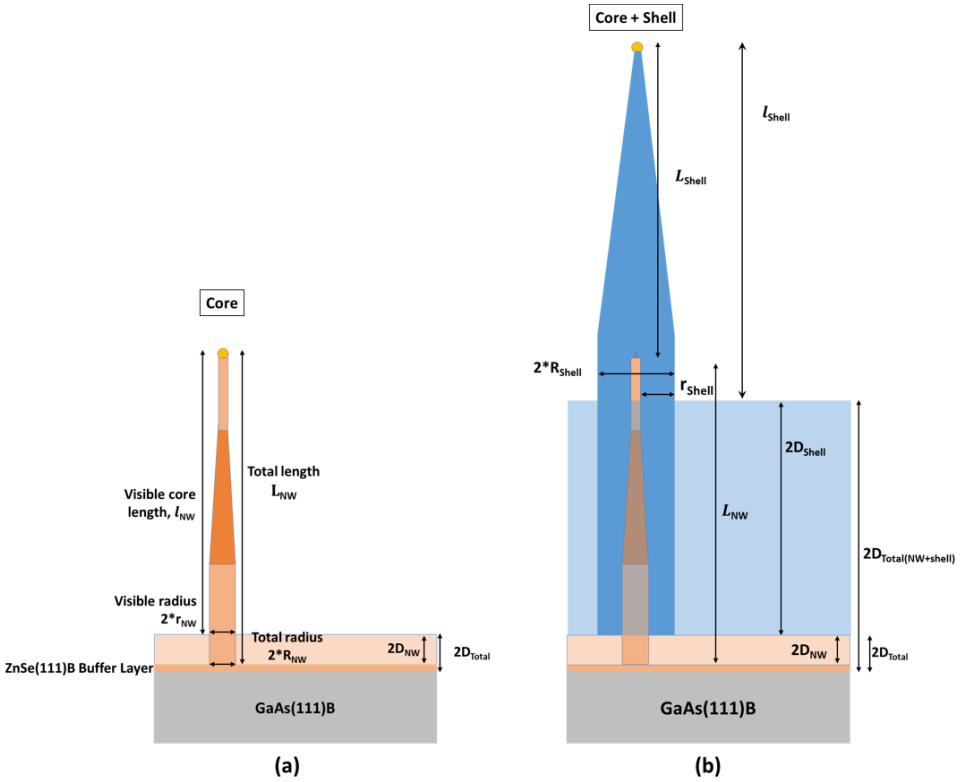

Figure 3.27: Scheme for the growth of the (a) core and the (b) core+shell defining all the measured and calculated parameters. The growth of shell and its associated 2D growth is indicated in blue. For the core+shell, the visible length l_{Shell} is measured from the tip of the NW to the 2D surface. The $2D_{Total(NW+Shell)}$ takes into account the 2D thickness of the core+shell+buffer. The visible base radius r_{Shell} is for the core+shell. The l_{Shell}, $2D_{Total(NW+Shell)}$ and r_{Shell} are measured directly from the SEM images. Calculated L_{Shell} is the length of the shell growth above the core, R_{Shell} is radius of the shell and $2D_{Shell}$ is the 2D growth associated with shell growth.

The main parameters that are measured and calculated for this system are now discussed. As with the growth of the core, there is a 2D associated with the growth of shell ($2D_{Shell}$). This 2D layer may or may not bury the core entirely. The $2D_{Shell}$ can be calculated as:

$$2D_{Shell} = 2D_{Total(NW+Shell)} - 2D_{Total} \tag{3.5}$$

where, $2D_{Total(NW+Shell)}$ is the 2D measured from SEM, which comprises 2D from buffer, core and shell growth. The axial growth of the shell is identified with the increase in length of the NW above the core and can be calculated as:

$$L_{Shell} = l_{Shell} + 2D_{Total(NW+Shell)} - L_{NW} \tag{3.6}$$

where l_{Shell} is the visible length of the core+shell NW measured with SEM from the 2D surface. Similarly, the radial growth of the shell is given as:

$$r_{Shell} = R_{Shell} - r_{Au} \tag{3.7}$$

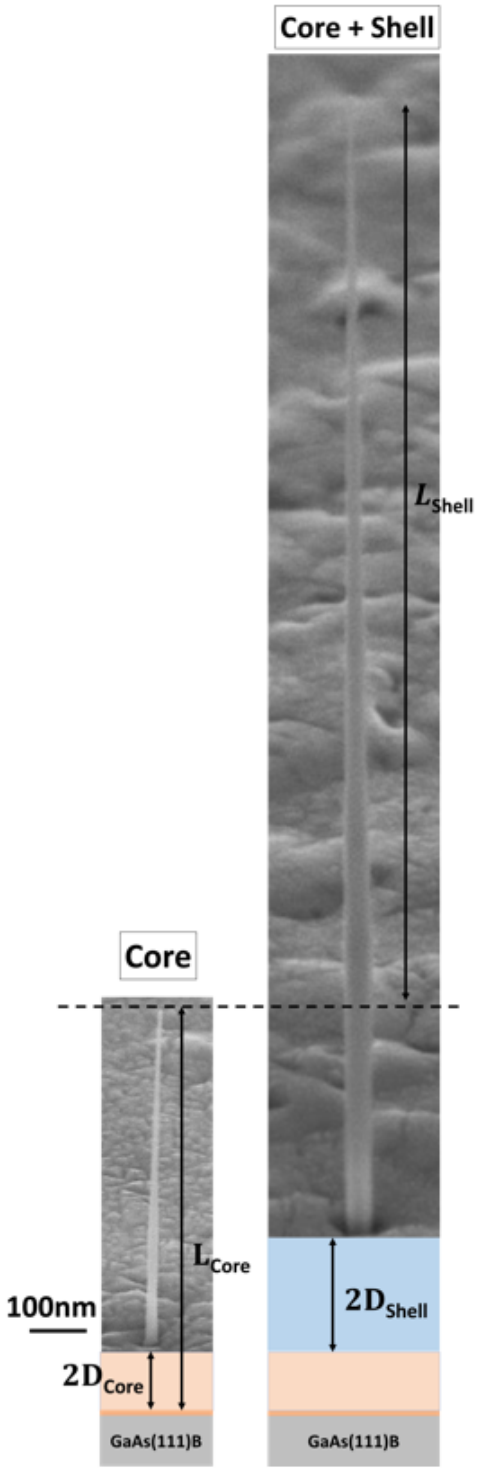

Figure 3.28: Side view SEM image (angle of 65°) of two NWs (a) without shell (just core, M3607) and another (b) with a shell (core+shell, M3609). The core for both NWs is grown at 350° C for 51 mins. The shell for the NW on the right is grown at 320° C - OFF AXIS (sample tilted by 10°) for 180 min. Zn and Se fluxes throughout the growth process were 0.4 and 1 ML/s for both NWs. In light orange and blue is the 2D layer associated with core and shell growth respectively. The L_{Core} is the total length of the core from the tip of the NW to the base buried in $2D_{NW}$. The L_{Shell} is the length of the NW from the tip of the core to the tip of the shell. The tip of the core in the core+shell NW (right) is estimated from the core sample (left).

where r_{Shell} is the radius of the NW measured with SEM and r_{Au} is the Au-NP radius.

In Fig 3.28, is shown an example of core+shell growth. SEM images of two NWs are shown: one with just core growth (M3607) and other with core+shell growth (M3609). For the both NWs, the core was grown for 51 min at 350 °C. And the shell was grown for 120 min at 320 °C in a tilted position (10° OFF AXIS). The Zn and Se fluxes for both NWs throughout the growth process were 0.4 and 1 ML/s.

The r_{NW}, L_{NW} and $2D_{Total}$ for core+shell sample M3609 are known from just core sample M3607 (table 3.2). The r_{Shell} (105±17 nm), l_{Shell} (4584±120 nm) and $2D_{Total(NW+Shell)}$ (1140±40 nm) are measured for core+shell sample M3609 with SEM. And therefore, the calculated r_{Shell}, L_{Shell} and $2D_{Shell}$ for the core+shell sample are about 101±17, 3985±145 and 845±40 nm respectively (table 3.4). Now, the core length that is not buried in the 2D layer is given as: $l_{Shell} - L_{Shell}$. Therefore, in core+shell sample M3609, about 600 nm of the core length is above the 2D surface of the sample.

Sample number	Growth type	Growth time (min)	Growth rate (mL/s)		Zn amount sent onto the sample during shell growth (nm)	Shell length L_{Shell} (nm) (avg.±SD)	Shell radius r_{Shell} (nm) (avg.±SD)	Total 2D $2D_{Shell}$
			Zn	Se				
M3448	Core	20	0.281	1.65	120	385±65	17.5±1.8	100±15
	Shell	30	0.281	1.65				
M3463	Core	20	0.288	1.65	245	730±50	29±3.5	225
	Shell	60	0.281	1.65				
M3605	Core	20	0.4	1	289	1270±170	22.5±6.5	160±20
	Shell	51	0.4	1				
M3462	Core	20	0.288	1.65	480	1690±60	48±5	420±50
	Shell	120	0.281	1.65				
M3606	Core	20	0.4	1	680	2380±75	74±7.5	528±20
	Shell	120	0.4	1				
M3609	Core	51	0.4	1	1020	3990±120	100±17	850±50
	Shell	180	0.4	1				

Table 3.4: Growth parameters used to study of core+shell samples. For all samples, core is grown at 350 °C and shell is grown at 320 °C - OFF AXIS. All samples were grown with same flux of Zn and Se. Samples are listed with increasing Zn amount sent onto the sample during shell growth. The calculated avg. ±SD for the shell length L_{Shell}, the shell radius r_{Shell} and the shell 2D thickness $2D_{Shell}$ are indicated for each sample.

A total of six core-shell samples were prepared with different core and shell growth times, with the core growth always at 350 °C and the shell growth always at 320 °C - OFF AXIS. These samples are detailed in table 3.4.

With the above approach, we can now directly compare growth of shells from core+shell samples with growth of NWs with no shell. In Fig 3.29 is shown (a) L_{Shell} and (b) r_{Shell} *vs.* Zn amount sent onto the sample surface during the growth of the shell for six core-shell samples with shell grown at 320 °C OFF-AXIS (10° sample tilt). A linear fit for these samples is shown in solid blue line and starts from the origin as Au-NP radius is already deducted from r_{Shell}. And a blue dashed line represents the linear fit for just NW (no shell) samples grown at 320 °C OFF-AXIS. The slope of both NW (no shell) and core-shell samples coincide within the error bars + dispersion.

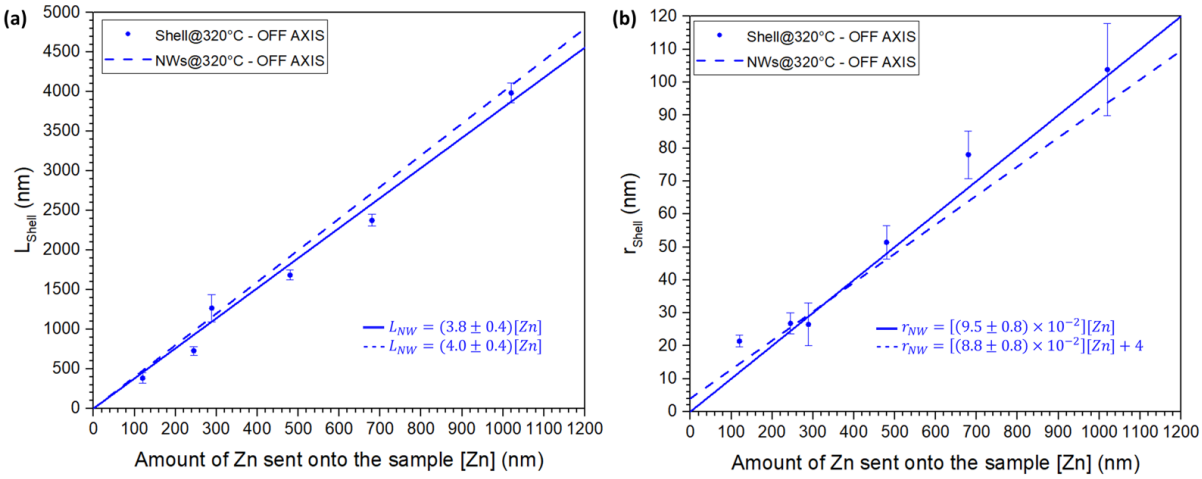

Figure 3.29: (a) Shell length L_{Shell} and (b) shell radius r_{Shell} for core-shell samples where the core is grown at 350 °C and the shell is grown at 320 °C - OFF AXIS, as a function of Zn amount sent onto the sample surface during the shell growth. In solid blue line is the linear fit of the samples core+shell samples. For comparison, linear fit of NW sample (no shell) at 320 °C - OFF AXIS is also provided in dashed blue lines.

3.8 Growth model

Previously, diffusion driven growth models have been proposed where the shape and size of the NWs is related to the diffusion lengths of the atoms on the substrate's surface and the NW's surface. Such models have been used to describe the growth of III-V and Si-NWs [87], CdTe NWs [88], and ZnTe NWs [63].

In this section, we present a purely diffusion-driven growth model to extract the physical parameters that describe our NWs and the sample (*i.e.* radius, length and 2D layer thickness), and model the effect of sample tilt during growth.

Since our samples have less than 1 NW/μm^2 density, we can consider a single NW for the growth model, with a length L and base radius R, see Fig 3.30. Along with the NW growth, there is a 2D layer growth. On top of the NW is the metal catalyst (Au-NP). The NP is assumed to be a quasi-sphere (as in the case with our NWs). The radius of this NP is R_{NP} and the radius at the NP/NW interface is R_{NW}.

Atoms impinging the NW sidewall surface are adsorbed on the surface. These adatoms can be incorporated into the NW either by adsorbing on the NW's surface with an incorporation time τ_{inc} or desorb from the NW's surface with a desorption time τ_{des}. The resident time of an adatom is then given as:

$$\frac{1}{\tau} = \frac{1}{\tau_{inc}} + \frac{1}{\tau_{des}} \tag{3.8}$$

Adatoms diffuse along the sidewall with a diffusion coefficient D. And the diffusion length associated to the resident time of the adatom is:

$$\lambda = \sqrt{D\tau} \tag{3.9}$$

The diffusion lengths associated with the incorporation or desorption of adatoms are:

$$\lambda_{inc} = \sqrt{D\tau_{inc}} \tag{3.10}$$

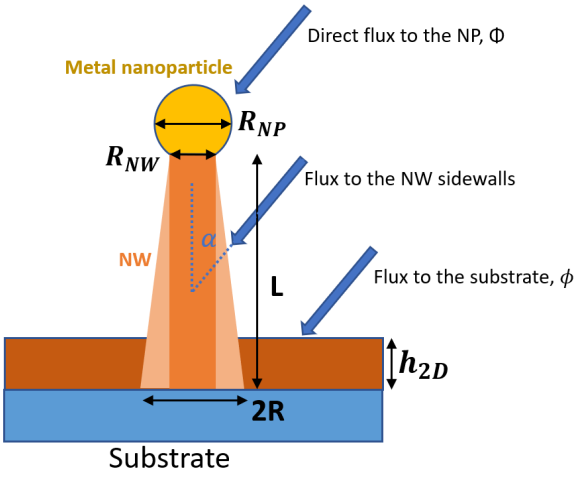

Figure 3.30: Scheme for the growth of NWs.

$$\lambda_{des} = \sqrt{D\tau_{des}} \tag{3.11}$$

In the standard position, the center of the moly-block (hence the sample) is on the cell axis. Now, flux ϕ, impinging the sample, is the flux on the axis of the cell, with an incident angle α with the normal to the substrate (NW axis).

The flux normal to the substrate is $\phi \cos\alpha$. Assuming all the adatoms impinging on the substrate incorporate in the 2D layer, then the 2D layer growth is $\frac{dh}{dt} = \phi \cos\alpha$. This holds for the initial calibration of the Zn flux, and for the "2D layer", hence the 2D thickness is:

$$h_{2D} = [Zn] = \int dt\phi \cos\alpha \tag{3.12}$$

where [Zn] is the Zn amount sent onto the sample in nm.

The axial growth of the NW is due to the completion of layers of an area πR_{NW}^2, resulting from two contributions:

- one, from the flux ϕ impinging a cross section or the quasi-spherical NP, or area πR_{NP}^2. This contributes a growth rate $\frac{dL}{dt} = \phi \frac{\pi R_{NP}^2}{\pi R_{NW}^2}$, obtained by equating the volume changes $\phi \pi R_{NP}^2$ (*i.e.* the volume impacting the NP per unit time) and $\frac{dL}{dt}\pi R_{NW}^2$ (growth rate of the NW volume).
- second, the flux impinging the NW sidewalls and diffusing to the NP. The flux normal to the sidewall is $\phi \sin\alpha$. The relevant cross section is defined by the radius of the NW and the diffusion length λ as $2R_{NW}\lambda$. Hence, the volume impinging the NW sidewall and transferred to the NP is $\phi \sin\alpha \; 2R_{NW}\lambda$. This flux also contributes to the volume growth rate of the NW as $\frac{dL}{dt}\pi R_{NW}^2$.

Adding the two contributions, the volume growth rate of the NW is given as:

$$\frac{dL}{dt}\pi R_{NW}^2 = \phi \pi R_{NP}^2 + \phi \sin\alpha \; 2R_{NW}\lambda \tag{3.13}$$

So that,

$$\frac{dL}{dt} = \phi \frac{\pi R_{NP}^2}{\pi R_{NW}^2} + \phi \sin\alpha \frac{2\lambda}{\pi R_{NW}} \tag{3.14}$$

and,

$$L = [Zn]\frac{1}{\cos\alpha}\left(\frac{R_{NP}}{R_{NW}}\right)^2 + [Zn]\frac{2}{\pi}\frac{\sin\alpha}{\cos\alpha}\frac{\lambda}{R_{NW}} \tag{3.15}$$

The radial growth of the NW starts on an initial radius R_{NW} and then increases due to the contribution of adatoms directly impinging onto the sides of NW. The radius of the NW is therefore given as:

$$\begin{aligned} R &= R_{NW} + \frac{\int dt\phi \sin\alpha}{\pi}\frac{\tau}{\tau_{inc}} \\ &= R_{NW} + [Zn]\frac{\tan\alpha}{\pi}\left(\frac{\lambda}{\lambda_{inc}}\right)^2 \end{aligned} \tag{3.16}$$

where the second term is the contribution of adatoms impinging onto the NW diameter averaged over the perimeter of the NW.

Now, if the sample is tilted by an angle of 10° towards the Zn cell, the incident angle α changes to α'. Values of incident angle of flux for normal position and for 10° tilted position are given in table 1.2. In the tilted position, the length , radius and the thickness of the 2D layer are then given as:

$$h_{2D} = \rho\left[\int dt\phi \cos\alpha'\right] = \rho\left[[Zn]\frac{\cos\alpha'}{\cos\alpha}\right] \tag{3.17}$$

$$\begin{aligned} L &= \rho\left[\int dt\phi \cos\alpha'\frac{\pi R_{NP}^2}{\pi R_{NW}^2} + \int dt\phi \sin\alpha'\frac{2\lambda}{\pi R_{NW}}\right] \\ &= \rho\left[[Zn]\left(\frac{\cos\alpha\prime}{\cos\alpha}\left(\frac{R_{NP}}{R_{NW}}\right)^2 + \frac{2}{\pi}\frac{\sin\alpha\prime}{\cos\alpha}\frac{\lambda}{R_{NW}}\right)\right] \end{aligned} \tag{3.18}$$

$$\begin{aligned} R &= \rho\left[R_{NW} + \frac{\int dt\phi \sin\alpha\prime}{\pi}\frac{\tau}{\tau_{inc}}\right] \\ &= \rho\left[R_{NW} + [Zn]\frac{1}{\pi}\frac{\sin\alpha\prime}{\cos\alpha}\left(\frac{\lambda}{\lambda_{inc}}\right)^2\right] \end{aligned} \tag{3.19}$$

where ρ is the reduction in flux on the sample when tilted by 10°. In the normal position the fluxes from all the effusion cells are centered at the center moly-block (on which the sample is glued). However, when the sample is tilted, the fluxes are now not on the axis of the effusion cell, hence the reduction factor ρ.

In Fig 3.31 is shown (a) length (L_{NW}), (b) radius (r_{NW}) and (c) 2D thickness ($2D_{Total}$) as a function of Zn amounts sent onto the sample for just core (section 3.5.1) and core+shell (section 3.7) samples grown at 320 °C in the normal position and in the tilted position (OFF AXIS). The red lines are calculated for samples grown in normal position, and he blue lines are calculated for samples grown in 10° tilted position, using the model. The agreements are reasonable, taking into account the residual dispersion of the experimental data.

The fitting parameters are R_{NP} = 4.9 nm and R_{NW} = 4.5 nm, within the range measured on TEM images. The values of the diffusion lengths λ_{inc} and λ_{des} were first determined from fit of samples in normal position and were found to be 35±5 nm and 25±5 nm respectively. Since, diffusion length is dependent mostly on the temperature, λ_{inc} and λ_{des} values were kept same for the fit of samples in tilted position. The flux reduction factor ρ was found to be 0.90±0.05. So, there is about 10 % reduction in the flux when the samples are tilted by 10 ° towards the Zn cell.

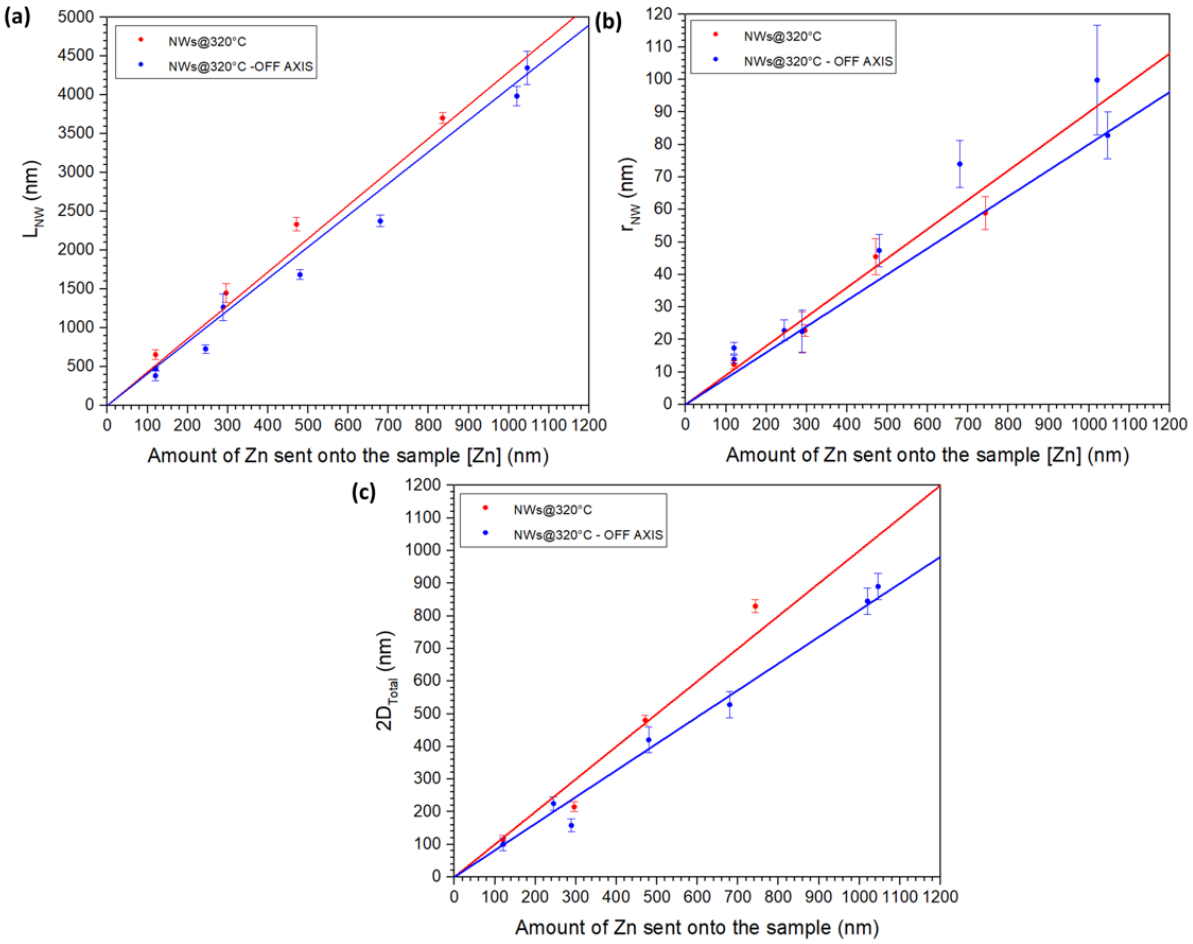

Figure 3.31: (a) Length (L_{NW}), (b) radius (r_{NW}) and (c) 2D thickness ($2D_{Total}$) as a function of Zn amounts sent onto the sample for samples in standard (red) and tilted position (blue) at 320 °C. The red lines are fit using eq. (3.12) for $2D_{Total}$, eq. (3.15) for L_{NW}, and eq. (3.16) for r_{NW}, for samples grown in normal position. The blue lines are fit using eq. (3.17) for $2D_{Total}$, eq. (3.18) for L_{NW}, and eq. (3.19) for r_{NW}, for samples grown in 10° tilted position.

With a 10° sample tilt, there is almost no change in the axial and radial growth of the samples, however the 2D growth is reduced. The diffusion lengths are slightly smaller than observed for ZnTe NWs (100 nm) [63], however, much less than observed for III-V materials, for *e.g.* for InAs it is 1 μm.

3.9 CdSe QD in ZnSe NW

The goal of this section is to describe the MBE growth process followed for the insertion of CdSe QDs in tapered ZnSe core-shell NWs (described in previous sections). In total four QD-NW samples were prepared. These samples are studied and reported for their optical properties in chapter 4.

The QD is the main component of our single-photon emitter. To control the emission from the QD, we want control over:

- A radial dipole. In previous studies on samples without shell, the CdSe QD insertion was observed in Zinc Blende phase [12]. For current samples it was not possible to confirm the QD phase due to a shell. Moreover, to have a radial dipole, the aspect ratio (length over diameter) must be small [12].
- The size of the QD. The size not only controls the emission energy but also the bi-exciton binding energy. The radius is controlled by the NP radius, and the length by the CdSe growth rate and insertion growth time. The interface between QD and NW is also a key parameter. Sharp interfaces are required.
- The radius of the shell. A thick and tapered shell is needed to ensure an efficient guiding of light. For this, a low growth temperature in the tilted sample position during shell growth is required.
- The quality of the QD and shell around the QD, and also the absence of a parasitic CdSe insertions. These two conditions are controlled with the growth temperatures of the QD and the shell.

3.9.1 General growth procedure for QD-NW sample

In Fig 3.32 is shown the scheme for the growth of a QD-NW sample. The growth procedure for a QD-NW sample is similar to just core-shell NW (in section 3.7). The difference lies in the core growth where the core growth is interrupted towards the end for the QD insertion.

After Au dewetting on ZnSe(111)B buffer, a core is first grown at 350 °C. Then towards the end of the core growth, Zn flux is interrupted for 10 s. This is done to consume all the Zn atoms in the Au-NP before the insertion of CdSe QD to have sharp NW/QD interface. After this interruption, Cd and Se fluxes are sent for 10 s for the growth of CdSe QD (also at 350 °C), followed by immediate interruption of Cd flux for 10 s. The goal of this second interruption is to consume all the Cd atoms in Au-NP for the ZnSe core regrowth for another 2 min. This is again done to have sharp QD/NW interface. The QD-core growth is followed by shell growth at lower temperatures as described in previous sections.

Sample number	Growth type	Growth Temperature (° C)	Growth time (min)	Growth rate (mL/s)		Total core length L_{NW} (nm)	Total core+shell length l_{Shell} + $2D_{Total\ (NW+Shell)}$ (nm) (avg.±SD)	Visible base radius R_{Shell} (nm) (avg.±SD)	Total 2D $2D_{Total\ (NW+Shell)}$ (nm)	QD position from 2D surface L_{NW} - $2D_{Total\ (NW+Shell)}$ (nm)
				Zn	Se					
S10a (M3532)	Core	350	30	0.4	1.65	1050±50	3740±150	140±12	810±30	240±100
	Shell	300 – OFF AXIS	120	0.27	1.65					
S10b (M3614)	Core	350	51	0.4	1	1740±150	2390±100	28±5	380±15	1350±100
	Shell	320 – OFF AXIS	30	0.4	1					
S10c (M3618)	Core	350	51	0.4	1	1740±150	5880±180	90±10	1100±50	640±150
	Shell	320 – OFF AXIS	180	0.4	1					
S7 (M3624)	Core	350	51	0.4	1	1740±150	7200±350	90±10	1120±50	620±150
	Shell	320 – OFF AXIS	180	0.4	1					

Table 3.5: Parameters used for the growth of QD-NW samples. For all samples, core is grown at 350 °C and shell is grown OFF AXIS. Sample S10a, S10b, S10c were grown with a 10 s QD insertion and sample S7 with a 7 s QD. Samples are listed in the order they were grown during this thesis work. Refer to Fig 3.27 for the calculated length, radius and 2D thickness values mentioned. The calculated QD position (close to the tip of core) from 2D surface is also mentioned.

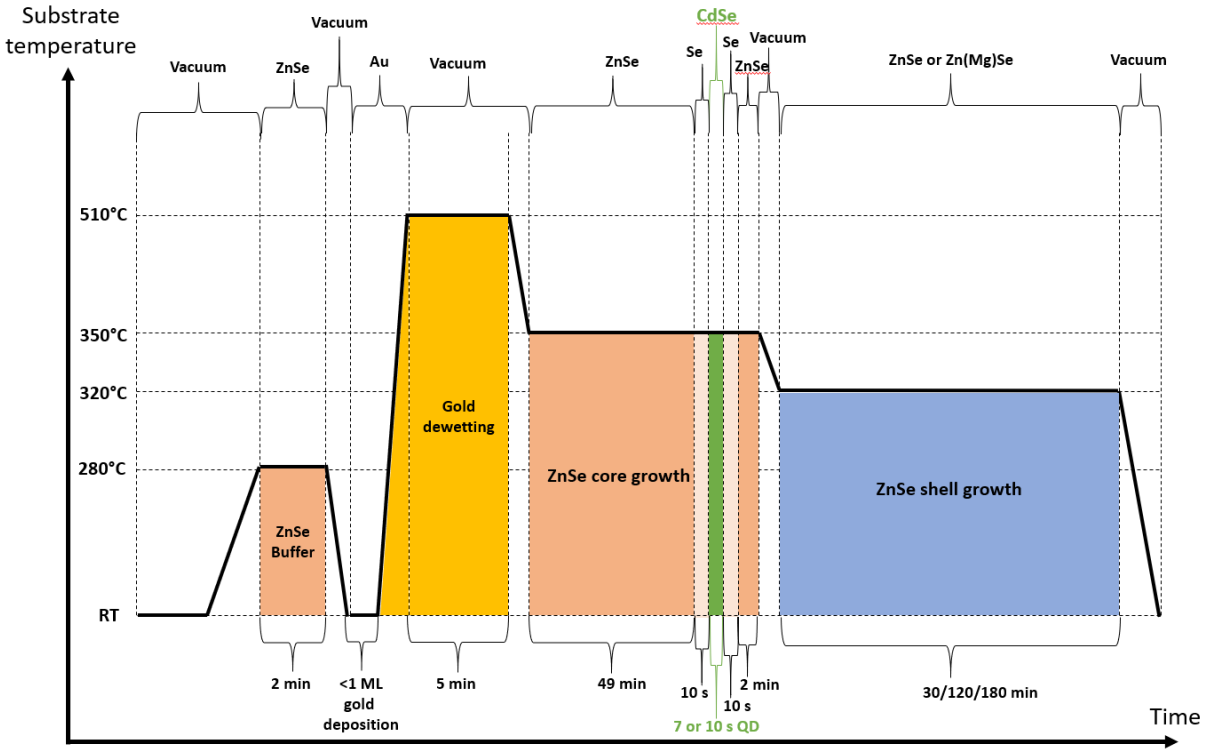

Figure 3.32: Scheme for the growth process of a CdSe-QD in a ZnSe core-shell NW sample. In green is indicated the QD growth which takes place towards the end of the core growth.

Four QD-NW samples were prepared: S10a, S10b, S10c and S7. The samples are named after the time for QD insertion, for *e.g.*, S10b has a 10 s QD insertion and S7 has a 7 s QD insertion. the samples are named in the order they were prepared during this thesis work. The growth details along with the average values of total core length (L_{NW}), total core+shell length ($l_{Shell} + 2D_{Total(NW+Shell)}$), visible base radius ($R_{Shell}$), total 2D thickness ($2D_{Total(NW+Shell)}$), and also QD position from the 2D surface ($L_{NW} - 2D_{Total(NW+Shell)}$)) for these samples are given in table 3.5. The Zn and Se fluxes for all the samples are also mentioned. The QD position is assumed to be the tip of the core.

3.9.2 10s QD

To characterize the shape and size of the CdSe QD in ZnSe NWs, sample S10b was prepared with a thin shell. The shell was grown at 320 °C - OFF AXIS for 30 min, resulting in a shell thickness of 28±5 nm.

In Fig 3.33 (a) is shown SEM images of sample S10b. The NW density is less than 1 NWμm^2. The NWs are mostly straight and the NW's surface looks smooth. However, for some (Fig 3.33 (b)), there is a bump in the NW in the middle. This bump position corresponds to the calculated QD position at about 1350±100 nm above the 2D surface. In the past we have observed a zinc blende phase of CdSe QD in ZnSe NWs [12], grown at 400 °C without an epitaxial shell. This bump at the QD position is hypothesized due to the insertion of a zinc blende CdSe QD in wurtzite ZnSe NW, but we could not confirm if it in the present sample.

To check the structural quality of these NWs, TEM studies were performed. In Fig 3.34 are shown

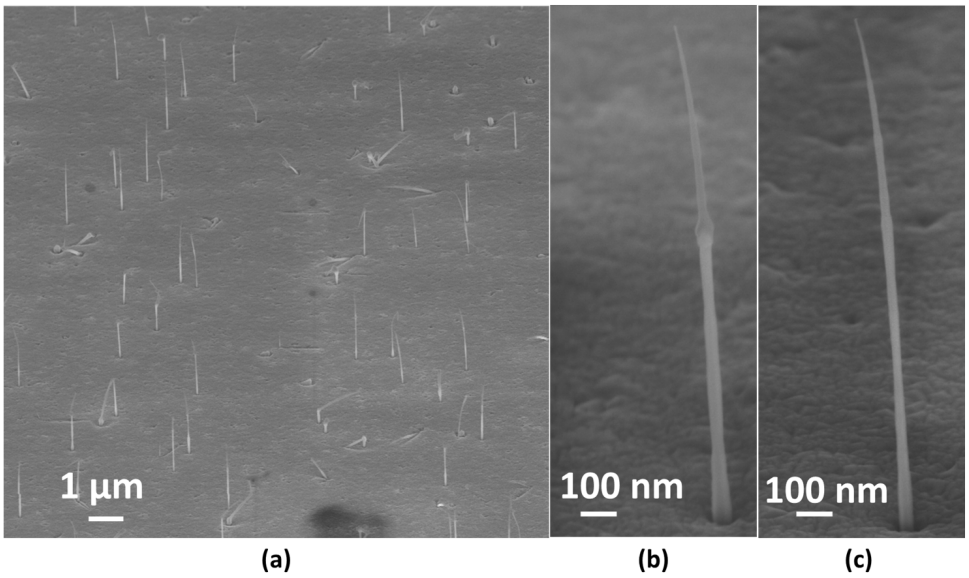

Figure 3.33: (a) Side view SEM image (angle of 65°) of (a) sample S10b (10 s QD) and of two single NWs from sample S10c in (b) and (c).

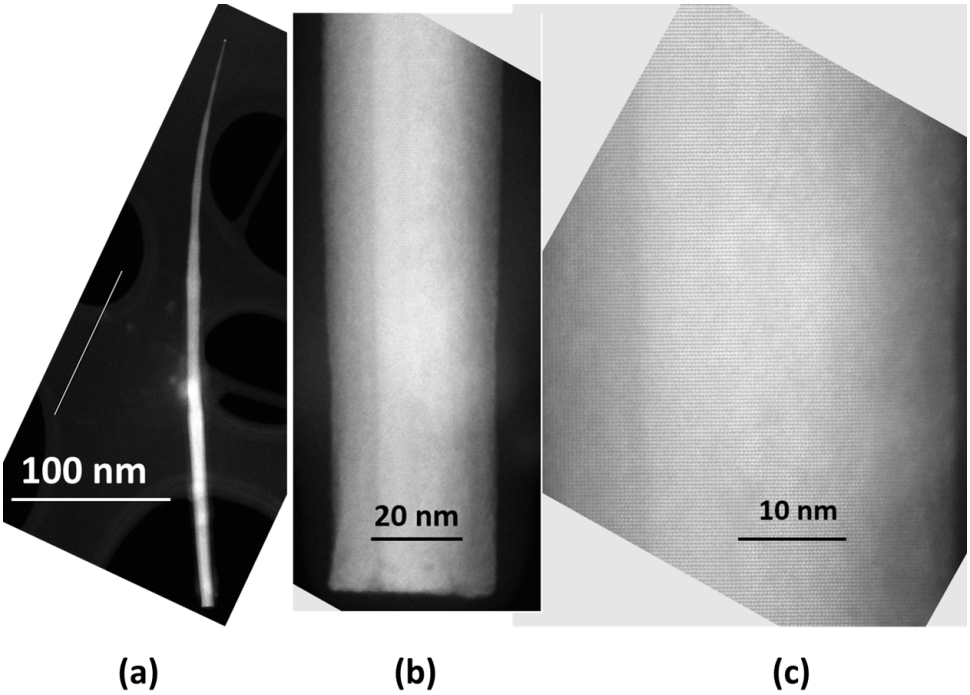

Figure 3.34: Dark field TEM images of a single NW from sample S10b (shell at 320 °C) dispersed on a copper grid. (a) Full NW. In (b) and (c) are shown magnified images of the same NW in the ZnSe region. The position of the images in (b) and (c) are along the NW in (a).

TEM images of a single NW from sample S10b dispersed on a copper grid. In (a) is shown the full NW and in (b) and (c) are shown magnified images of the NW section. The Au-NP can be seen at the top of the NW. The NW's crystal quality is very good with very few defects all along the length of the NW.

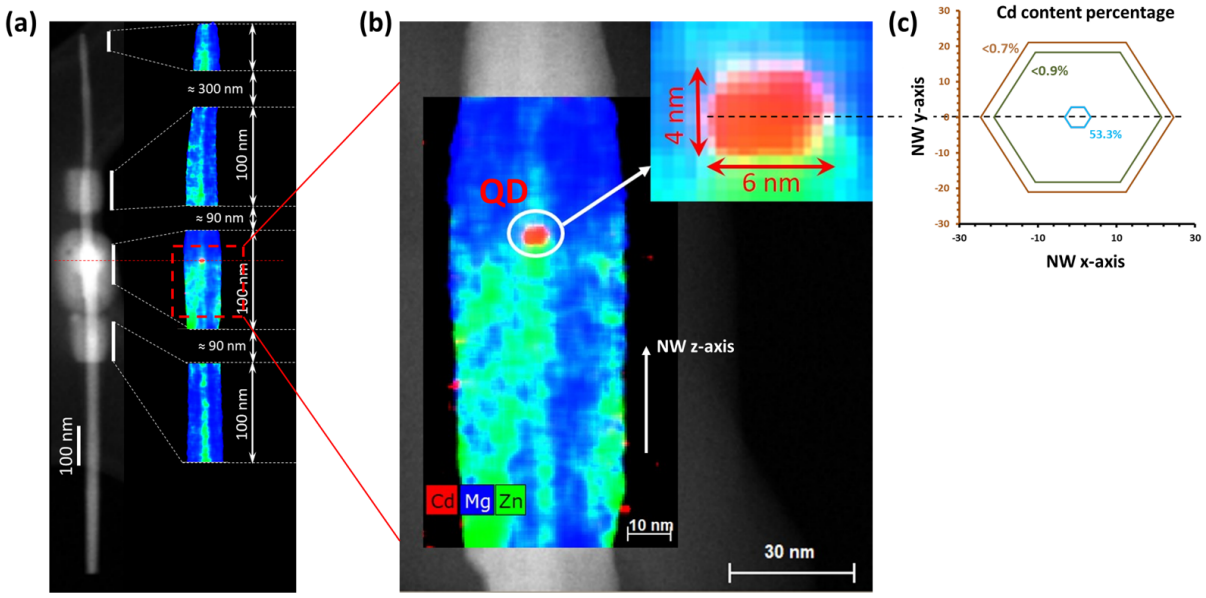

Figure 3.35: (a) EDX image of a single NW from QD-NW sample S10b (10 s QD). QD is shown in red. (b) Zoomed EDX image of the QD section position in a NW in sample S10b. Inset shows a magnified image of the QD in red. (c) Cd content in percentage at the cross-section of the QD in the same NW.

In Fig 3.35 (a) is shown an EDX image of a QD-NW from sample S10b. In green, blue and red are shown the Zn, Mg (as this sample has a ZnMgSe shell) and Cd concentrations in the NW. However, the image is not a depiction of the concentrations in the NW as a threshold for detection was set for each element, and concentrations below this threshold are not shown in this image. Still, a ZnSe core can be appreciated in the middle of the NW. At the level of the bump in the NW, a red dot can be seen. This red dot is the QD. A zoom image of this section is shown in Fig 3.35 (b). The CdSe QD (red dot) radius is about 3 nm and the height is about 4 nm. In Fig 3.35 (c) is shown the Cd content profile of the cross-section of the QD-NW at the QD position, method explained in [89]. Within the 3 nm radius area (blue hexagon), the Cd content percentage is highest at about 53 %. Outside this area, the Cd content is negligible.

Two other QD-NW samples were prepared with a 10 s QD insertion in the NW core but with a thicker shell: samples S10a and S10c. The growth parameters and average size dimensions of the two samples are given in table 3.5. Sample S10a was the first QD-NW sample prepared. And therefore also the least optimized. With respect to S10b, the core is shorter (30 min instead of 51) and the shell was grown at lower temperature (300 °C). In Fig 3.36 (a) is shown a side view SEM image of sample S10a. The NWs are tapered and thick at the bottom (about 140 nm radius). However, the surface of the NWs has sections with different orientations. In Fig 3.36 (b) is shown a TEM image of a single NW from the same sample. Unlike the NW grown at 320 °C (Fig 3.34), the NW here is full of stacking faults (visible as black regions) all along the length of the NW. Another problem with this sample is that the QD is just 240±150 nm above the 2D surface. And therefore, there is a high probability that the QD is buried in

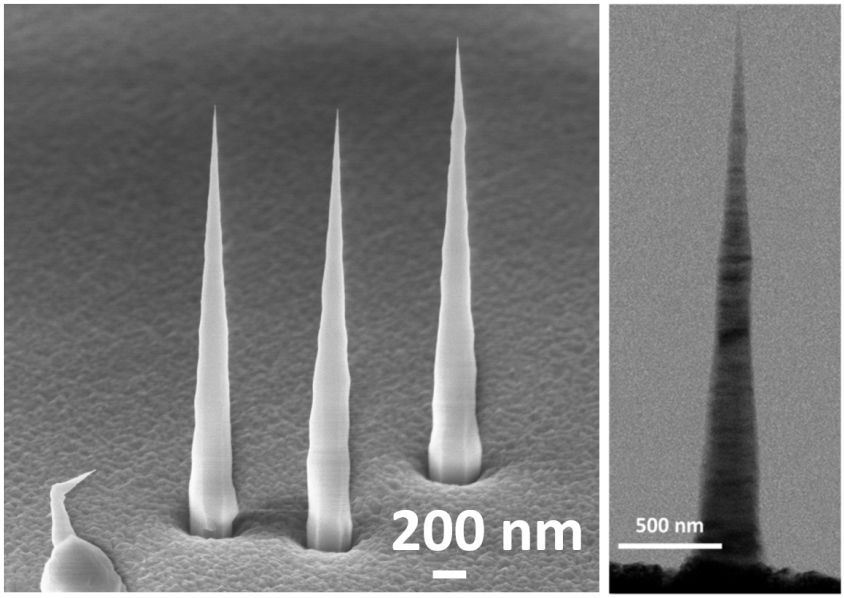

Figure 3.36: (a) Side view SEM image (angle of 65°) of sample S10a (10 s QD, shell at 300 °C). Dark-field TEM image of a NW from sample S10a. The NW is full of stacking faults (visible as black regions) all along the length of the NW.

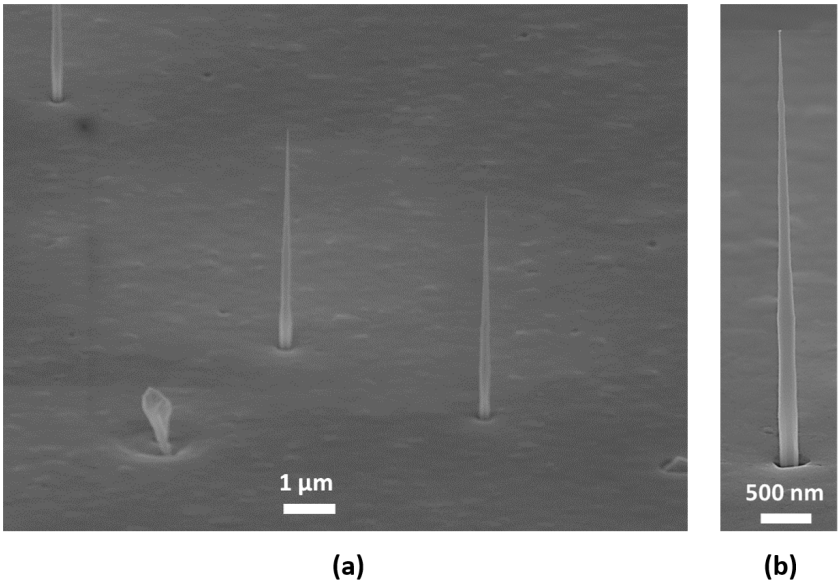

Figure 3.37: (a) Side view SEM image (angle of 65°) of (a) sample S10c (10 s QD, shell at 320 °C) and of a single NW from sample S10c in (b).

the 2D surface.

Since the shell at 300 °C is full of stacking faults, the next sample grown for single-photon emission

was sample S10c with a shell grown at 320 °C - OFF AXIS for 180 min. The growth process is similar to core-shell sample M3609 (see table 3.4), but this time a 10 s QD was inserted in the 51 min core. In Fig 3.37 are shown side view SEM images of sample S10c. The NW density is much less than 1 NWμm^2. The base radius of 90±10 nm is ideal for guiding light along the principle mode of the NW according to numerical calculations (see chapter 2). Also, the QD is more than 500 nm above the 2D surface and therefore the QDs in this sample are not buried. The NW are tapered and surface looks smooth. The size of the NWs and the 2D thickness are similar to sample M3609, which shows the good reproducibility of the growth process.

3.9.3 7s QD-NW sample

A fourth sample S7 was also prepared but with a 7 s QD insertion. This 7 s QD is important to reduce the size of the QD which directly affects its optical properties, as is seen in chapter 4. The growth process is same as sample S10c. But instead of a 10 s QD, a 7 s QD was inserted. The growth parameters and dimensions of the NW and 2D layer are given in table 3.5.

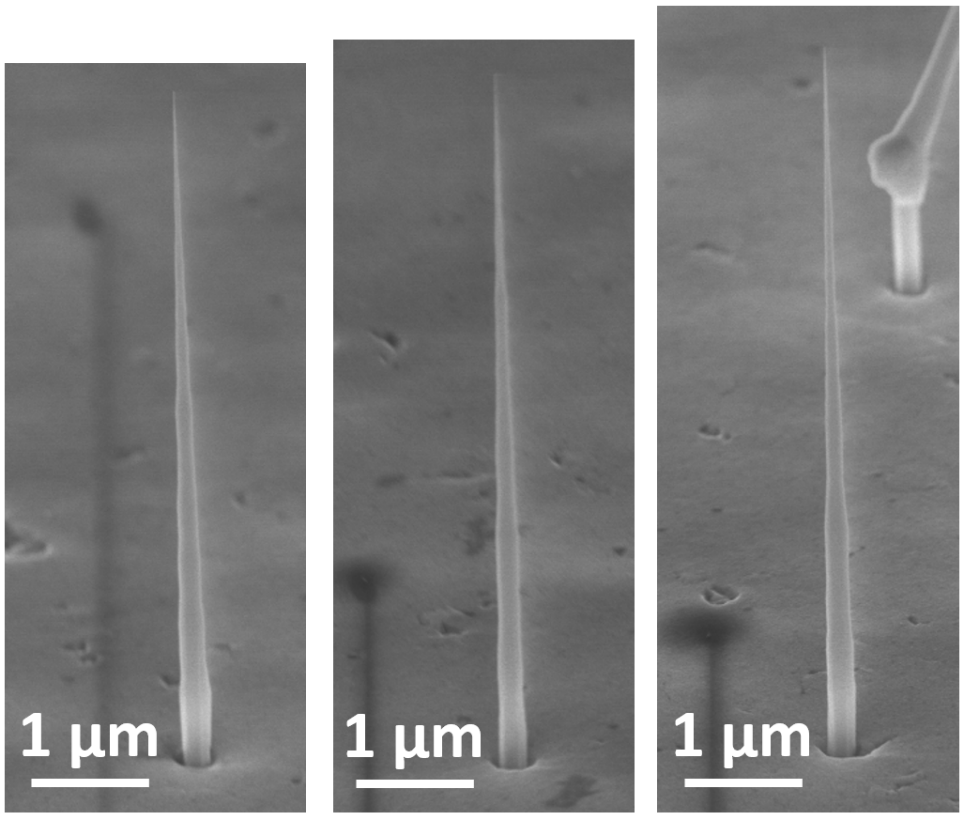

Figure 3.38: (a) Side view SEM images (angle of 65°) of three single NWs from sample S7 (7 s QD, shell at 320 °C).

In Fig 3.38 (a) are shown side view SEM images of sample S10c. The density of NWs is again less than 1 NW/μm^2. This is ideal for probing a single NW directly on grown sample for their optical studies. The NWs have a smooth surface with a tapered and thick shape. The average base radius is 90±10 nm,

same as S10c. The QD position from the 2D surface is also similar to S10c. However, the visible length is higher for sample S7.

These two QD-NWs samples (S10c and S7) are promising for our purpose of realizing a single-photon emitter with high extraction efficiency. Their optical properties is the focus of chapter 4.

3.10 Conclusion

In this chapter, the growth of CdSe QD in thick and tapered ZnSe core-shell NWs of good crystal quality is demonstrated.

Growth of vertical ZnSe NWs on ZnSe(111)B surface was achieved under Se excess, where it was observed that as long as the Se is at least twice the Zn amounts, the growth is essentially governed by the Zn flux and the temperature.

The NW shape evolved with Zn amounts and growth temperatures. With NW growth at 350 °C, three types of shapes were observed: 1. short NWs (less than 150 nm in length) which are made of thin cylinders (with or without a pedestal at the bottom). The radius of the cylinder is close to or slightly smaller than the Au-NP radius (4-5 nm). 2. Intermediate NWs (between 150 to 300 nm) which develop an open cone below the thin cylinders. 3. Long NWs (more than 300 nm), where the cone angle decreases towards a constant value, which means that the base radius increases as the length increases *i.e.* tapering of the NW. The thin cylindrical section at the top is perfect for QD insertion.

In general low radial growth of NWs was observed, with high 2D growth and not considerably enhanced axial growth. Growth temperatures were changed to observe the effect on radial growth of the NWs, to realize thin NWs for QD insertion in core and to achieve optimum NW shell radius for light guiding (80-100 nm). At 400 °C growth temperature, the radial growth and 2D growth were strongly suppressed, and the axial growth was weakly affected. As expected, lowering the growth temperatures resulted in an increased radial growth but even more enhanced 2D growth. Again, the axial growth was not affected much. At 300 °C, the radial growth rates were high enough to induce strong tapering of the NWs. However, the NWs at this temperature were full of defects. Moreover, the 2D growth rate were high enough to reach even 1 μm in thickness before optimum radius of 80-100 nm are reached. For some QD-NW samples, the core length is about 1μm. Optimum temperatures were found at 320 °C for the shell to favor radial growth and 350 °C for the core and QD to reduce formation of steps (which acts as nucleation centers for parasitic CdSe insertions) on the NW sidewalls. At both temperatures, good crystal quality of NWs was observed.

A few samples were regrown with same growth parameters and reasonable reproducibility was attained for most samples with small standard deviations in length, radius and 2D thickness. For the samples grown towards the end of the thesis, good reproducibility was seen.

Purely diffusion-driven growth model based on Zn amounts sent to sample was applied to the present results. The model takes into account the total Zn amounts directly sent to the NP, and the total Zn amount impinging the NW sidewalls and then diffusing into the NP. The intrinsic material properties identified are the diffusion length of adatoms limited by the incorporation in the NW, resulting in radial growth, and the diffusion length of adatoms limited by the desorption from the NW's surface. The effect of sample tilt is also modeled explicitly taking into account the angle between the NW and Zn cell axis. A reasonable agreement between the growth experiments and the model is achieved, within the standard deviation of experimental data. Diffusion length of the order of tens of nm is calculated which explains the rather small axial growth rates compared to III-V materials. Tilt effect was modeled successfully if

a small reduction in flux is assumed in the tilted position.
CdSe insertion in ZnSe NWs was successfully achieved. EDX imaging technique is used to observe the size of the QD. A QD of 3 nm in radius and 4 nm in height for a 10 s QD insertion was observed.

Finally, four samples were grown with a CdSe QD in the visible part of a tapered ZnSe or ZnMgSe NW, with the following optimized recipe:

- First, the growth of ZnSe core at 350 °C, very small tapering in order to avoid the formation of parasitic CdSe on the sidewalls
- then, the insertion of CdSe at 350 °C
- lastly, the growth of ZnSe or ZnMgSe shell at 320 °C, with a sample tilt towards the Zn cell, in order to favor the radial growth with respect to the 2D growth.

The first three QD-NW sample had a 10 s QD insertion and the last QD-NW had a 7 s QD insertion. These samples were characterized and their optical properties are reported in chapter 4.

Chapter 4

Emission properties of a CdSe-QD in a ZnSe/ZnMgSe-NW

Contents

In the previous chapter, we discussed the MBE process for the growth of CdSe-QD in ZnSe-NW encapsulated by a tapered and thick ZnSe (or ZnMgSe) shell required for efficient light extraction along the NW-axis. In this chapter, we discuss the optical and single-photon emission properties of these QD-NWs.

This chapter is divided into three parts. Part A discusses the emission properties of our QD-NWs when excited with a continuous wave (CW) laser. The experiments which allowed us to identify and label the emission lines to a certain excitonic transition are discussed. The single-photon capabilities of our QD-NW at cryogenic temperatures under CW excitation are also reported. Part B presents the emission properties of our QD-NWs when excited with a pulse laser. Here, we discuss what role dark-exciton (dark-X) and traps may play in the decay of the X and the XX and how it affects the measurement of the auto-correlation function $g^2(\triangle t)$ in pulsed mode excitation but rather not in CW mode. In part C, are shown characterization of our QDs for single-photon emission at room temperatures.

4.1 Quantum dot-nanowire samples studied

A total of four QD-NW samples were prepared throughout this thesis work in the order: S10a, S10b, S10c and finally S7. The complete growth process of these QD-NW samples is described in section 3.9. The samples are named after the CdSe QD insertion time in ZnSe core with a ZnSe (or ZnMgSe shell). Sample S10a, S10b, S10c have a 10 s QD insertion while sample S7 has a 7 s QD. The MBE growth optimization process improved with time. Therefore, the growth parameters were the least optimized for sample S10a, while they were the most optimized for sample S7.

In Fig 4.1 (a) is shown a general scheme of our QD-NW sample. The four important parameters to describe the shape and size of our QD-NW samples are: the NW visible length from the 2D surface (l_{NW}), the radius of the NW at the level of the QD (r_{NW-QD}), the distance between the 2D surface and the QD (l_{NW-QD}), and finally the $\theta/2$. In Fig 4.1 (b) are given the values of these parameters for the four samples. It is to note that for sample S10a, the QD is just 240±150 nm above the 2D surface. Therefore, there is high probability that for many NWs the QD is in fact buried in the 2D layers. For the other three samples the QD is at least 500 nm above the 2D surface. Also, for samples S10c and S7, the r_{NW-QD}

is within the range required for maximum light extraction along the NW axis (80-100 nm, as seen from numerical calculations in chapter 2).

To measure the size of the QD in all 10 s QD samples, sample S10b was prepared with a 10 s QD insertion in the ZnSe core with a thin shell. The energy-dispersive X-ray (EDX) analysis revealed a QD of 3 nm radius and 4 nm height (see Fig 3.35).

Probing a single NW

In this manuscript, a single NW is labeled with a reference to the sample name. For instance, NW S10a_n is the nth NW studied in sample S10a.

Although the density of NWs in all four samples was less than 1 NW/μm^2 (see section 3.9), the samples did not had any marks patterned on the substrate. Therefore, we could not go back to any random NW on the sample to perform a series of optical measurements. To identify NWs, we relied on some dust particles and defects/cracks on the sample which were easily visible. In Fig 4.2 (a) is shown an SEM image where an object (dust particle here) is used to identify location of NWs. Such objects when close to the edge of the sample can be easily located under an optical microscope. Using such objects, we were able to come back to these NWs to perform a series of experiments. One such NW is S10a_1 which is shown in Fig 4.2 (a) in orange circle. Only low magnification SEM images of the NWs (for optics) were taken since we risk destroying the NWs with high energy electron beam.

With SEM images as reference, we were able to locate the NWs in our μ-photo-luminescence (PL) setup. In Fig 4.2 (b) is shown an optical image captured in our μ-PL setup for an as-grown sample. The three short objects are NWs which are either tilted or broken and lying flat on the sample. In 4.2 (c) is shown another image captured in our setup, with a circular dark spot at the center. This is a vertical NW on an as-grown sample. All vertical NWs appeared as a circular spot on the camera. This was cross-checked using SEM images.

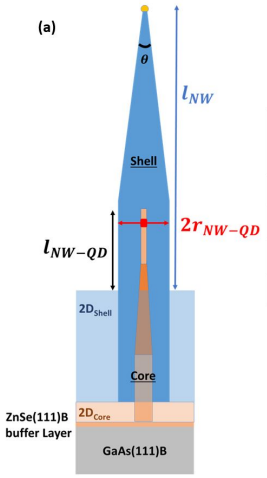

(b)

Sample name	S10a (M3532)	S10b (M3614)	S10c (M3618)	S7 (M3624)
l_{NW} (nm)	2900±100	2000±100	4900±180	6300±400
r_{NW-QD} (nm)	140±12	28±5	90±10	90±10
l_{NW-QD} (nm)	240±150	1350±100	640±100	620±100
$\theta/2$ (°)	2.7±0.2	0.8±0.2	1.1±0.2	0.8±0.2

Figure 4.1: (a) General scheme of a QD-NW sample. First a ZnSe core is grown at 350° C with a QD insertion near the tip of the core, followed by Zn(Mg)Se shell growth at a lower temperature. QD growth is indicated in red and shell growth in blue. (b) Table summarizing the values of important parameters described in scheme (a).

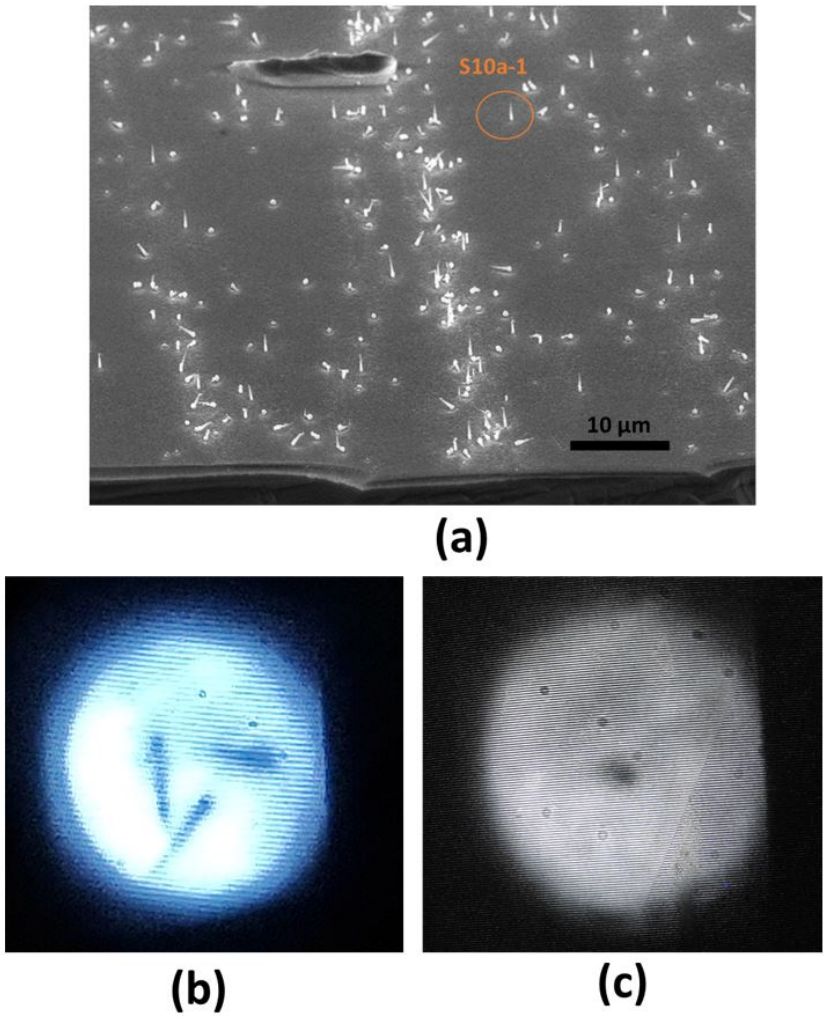

Figure 4.2: In (a) is shown NW S10a_1 whose location was marked using a big dust particle close to the surface. In (b) is shown a optical image taken in our μ-PL setup. The three objects are NWs either tilted or lying flat on the sample surface. While in (c) is an optical image of a vertical NW which is visible as a dark circular spot.

Part A: Continuous mode excitation

4.2 Typical emission at cryogenic temperatures

In this section, we describe the typical emission from a CdSe-QD in a ZnSe-NW at cryogenic temperatures (~5 K).

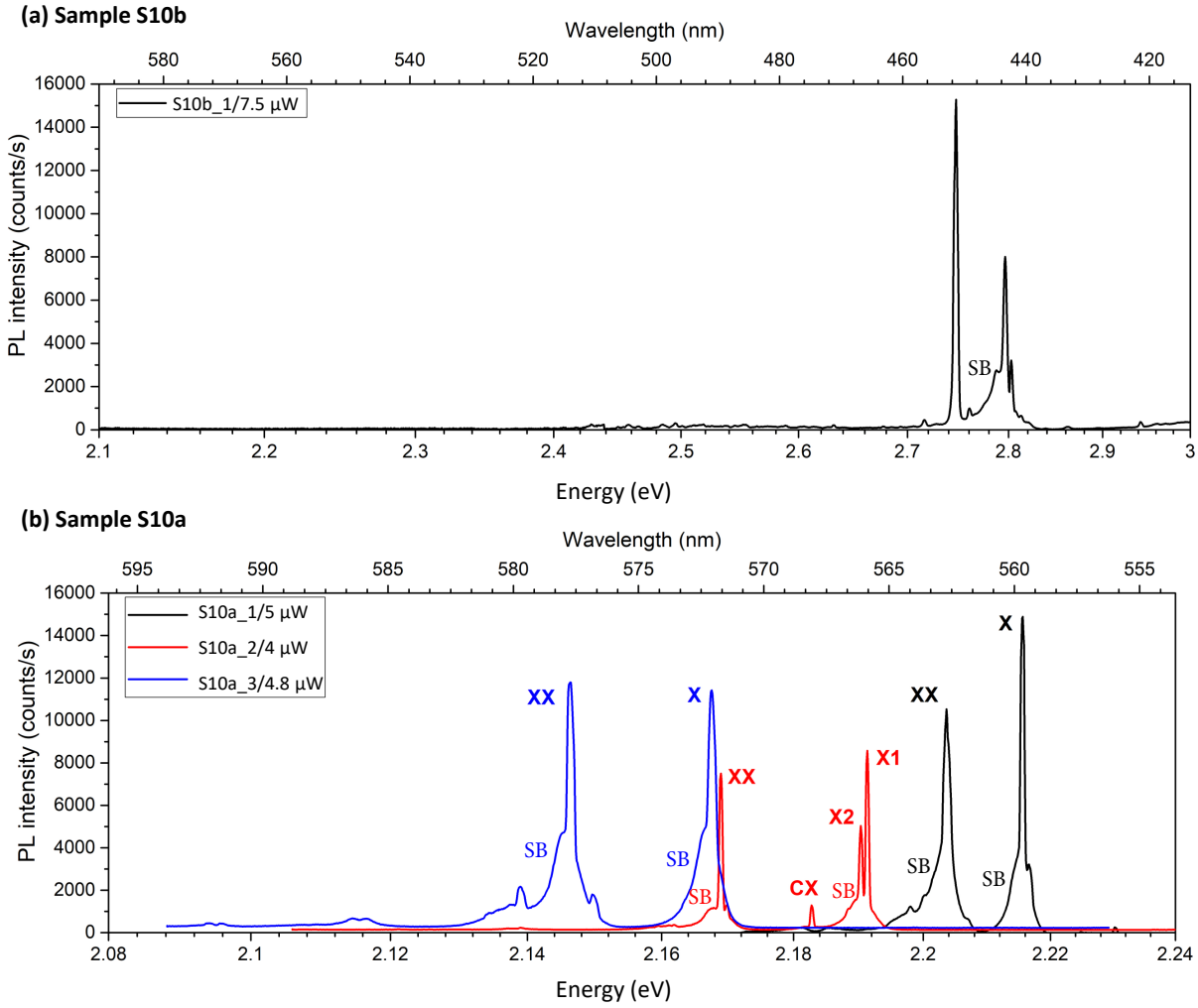

Figure 4.3: Emission spectra of selected NWs for sample (a) S10b (b) S10a under CW excitation. The peaks are labeled with X, XX, CX, MX and SB which refers to exciton, bi-exciton, charged-X (or charged-XX), multi-exciton peaks and their sidebands respectively, as identified below. Excitation power is also given for all NWs.

The μ-PL measurements were performed using the setup described in section 1.4.3.1. A 405 nm (3.06 eV) diode laser was used to excite a QD-NW in CW mode. Emission from each NW was collected from the top (as-grown).

In Fig 4.3 (a) are shown emission spectra of a NW in sample S10b. While, emission peaks around 440 nm (2.81 eV) are observed, no emission is observed in the QD emission region 550-600 nm (2.25-2.06 eV). In fact, no emission in the 500-600 nm range was seen for more than 20 NWs. The peaks around 440 nm (2.81 eV) are due to the emission from the ZnSe core. V. Zannier *et al.* [39] observed PL lines close to 2.80 eV from ZnSe NWs which they attributed to Wurtzite (WZ) and Zinc Blende (ZB) phases of ZnSe.

Notice that a small r_{NW-QD} of 20±5 nm is not enough to protect the NW from dielectric screening of the QD. Since, the NWs are excited along their axis, the incident electric field is orthogonal to the NW axis and therefore the QD is very weakly excited. Dielectric screening is explained in section 2.2.2 in detail. Emission from QD-NW with no or very thin shell was previously reported from our group [11], [12]. But these QD-NWs were always excited orthogonal to the NW axis (lying flat on a substrate) which means that the incident electric field is along the NW-axis. And in such a case the dielectric screening is minimized.

For sample S10a, emission in the QD region was observed for most NWs. Criteria we used to identify potential NWs with an exciton and bi-exciton was: few emission lines separated by more than 2-3 nm (about 10 meV) and a crossing of intensity between any two emission lines with increase in laser power (which could correspond to exciton and bi-exciton transitions as is seen in section 4.4). Most NWs in this sample showed a broad peak or several emission lines very close to each other (few meV line separation) in the 550-600 nm (2.25-2.06 eV) region. Therefore, most NWs in this sample were discarded for a detailed study. Selected three NWs (S10a_1, S10a_2, S10a_3) spectra are shown in Fig 4.3 (b). Low magnification SEM image of NW S10a_1 from this sample is shown in Fig 4.2 (a). All three NWs emit within the 550-600 nm range and emit with similar intensity for similar powers. Also, along with the emission lines, a sideband which extends for several meV can be identified as "SB" in Fig 4.3.

Before identifying the emission lines in Fig 4.3 (b) to a certain excitonic transition (section 4.4), their linewidth is reported in the following section.

4.3 Linewidth at cryogenic temperatures

In this section we discuss the linewidth of emission lines for our QD-NWs.

Linewidth was measured using the high energy line (559.45 nm/2.216 eV) from μ-PL spectrum of NW S10a_1 measured at 5K (see Fig 4.3 (a)) with 5 μW CW-excitation. This power gives maximum intensity for the high energy line and since linewidth has shown to increase with increasing power [90], [91], 5 μW probably provides an upper bound to the linewidth for this emission line. The linewidth obtained from a Lorentzian fit is 0.26 meV. This linewidth is slightly affected by our spectrometer which uses a grating of 1800 lines/mm and provides an optical resolution at best of 0.08 meV (0.02 nm). Other NWs studied in this work also have similar linewidths (0.21 meV for the X of NW S7_3, section 4.6.1) .

Fig 4.4 (a) provides a comparison of spectrum for CdSe-QDs in two different ZnSe NWs (with and without a shell) at 5 K. One was grown in our group in 2012 (black), named NW-2012 [19], [11] and the other (S10a_1) is from this work. For NW-2012, no shell was grown on purpose, however, a very thin layer of thickness less than 1 nm covered the sides of the QD. Since this layer is negligible, we approximate for NW-2012 to have "No-shell". Clearly, the linewidth of NW S10a_1 (of X line) is smaller than that of NW-2012 (of XX line).

Fig 4.4 shows a comparison of (b) linewidths and (c) linewidths normalized to QD's emission en-

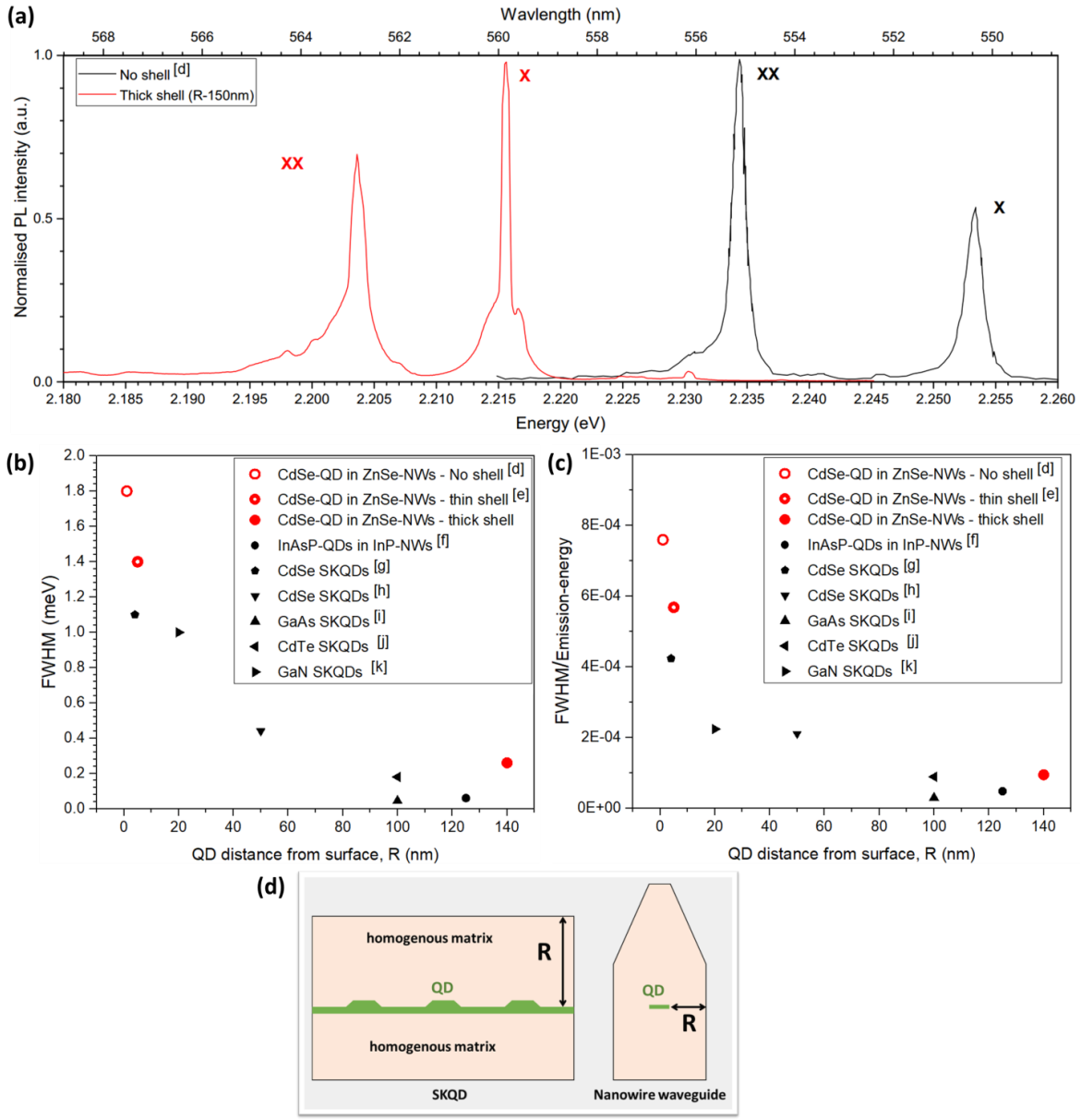

Figure 4.4: (a) μ-PL measurement of 2 ZnSe-CdSe NW-QD: one with no-shell in black and one with thick shell in red (S10a_1). (b) Comparison of linewidths of different QD systems (NW-QDs and SKQDs). (c) Linewidth normalized to QD emission energy for different QD systems. CdSe-ZnSe QD-NW are in red and all other systems are in black. (c) Definition of R-distance for a SKQD and for a QD-NW. For the SKQD, we take the distance from the QD to the first non-epitaxial layer at the top, and for the QD-NW the radius of the NW at the QD level. The references are taken from: d [11], e [12], f [10], g [33], h [31], i [92], j [93] and k [94].

ergy, recorded at cryogenic temperatures for different epitaxially grown QDs systems with different QD-surface distance (R): the three CdSe-ZnSe NW-QDs (in red), different material SKQDs, and InAsP-InP QD-NW (in black). The linewidth for all is calculated from a Lorentzian fit. For QD-NWs, the R distance is the thickness of the shell at the QD level. And for SKQDs it is the distance from QD to the nearest (top) surface (Fig 4.4 (d)).

For the comparison of FWHM of CdSe-QD in ZnSe-NWs, we have NW-2012 (no shell), NW-2016 (thin shell, also from our group) [12], and S10a_1 (thick shell). There is a systematic decrease in linewidth for CdSe QD from NW-2012 (R~1 nm, 1.8 meV) to NW-2016 (R~5 nm, 1.4 meV) to S10a_1 (R~140 nm, 0.26 meV). The FWHM of S10a_1 is also similar to FWHM of InAs-QD in InP NWs (0.18 meV) with similar R of 130 nm.

When compared to SKQDs, CdSe-SKQDs with R distances of 2 [33] and 50 nm [31] have larger linewidths of 1 meV and 0.4 meV respectively. The linewidths of GaAs-SKQD (R>100 nm, 0.04 meV) [92] and CdTe SKQDs (R>100 nm, 0.18 meV) [93] are narrower compared to GaN-SKQD (R=20 nm, 1 meV) [94].

The general trend is that the QD-systems with small R distances have large linewidths compared to those with large distances which have considerably smaller linewidths.

In the zero-temperature limit, an optimal linewidth corresponds to the lifetime of the excited state. This natural broadening of the spectral line is a result of the Heisenberg uncertainty principle *i.e* $\triangle E \triangle \tau \geqslant h/4\pi$, where $\triangle E$ is the uncertainty in the change of emission energy and $\triangle \tau$ the lifetime of the excited state. A very short lifetime, therefore, results in a broad optical line. For example, the lifetime measured for high and low energy lines of NW S10a_1 are 0.65 and 0.3 ns respectively (section 4.11), which gives a natural broadening of the X and XX peaks as 1 μeV and 2.2 μeV, negligible compared to the observed linewidth of 0.26 meV.

When the QD is excited resonantly, linewidth as low as 1.27μeV has been observed [95]. However, when the QD is not excited resonantly (as is the case with all the QD systems mentioned above), defects, localized charges, and impurities in the vicinity of QD can induce fluctuating electric fields that can shift the QD´s emission line through the quantum-confined Stark effect. This spectral diffusion due to random changes in the QD optical emission frequencies becomes a big issue whenever a QD sits close to the 2D surface ($\leqslant$ 100 nm for GaAs SKQDs) or NW surface [96], [97]. This is due to the presence of a large density of surface states (*e.g.* $12.5 \pm 10.0 \times 10^{13}$ eV/cm^2 at 300 K for GaAs [98]) around the QD. In general, SKQDs have lower FWHM values compared to QD inserted in NWs. This is indeed because SKQDs usually have a thick epitaxial layer on top of the QD which can keep these surface states far away from the QD. Whereas a QD-NW geometry provides this protection only in 1D along the NW-axis (top and bottom). With a thick shell, the QD can be protected from all three directions. Several groups have consistently observed a systematic decrease in the emission linewidth of QD when the QD to surface distance is increased [99], [100]. Therefore, an increase in the distance is important to reduce charge fluctuations and hence spectral diffusion due to defects, impurities, dangling bonds, *etc.* at the surface which acts as trap states for charge carriers.

Since the environment of the QD decides the linewidth of the emission lines, we could expect that all emission lines coming from the same QD have the same linewidth. This is because the spectral diffusion linewidth is much larger than the lifetime-limited linewidth. And therefore, the linewidth of the X and XX peaks should be nearly the same for the same QD. A larger linewidth for XX (~0.86 meV) compared to X (0.26 meV)) in this NW (S10a_1) may suggest contribution from other peaks in the vicinity of the XX line which could not be resolved completely with our spectrometer. However, a narrow and similar linewidth for XX and X were observed for other NWs (see Fig 4.13 and Fig 4.15 (a)).

To the best of our knowledge, the linewidth of 0.26 meV for NW S10a_1 and 0.21 meV for NW S7_3 are the smallest ever reported for CdSe-QDs (both CdSe SKQDs and QD-NW systems) and is of the order of those for other SKQD (GaAs and CdTe) systems with high R distances mentioned above.

4.4 How to identify exciton and multi-exciton states?

In this section, the origins of the emission lines observed for NW S10a_1 in Fig 4.3 (b) are identified to the exciton (X) (one electron and one hole in the QD) for the high energy line and the bi-exciton (XX) (two electrons and two holes in the QD) for the low energy line.

4.4.1 Power dependence measurements

The X and XX transitions in a QD can be identified by observing the power-dependence of the emission lines. At low excitation power, a linear dependence of the intensity of the exciton and a quadratic dependence of the bi-exciton intensity on excitation power was first reported by Santori *et al.* [17].

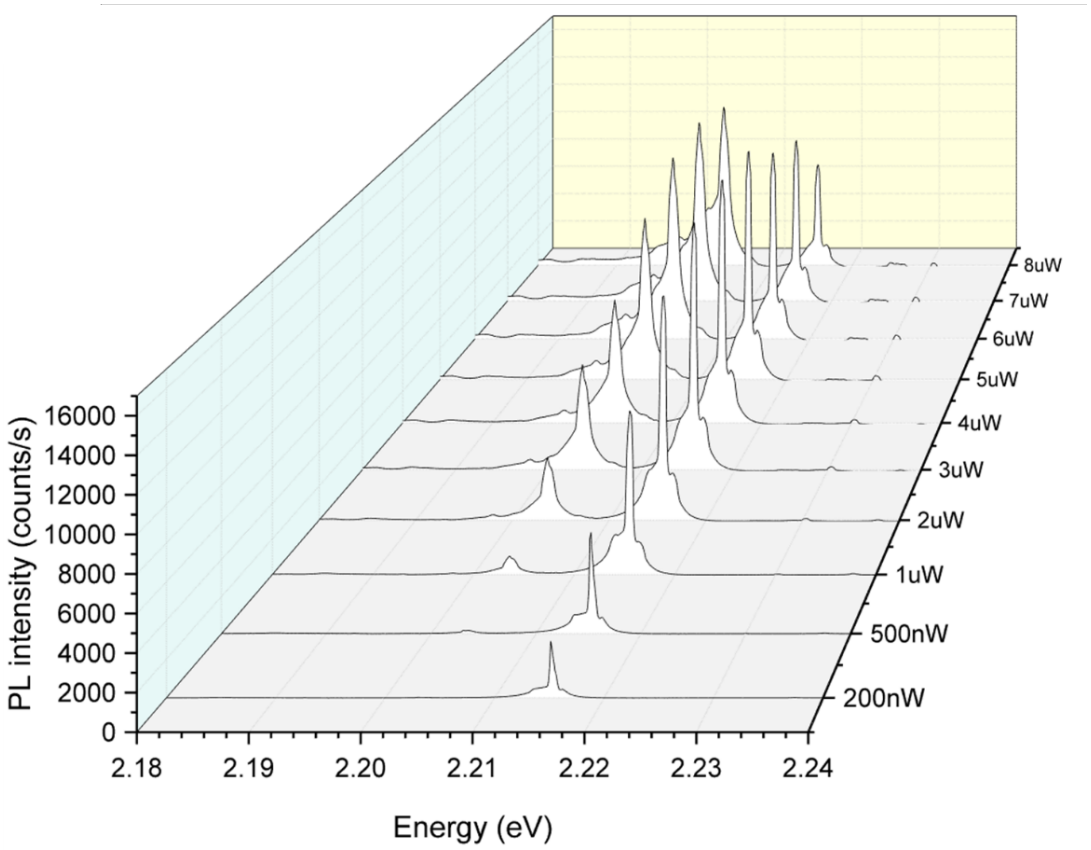

Figure 4.5: Power-dependent μ-PL measurements on NW S10a_1 at 5 K using a 405 nm CW laser and a spectrometer grating of 600 lines/nm (optical resolution of 0.04 meV (0.09 nm)).

We will use NW S10a_1 to observe this behavior. Fig 4.5 shows the spectra recorded at 5 K for a CW excitation power varying between 0.2 μW and 8 μW. The excitation is above the ZnSe barrier, using

the 405 nm CW laser. And a low spectrometer grating of 600 lines/mm was used, which provides an optical resolution of 0.04 meV (0.09 nm).

At low powers (0.2 and 0.5 μW), the spectrum is dominated by the presence of an emission line at 559.45 nm (2.216 eV). As the power increases, around 1 μW, a second line at lower energies (562.56 nm/2.204 eV) emerges and quickly becomes the dominant one at very high powers (above 4 μW).

Fig 4.5 shows the dependence of the integrated PL intensity for the two emission lines on the excitation power. The intensity is integrated within a fixed energy window of 5 meV for all powers. At weak excitation, while the integrated intensity of the high energy line has a linear dependence on power, the dependence of the low energy line is quadratic. The intensities of two emission lines cross around 4 μW. At strong excitement, we observe that both emission lines reach a maximum and then decrease.

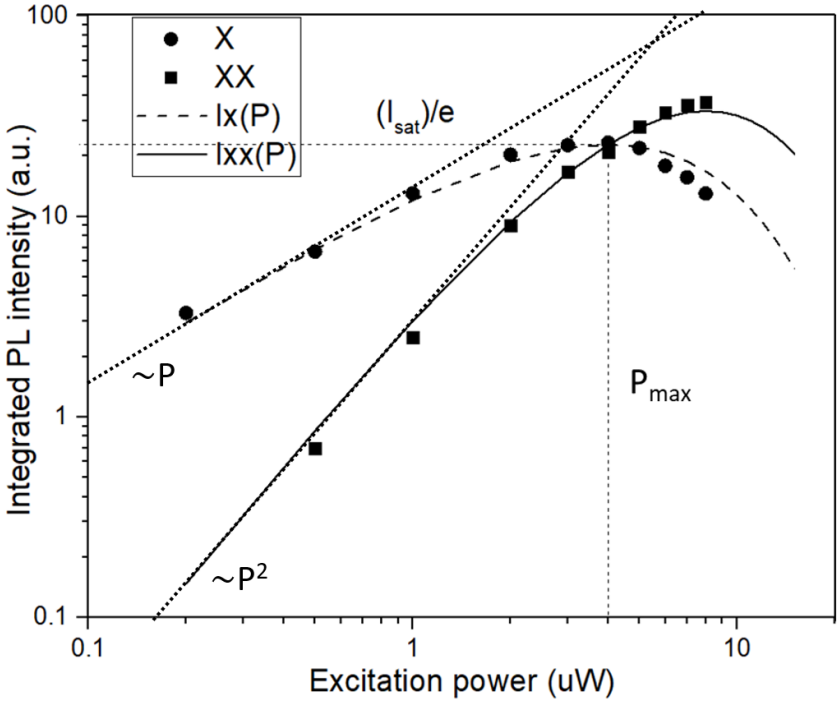

Figure 4.6: Integrated intensity plot as a function of excitation power for NW S10a_1 at 5 K. Circles and squares represent integrated intensity for the high energy (assigned to exciton) and the low energy (assigned to bi-exciton) peaks respectively, calculated in a 5 meV energy window. Dashed lines and solid lines represent fit using eq. (4.7) and eq. (4.8) respectively. At power P_{max}, the X intensity reaches a maximum. Dotted lines show the P and P^2 dependencies.

4.4.2 Model to fit exciton and bi-exciton states

To confirm the nature of the two emission lines, we will now use a simple rate equation model, developed by Emmanuel Moreau during his Ph.D. thesis [101], to fit the integrated PL plot in Fig 4.5. To keep the model simple, he made two assumptions: first, the QD captures only pairs of carriers *i.e.* one electron and one hole, and no other electron-hole arrangements such as CX or CXX. Second, the capture process is random and independent of charge pairs already present in the QD. By introducing the recombination

times at the different charge states of the QD, the probability $P(n)$ of having n pairs of carriers inside the QD can be found by solving the rate equation of the excitation-emission process. It should be noted that here the dark-X state (see Fig 1.2) is not taken into consideration.

Let $1/\tau_a$ be the injection rate and $1/\tau_n$ be the recombination rate of the electron-hole pairs. $1/\tau_a$ is related to the incident power P by the relation $P = B/\tau_a$ where B is a simple coefficient. The probability $P(n)$ of having n pairs present in the QD for $n \geq 1$ is then given by the following differential equation:

$$\frac{dP(n)}{dt} = \frac{P(n+1)}{\tau_{n+1}} + \frac{P(n-1)}{\tau_a} - P(n)\left(\frac{1}{\tau_a} + \frac{1}{\tau_n}\right) \tag{4.1}$$

$P(n)$ can increase either due to recombination of an exciton in the $(n+1)$ state (first term of the equation) or through injection (or trapping) of an exciton in the QD in the $(n-1)$ state (second term). Similarly, $P(n)$ can decrease due to the injection of an exciton ($\frac{1}{\tau_a}$ term) or recombination of an exciton ($\frac{1}{\tau_n}$ term) in the QD in the n state. Now, if we assume that the recombination rate associated with n electron-hole pairs is equal to n times the recombination rate of each electron-hole pair, $\frac{1}{\tau_r}$, then:

$$\frac{1}{\tau_n} = \frac{n}{\tau_r} \tag{4.2}$$

This would mean for example that the lifetime of the exciton is twice as long as that of the bi-exciton. This is the case when spin-flip from the dark to the bright state is not considered (which is the case in this model), as the dark-exciton is long-lived and a spin-flip from the dark-exciton to bright-exciton can increase the lifetime of the exciton [102], [103]. We also assume that τ_a is same for all. Under this assumption, the above rate equation can be written as:

$$\frac{dP(n)}{dt} = \frac{(n+1)P(n+1)}{\tau_r} + \frac{P(n-1)}{\tau_a} - P(n)\left(\frac{1}{\tau_a} + \frac{n}{\tau_r}\right) \tag{4.3}$$

The steady-state solution ($\frac{dP(n)}{dt} = 0$) to the above equation then follows Poisson statistics, and is given as:

$$P(n) = \frac{e^{\frac{-\tau_r}{\tau_a}}}{n!}\left(\frac{\tau_r}{\tau_a}\right)^n \tag{4.4}$$

The intensity of an exciton in the n state is proportional to the probability of the presence of an electron-hole pair $P(n)$ multiplied by the probability that this pair recombine $\frac{1}{\tau_n}$. Thus, the intensities of the lines associated with the exciton state ($(I_X(P))$) and the bi-exciton state ($I_{XX}(P)$) are expressed as a function of the incident power P $\left(= \frac{B}{\tau_a}\right)$ in the following way:

$$I_X(P) = A\frac{P(1)}{\tau_1} = Ae^{-\frac{\tau_r}{\tau_a}}\left(\frac{\tau_r}{\tau_a}\right)\left(\frac{1}{\tau_r}\right) = \frac{A}{B}Pe^{-\frac{P\tau_r}{B}} \tag{4.5}$$

$$I_{XX}(P) = A\frac{P(2)}{\tau_2} = \frac{A\tau_r}{B^2}P^2e^{-\frac{P\tau_r}{B}} \tag{4.6}$$

where A is another coefficient. $I_X(P)$ is maximum at $\frac{P\tau_r}{B} = 1$. By defining $I_a = \frac{A}{\tau_r}$ and $P_{max} = \frac{B}{\tau_r}$, we can rewrite the above equations as:

$$I_X(P) = I_a\frac{P}{P_{max}}e^{-\frac{P}{P_{max}}} \tag{4.7}$$

$$I_{XX}(P) = I_a \frac{P^2}{P_{max}^2} e^{-\frac{P}{P_{max}}} \tag{4.8}$$

It can be deduced that at power which gives maximum intensity for X *i.e.* for $P = P_{max}$, $I_X(P) = I_{XX}(P) = I_a$. The above two equations were used to fit the power dependence measurement data in Fig 4.5. The solid lines are the fit obtained using the above 2 equations, where $\frac{I_a}{e} = 62$ and $P_{max} = 4\,\mu W$.

The power dependence is well fitted by the model for an exciton and a bi-exciton. Thus, we conclude that the 2 peaks in S10a_1 indeed correspond to the exciton (2.216 eV) and the bi-exciton (2.204 eV) recombination.

The energy separation between the X and XX lines in NW S10a_1 is 12 meV, which is lower than previously observed (about 20 meV) for CdSe-SKQDs in [001] direction [32], [33]. This energy separation between the X and XX lines is also called the bi-exciton binding energy (B_{XX}). We will talk about B_{XX} in detail in section 4.6.3.

4.5 Effect of temperature on emission characteristics

The ultimate goal of this thesis is to realize a single-photon emitter that is operable up to room temperature. High temperatures activate non-radiative recombinations of electron-hole pairs which directly influence the emission properties of a QD. And therefore, it is important to study the luminescence as a function of temperature to test the robustness of our QD. In this section, the emission properties of CdSe QD in ZnSe NW are investigated using NW S10a_1 by following the evolution of its emission peaks and their sidebands as temperature is increased. A fitting procedure for the emission lines is also discussed.

Fig 4.7 represents a set of μ-PL spectra recorded at different temperatures for the NW S10a_1 at 5 μW CW laser excitation (which provides maximum intensity for the X state at 5 K) and with a spectral resolution of 0.02 nm (0.08 meV). At low temperatures (5 K), the spectrum consist of two well-separated X and XX emission lines accompanied by sidebands extending up to several meV. The X peak is accompanied by an extra peak, X_a. We suspect that the XX peak has contributions from additional peaks which could not be resolved. As temperature increases, three characteristic changes in the emission spectra can be observed: 1. emission energy red-shifts, 2. emission lines broaden and 3. above 175 K, exciton intensity decreases and bi-exciton becomes the dominant emitter. In the following section, these three characteristic changes are discussed.

4.5.1 Red-shift in emission energy

Emission energies, as a function of temperature, for exciton and bi-exciton of NW S10a_1 is plotted in Fig 4.8. All emission lines shift to low energies with increasing temperature. A total red-shift in emission energy of about 55 meV is observed as temperature increases from 5 to 300 K. This red-shift is due to the narrowing of the band-gap with increasing temperature and the temperature dependence of semiconductor band-gaps can be well traced. The Varshni semi-empirical formula [104]:

$$E_g(T) = E_g(0) - \frac{\alpha T^2}{(T + \beta)} \tag{4.9}$$

where $E_g(0)$ is the gap energy at 0 K and, α and β are fitting parameters characteristic of a given material. β is close to the Debye temperature of the material. Varshni formula is widely used to fit the temperature dependence of band-gap for bulk semiconductor materials. Solid lines in Fig 4.8 are fitted

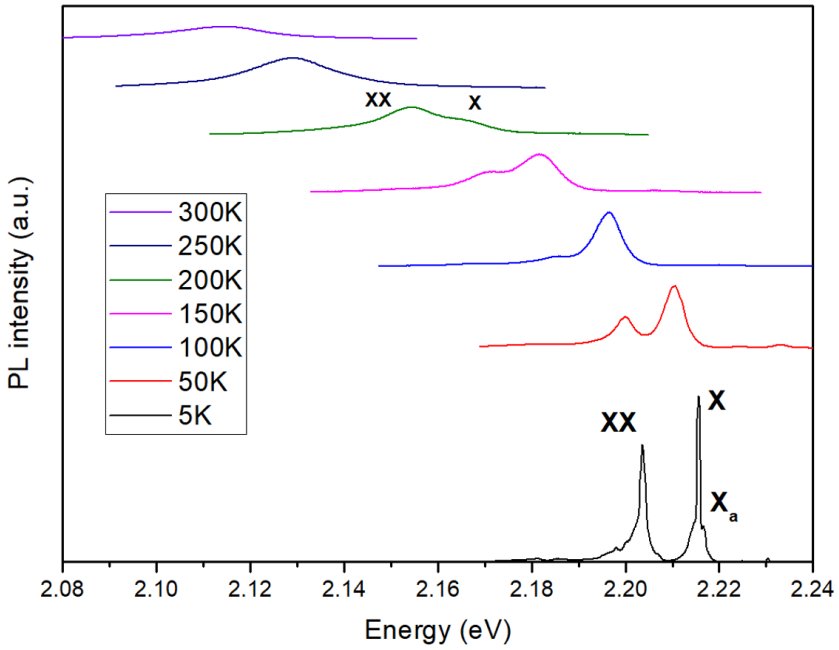

Figure 4.7: Temperature dependence μ-PL measurements on NW S10a_1 at 5 μW CW excitation.

using eq. (4.9). With $E_g(0) = 2.211$ eV, $\alpha = 0.63\ \frac{meV}{K}$ and $\beta = 290\ K$, which are in reasonable agreement with those reported for bulk zinc-blende CdSe ($\alpha = 0.69\ \frac{meV}{K}$ and $\beta = 281\ K$) [105]. Varshni's α and β parameters for bulk CdSe and bulk ZnSe are given in table 4.1. The three blue data points in Fig 4.8 above 200 K are close to the XX Varshni function.

This indicates that single peaks above 200 K are represented mainly by the XX peak with a small overlap from the X peak, (which is further observed in the following sections). For instance, at 300 K only a single peak is observed centered at 2.105 eV with a linewidth of 30 meV while X-XX separation is only 12 meV. Here, using the Varshni formula we can get an idea of the position of X and XX peaks, which are 2.113 eV and 2.102 eV.

Material	E_g(0K) (eV)	α (meV/K)	β (K)
S10a_1	2.211	0.63	290
Bulk CdSe (ZB) [a]	1.766	0.69	281
Bulk CdSe (WZ) [b]	1.757	0.37	150
Bulk ZnSe (ZB) [c]	2.82	0.45	400

Table 4.1: Parameters of Varshni function for the NW S10a_1, and for CdSe and ZnSe bulk phase materials for different crystalline phases. References taken from: a [105], b [106] and c [107].

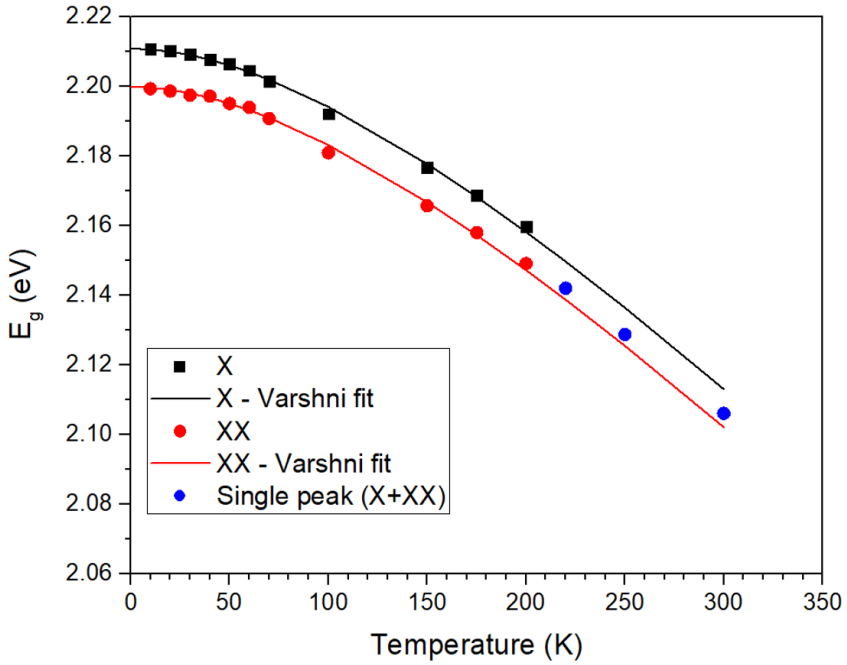

Figure 4.8: Emission energy as a function of temperature for exciton (black) and bi-exciton (red) of NW S10a_1. Solid lines are Varshni fit of emission energies of X and XX. Blue points represent emission energy for single peaks above 200 K.

4.5.2 Fitting of emission peaks

The evolution of emission lines with temperature can be discussed correctly only after the fitting of each emission peak.

In Fig 4.9 are represented 3 spectra of just the X-peak of NW S10a_1 at 10 K, 40 K, and 100 K, as a reference to describe the fitting procedure. The main X peak of this NW is closely surrounded by two side peaks: X_a and X_b. The origins of the two extra peaks are unknown for now.

Each emission peak is fitted with a sharp component and a broad component extending to several meV. We attribute the sharp component to the zero-phonon line (ZPL) which has no contribution from the phonons. The broad component is attributed to a phonon side-band which arises from the radiative recombination of electron-hole pairs along with the emission (lower frequency side) and the absorption (higher frequency side) of acoustic phonons [108]. The energy difference between the ZPL and the side-band peak is the corresponding phonon energy.

The shape of the ZPL line is well fitted with a Lorentzian function, whereas the shape of the phonon side-band is quite complex and asymmetric. We approximate the side-band with an asymmetric Voigt profile *i.e.* the concatenation of two Voigt profiles, with different FWHM for the left and right sides of the peak. This is used for temperatures till about 30 K. For temperatures above 30 K, a symmetric Voigt profile give a good fit. For very high temperatures, mostly above 100 K, the entire peak can be fitted with just one symmetric Voigt profile without the need for a Lorentzian ZPL. Indeed, at high temperatures, there is enough thermal energy to excite many phonons and the probability of zero-phonon transition comes close to zero.

The fitting of the ZPL and side-band can be simplified when the ZPL and the side-band have the

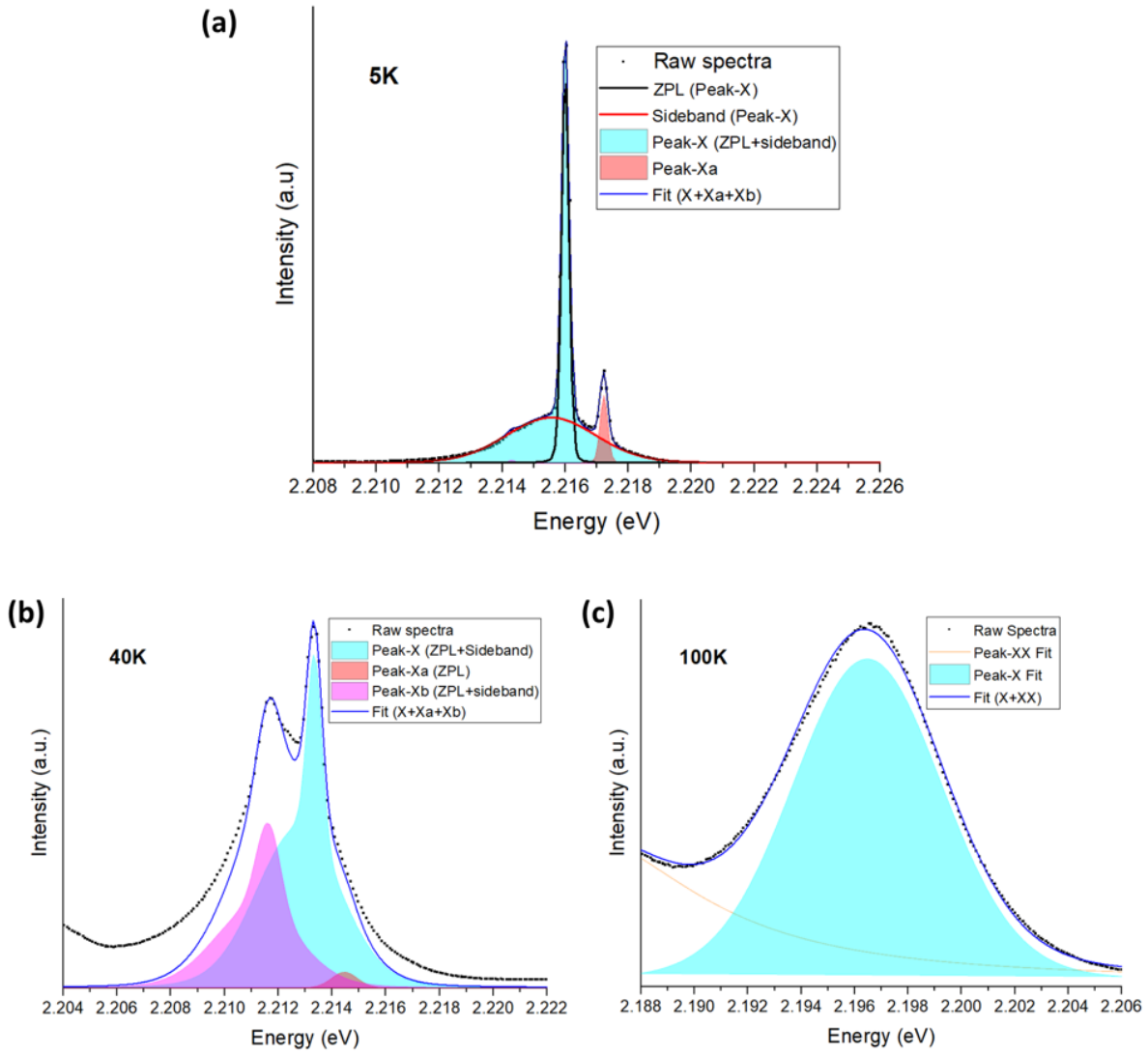

Figure 4.9: μ-PL spectra of NW S10a_1 excited with 5 μW CW power and fitted with a ZPL and a phonon side-band at (a) 10 K, (b) 40 K, and (c) 100 K.

same (or very close) peak centers. But for our QDs, as can be seen from 4.9 (a) the side-band is centered at the low energy side of the ZPL and a good fit is only achieved when both the ZPL and side-band are fitted separately. Fitting becomes quite complicated when two or more peaks are situated close to each other as in the case of NW S10a_1, as every peak has to be fitted with a ZPL and its side-band. The situation is even more complex when temperatures are increased since the evolution of side-bands and ZPLs are different.

Each fit deals with 2 fitting parameters, linewidth (FWHM) and height (peak-intensity). This would mean that there are a total of 12 fitting parameters for 3 ZPLs and 3 side-bands. This makes the whole fitting process highly complex. But this process can be simplified. Since, all emission peaks come from the same QD, we assume that the shape of all the ZPLs and all the side-bands are the same for a given temperature. This would mean that the linewidth for all ZPLs (l_{zpl}) and all sidebands (l_{band}) are the same

for a given temperature *i.e.*

$$l_{ZPL}(X) = l_{ZPL}(X_a) = l_{ZPL}(X_b) \quad and \quad l_{band}(X) = l_{band}(X_a) = l_{band}(X_b) \tag{4.10}$$

Moreover, the ratios of ZPL to side-band peak-intensity should also be the same for every peak for a given temperature *i.e.*

$$\frac{I_{ZPL}(X)}{I_{band}(X)} = \frac{I_{ZPL}(X_a)}{I_{band}(X_a)} = \frac{I_{ZPL}(X_b)}{I_{band}(X_b)} \tag{4.11}$$

To keep the fitting procedure simple, the energy separation between the ZPL and side-band was also kept the same for all peaks for a given temperature.

Temperature (K)	$I_{ZPL}(X)$ (counts)	$I_{ZPL}(X_a)$ (counts)	$I_{ZPL}(X_b)$ (counts)	$I_{band}(X)$ (counts)	$I_{band}(X_a)$ (counts)	$I_{band}(X_b)$ (counts)	l_{ZPL} (meV)	l_{band} (meV)
5	16000	0	2700	1970	0	0	0.26	3.1
40	5630	2690	470	4740	2370	0	0.65	3.7
100	0	0	0	1050	3660	0	0	7.4

Table 4.2: Fitting parameters of the X, X_a and X_b peaks of μ-PL spectra in Fig 4.9 at 5, 40, and 100 K.

In table 4.2 are given all the fitting parameters used to fit the three spectra in Fig 4.9. At 10 K, X is fitted with a ZPL of l_{zpl}(X) = 0.26 meV and a side-band of l_{band}(X) = 3.1 meV. Peak X_a and X_b are fitted only with a ZPL as the side-bands are small enough to be neglected. The X peak side-band is fitted with an asymmetric Voigt profile, shifted towards the lower frequency side of the ZPL.

At 40 K, X and X_b are fitted with a Lorentzian ZPL and symmetric Voigt side-band, and the X_a side-band was neglected and only fitted with a ZPL. All ZPLs and side-bands experience the same red-shift with increasing temperature. The tail of the peaks at the low energy side is not fitted perfectly as their is contribution from the XX peak.

At 100 K, the ZPLs of all the three peaks are negligible and their side-bands FWHM are large enough to overlap each other completely and therefore these three peaks can be fitted with just one side-band with symmetric Voigt profile.

Now with a procedure for fitting the emission peaks, we can start to discuss the other characteristics changes in emission peaks with temperature.

4.5.3 Line broadening due to temperature

Both ZPL and side-band experience broadening of the linewidth with temperature due to coupling with phonons. After proper fitting, the real FWHM of the ZPL (black) and side-band (red) of the main X peak in NW S10a_1 could be extracted and is shown in Fig 4.10. The blue line represents the experimentally observed overall FWHM (which is the procedure used in previous studies [109]).

At low temperatures (0-50 K), the FWHM is given by the ZPL, as the zero phonon transitions are strong. At higher temperatures (above 100 K), the ZPL is negligible and the FWHM is given by the side-band. As temperatures are increased exciton-phonon interactions become stronger and as a result, phonon side-band increases in intensity and broadens.

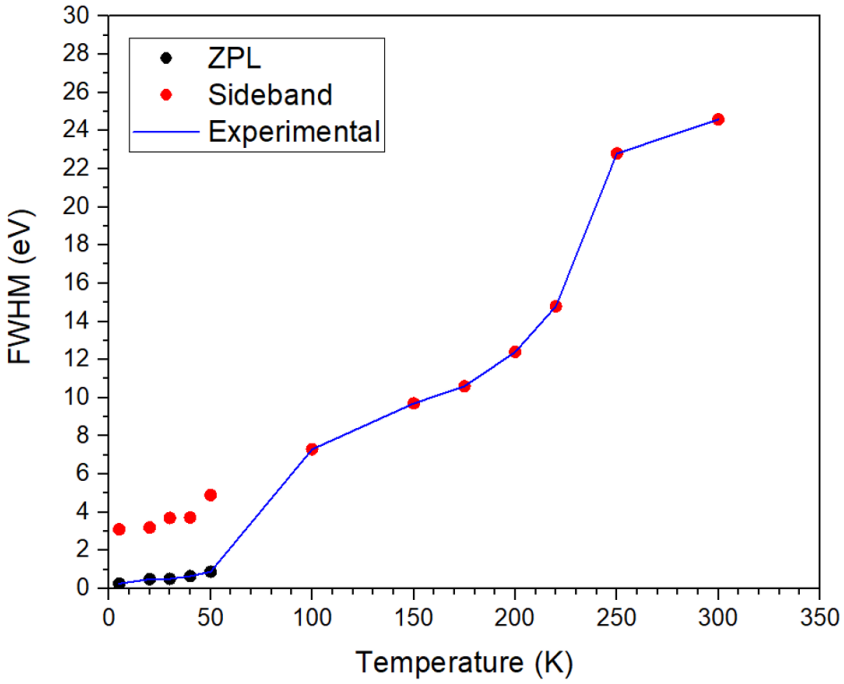

Figure 4.10: FWHM obtained for the X peak of NW S10a_1 from fit of ZPL and phonon side-band at different temperatures. In red are presented FWHM values for the ZPL and in black for the side-band. In blue is represented the experimental FWHM.

A comparison of FWHM for CdSe QDs at high temperatures is given in table 4.5. In all the cases mentioned except for NW S10a_1, the FWHM were calculated using a single Lorentzian fit for both the ZPL and the side-band. For NW S10a_1, both ZPL and side-band were fitted separately.

The values for NW S10a_1 are lower than what are reported in literature for different CdSe QD systems (see table 4.3) except for CdSe-ZnSe QD-NW (15 meV, NW-2012), observed previously in our group at 300 K. However, this low linewidth at 300 K was only reported for one NW.

Temperature (K)	5	50	80	100	300
S10a_1	0.26 meV	0.8 meV		7 meV	24 meV
NW-2012 (no shell) [a]	1.8 meV				15 meV
NW-2016 (thin shell) [b]	1.4 meV				
CdSe-SKQD [c]	0.4 meV		3.5 meV		
CdSe nanocrystal [d]					50 meV
CdSe/ZnSSe-SKQD [e]					25 meV

Table 4.3: FWHM values for different CdSe QDs at different temperatures for the S10a_1 NW and data taken from literature, a [11], b [12], c [31], d [84] and e [33].

The emission lines broadening has an impact on the single-photon purity at high temperatures. The key

to single-photon emission at room temperature is the identification and separation of each of those peaks whose convolution result in a broad peak. This means that the linewidth of the X or XX peaks should be less than the separation between the X and XX peaks (the so called XX binding energy Bxx). For NW S10a_1, B_{XX} is 11 meV while linewidth at 300 K is 25 meV. Therefore, resolving the X and XX 300 K is difficult and so is achieving anti-bunching at 300 K.

4.5.4 Bi-exciton as the dominant emitter

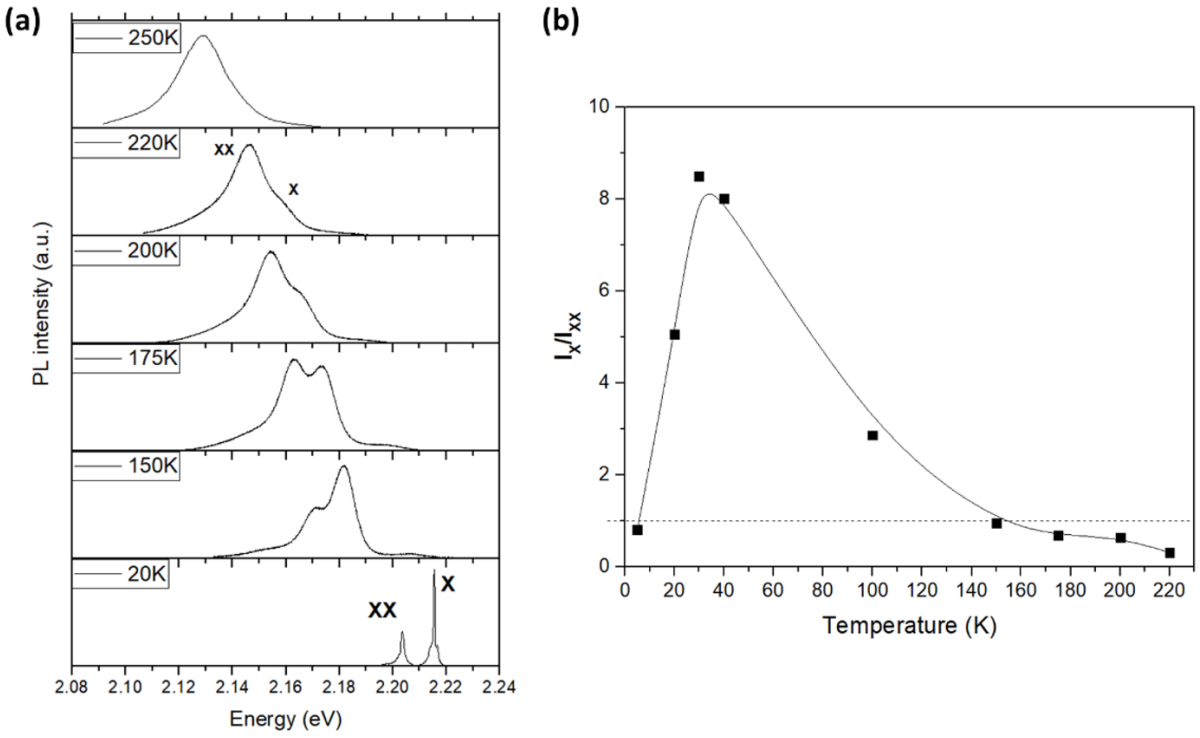

Figure 4.11: (a) Temperature-dependent μ-PL spectra of NW S10a_1 at 5 μW CW excitation (same as Fig 4.7, normalized with peak intensity). Above 175 K, XX is the dominant emitter. (b) The ratio of integrated intensity of X and XX at 5 μW (which provides maximum intensity for the X-state under CW excitation).

In Fig 4.11 (a) is shown the temperature dependence of NW S10a_1 emission from 20 K to 250 K at 5 μW CW excitation. It can be seen that at 175 K and above, XX intensity dominates X. In Fig 4.11 (b), is plotted the ratio of the integrated intensity of the exciton and the bi-exciton (ZPL+sideband) I_X/I_{XX}, after fitting each peak according to the procedure described in section 4.5.2. From 50 to 100 K, fitting of the X and XX peaks was difficult and therefore these points are missing in 4.11 (b). Above 100 K, the ZPL became negligible and therefore the fitting was simpler.

As temperature increases, X intensity increases and can be seen as the dominant emitter up to about 150 K ($I_X/I_{XX} > 1$). After 50 K, X intensity starts to decrease. Above 150 K, XX is the dominant emitter ($I_X/I_{XX} < 1$).

This observation can be explained with non-radiative relaxation channels of the bi-exciton and exci-

ton, and particularly the dark-exciton state of the exciton [110].

Both bi-exciton and exciton can lose their carriers to trap states where recombination then takes place non-radiatively (see scheme in Fig 4.12). Moreover, the exciton is split into bright-exciton and dark-exciton states. The dark-exciton can spin flip to bright-exciton [111] or recombine non-radiatively. And therefore the exciton, has two non-radiative channels: one through trap states and one through the dark-exciton.

At low temperature, non-radiative channels are suppressed and the carriers relax mostly radiatively through the XX→X and bright-X→0 transitions. As temperature increases, charge carriers in the dark-exciton can now have enough energy to repopulate the bright-exciton through the spin-flip process, and therefore we see an increase in intensity of the X line (up to 50 K). However, above 50 K, the intensity of the X line decreases because high temperature increases non-radiative transitions of both bright-exciton and dark-exciton which overwhelm the re-population of the bright-exciton from the dark-exciton and this results in a decrease of exciton intensity. This trend was also observed for NW S10a_2 and S10a_3 for the low and high energy peaks in Fig 4.3.

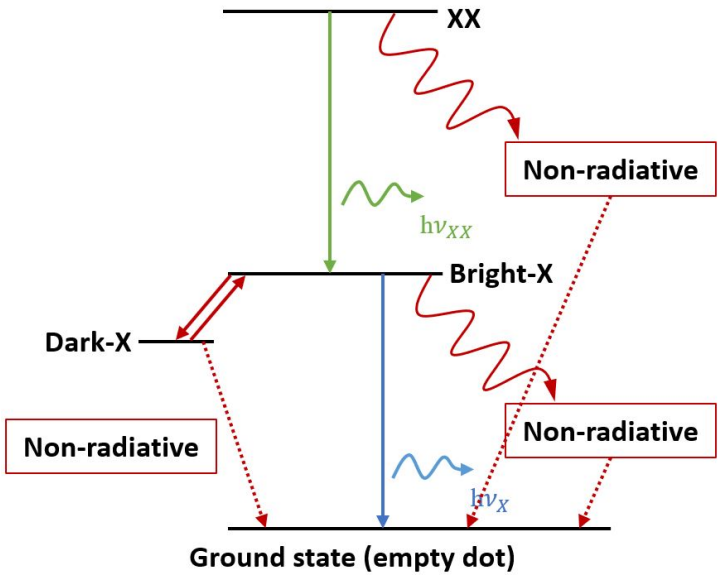

Figure 4.12: Scheme to illustrate non-radiative channels for the exciton and bi-exciton.

At high temperatures, emission peaks are very broad and are usually a sum of more than one peak and therefore, the single-photon property of one is degraded by the other. This domination of the bi-exciton and decrease of the exciton is of great importance when targeting anti-bunching at room temperature (Part C).

4.6 Effect of QD growth time/length

In sample S10a, more than 100 NWs were checked for their emission and only for NW S10a_1 an exciton and bi-exciton state could be confirmed properly by fitting their integrated intensities to the model described in section 4.4. For NWs S10a_2 and S10a_3 in Fig 4.3, although a crossing of intensities between the high energy and low energy peaks was observed with increasing excitation powers which

is an indication of X and XX states, we could not fit the emission lines to the X and XX states using the above model. In fact, for most NWs in this sample, a broad emission peak or several emission lines were observed in 500-600 nm range. As said before, for NWs in this sample, the QD (and the entire ZnSe core) could be buried in the 2D layers. Moreover the shell for this NW was grown at 300 °C and as discussed in chapter 3, shell grown at this temperature is full of defects (see Fig 3.36). Sample S10a was the first QD sample prepared and therefore was also the least optimized.

After optimizing the growth conditions, sample S10c was prepared, again with a 10 s CdSe QD in a long core (51 min growth), and a shell grown at 320 °C. For the NWs in this sample we expect the QD to be not buried in the 2D layers with a NW radius optimum for light extraction (see Fig 4.1 (b).)

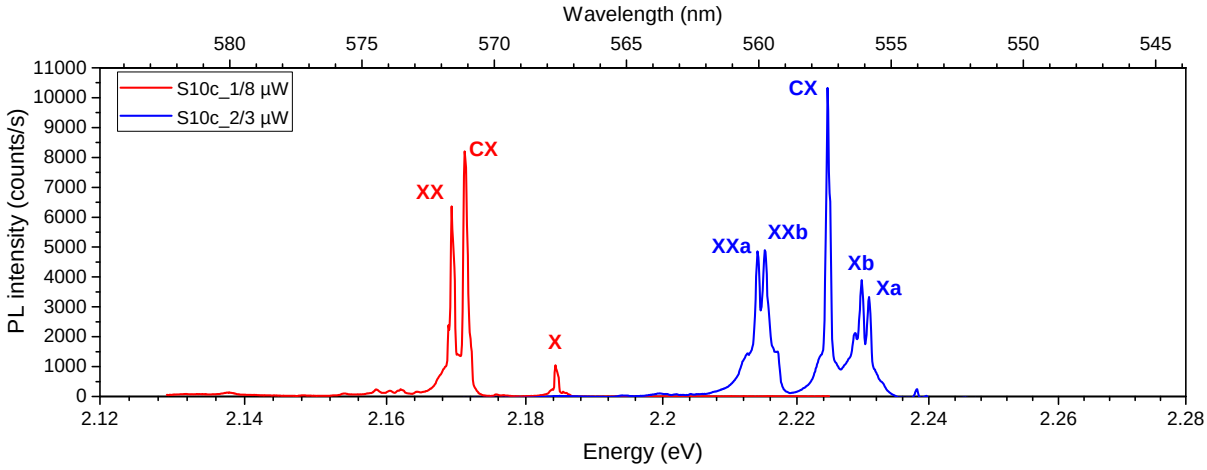

Figure 4.13: μ-PL spectra of two NWs (S10c_1 and S10c_2) from sample S10c at 5 K. Excitation power is mentioned for each NWs.

Emission from most NWs was observed within the 550-600 nm range (besides the ZnSe core emission around 440 nm/2.81 eV) with fewer emission lines than in sample S10a. Two NWs (S10c_1 and S10c_2) are shown for this sample in Fig 4.13 as examples. For NW S10c_1, three main emission lines are observed, while for for NW S10c_2 a doublet is observed for both the high and low energy peaks. The linewidth for the low energy peak at 2.169 eV for NW S10c_1 was calculated using a Lorentzian fit and is 0.28 meV, similar to the linewidth of the X peak for NW S10a_1 (0.26 meV).

The integrated intensity plots as a function of power for these two NWs are given in Fig 4.14. Using the model described in section 4.4.2, from the fit we were able to identify the exciton and bi-exciton peaks at 2.184 eV and 2.169 eV for NW S10c_1, and the combined integrated intensity of the doublets at Xa and Xb (2.230 and 2.229 eV respectively), and XXa and XXb (2.214 and 2.215 eV respectively) for NW S10c_2.

An intermediate peak between the X and XX peak is visible for both NWs which could arise either from the presence of a charged exciton (CX) or charged bi-exciton (CXX) state. In fact, for NW S10c_1, is shown in section 4.8.3 that the peak CX belongs to a charged-QD state. There are also additional smaller intensity peaks which accompany the X and XX transition peaks only at higher powers and hence, possibly have multi-X (MX) origins.

The B_{XX} for NW S10c_1 is 15 meV and for NW S10c_2 is 16 meV ($E_{Xa} - E_{XXa}$), the values are larger than for NW S10a_1. But are still less than usually observed 20 meV B_{XX} for CdSe SKQDs [33],

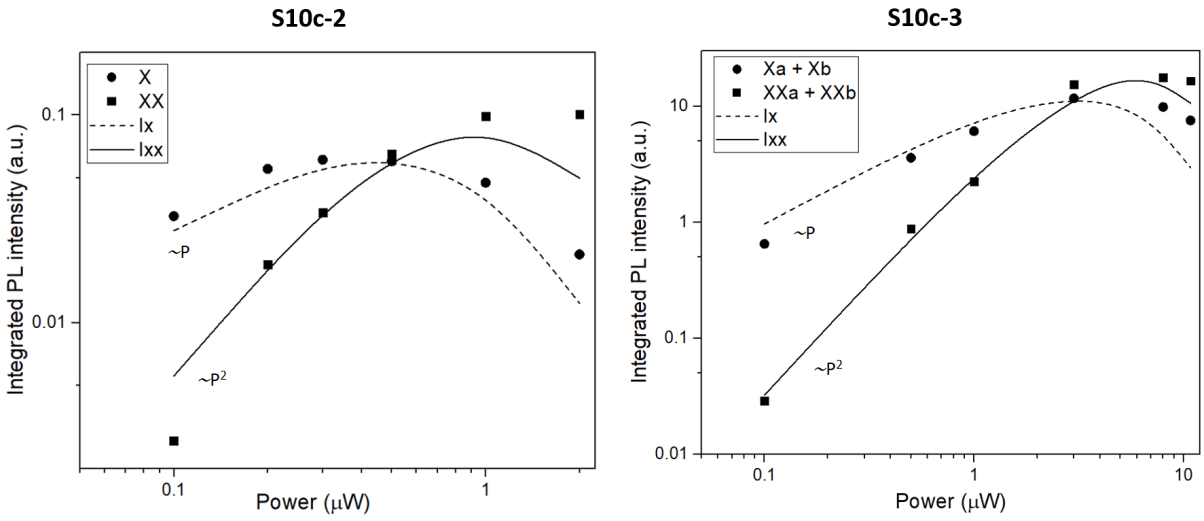

Figure 4.14: Integrated intensity plot as a function of power for NW S10c_1 and S10c_2 at 5 K. Circles and squares represent integrated intensity for the high energy (assigned to X) and the low energy (assigned to XX) peaks respectively, calculated in a 5 meV energy window. Dashed lines and solid lines represent fit using eq. (4.7) and eq. (4.8) respectively.

[32]. In fact, for most other NWs in sample S10c we observed emission lines in the 550-600 nm range with less than 15 meV energy separation between X and XX lines.

4.6.1 Emission energy 7s QD vs 10s QD

With hopes of increasing the B_{XX}, the next sample prepared was S7, with growth scheme same as sample S10c, but with a CdSe QD insertion of shorter time of 7 s in the ZnSe core. The radius, visible length and QD distance from the 2D surface are given in Fig 4.1 (b).

Only 6 NWs were checked for their emission in sample S7 at 5 K, and for 4 NWs two main emission lines were observed with about 20 meV separation. Selected 3 NWs emission spectra out of these 6 NWs are shown in Fig 4.15 (a) at CW excitation power of 5 μW. Emission lines are observed between 2.48-2.066 eV (500-550 nm), hence at higher energy than in the 10 s QD samples. For comparison, emission spectra of NWs from sample S10a (black), from sample S10c (blue) and from sample S7 (red) are shown in Fig 4.15 (b). This blue shift in emission energy is tentatively attributed to a reduction in the QD height expected with a 7 s CdSe insertion, which means higher confinement in the QD and therefore increase in the emission energy.

The linewidth for sample S7 was calculated after fitting the high energy peak at 2.391 eV of NW S7_3 with a Lorentzian peak and was found to be 0.21 meV (same for the low energy peak at 2.371 eV). For all three NWs, X and XX peaks were identified and fitted with the model described in section 4.4.2. The integrated intensity as a function of CW excitation power for the X and XX of the three NWs are shown in Fig 4.16. Out of the three NWs, NW S7_3 is very interesting for us, since it shows a very clean spectrum with two main X and XX lines separated by 21 meV and high intensity with just 5 μW excitation.

For NW S7_1, a doublet is observed for the exciton and bi-exciton, similar to NW S10c_2. The X doublet is observed at 2.362 eV (X_a) and 2.361 eV (X_b). While the XX doublet is at 2.341 eV (XX_b)

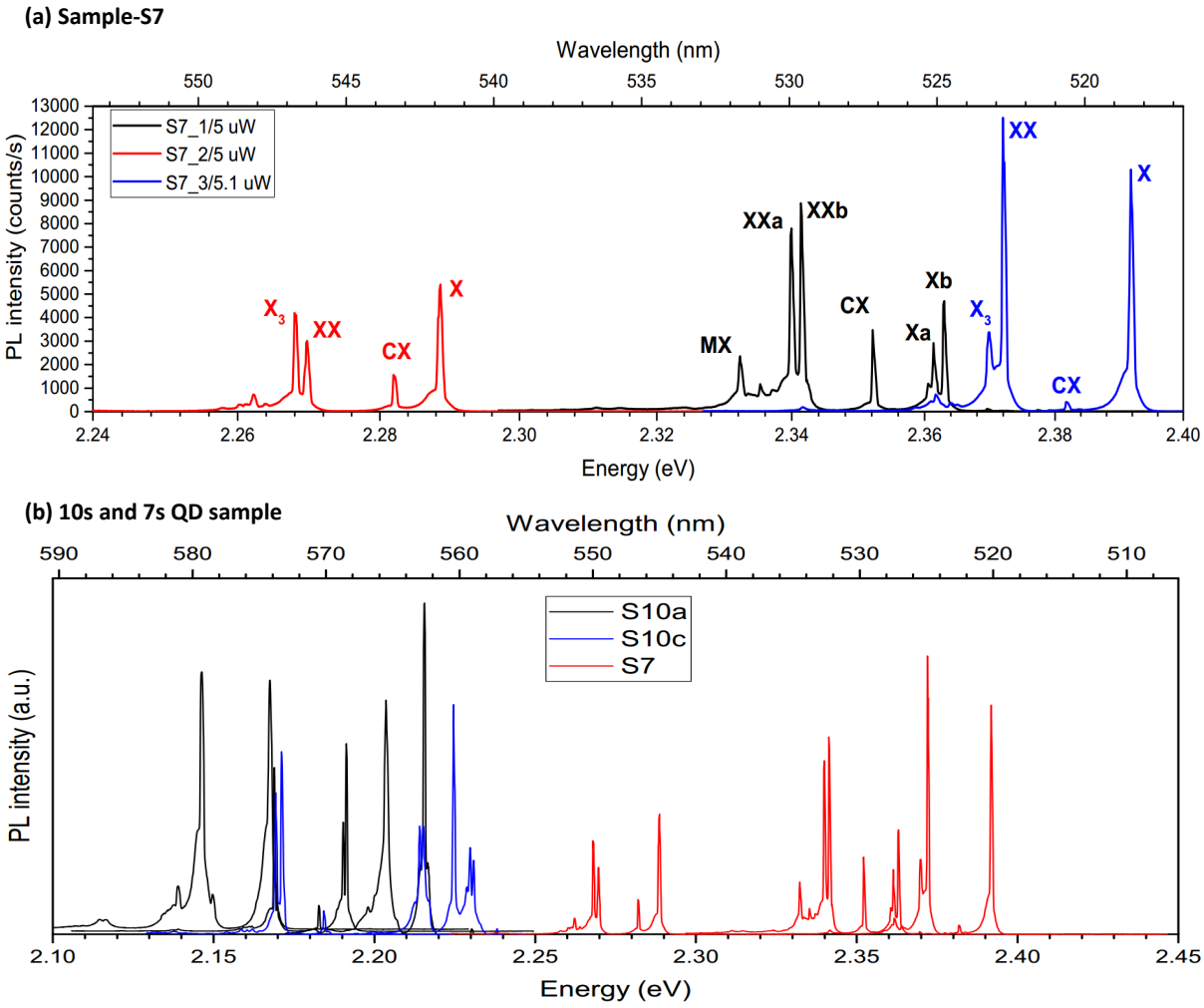

Figure 4.15: μ-PL spectra of three selected NWs from sample S7 at 5 K under CW excitation, with excitation power mentioned for each NW. (b) Comparison of emission energy of NWs from sample S10a (black), S10c (blue) and S7 (red).

and 2.340 eV (XX_a). The origins of these doublets is discussed in section 4.7 as possibly resulting from the fine structure splitting (FSS) of the exciton.

4.6.2 Multi-exciton transitions

Besides, the exciton and bi-exciton lines, multi-exciton lines can also be observed. For all three NWs of sample S7 shown in Fig 4.15 (a), additional emission peaks are observed on the low energy side of the XX, only at high powers. We will show with NW S7_3 that these additional peaks belong to multi-exciton states.

For NW S7_3, the μ-PL spectra for 0.1, 1, 10 and 100 μW CW excitation is shown in Fig 4.16 (c) and integrated intensities of X and XX as a function of excitation power is shown in (d). At very low power (0.1 μW), only X peak is visible. While above 0.1 μW, the quadratic rise of XX is clear. Similar

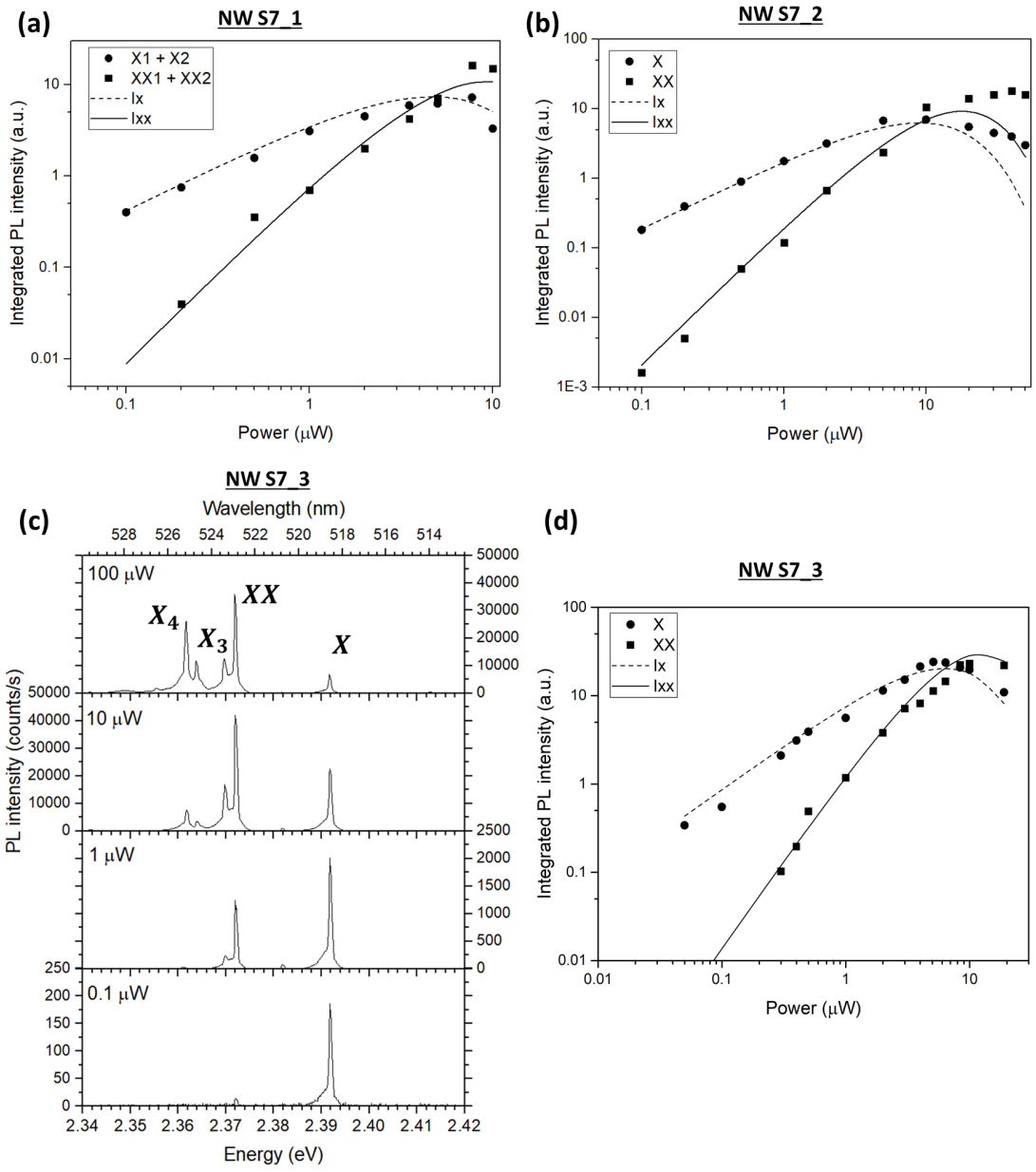

Figure 4.16: Integrated intensity plot as a function of power for (a) NW S7_1 and (b) S7_2 at 5 K. Circles and squares represent integrated intensity for the high energy (assigned to the exciton) and the low energy (assigned to the bi-exciton) peaks respectively, calculated in a 5 meV energy window. Dashed lines and solid lines represent fit using eq. (4.7) and eq. (4.8) respectively. (c) μ-PL spectra of NW S7_3 for excitation powers of 0.1, 1, 10 and 100 μW under CW excitation. (d) Integrated intensity plot as a function of power for NW S7_3.

to sample S10c, an intermediate peak between the X and XX peak is seen which could belong to the CX or CXX state.

At 1 μW, only two main X and XX peaks are observed with an extra very low intensity peak X_3 at

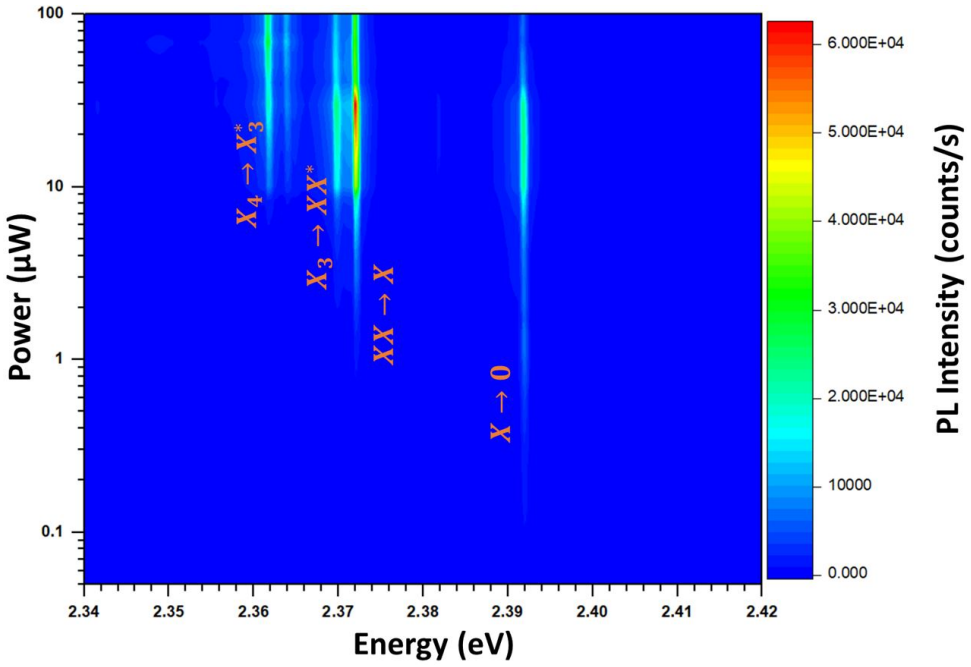

Figure 4.17: Contour plot of the variation of emission energy of NW S7_3 vs. excitation power and vs. emission energy.

2.369 eV in the tail of XX peak on the low energy side. At 10 μW, few extra peaks on the low energy side of the XX emerges. The X_3 peak is now higher in intensity with two other peaks at low energy side. For comparison, PL intensity scales for 10 and 100 μW are same. At 100 μW, the XX and X intensity has decreased and the intensity of X_4 peak has increased considerably.

In Fig 4.17 a contour plot of the variation of emission energy of NW S7_3 vs. excitation power and vs. emission energy is plotted. At low excitation power, PL intensity only at X peak is observed for the $X \rightarrow 0$ transition. Next above 1 μW, PL intensity at XX peak appears which corresponds to the $XX \rightarrow X$ transition.

Electron and hole ground states are fully occupied with two excitons in the bi-exciton state. Further increase in excitation power leads to an creation of an additional electron hole pair. Due to Pauli exclusion principle, the third electron (and hole in the valence band) must occupy the higher p-state. The X_3 ground state thus consists of two electron-hole pairs in the s state and one pair in the p state. Now, two radiative channels exists for the recombination of this X_3 state: either recombination in the p-shell can occur which leads to an emission line ($X_3 \rightarrow XX$) on the high energy side of the exciton. Or recombination in the s-shell can occur, leaving an excited state of the bi-exciton (XX^*), which consists of one electron-hole pair in s and one in first-excited p shell. This recombination ($X_3 \rightarrow XX^*$) leads to an emission on the low energy side of the XX. This is what we observe at 2.369 eV. Similarly, the peak at X_4 is probably due to recombination of a four electron-hole pair state *i.e.* $X_4 \rightarrow X_3^*$.

4.6.3 Biexciton binding energy

From the emission spectra the bi-exciton binding energy (B_{XX}) can be easily calculated as the difference in energies of the exciton and bi-exciton lines.

Nanowire	Exciton position (eV)		Bi-exciton position (eV)		Bi-exciton binding energy (meV)
S10a_1	2.215		2.203		12
S10c_1	2.216		2.202		14
	Xa	Xb	XXa	XXb	
S10c_2	2.230	2.229	2.214	2.215	16
S7_1	2.362	2.361	2.340	2.341	21
S7_2	2.288		2.269		19
S7_2	2.391		2.371		20

Table 4.4: B_{XX}, X and XX position of different QDs studied so far.

For all the NWs studied so far, the B_{XX} is given in table 4.6 along with the position of the exciton and bi-exciton lines. For NWs where a doublet is observed for exciton and bi-exciton lines, the B_{XX} is taken as the difference between the Xa and the XXa peaks as they belong to the same radiative cascade emission (as shown in the following section 4.7).

For sample S10a and S10c with 10 s CdSe insertion, the B_{XX} is less than 16 meV for all three NWs studied. In fact, for most NWs in these samples, we found emission lines very close to each other (about 10 meV). These NWs were discarded from the study. For sample S7 with a 7 s CdSe insertion, the B_{XX} for all three NWs is 20 meV or above, as observed for CdSe-SKQDs in [001] direction [33], [32].

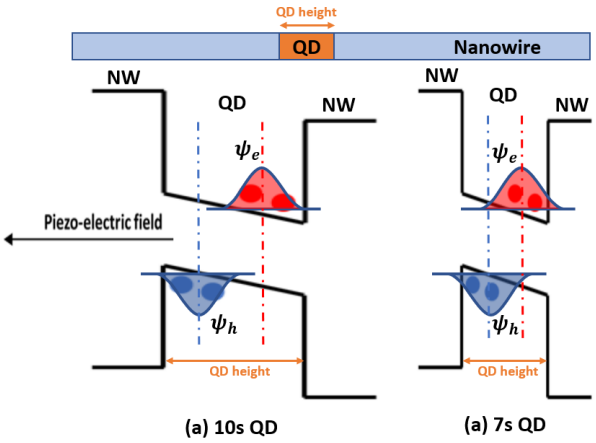

Figure 4.18: Energy bands for a QD-NW with a QD of (a) large height and (b) small height in the presence of a lateral piezo-electric field. The QD with smaller height have a higher electron-hole wave-function overlap which leads to a higher bie-exciton binding energy (BXX).

A small QD size results in a reduction of the size of the envelop function, hence a stronger electron hole overlap and a larger B_{XX}. In addition, due to the piezo-electric field present inside the QD, the charge carriers (electron and holes) are subject to a potential gradient that tilts the energy bands inside the QD. These fields push the electrons and holes to opposite ends of the QD and increase the electron-hole separation in the QD. The (111) geometry polar crystals with ZB structure (as we suppose in

this case) such as for GaAs, InAs, and also QDs with large sizes have been shown to have a strong piezoelectric field [112], [113].

In Fig 4.18 is shown energy band diagram of QD-NWs with two different QD heights. Assuming the height of the QD in sample with 7 s QD growth is smaller than the height of the QD with 10 s QD growth, the electron wave-function (ψ_e) overlap with the hole wave-function (ψ_h) is higher for the 7 s QD than for the 10 s QD. Moreover, if a piezo-electric field is present in the QD, the electron-hole wave function overlap is further decreased. A lower electron-hole overlap means a lower B_{XX} and therefore we expect a lower B_{XX} for the 10 s QD sample than the 7 s QD sample.

4.7 Fine structure splitting

NW S7_1

For very few NWs we observed a doublet instead of a single emission line. This doublet could be due to the fine structure splitting (FSS) of the exciton state. In this section, as an example, we are going to discuss FSS which was observed for NW S10c_2 and S7_2 and confirmed with polarization experiments.

For NW S7_1, a doublet is observed for the X and XX (Fig 4.15). The X doublet is observed at 2.362 eV (X_a) and 2.361 eV (X_b). While the XX doublet is at 2.341 eV (XX_b) and 2.340 eV (XX_a). We measured the PL intensity of these doublets with respect to the polarization directions by using a rotating $\lambda/2$ waveplate in front of a linear polarizer at 5 K and 5 μW CW excitation. In Fig 4.19 (a) is shown μ-PL spectra measured in two polarization directions (120 and 210°) perpendicular to each other. The peak intensity for different polarization directions is shown in Fig 4.19 (c) for the doublet of X peak and (d) for the doublet of XX peak. The polarization directions are also perpendicular to the NW axis *i.e.* the [111] crystallographic direction.

For 30 or 210° (30°+180°) polarization direction, the X_a and XX_a are at maximum intensity, while the X_b peak is almost non-existent. The reverse is true for perpendicular polarization directions 120 or 300° (120°+180°). The X_a peak is cross-polarized with X_b in perpendicular directions, whereas intensity of X_a peak is co-polarized with XX_a peak. Such a behavior is expected from the FSS of the exciton (X).

The FSS arises from the anisotropy of the exchange interaction between an electron and a hole which form the neutral exciton. Its general Hamiltonian is given as:

$$\mathcal{H}_{exchange} = -\sum_{x,y,z}(a_i S_{h,i} S_{e,i} + b_i S^3_{h,i} S_{e,i}) \tag{4.12}$$

where a_i and b_i are spin-spin coupling constants, and S_h and S_e are spin of a hole and an electron respectively. Due to this electron-hole exchange interaction, for a QD, where the confining potential is isotropic (D_{2d} symmetry), the bright-exciton and the dark-exciton form two doublets split by energy δ_0 which is of the order of 1 meV for most systems. In D_{2d} symmetry, the bright-exciton is not split, while the degeneracy of the dark-exciton state is lifted. When the confining potential is anisotropic *i.e.* for symmetry lower than D_{2d} (for *e.g.*, C_2 or C_{2v}), the bright-exciton is also split into two energy states by an energy δ_1 [114]. This anisotropy can be due to a variety of reasons, for *e.g.*, due to elongation of the QD in the plane during growth.

The bi-exciton state has no FSS as it consists of two excitons of opposite spins. If the exciton has a FSS (see Fig 4.20 (a)), the bi-exciton can relax into any of the two exciton states, which results in two

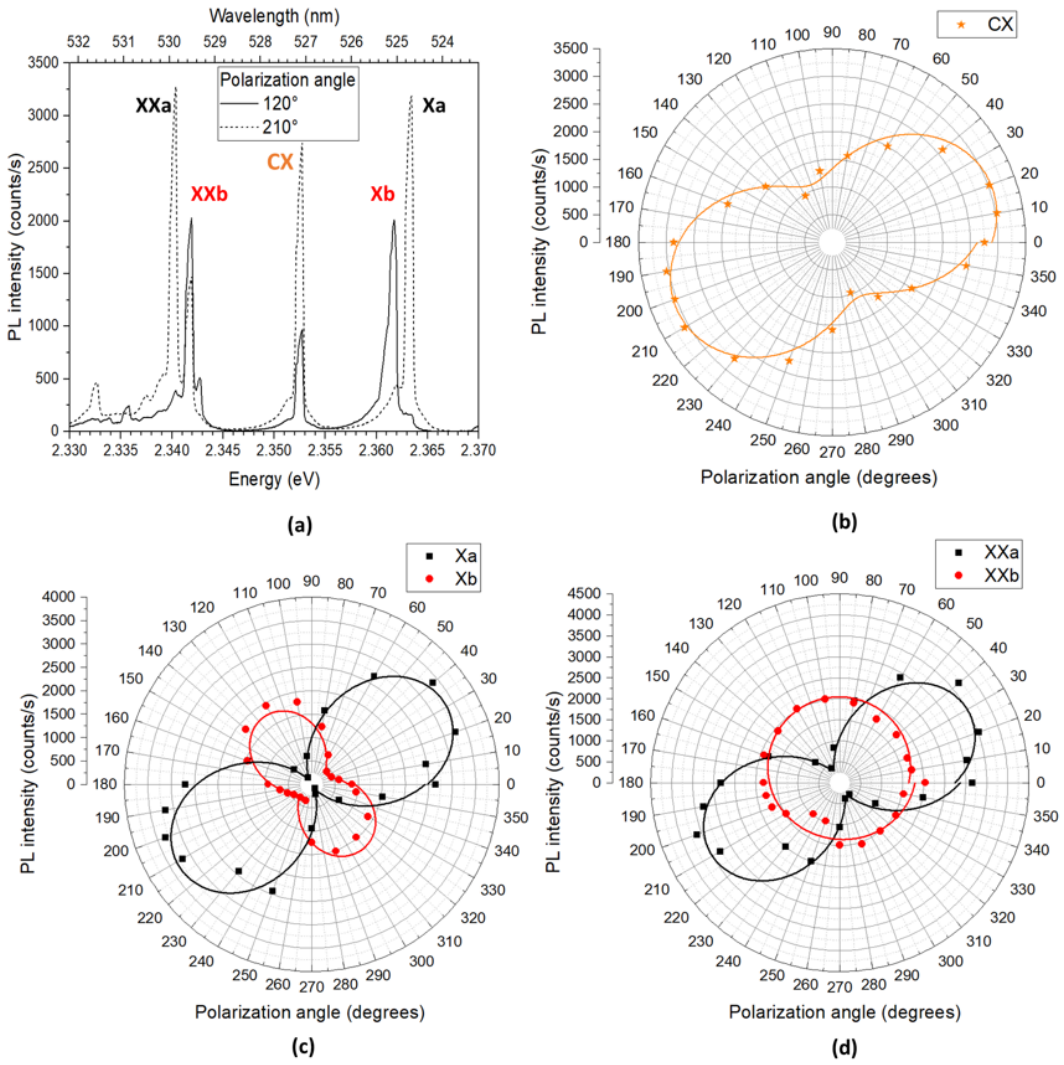

Figure 4.19: (a) Spectra of NW S7_2 at 120 and 210° polarization angles at 5 K and 5 μW CW excitation. Polarization measurements on doublet of (b) X and (c) XX peaks in NW S7_2.

emission lines *i.e.* XX_a and XX_b. The two exciton states can then relax to the ground state resulting in emission lines X_a and X_b. The $XX_a \rightarrow X_a \rightarrow 0$ follows one radiative cascade and $XX_b \rightarrow X_b \rightarrow 0$ follows another. The XX_a and X_a (also XX_b and X_b) are co-polarized while, XX_a and XX_b (also X_a and X_b) are cross-polarized. This spectral correlation of polarization provides a very unique identification of the exciton and bi-exciton states in the same QD.

The magnitude of the FSS is defined by δ_1 which is the energy separation between the Xa and Xb (or XXa and XXb) peaks and is less than 1.0 meV in this QD. It should be noted the maximum PL intensity of Xa and Xb (also XXa and XXb) should be the same at perpendicular polarization.

However, there are two odd observations in our polarization measurements: one, the maximum PL intensity of Xa at 120° polarization is almost twice the maximum PL intensity of Xb at 210° polarization. And second, XXb is not polarized. Had XXb been polarized along the 120° direction (same as Xb), we could have confirmed the FSS of X in this QD. But, we also observe polarization of the charged-exciton

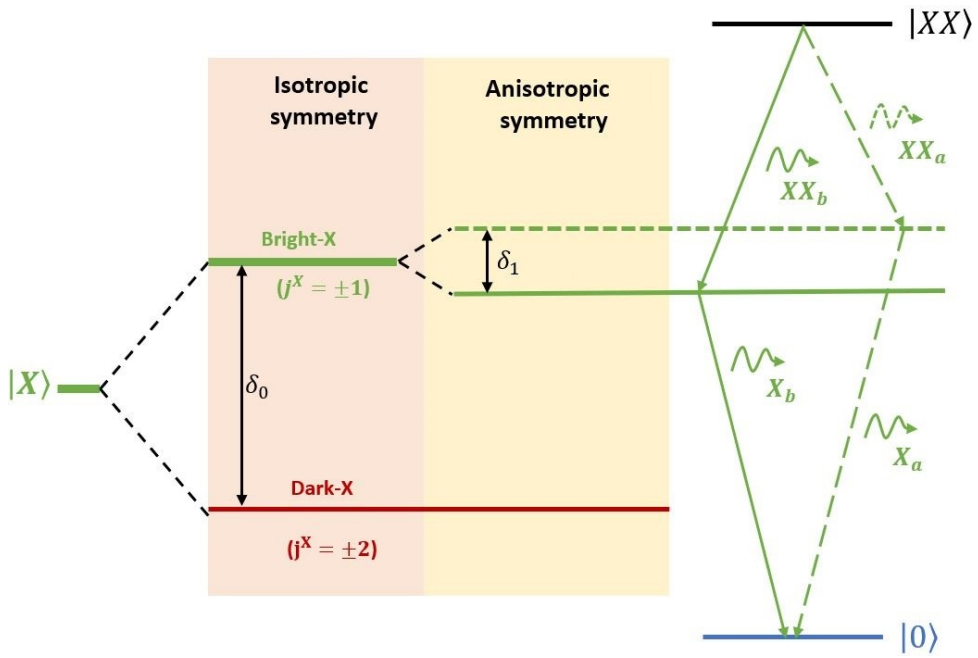

Figure 4.20: (a) Scheme for the energy level splitting of the exciton state. The exciton is split into bright-exciton (bright-X) and dark-exciton (dark-X). The fine structure splitting (FSS) of the bright-exciton does not exits for a QD with isotropic symmetry while it exists for an-isotropic symmetry. The bi-exciton can relax into any of the two exciton states. Photons due to XX_a and X_a transitions (similarly XX_b and X_b) are co-polarized in intensity and XX_a and XX_b transitions (also X_a and X_b) are cross-polarized in intensity.

(CX) in Fig 4.19 (b) along the 210° direction. The CX is not expected to be polarized due to the FSS of the X in the QD. The polarization of the CX could be due to the guiding effect of the NW, *i.e.* an additional polarization induced by the asymmetry of the NW cross section. This was indeed observed in InAs/InP NW-QD.

Nicolas Chauvin *et al.* [115] realized InAs QD in asymmetric InP NWs where the NW cross-section is elongated along one of the two axis. The QD emission was observed to be polarized along this elongated axis. The polarization of the CX in our QD could be due to a possible asymmetric feature of the NW. In fact, for very few NWs, the shell growth was observed to be asymmetric around the QD region. Although a high magnification SEM image of NW S7_1 is not available, an example of such a NW is shown in Fig 4.21. Around the QD position, the NW has an asymmetric shape. The fact that the emission of Xa and XXa are polarized along the CX polarization direction and that the emission of Xb is reduced at orthogonal directions, points towards the asymmetry in NW S7_1 along the 210 and 120° directions.

NW S10c_2

We also observed a hint towards fine structure splitting of exciton in NW S10c_2. In Fig 4.22 (a) are shown μ-PL spectra at 3 μW CW excitation at 5 K, measured in two polarization directions (20

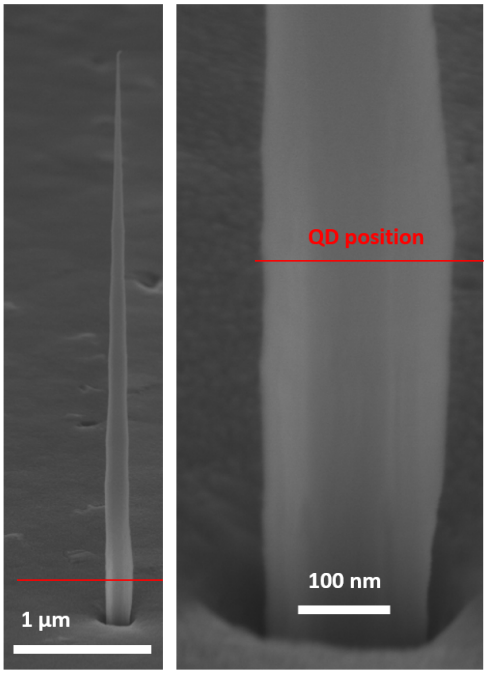

Figure 4.21: Random NW from sample S7. Around the QD position, the NW shape is not regular and possibly asymmetric.

and 110°) perpendicular to each other. The peak intensity for all other polarization directions are shown in Fig 4.22 (b) for Xa and Xb peak and in (c) for XXa and XXb. There are additional peaks observed: Xc and XXc. The intensities of these peaks are very low.

The Xa peak intensity is cross-polarized with Xb (also XXa with XXb) in perpendicular directions, whereas intensity of Xa peak is co-polarized with XXa peak (also Xb with XXb). This is due to the FSS of X. However, again the PL intensity of Xb is twice the XXb at maximum polarization directions, and also of XXa is more than twice of XXb. Unlike in NW S7_1, a preferential polarization along one direction is not observed *i.e* although Xb emission intensity is higher along 20° direction, XXb intensity is twice less than Xa intensity along the same direction. Moreover, a doublet is also observed for peak-CX, and both peaks (CXd and CXe) are polarized along one directions. Also additional Xc and XXc peaks are observed.

This odd behavior cannot be explained just with the asymmetry of the NW shape. For now the origins of such a behavior is still not understood.

4.8 Antibunching under CW excitation

The ultimate test for a single photon-emitter is the anti-bunching experiment (see section 1.4.3.3) where the auto-correlation function $g^2(t)$ at zero delay gives the purity of the single-photon emitter. In this section, anti-bunching experiments performed using a Hanbury-Brown Twiss setup under CW mode excitation at 5 K on NW S10a_1, S10c_1, S10c_2 and S7_3 are presented. Later, in section 4.12 is shown why anti-bunching with CW excitation is not enough to identify an ideal single-photon emitter and further complementary characterization are required with pulsed excitation.

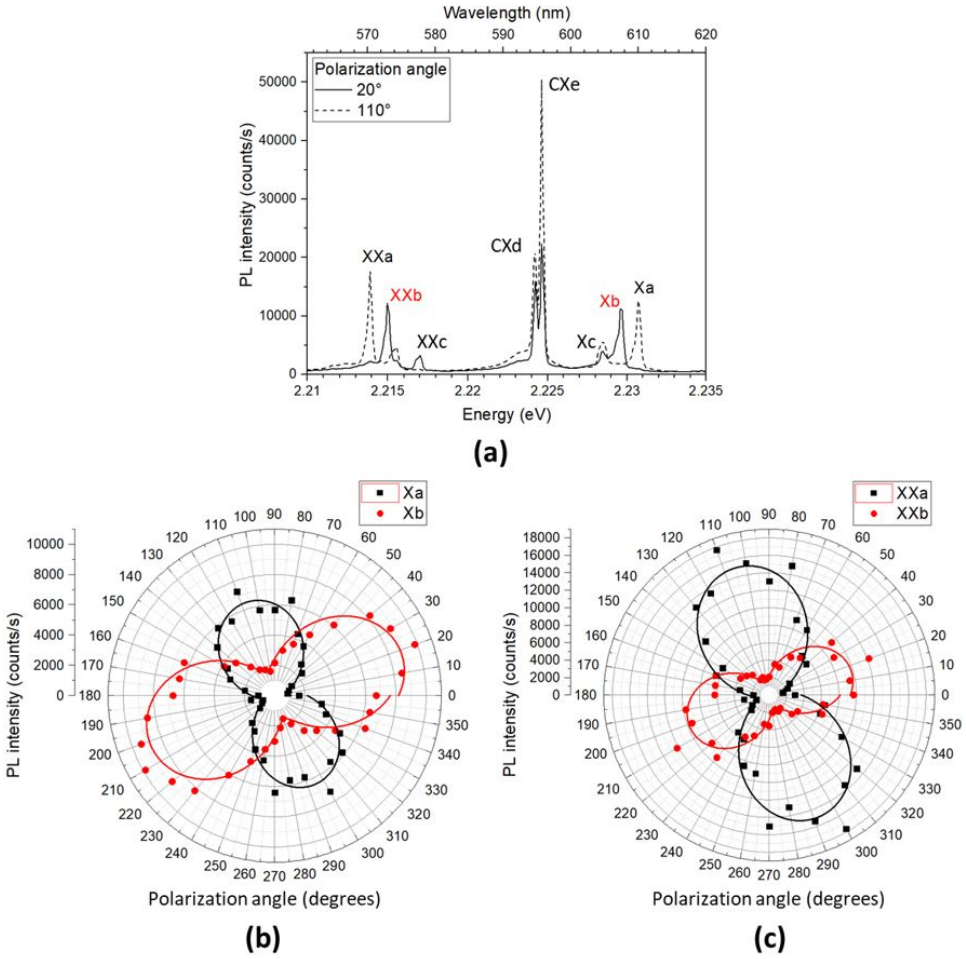

Figure 4.22: (a) Spectra of S10c_2 at 20 and 110° polarization angles at 5 K and 3 μW CW excitation. Polarization measurements on doublets of (b) exciton and (c) bi-exciton peaks in NW S10c_2.

4.8.1 Antibunching on exciton

In Fig 4.23 (a) is shown a spectrum of NW S10a_1 under CW excitation of 5 μW at 5 K. The yellow shaded region gives the spectral window (4.1 meV/1.05 nm) for which the auto-correlation function $g^2(t)$ measurements were performed on the exciton line at 2.216 eV (559.4 nm), as shown in Fig 4.23 (b). The measurement is integrated for 10 min. About 250,000 counts/s were recorded on one of the two APDs.

The $g^2(t)$ spectrum shows a dip at zero delay giving a clear evidence of anti-bunching. The experimental signal was first fitted using the relation:

$$g^2(t) = 1 - A_c e^{\frac{-|t|}{T_{ac}}} \tag{4.13}$$

where T_{ac} gives the estimate for the width of the dip in the correlation function at zero delay and is directly related to the lifetime and excitation time of the excited state. And $(1 - A_c)$ gives the $g^2(t)$ value at zero delay. The fit function is the convolution of this model function with a Gaussian function of width σ=0.1 ns, which represents the temporal resolution of the two APDs (50 ps for one APD). From the convoluted curve, $g^2(0)$ for the exciton line was then estimated to be 0.25 with T_{ac} = 0.27 ns.

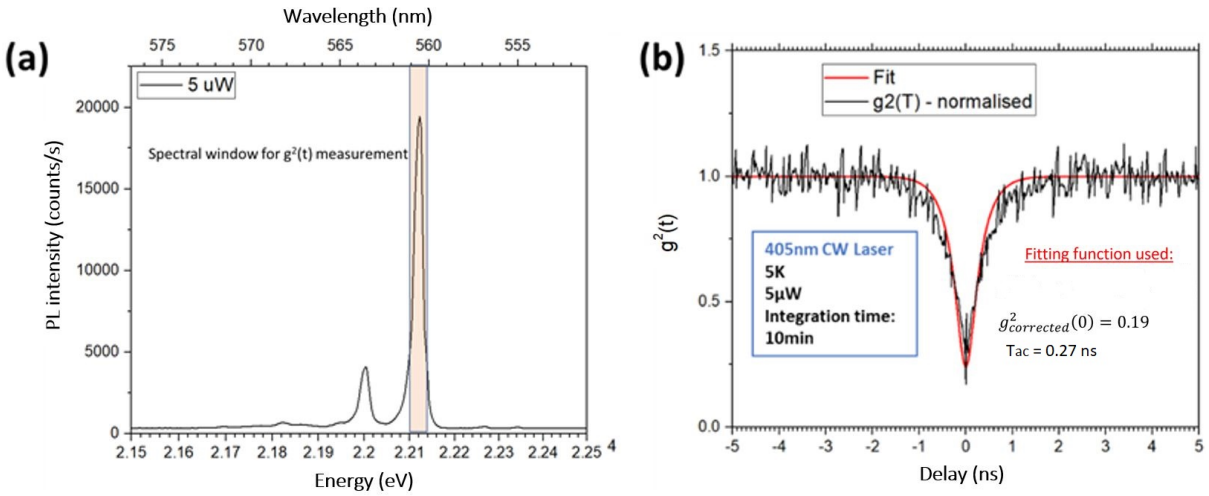

Figure 4.23: (a) μ-PL spectra of S10a_1 at 5 K and 5 μW CW excitation. The yellow shaded region of 4.1 meV (1.05 nm) represents the spectral window in which auto-correlation function $g^2(t)$ was recorded. (b) Normalized $g^2(t)$ using exciton line.

Usually, there is a degradation of the antibunching due to the noise coming from the luminescence background and the APD's dark counts. This noise is characterized by a non-correlated, random arrival of photons. Noise was estimated from the spectrum in Fig 4.24 (a) by defining the ratio $\rho = \frac{S}{S+B}$, where S is the signal and B is the noise intensity, then the corrected $g^2(0)$ is [19]:

$$g^2_{corrected}(0) = \frac{g^2(0) - (1-\rho^2)}{\rho^2} \tag{4.14}$$

After applying the correction, the $g^2_{corrected}(0)$ was found to be 0.19.

4.8.2 Antibunching on multi-exciton

QD emits photons in a radiative cascade and in principle any of the exciton or multi-exciton emission lines can be used to realize a single photon-emitter, given that the emission lines are well separated in energy. However, for most QD systems, the multi-exciton lines are difficult to completely resolve even at cryogenic temperatures, which limits the $g^2(0)$ values. To test our QD-NW system, we also performed anti-bunching experiments on the X_3 peak (along with the X and XX peaks) of NW S7_3.

In Fig 4.24 (a) is shown the μ-PL spectrum of NW S7_3 at 5 K and 5 μW CW excitation and the anti-bunching spectra for the X, XX and X_3 peaks (as confirmed with power dependent measurements, see Fig 4.17) are shown in Fig 4.24 (b), (c) and (d) respectively. The integration time was 10 min for all three peaks. Zero delay dip is clearly visible for all three peaks and therefore a single-photon emitter can be realized using any of the three X transitions at 5 K in this NW. It can also be seen that the width of the zero delay dip visibly decreases from X to XX to X_3. From the $g^2(t)$ fit, it can be seen that there is degradation of $g^2(0)$ for XX and X_3 peaks at least due to the fact that the two peaks are very close to each other and pollute the emission profile of each other.

It is shown in section 4.12.3 that the $g^2(0)$ obtained under pulsed mode excitation using the X line in this NW is less than 0.05 without any correction, a value lower than obtained under CW excitation.

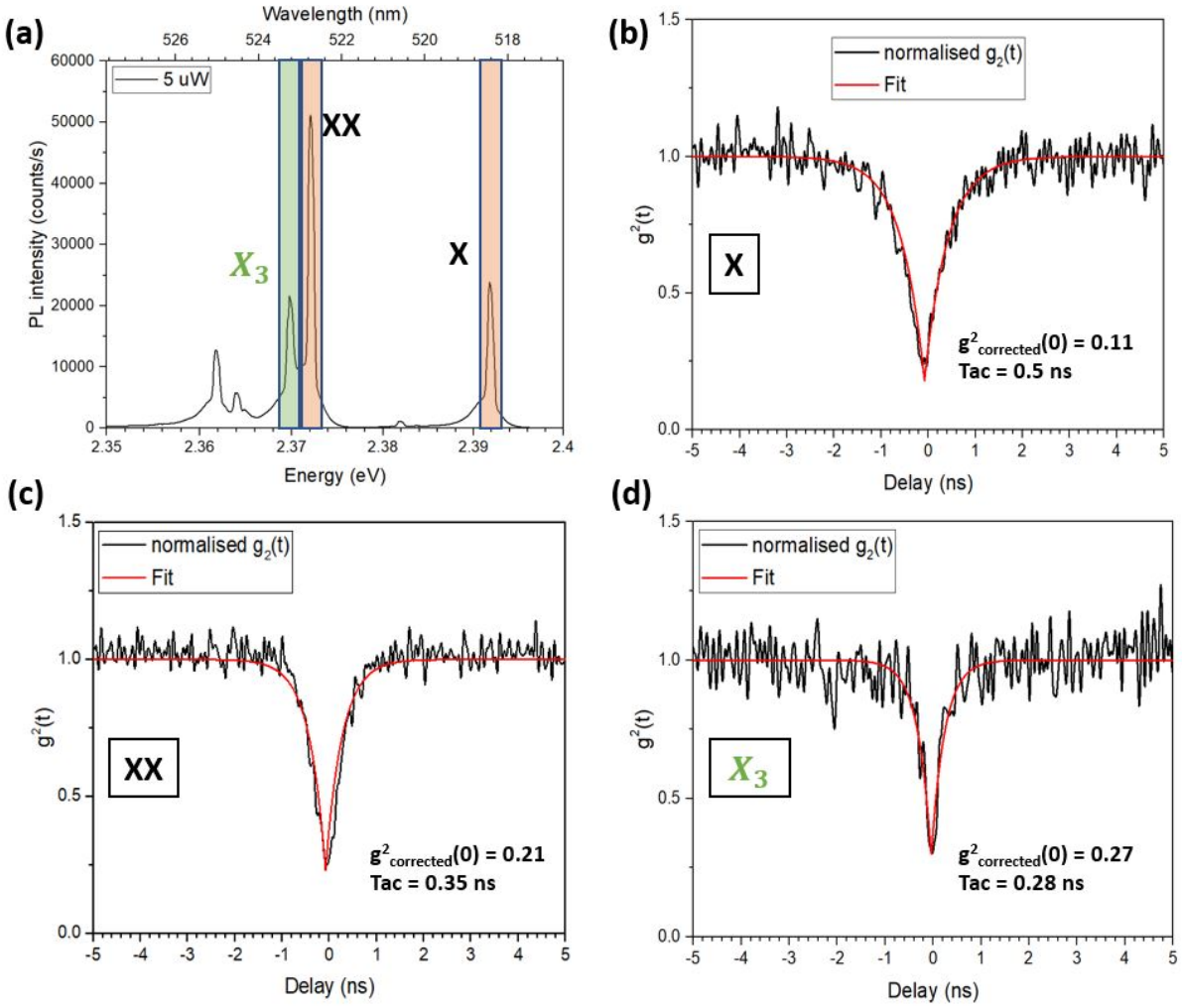

Figure 4.24: (a) μ-PL spectrum of S7_3 at 5 K and 5 μW CW excitation. The shaded region of 1.05 nm represents the spectral window in which $g^2(t)$ was obtained. The green shaded region corresponds to the spectral window for multi-X anti-bunching. Normalized $g^2(t)$ function obtained at 5 K and 5 μW CW excitation for (b) X, (c) XX and (d) multi-X peaks

A reduction in T_{ac} from X to XX to tri-exciton (X_3) is consistent with the fact that T_{ac} is related to the decay rate and pump rate of the excited state ($1/T_{ac} = 1/\tau_{decay} + 1/\tau_{pump}$). And an X_3 state has a higher probability to decay than a bi-exciton state, which in turn decays faster than the exciton state.

4.8.3 Antibunching on biexciton + charged exciton

So far we have seen anti-bunching on exciton, bi-exciton and multi-exciton states, but on single emission peaks. We have also seen that the anti-bunching characteristics can degrade if two peaks are very close to each other. Now, we will see that it is also possible to achieve anti-bunching on two different peaks together *i.e.* when the spectral window is big enough to accommodate two different peaks.

In Fig 4.25 (a) are shown μ-PL spectra of NW S10c_1 at 5 K and 10 μW CW excitation. The X

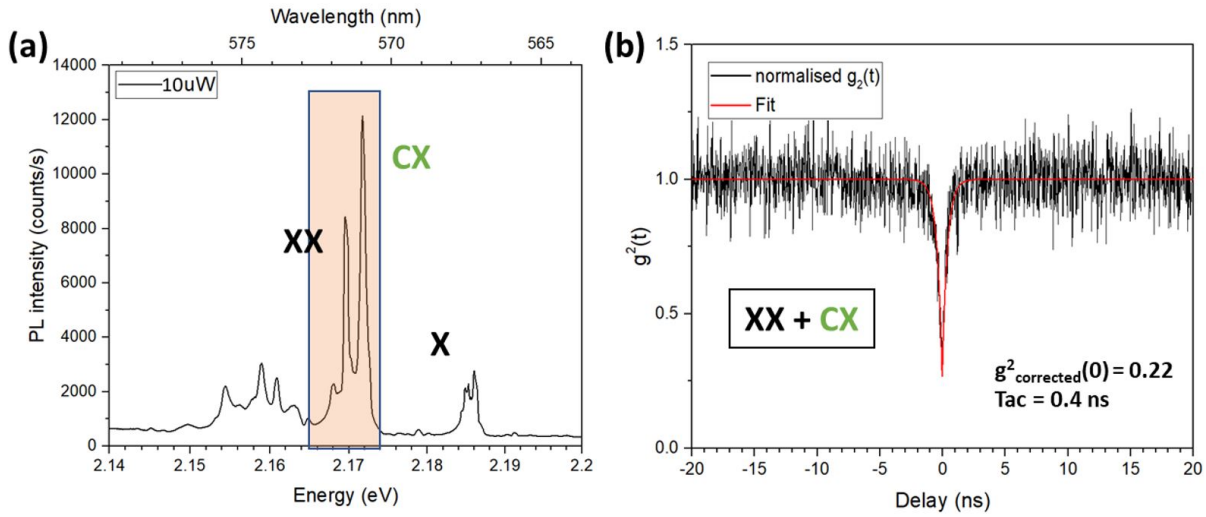

Figure 4.25: (a) μ-PL spectrum of NW S10c_1 at 5 K and 5 μW CW excitation and 10 μW CW excitation. (b) Normalised $g^2(t)$ function obtained at 5 K and 5 μW CW excitation for XX and CX together with a large spectral window of 2.5 nm.

and the XX transition peaks are at 2.184 eV (567.7 nm) and 2.169 eV (571.6 nm) as seen before. There is another peak "CX" at 2.171 eV (571.1 nm). We observed anti-bunching with a big spectral window of 2.5 nm (shaded region in Fig 4.25 (a)) to collect emission from both XX and CX peaks. The $g^2(t)$ spectrum for this case shown in Fig 4.25 (b) is similar to what is observed for a single-photon emitter with a sharp dip at zero delay. The experimental data was fitted using eq. (4.13) with a T_{ac} = 0.4 ns and a $g^2_{corrected}(0)$ = 0.22. This behavior is quite strange because usually emission of one peak hinders the single-photon capability of a nearby peak. But here we have collected photons coming from both XX and "CX" peaks and still observed anti-bunching.

To understand this peculiar behavior, we measured $g^2(t)$ on the XX (Fig 4.26 (b)) within a spectral window of 0.35 nm (shaded region in Fig 4.26 (a)). In addition to a sharp and anti-bunching feature at zero delay time, a slight bunching behavior at finite delay times is also observed. The experimental data is thus fitted with the following function:

$$g^2(t) = 1 - Ae^{\frac{-|t|}{T_{ac}}} + (A - 1 + g^2(0))e^{\frac{-|t|}{T_b}} \tag{4.15}$$

where T_{ac} and T_b gives the characteristic timescale of the observed anti-bunching and bunching, and A is one of the fitting parameters. To fit the bi-exciton $g^2(t)$, values used for A, $g^2(0)$, T_{ac} and T_b are 1.0, 0.22, 0.43 ns and 3.4 ns respectively.

Then, we also measured $g^2(t)$ on charged-exciton (CX) peak, Fig 4.26 (d). The measurements were carried out within a thin spectral window of 0.35 nm (shaded region in Fig 4.26 (c)). The experimental data was again fitted using eq. (4.15) and the values for A, $g^2(0)$, T_{ac} and T_b are 1.53, 0.37, 0.45 ns and 6.9 ns respectively. Although the characteristic anti-bunching times T_a are similar, the bunching timescale T_b for the charged-exciton peak is twice longer.

Now, we can explain this peculiar behavior with the neutral (XX) and charged states (CX) of the QD. A QD, at a given instant of time, is either in a charged state with an extra electron or hole, or is in

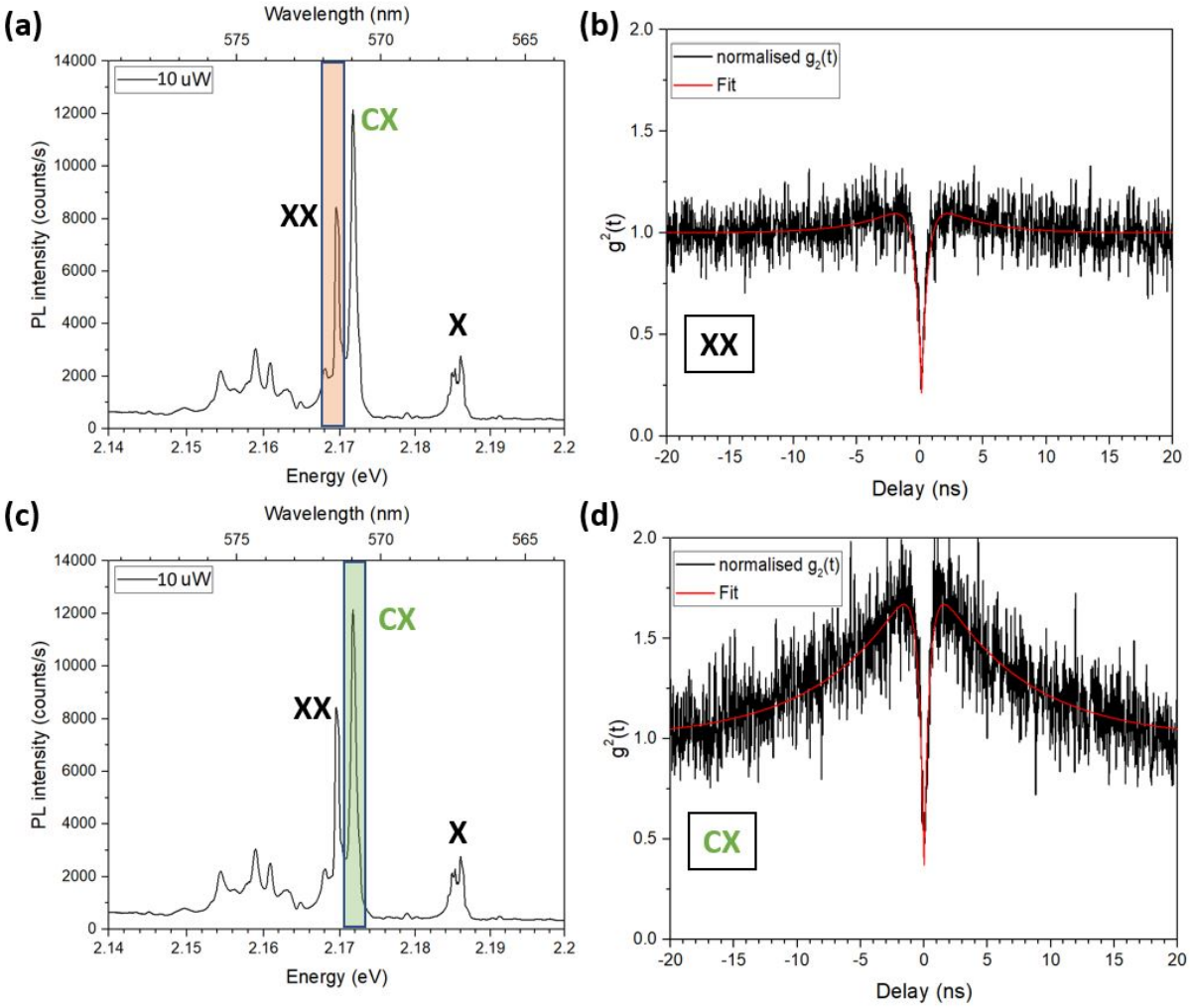

Figure 4.26: (a) μ-PL spectrum of NW S10c_1 at 5 K and 10 μW CW excitation. The shaded region is the spectral windown in which $g^2(t)$ measurements were performed and shown in (b). (c) μ-PL spectrum of NW S10c_1 with green shaded region as the spectral window for CX $g^2(t)$ measurements shown in (d). The spectral window in both cases is 0.35 nm.

neutral state with equal amounts of electrons and holes. The QD either emits a photon from XX $\rightarrow$ X (or X $\rightarrow$ 0) transition when it is in a neutral state or it emits a photon due to relaxation of a CXX (or CX) state. But cannot emit a XX (or X) and a CXX (or CX) at the same time.

Since, we observed sharp antibunching with for both XX and CX peaks together. This means that the peak-CX belong to a charged state of the QD and the QD hops from the charged state to neutral state and vice-versa. This is why we observe bunching effect close on XX and CX peaks when measured separately in Fig 4.25 (b) (see Fig 4.27 for visualization).

It is tempting to attribute time T_b to the timescale from the same transition, 3.4 ns for the bi-exciton and 6.9 ns for the charged-exciton. But, a complete set of rate equations are needed, helped with cross-correlation data on the bi-exciton and charged-exciton lines [116].

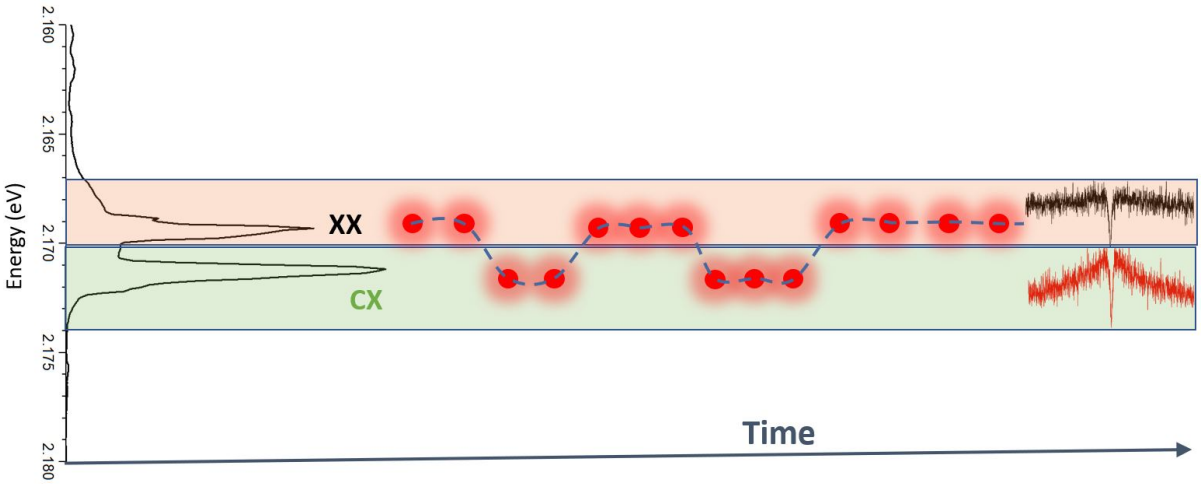

Figure 4.27: Scheme to show emission of photon from the neutral and charged state of the QD in NW S1c2. The QD hops between the XX and CX to emit a photon one by one.

4.9 Summary of Part A

So far, we have discussed characterization of QD-NW samples with a 10 s and 7 s QD insertion under continuous wave excitation. We saw that the surrounding of the QD affects the linewidth of its emission lines. A linewidth of about 0.21 meV was observed for the QD-NW of large radius. We discussed how with power dependence measurements, exciton and multi-exciton states can be identified. Then we saw how the emission peaks evolve with temperature: at high temperatures, the linewidth of the peaks is given mainly by the phonon sidebands and the bi-exciton peak dominates the exciton peak.

We also saw the effect of QD size on bi-exciton binding energy (B_{XX}). The B_{XX} is larger for the sample with a 7 s QD insertion (about 20 meV for all three NWs that were checked). And a blue shift in emission energy is also observed from 10 s to 7 s QD.

In agreement with a smaller size, anti-bunching with $g^2(0)$ values of about 0.1 were achieved at 5 K under continuous excitation using the X, XX and also multi-X peaks. In fact, we also observed anti-bunching on two peaks together (XX + charged-X), where the QD hops between the neutral and excited state.

For practical application, an on-demand fast single-photon emitter is required. And therefore, the QD-NWs were also characterized under pulsed mode excitation, reported in the following section.

Part B: Pulsed mode excitation

4.10 Power dependence with pulsed excitation

In this section, is shown typical behavior of exciton and bi-exciton peaks under pulsed excitation.

In Fig 4.28 (a) are shown μPL spectra of S10c_2 at different powers under pulsed excitation at 5 K with a 440 nm (2.818 eV) laser with a repetition time of 13.1 ns (76 MHz). At high powers besides peak Xa, Xb and XXa, XXb (which arise due to fine structure of X), other nearby peaks appear (XXc, XXd, Xc, *etc.*). The origin of these peaks in not clear, but they appear only at high powers (above 3 μW). At very high power of 8 and 9 μW, the intensity of Xa, Xb, XXa and XXb remains unchanged.

In Fig 4.28 (b), is plotted the integrated intensity of Xa+Xb and XXa+XXb as function of pulsed excitation power. There are error bars which comes from the measurement of very low excitation powers. It can be seen that above a certain power (5 μW here) the intensities saturate. Unlike in CW excitation mode where the bi-exciton state (or higher multi-X states) can be re-excited before a complete radiative cascade takes place with relaxation of exciton to empty the QD, in pulsed mode excitation, with each pulse a complete radiative cascade takes place to empty the QD and the bi-exciton is not re-excited since the next excitation pulse comes only after the QD is emptied [117]. This is true unless, the laser pulse repetition time is less than the QD decay time or if the QD is re-fed with carriers (such as from trap states) before the next laser pulse.

It can also be observed that the saturation intensity of the X is lower than the XX. This may be attributed to the fact that the X looses some of its intensity to dark-X, whereas dark-XX does not recombine. More generally, it suggests the presence of non-radiative channels.

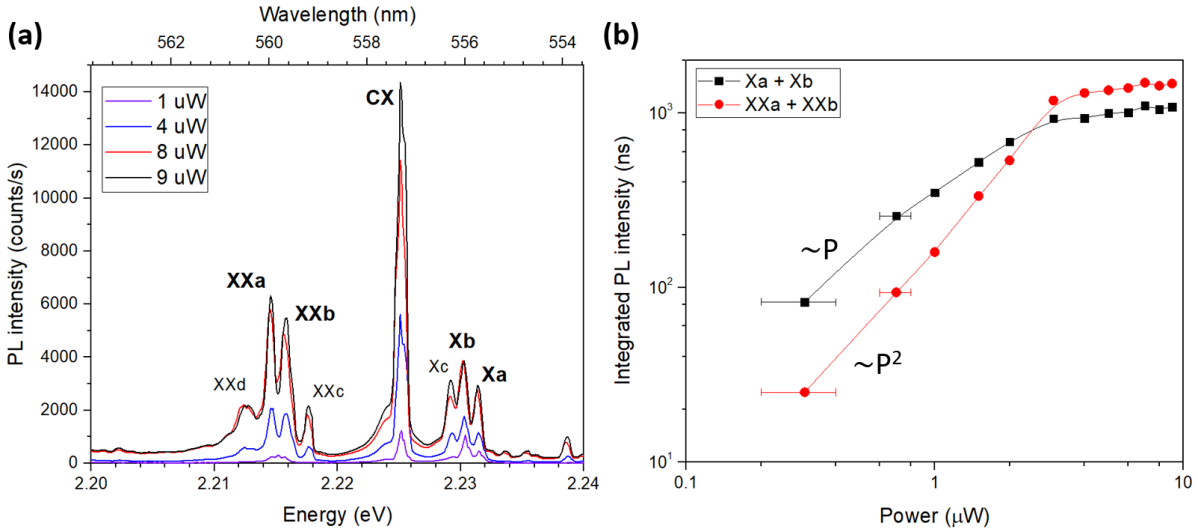

Figure 4.28: (a) μ-PL spectra of NW S10c_2 at 5 K and varying power with 440 nm pulsed excitation. (b) Integrated intensity as a function of power in pulsed mode excitation. The error bars at low powers comes from the measurement. The solid is just an eye guide.

4.11 Lifetime of excited states

Lifetime of an exciton (X) is an important parameter that tells us the QD maximum achievable emission rate for qubit manipulation.

In this section, the lifetime of X and XX states for NW S10a_1 is reported as a function of increasing excitation power and temperature using time-resolved spectroscopy described in section 1.4.3.2.

4.11.1 Signal and background

While performing time resolved measurements, we observed a large residual intensity of decay curves. Therefore, before extracting the lifetime from the decay spectra, it became important to separate the decay time signal from the background. In Fig 4.29 (b) is shown the PL intensity decay for exciton and bi-exciton at 5 K at an average pulsed excitation of 0.5 μW for a spectral window of 1.05 nm (4.5 meV). Its corresponding μ-PL spectra are represented in Fig 4.29 (a). The intensity is integrated over 10 min. Background intensity is taken at 570 nm (2.175 eV) where no emission peak is observed. Instrumental resolution is taken as 50 ps (0.05 ns) which is the response time of the fast APDs used here.

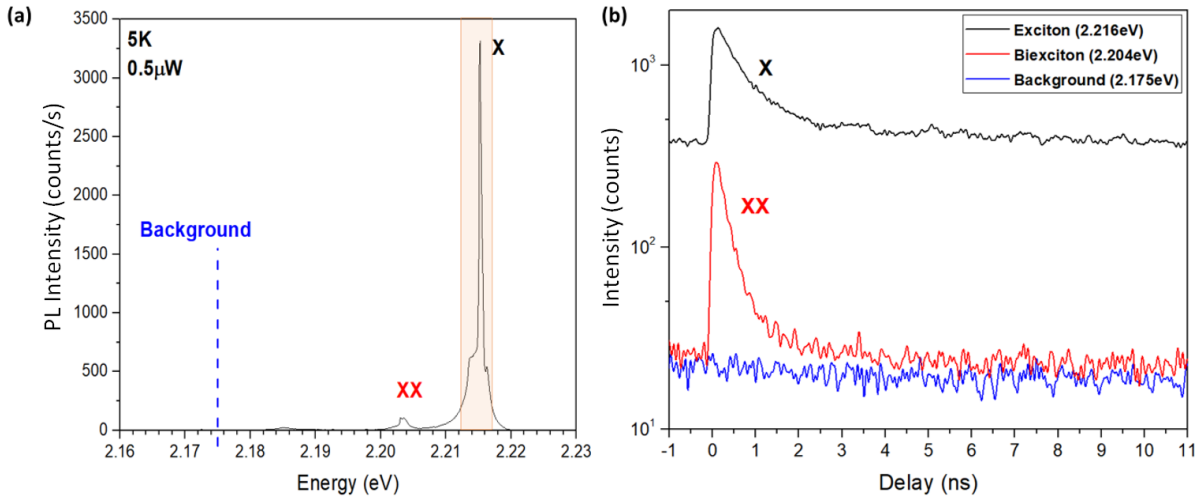

Figure 4.29: (a) μ-PL spectra of NW S10a_1 at 5 K and 0.5 μW pulsed excitation at 440 nm, 13.1 ns repetition rate. Shaded region presents the spectral window for decay measurements. Background was collected at 2.175 eV (570.1 nm) where no emission peak is observed. (b) Decay spectra under same conditions.

In Fig 4.29, the X decay intensity integrated within 0-11 ns time window is more than 15 times higher than the XX intensity and 25 times higher than the background integrated intensity. For both X and XX, the experimental signal does not decay completely to the level of the background within the laser repetition time (13.1 ns) and it appears that at least for X, along with a short decay time, a very long decay time exists with values much larger than the laser pulse repetition time.

Fig 4.30, shows the same decay time curve for X and XX, but with the experimental background subtracted from the experimental signal. Solid lines correspond to fits using exponential rise and decay functions. The decay part of the curve could not be fitted with a mono-exponential decay function. A multi-exponential decay function was thus used to fit the decay curve and the complete fitting function

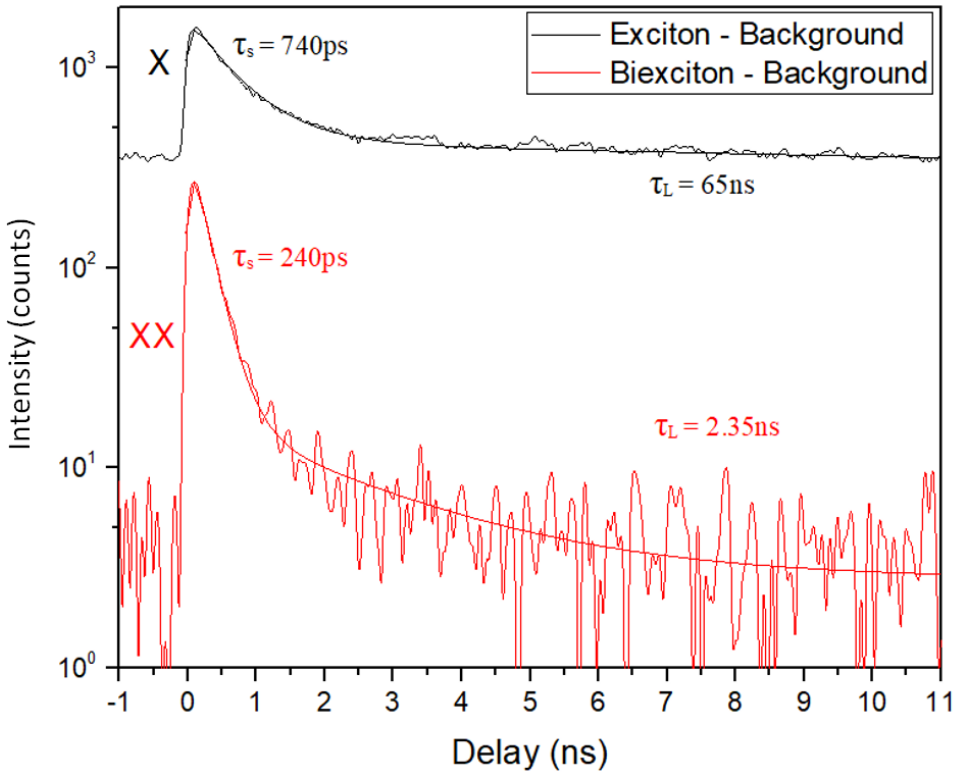

Figure 4.30: Decay signal for X and XX of S10a_1 after removal of background. The X and XX do not decay completely during the pulse repetition time. For both X and XX, a short and a long time component exist.

takes the form:

$$I(t) = -A_r e^{(-t/\tau_r)} + A_s e^{(-t/\tau_s)} + A_l e^{(-t/\tau_l)} + C \tag{4.16}$$

where, τ_r, τ_s, τ_l, A_r, A_s and A_l are fitting parameters. The first term provides the rise time (τ_r) which corresponds to the population of excited states with each laser pulse. The second and third term give a short decay time (τ_s) and a long decay time (τ_l). A_r, A_s and A_l acts as weights to the exponential rise and decay functions used here. C is the parameter that provides a constant baseline to the fitting function. The X decay curve could be fitted with zero values for C, while for XX, a non-zero positive value of C was required for a good fit. The non-zero C values are smaller than the background correction and may arise due to an underestimation of the background.

	τ_r (ns)	A_r	τ_s (ns)	A_s	τ_l (ns)	A_l	C
X	0.05±0.05	140	0.74±0.05	1340	65±5	420	0
XX	0.08±0.05	260	0.24±0.05	450	2.35±0.2	17	2.7±0.1

Table 4.5: Fitting parameters obtained after fitting of X and XX decay curves of S10a_1 in Fig 4.30 (b and c) with eq. (4.16)

The obtained fitting parameters are given in table 4.5. The τ_r for both X and XX for this excitation power (0.5 μW) is limited by the instrumental resolution of 50 ps.

For CdSe QDs, radiative lifetimes of X and XX, similar to the present values of τ_s, were reported earlier. Samir Bounouar *et al.* [11] reported a radiative lifetime of 0.5±0.05 ns and 0.3±0.05 ns for X and XX respectively in a CdSe QD in ZnSe NW. Similar lifetimes were also reported for X in CdSe SKQDs: 0.3 ns [118] and 0.38 ns [31]. Therefore, we tentatively attribute the τ_s for both the X and XX to their radiative lifetimes, where τ_s of XX is shorter than X. Long times τ_l of 65±5 and 2.35±0.2 ns are observed for X and XX respectively. For X, τ_l is much longer than the repetition time of the laser (13.1 ns).

4.11.2 Temperature dependence of lifetime

To investigate the origin of the very long decay time present both for exciton and bi-exciton of NW S10a_1, we performed time-resolved measurements for different temperatures. In Fig 4.31 (b) and (c) are shown temperature-dependent time-resolved decay curves for exciton and bi-exciton for four temperatures: 5, 30, 50, and 70 K at 3 μW average pulsed excitation for a spectral window of 1.05 nm (4.5 meV). The corresponding μ-PL plots are shown in Fig 4.31 (a). For the bi-exciton, at 50 K, the decay signal is very weak due to misalignment of laser and therefore it is not considered in the following discussion. For both exciton and bi-exciton, at low temperatures (5 and 30 K), the curve is clearly of a bi-exponential decay type. But with an increase in temperature, at 70 K, the curves shows more of a mono-exponential type behavior.

The solid lines represent the fit achieved using eq. (4.16). As we attributed the short time to the radiative lifetime of X (or XX), we kept the same value τ_s for all temperatures. τ_s was first extracted from the low power (0.5 μW) excitation decay curve. The obtained fitting parameters are given in table 4.6.

In table 4.6, I_r, I_s and I_l are the decay intensities integrated in the range of 0-11 ns separately for each of the exponential rise (τ_r) and two decay (τ_s and τ_l) functions respectively. Since the intensities and the decay times of all the curves are different, for comparison integrated intensities are more meaningful. It should be noted that for the long component of the decay curve, the integrated intensity I_l ($= \int_0^{13.1\,ns} A_l\, e^{(-t/\tau_l)} dt$) observed here is not coming from a single pulse excitation. For τ_l longer than the repetition time of the laser, A_l (and therefore I_l) has contributions from the long-time component of the decay curve coming from previous laser pulses and can be expressed as:

$$A_l = A_l^* \left(1 + e^{\frac{-T_0}{\tau_l}} + e^{\frac{-2T_0}{\tau_l}} + e^{\frac{-3T_0}{\tau_l}} + ...\right) = \frac{A_l^*}{1 - e^{\frac{-T_0}{\tau_l}}} \tag{4.17}$$

where T_0 is the repetition time of the laser (13.1ns) and A_l^* is the real weight of the long component of the decay curve without any contribution from previous pulses. Derived I_l^* is mentioned in table 4.6. I_l^* would have been observed experimentally had the long component decayed completely within the laser repetition rate.

The signal (I_r, I_s and I_l^*) in general, can be seen to decrease with increasing temperature. The τ_r values for all temperatures for both X and XX are within the instrumental limit (50 ps), except for X at 70 K where it increases to 0.32 ns. Also, the ratio $I_l^*/(I_s + I_l^*)$ (which gives the relative contribution of long-time component in the decay curve) increases with temperature (see table 4.6).

A long decay time of X has been linked to the presence of a dark-X [119], [19]. However, we observe long decay time for both X and XX and a dark state does not exist for the XX. We will come back to the

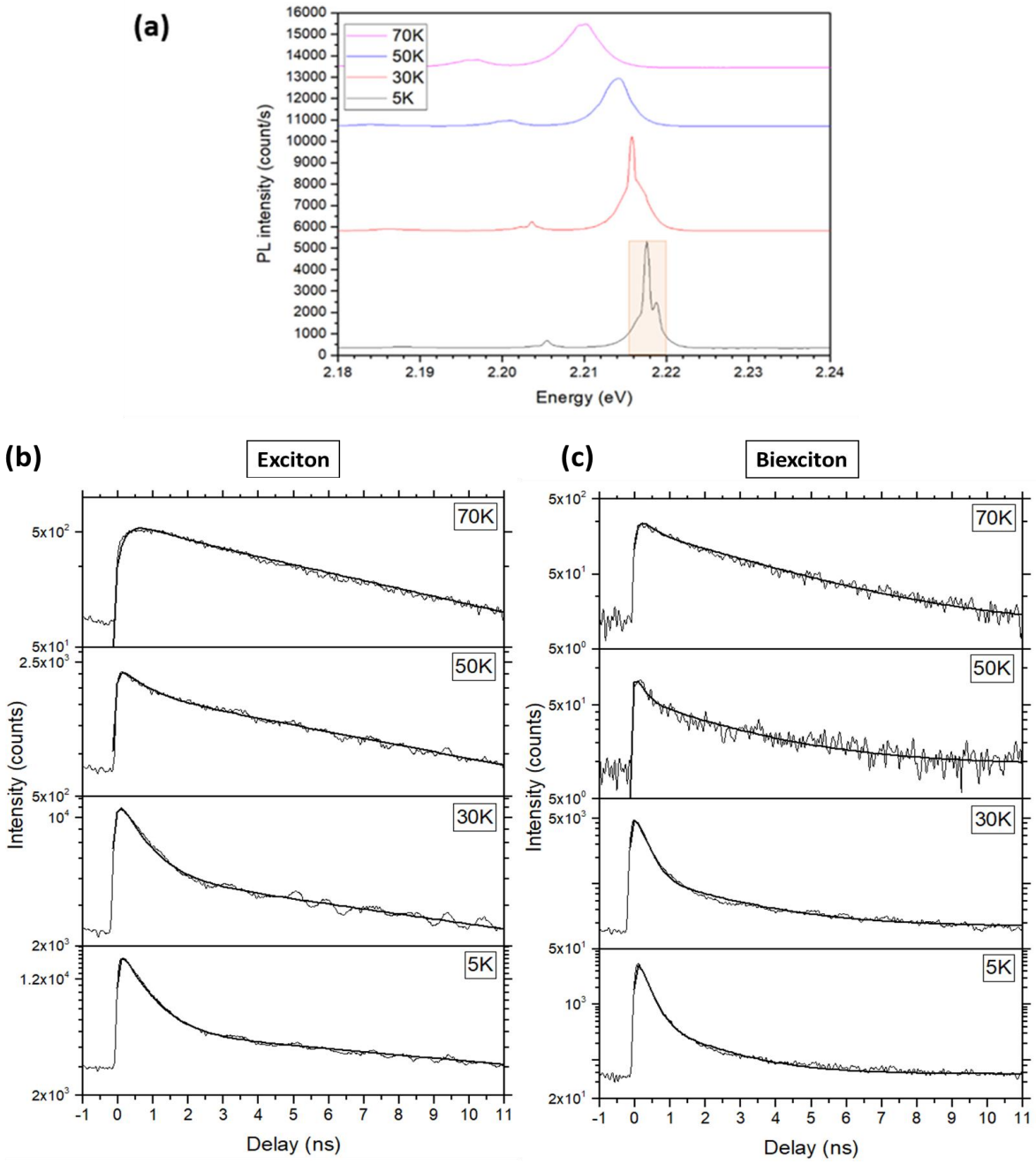

Figure 4.31: (a) μ-PL spectra spectra of S10a_1 at 3 μW at different temperatures. The yellow shaded region presents the spectral window for decay measurements for the X and the XX line. Spectral window is 1.05 nm (4.5 meV) and is fixed for all temperatures for both X and XX. Decay spectra for (b) X and (c) XX. The solid lines represent fits using a rise and two decay (short and long) exponential functions.

	Temp. (K)	τ_r (ns)	τ_s (ns)	τ_l (ns)	C	I_r	I_s	I_l	I_l^*	$I_l^*/(I_s + I_l^*)$
X	5	0.08±0.05	0.74±0.05	21±2	0	-585	11150	46800	21720	0.66
	30	0.11±0.05	0.74±0.05	16±2	0	-230	6080	39235	21930	0.78
	50	0.1±0.05	0.74±0.05	12.5±1	0	-40	500	12885	8365	0.94
	70	0.32±0.05	0.74±0.05	6.3±0.5	0	-160	150	3010	2630	0.95
XX	5	0.08±0.05	0.24±0.05	1.50±0.2	56±2	-540	2360	760	760	0.25
	30	0.12±0.05	0.24±0.05	2.2±0.2	110±5	-465	1875	1310	1310	0.41
	70	0.15±0.05	0.24±0.05	2.95±0.2	10±1	-60	90	560	560	0.86

Table 4.6: Fitting parameters obtained after fitting of X and XX decay curves of S10a_1 in Fig 4.31 (b and c) with eq. (4.16)

origin of these slow components in section 4.13.

4.11.3 Power dependence of lifetime

To investigate further the origins of the long decay time present for both exciton and bi-exciton, we will now look at the time-resolved measurements for different powers, at 5 K.

In Fig 4.32 (b) and (c) are shown, decay curves for the X and XX lines of NW S10a_1 at 5K for three different excitation powers: low (0.5 μW), intermediate (3 μW), and high (13 μW). Their corresponding μ-PL plots are shown in Fig 4.32 (a). The solid lines represent the fit achieved using eq. (4.17). Again, the radiative time τ_s obtained from low power (0.5 μW) was fixed for both X and XX. Table 4.7 summarizes the rise and decay times obtained from the fit.

For the X, for high powers, very long τ_l are observed (60±5 ns for 13 μW) which decrease with increasing power. For XX, a decrease in τ_l is also observed from 0.5 to 3 μW, while a change from 3 to 13 μW is within the error bars. Similarly, at low powers (0.5 and 3 μW), the rise time τ_r for exciton is limited by the APDs, but a clear increase is observed at 13 μW (τ_r = 0.27±0.05 ns). For bi-exciton, change in τ_r is limited by APDs for all powers.

At 13 μW, τ_r for X is of the order of τ_s for XX (0.24±0.05 ns). We thus ascribe it to the feeding of the X from XX at high powers, while it's intensity is too small to be detected safely at lower powers.

The τ_l decreases while $I_l^*/(I_s + I_l^*)$ increases with increasing power for both exciton and bi-exciton. This shows that the mechanism involved with the re-population of the exciton and bi-exciton states (and hence the slow component) becomes faster and more efficient with increasing excitation power.

While the presence of a long time in exciton could be explained with the dark-X, it does not explain the dark-exciton feeding becoming more efficient and faster with increasing power, unless the QD-NW is heated at high excitation powers. And a dark state does not exist for the bi-exciton. It is clear that the dark-state cannot be treated as the only source responsible for the nanosecond-long decay times. To gain further insight, we also performed anti-bunching measurements, reported in the following section. The origins of the slow component are then discussed in section 4.13.

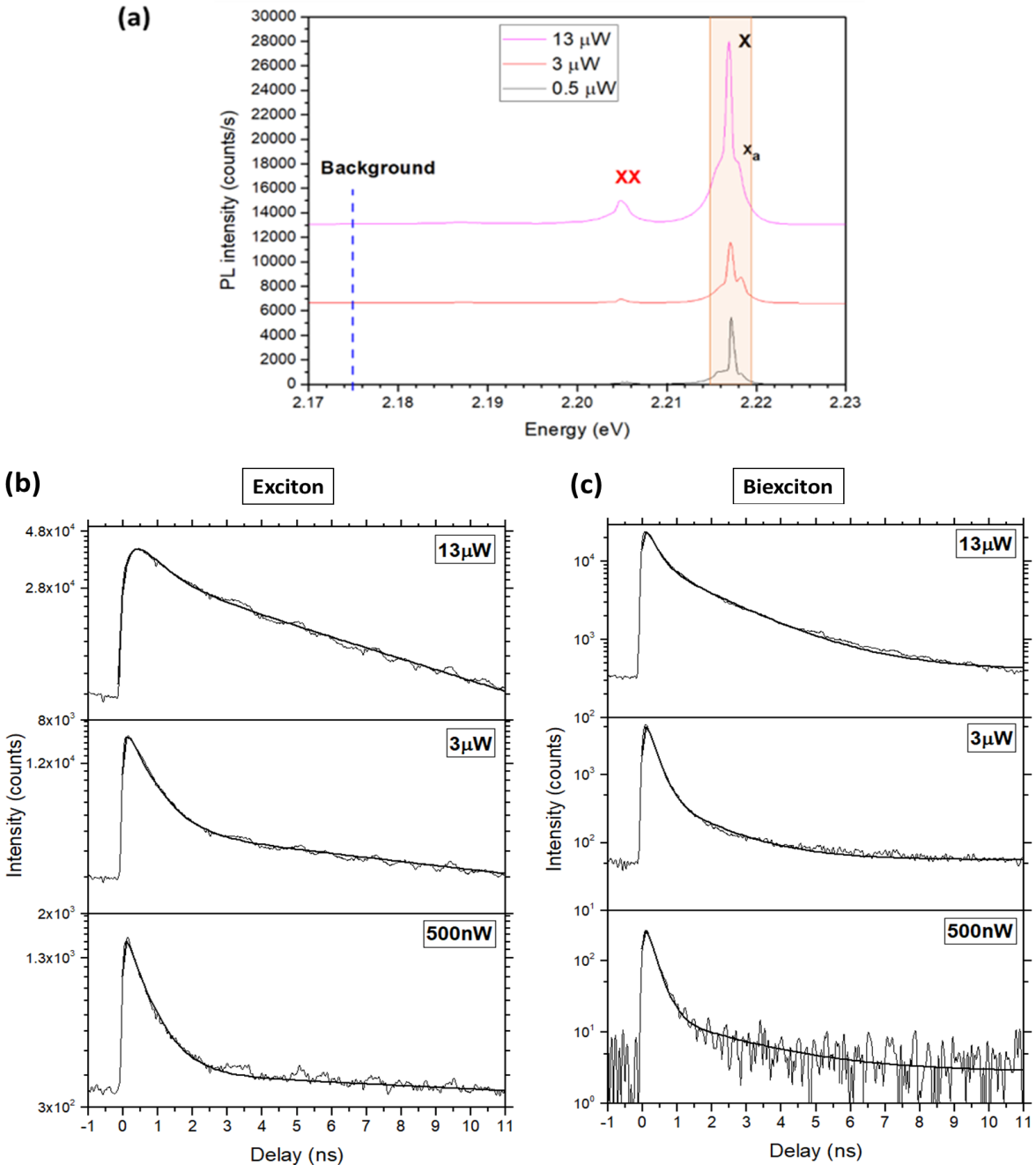

Figure 4.32: (a) μ-PL spectra of NW S10a_1 at 5 K for different excitation powers under pulsed excitation. The shaded region presents the spectral window for decay measurements (1.05 nm/4.5meV). Decay spectra for (b) X and (c) XX of S10a_1 for different powers at 5 K. The solid lines represent fits using a rise and two decay (short and long) exponential functions.

	Power (μW)	τ_r (ns)	τ_s (ns)	τ_l (ns)	C	I_r	I_s	I_l	I_l^*	$I_l^*/(I_s+I_l^*)$
X	0.5	0.06±0.05	0.74±0.05	60±5	0	-30	970	4270	840	0.46
	3	0.08±0.05	0.74±0.05	21±2	0	-585	11150	46800	38000	0.77
	13	0.27±0.05	0.74±0.05	9.7±1	0	-8740	20960	215670	159790	0.88
XX	0.5	0.08±0.05	0.24±0.05	2.35±0.2	2.7±0.5	-25	120	40	40	0.25
	3	0.08±0.05	0.24±0.05	1.5±0.2	56±2	-540	2360	760	760	0.25
	13	0.1±0.05	0.24±0.05	1.9±0.2	405±10	-2590	2960	19120	19045	0.86

Table 4.7: Fitting parameters obtained after fitting of X and XX decay curves in Fig 4.32 (b and c) with eq. (4.17).

4.12 Anti-bunching under pulsed excitation

It's important to evaluate the anti-bunching properties of a single-photon emitter using pulsed excitation as it tests if the source is deterministic and emits single-photons on demand. In this section is shown anti-bunching capabilities of our QD-NWs under pulsed excitation. At the same time is shown that the origin of the slow component in the decay curve is not the dark state.

4.12.1 Effect of a long decay time

In section 4.8.1 we saw anti-bunching on X of NW S10a_1 from sample S10a with CW excitation. In this section, we discuss how a long decay time affects the anti-bunching measurements on the same NW and how it is revealed under pulsed mode excitation.

In Fig 4.33 is shown an example of how the $g^2(t)$ curve usually looks like for pulsed excitation where the absence of zero-delay peak confirms single-photon emission. In Fig 4.34 is shown the $g^2(t)$ measurement for the X and XX line under pulsed excitation at 5 K for a spectral window of 4.5 meV (1.05 nm) of NW S10a_1.

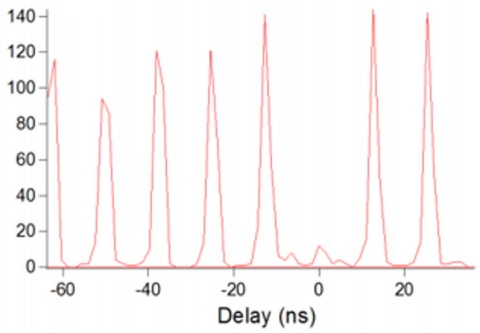

Figure 4.33: General anti-bunching histogram for pulsed mode excitation [19].

This unfamiliar $g^2(t)$ curve is observed for both the exciton and the bi-exciton. The peaks at ±13.1 ns delay correspond to detection of photons induced by two different laser pulses. For the exciton, instead of an absence of a zero-delay peak, we observed a narrow (FWHM=0.6 ns) dip at zero delay. Also, a strong "offset" (or constant component at delay time far away from zero) of the measured correlation is observed. This offset is not due to background as the zero-delay dip is much below the offset. For the bi-exciton, within the order of 5 ns, increase (bunching) of correlation is observed with a sharp dip at the zero-delay. An offset of the measured correlation is also observed for bi-exciton, although not as strong

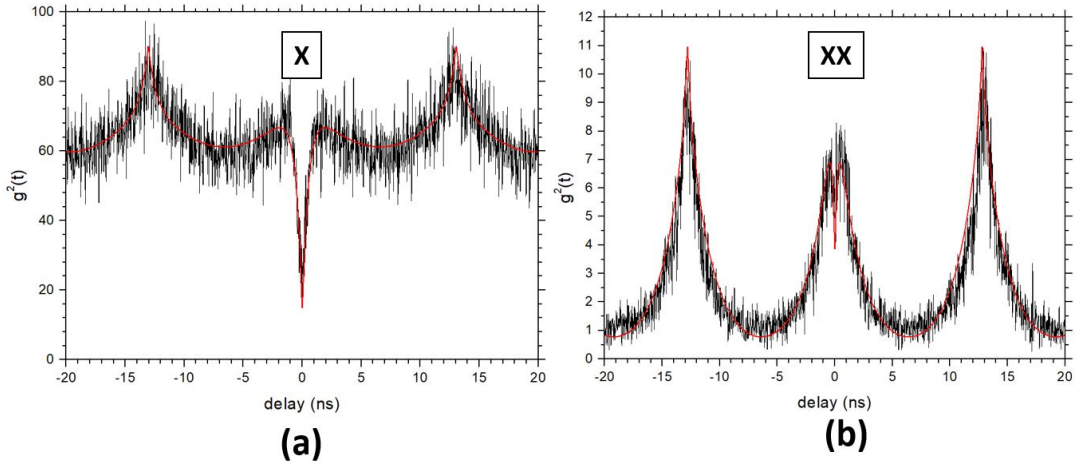

Figure 4.34: $g^2(t)$ correlation measured at 5 K and 13 μW 440 nm pulsed excitation on (X) and (XX) of NW S10a_1. Red solid lines are fit obtained with eq. (4.22). The excitation power and the integration time for both X and XX was 13 μW and 20 min respectively.

as exciton.

4.12.2 Fitting the $g^2(t)$ curves

As we have seen in the previous section, the exciton and the bi-exciton have a long decay time, and for the exciton it is longer than the laser repetition time. These measured $g^2(t)$ curves for exciton and bi-exciton under pulsed excitation seems to have contributions of both (ideal) pulsed and CW $g^2(t)$ curves. To understand this peculiar anti-bunching behavior, we will first try to fit the high order peaks corresponding to the laser repetition rate using a decay function with a short ($\tau'_s < 1$ ns) and long ($\tau'_l > 1$ ns) decay time, without introducing single photon behavior.
A single exponentially decaying pulse symmetrized around the origin can be expressed as:

$$F_1(t, \tau_a) = \exp \frac{-|t|}{\tau_a} \tag{4.18}$$

where τ_a is the decay time of the pulse. In Fig 4.35 (a) is plotted expression $F_1(t, \tau_a)$ with a τ_a of 0.5, 3, 5 and 10 ns. For τ_a of 5 and 10 ns, the tail of the pulse extends appreciably beyond the ±13.1 ns time. Now the expression for the above decay signal repeated for the repetition time of the laser (T_0=13.1 ns) is given as:

$$F_2(t, \tau_a) = \sum_{p=-\infty}^{+\infty} F_1(t - pT_0, \tau_a) \tag{4.19}$$

In Fig 4.35 (b) is plotted expression $F_2(t, \tau_a)$ for a short decay time *i.e.* $\tau_a = \tau'_s = 0.5$ ns and a long decay time *i.e* $\tau_a = \tau'_l = 5$ and 100 ns. For τ'_s of 0.5 ns, the pulse signal decays before the arrival of a second pulse. But for τ'_l of 5 ns, the tail of the pulse contributes to the signal of the following pulse. If the τ_a is very long (100 ns), eventually a straight horizontal line signal is observed.

The usual anti-bunching feature for a $g^2(t)$ curve under pulsed excitation is the absence of a peak at zero delay (see Fig 4.33) with a decay time much shorter than T_0. The signal in expression $F_2(t,\tau'_s)$ with amplitude A'_s and with the peak at zero delay suppressed is therefore given by the following expression:

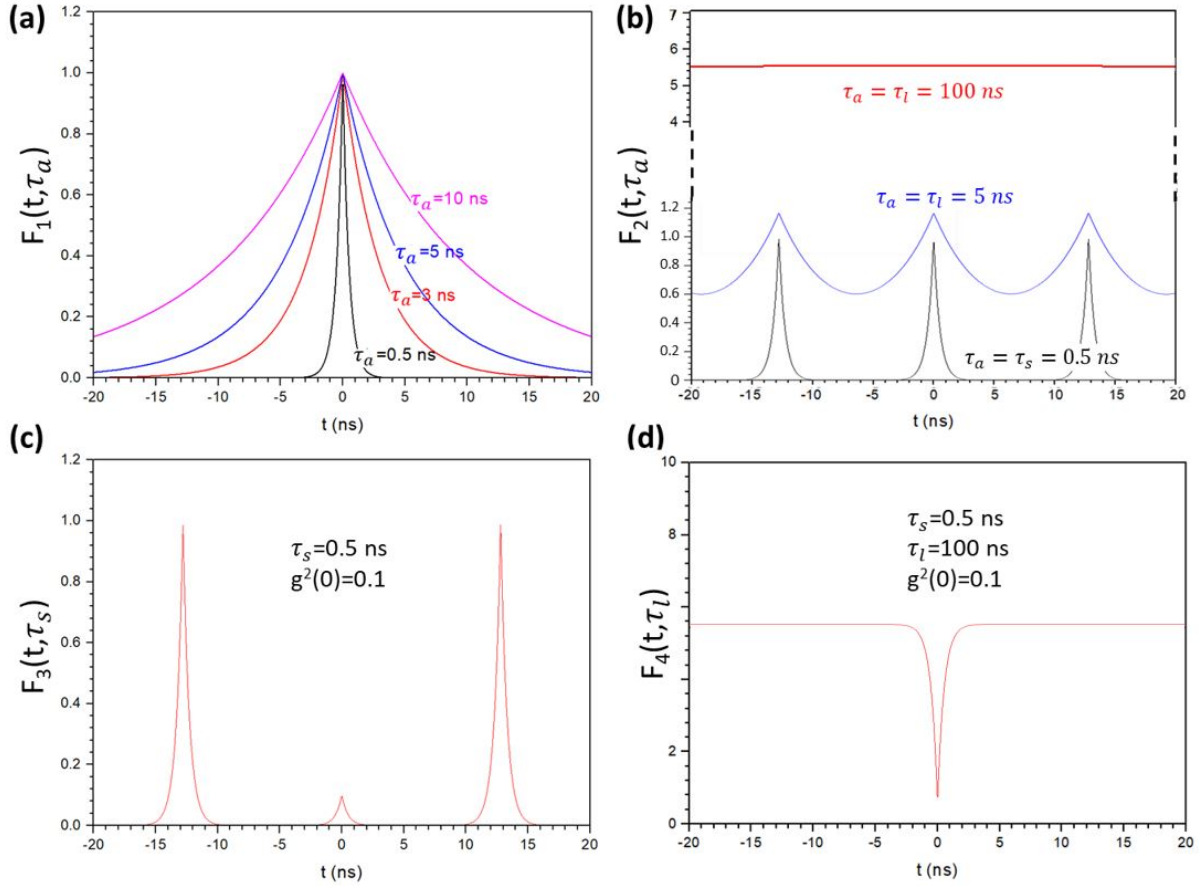

Figure 4.35: (a) Expression F_1 plotted for different τ_a representing a single pulse signal. (b) Expression F_2 single pulse signal repeated for repetition time of laser for τ_a of 0.5, 5 and 100 ns. (c) Expression F_3 for a short decay time of 0.5 ns representing a usually observed $g^2(t)$ curve under pulsed excitation. (d) Expression F_4 for a very long decay time of 100 ns representing a usually observed $g^2(t)$ curve under CW excitation.

$$F_3(t,\tau_s') = A_s' \left[F_2(t,\tau_s') - hF_1(t,\tau_s')\right] \tag{4.20}$$

where $h = 1 - g^2(0)$. In Fig 4.35 (c) is plotted expression $F_3(t,\tau_s')$ with a τ_s' of 0.5 ns and $g^2(0)$ value of 0.1, and resembles an anti-bunching curve usually observed under pulsed excitation, similar to in Fig 4.33.

For very long $\tau_l = 100$ ns values where signal $F_2(t,\tau_l')$ is a straight horizontal line, a dip in the signal at zero delay is similar to a $g^2(t)$ curve under CW excitation and can be expressed as follows:

$$F_4(t,\tau_l') = A_l'[F_2(t,\tau_l')][1 - gF_1(t,\tau_s')] \tag{4.21}$$

In Fig 4.35 (d) is shown signal $F_4(t,\tau_l')$ for $\tau_l' = 100$ ns and the dip represented by $\tau_s' = 0.5$ ns and $g^2(0) = 0.1$. Now the expression to describe the $g^2(t)$ comprising of a short and long decay time along with a single-photon behavior can be given as:

$$F_5(t) = F_3(t, \tau'_s) + F_4(t, \tau'_l) \tag{4.22}$$

In Fig 4.36 is the plotted expression $F_5(t)$ for fixed τ'_s = 0.1 ns, A'_s = 1, A'_l = 10 and $g^2(0)$ = 0.9 but varying τ'_l from 0.1 to 100 ns. For, τ'_l=0.1 ns, the signal behaves like a normal $g^2(t)$ curve under pulsed excitation. τ'_l=1 ns represent an intermediate case where the high order peaks corresponding to $\pm T_0$ are relatively broader and an increase of signal within the order of a few ns is observed with a sharp dip at zero-time. Also, an offset of the total signal is observed. For τ'_l=10 ns, the high order peaks are much broader and start to overlap and this creates and even higher offset of the total signal. But the single-photon behavior is still observed at zero-time with a sharp dip. τ'_l=100 ns represent an extreme case where the high order peak broadening is strong enough to appear as a straight line. But the single-photon dip at zero-time is still strong. The curve is similar to an anti-bunching curve observed under CW excitation.

We used the expression in eq. (4.22) to fit the auto-correlation curves for the exciton and the bi-exciton of NW S10a_1 in Fig 4.34 (red solid lines). The $g^2(t)$ curve for the exciton be fitted with values of τ'_s = 0.65±0.05 ns similar to the ones obtained from the fit of the decay curve (0.74±0.05 ns) at the same excitation power of 13 μW. Also, τ'_l = 9.7 ns was kept exactly the same as obtained from fit of decay curve. Values of A'_s, A'_l and $g^2(0)$ obtained were 15±2, 45±5 and 0.14±0.02 respectively. The $g^2(0)$ value of 0.14±0.02 is very similar to $g^2_{corrected}(0)$ = 0.19 obtained under CW excitation for X.

For the bi-exciton, the best fit was obtained with τ'_s = 0.24±0.02 ns and τ'_l = 2±0.02 ns values taken similar to that from the decay curve at the same power of 13 μW. The values of A'_s, A'_l and the $g^2(0)$ for the bi-exciton were 1.5±0.2, 9.5±0.5 and 0.31±0.02 respectively.

The $g^2(t)$ curve of the exciton is similar to intermediate case of τ'_l = 10 ns of Fig 4.36, whereas the XX $g^2(t)$ curve is similar to the τ'_l = 1 ns case.

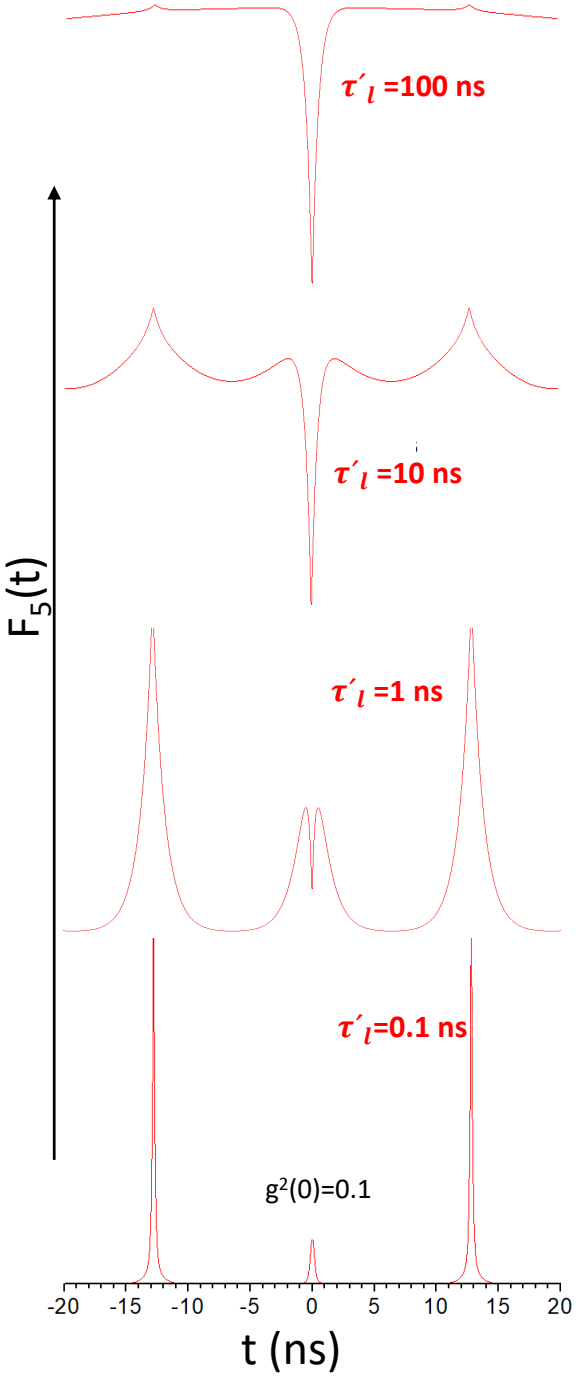

Figure 4.36: Expression F_5 in eq. (4.22) plotted for different τ'_l of 0.1, 1, 10 and 100 ns for fixed τ'_s = 0.1 ns, A'_s = 1, A'_l = 10 and $g^2(0)$ = 0.9.

For the X here, the τ_l' value is large and therefore the correlation peaks are even broader which overlap and create a big offset in correlation. But the anti-bunching feature is strong with a sharp dip.

NW S10c_2

We observed similar anti-bunching curves for other NWs. For example, from sample S10c, we performed anti-bunching measurements on the X_b and XX_b lines of NW S10c_2 (see Fig 4.28 (a)) with a spectral window of 1.05 nm. In Fig 4.37 are shown the corresponding $g^2(t)$ curves.

The correlation curve for the X_b looks similar to the correlation function of the exciton of NW S10a_1, but with high order peaks which are comparatively less broad and a zero-delay dip which is less intense. The XX_b curve is also similar to that of the bi-exciton of NW S10a_1, but with a zero-delay dip that looks more intense. Clearly, a long time also exists for NW S10c_2. The red solid lines represents the fits obtained using eq. (4.22). The obtained values of τ_s', τ_l', A_s', A_l' and $g^2(0)$ for the X and XX are given in table 4.8.

The obtained τ_s' for both X_b (0.75±0.05 ns) and XX_b (0.35±0.05 ns) are similar to that for NW S10a_1. But the τ_l' and A_l' are less than for NW S10a_1, where A_l' is twice less. The effect of long time on the correlation curves is less than for NW S10a_1.

Clearly, a long decay time affects the anti-bunching measurement in the condition of pulsed excitation. And CW excitation characterization are not enough to evaluate the characteristics of a single-photon emitter. Before we discuss the origins of this long time in section 4.13, in the following section, is reported the case of anti-bunching measurements in a sample where the long time contribution is low.

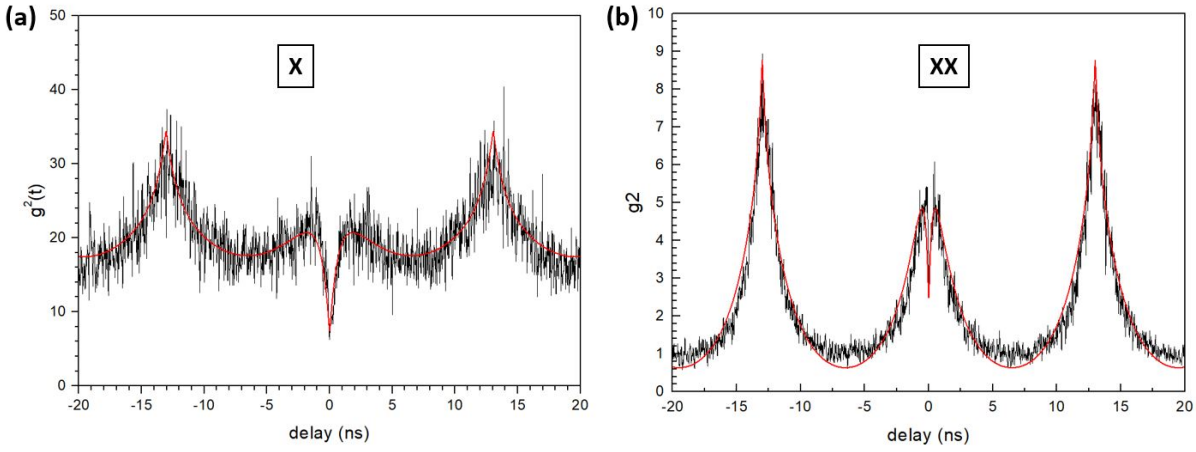

Figure 4.37: $g^2(t)$ correlation measured at 5 K and 10 μW 440 nm pulsed excitation on (X_b) and (XX_b) of NW S10c_2. Red solid lines are fit obtained with eq. (4.22). The integration time for both X and XX was 20 min each.

4.12.3 Ideal anti-bunching behavior

For NWs in sample S7 (most optimized sample with a 7 s QD), the effect of a long decay time on anti-bunching curves was observed to be less. As an example, characterization of NW S7_3 at 5 K under

NW	S10a_1		S10c_2		S7_3	
	X (13 µW)	XX (13 µW)	X (10 µW)	XX (10 µW)	X (1 µW)	XX (20 µW)
τ'_s	0.65±0.05	0.24±0.05	0.75±0.05	0.35±0.05	0.6±0.05	0.5±0.05
τ'_l	9.7±0.5	2±0.02	6.7±0.5	2.1±0.5	30±5	6.8±0.5
A'_s	15±2	1.5±0.2	8±0.5	1.8±0.5	89±5	15±2
A'_l	45±5	9.5±0.5	20±1	7±0.1	0.89±0.05	0.23±5
$g^2(0)$	0.14±0.02	0.31±0.02	0.2±0.02	0.25±0.02	0.02±0.005	0.1±0.02

Table 4.8: Fitting parameters obtained after fitting of $g^2(t)$ curves of the exciton and the bi-exciton in NW S10a_1, S10c_2 and S7_3 in Fig 4.34, 4.37 and 4.39 respectively using eq. (4.22).

pulsed excitation is presented in this section.

First, decay time measurements were performed at 5 K for a low (1 μW) and high power (18 μW). In Fig 4.38 (a), is shown μ-PL spectrum of NW S7_3 at 18 μW and 5 K. At 18 μW, the exciton and bi-exciton are already saturated in intensity. The decay measurements were performed on the exciton, bi-exciton and the tri-exciton (X_3) peaks with spectral window of 1.05 nm (shown as shaded region, see Fig 4.38 (b)).

Clearly, the slope of the decay curve decreases from X to XX to X_3. In Fig 4.38 (c) and (d) are shown decay curves for the X and XX respectively at 1 μW and again for 18 μW for comparison. The decay curves are fitted with a rise, short and long decay function. The fitting values are given in table 4.9. For the exciton, a constant baseline of 300 count was added to both decay curves to improve the fit. Since the baseline is similar for both powers, it could be present due to background from a nearby peak.

The short/radiative time (τ_s) decreases from X to XX to X_3. Indeed, higher-exciton states have higher probability to decay.

The τ_s of the XX is similar to the rise time (τ_r) of the X and is within the error bars. Similarly, the τ_s of X_3 is similar to τ_r of XX. This is likely due to the feeding of the X by the XX recombination and a possible feeding of the XX by the X_3 recombination.

It can also be observed that τ_s decreases from NW S10a_1 (10 s QD) to S7_3 (7 s QD). We expect a decrease in height from 10 s to 7 s QD which implies a stronger overlap, hence an increase in probability of exciton recombination for 7 s QD , and therefore a decrease in τ_s.

The long time (τ_l) is similar for both powers for both X and XX. Even though the I_l^* increases with power, similar to NW S10c_2, the long time contribution to the total decay curve ($I_l^*/(I_s + I_l^*)$) is already very low at about 5 and 7 % at 1 and 18 μW respectively. For the exciton X therefore, the long time contribution is almost negligible.

Next, anti-bunching measurements were performed at 5 K and 20 μW excitation with a 440 nm pulse laser for the X and XX peaks within the same spectral window of 1.05 nm, see Fig 4.39. Unlike NW S101_1, the $g^2(t)$ spectrum is similar to what is usually expected *i.e.* presence of high order peaks corresponding (repetition time of the laser) along with a quasi-absence of a zero-delay peak. For both the exciton and the bi-exciton, the high order peaks are narrow with no visible peak at zero-delay for the exciton and a very small bunching peak for the bi-exciton. Such a behavior is expected for the exciton in this NW after we saw that the long time has little contribution in the total decay of the exciton.

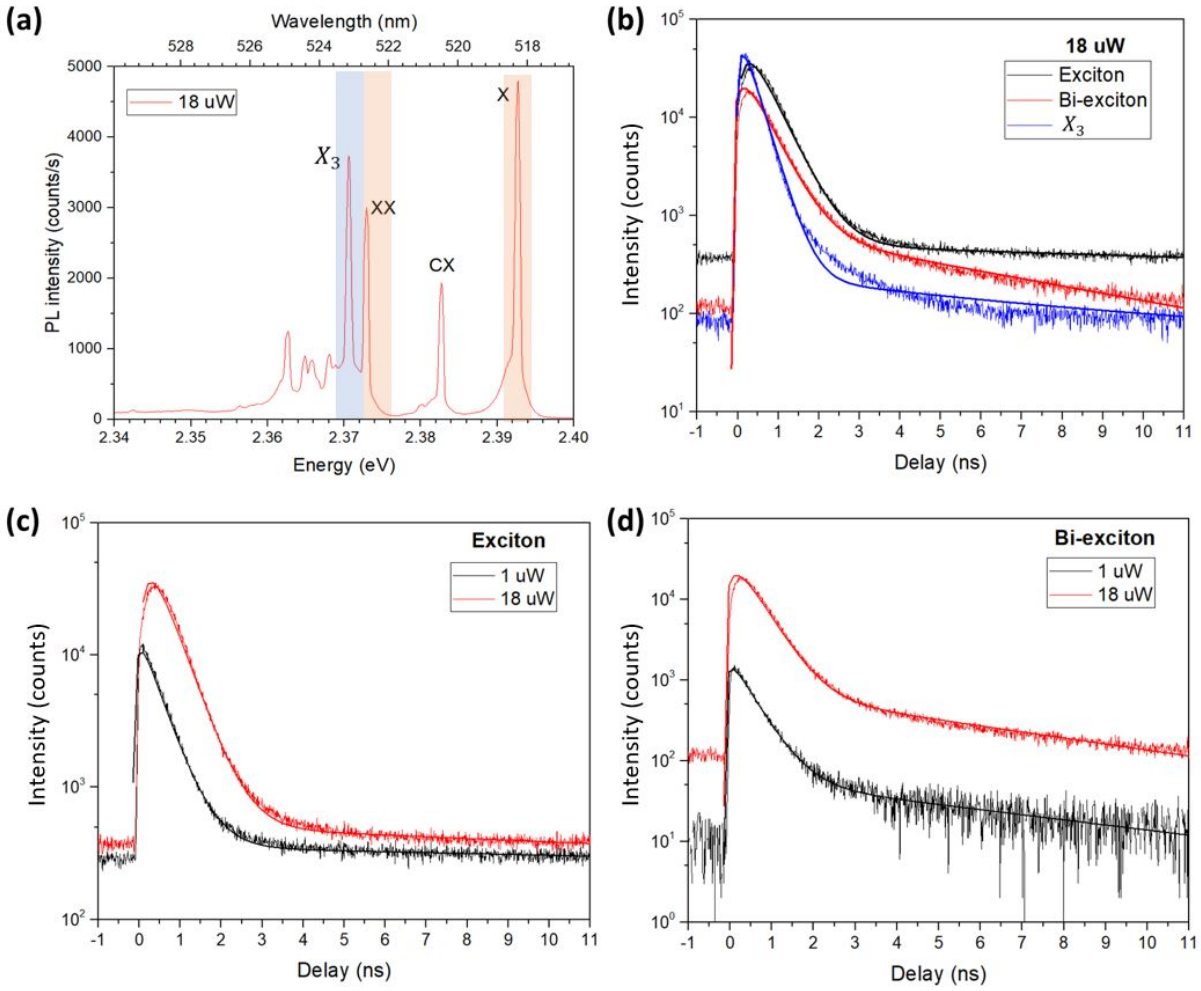

Figure 4.38: (a) μPL spectrum of NW S7_3 at 5 K and 18 μW 440 nm pulsed excitation. Decay plots for (b) X, XX and X_3 at 18 μW of NW S7_3. Decay plots of (c) X and (d) XX of NW S7_3 for 1 and 18 μW power. The solid lines represent fits using a rise and two decay (short and long) exponential functions and the table where are the results . The yellow shaded region presents the spectral window for decay measurements (1.05 nm/4.5meV).

However for the exciton, a small offset in correlation is still observed. A fit was obtained for both exciton and bi-exciton using eq. (4.22). The extracted fitting parameters are given in table 4.8. For both exciton and bi-exciton, τ_s' (from the fit) values are similar to τ_s (from the decay curve). For the exciton, although a very long τ_l' of 30±5 ns was used, its amplitude A_l' (0.89±0.05) is negligible compared to amplitude of short time A_s' (89±5). The presence of this long time is what results in the small offset in correlation at non-zero times.

The $g^2(0)$ was calculated from the experimental data directly and from the fit. From the $g^2(t)$ curve, first the correlation counts are integrated for each peak within a 5 ns window, and are mentioned for both X and XX in Fig 4.39 above each peak. The $g^2_{avg}(0)$ is then the ratio between the integrated correlation counts at zero-delay and the average of all high order peaks. For the X, the $g^2_{avg}(0)$ was calculated to be

	Power (μW)	τ_r (ns)	τ_s (ns)	τ_l (ns)	C	I_r	I_s	I_l	I_l^*	$I_l^*/(I_s+I_l^*)$
X	0.1	0.1±0.05	0.57±0.05	5±1	300±10	-420	8200	500	460	0.05
	18	0.32±0.05	0.57±0.05	5±1	310±10	-585	23000	2050	1900	0.07
XX	0.1	0.1±0.05	0.4±0.05	6.86±0.2	0	-60	750	403	350	0.32
	18	0.3±0.05	0.4±0.05	5.8±0.2	0	-5910	18160	4419	3970	0.18
MX	18	0.1±0.05	0.31±0.05	7±1	50	7000	29500	1470	1240	0.04

Table 4.9: Fitting parameters obtained after fitting of X, XX and MX decay curves in Fig 4.38 using eq. (4.16).

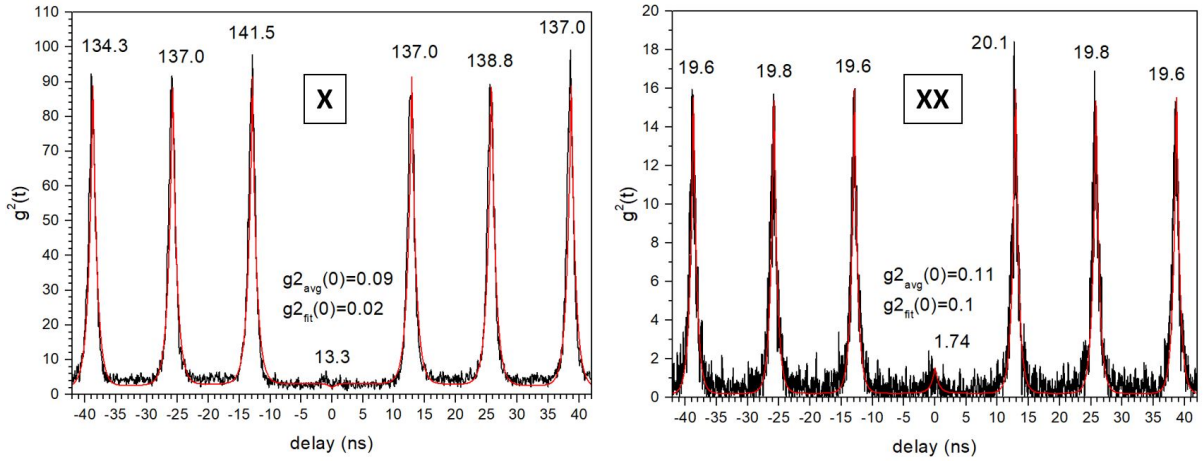

Figure 4.39: $g^2(t)$ correlation measured at 5 K and 20 μW 440 nm pulsed excitation on (X) and (XX) of NW S7_3. Red solid lines are fit obtained with eq. (4.22). On every peak is mentioned average correlation counts integrated within a spectral window of 5 nm. $g^2_{avg}(0)$ is the ratio of integrated correlation counts of zero delay peak and average of all high order peaks. The average integrated intensity of all high order peaks is also given/marked.

0.09 and 0.11 for the XX. For the XX, a small bunching at the zero-delay peak is observed which could be due to nearby X_3 peak. The $g^2(0)$ obtained from the fit was 0.02±0.01 for the X and 0.1±0.02 for the XX. The $g^2(0)$ values obtained are less than that seen with anti-bunching measurements with CW excitation ($g^2_{corrected}$=0.11 for the X and 0.21 for XX) for this NW. Therefore, further corrections need to be applied on the $g^2(0)$ obtained with CW excitation.

A $g^2_{avg}(0)$ value of 0.09 for X of NW S7_3 is better than reported for CdSe SKQDs by M.V. Rakhlin *et al.* (0.2) [31] under CW excitation and under pulsed excitation by O. Fedorych *et al.* (0.16) [33], and similar to reported by K. Sebald *et al.* (0.05) [32].

4.13 Origins of slow decay - discussion

So far, we have studied the emission of three different NWs from three different samples under pulsed excitation. For all three NWs, we have observed a short and long decay time present for both exciton and bi-exciton. This short time can be attributed to the radiative lifetime of the excited states. But the origin of the long time is still unknown.

The presence of a long decay time with a temperature dependence shows that there is one or several states involved in addition to the bright-exciton and bi-exciton. For the bright-exciton, a possible candidate is the dark-exciton, as in Ref [110]. And traps form another candidate, which could be efficient for both bright-exciton and bi-exciton.

The $g^2(t)$ data invalidate the contribution of just dark-exciton. The first photon detected at $t = 0$, tells that the QD contains a bright-exciton which emits a photon and empties the QD: no dark-exciton. However, the bunching component of $g^2(t)$ data at times shorter than the repetition rate indicates feeding of the QD from an external systems that we call "traps'.

Moreover, with the time-resolved measurements on NW S10a_1, two observations are made: 1. At a given excitation power, with increase in temperature, the long decay time τ_l decreases but the contribution of the long decay time (integrated intensity I_l^*) to the total decay curve increases (section 4.11.2). 2. The same is observed for increase in power at a given temperature (section 4.11.3). These behaviors can be explained with the type of traps surrounding the QD.

NW and QD surfaces are prone to a high density of extended defects and centers which can trap charge carriers. When a QD-NW is excited, these traps states are filled with excitons and the trap states in the vicinity of the QD can then feed the QD with charge carriers. It is suggested that there are at least two main types of trap states: 1) shallow trap states in which the charge can be highly mobile and can therefore access a large amount of material, and 2) deep trap states, in which the charge is largely localized within a small region of the material [120]. Deep traps are "deep" in the sense that the energy required to remove an electron or hole from this trap to the conduction or the valence band is much larger than the characteristic thermal energy: k_BT, where k_B is the Boltzmann constant and T is the temperature. Fig 4.40 explains how these trap states can be excited and how they can contribute to the re-population of the exciton or multi-exciton states.

After a visible photo-excitation through absorption of a high energy photon, the hot carriers (electron and hole) can relax into their lowest energy state and this takes less than a picosecond. The hot carriers can form an exciton (or more) in the QD from where they can emit a photon or get captured by the shallow or deep traps. The carriers in the traps can relax to the ground state non-radiatively or repopulate the QD.

At a given power, with increase in temperature, the de-trapping rate increases. This results in a faster feeding from traps to QD and therefore a decrease in the long decay time. However, when temperature increases, carriers in more trap states become mobile and therefore more trap states feed the QD *i.e.* the total contribution of the total decay time (I_l^*) increases.

At low temperatures, and at low powers, only deep traps are filled with excitons. De-trapping carriers from deep-traps can be difficult and slow. A long decay time is thus associated with these long-lived traps (60 ns at 500 nW excitation for exciton of NW S10a_1). Also, the I_l^* is low as only a few traps are filled with excitons which may feed the QD.

As power increases, more traps are excited. With an increase in excitation powers, high energy shallow trapping of carriers also increases. Shallow traps should de-trap almost immediately to the conduction band, driven by thermal energy, and migrate to other traps to generate a broad distribution

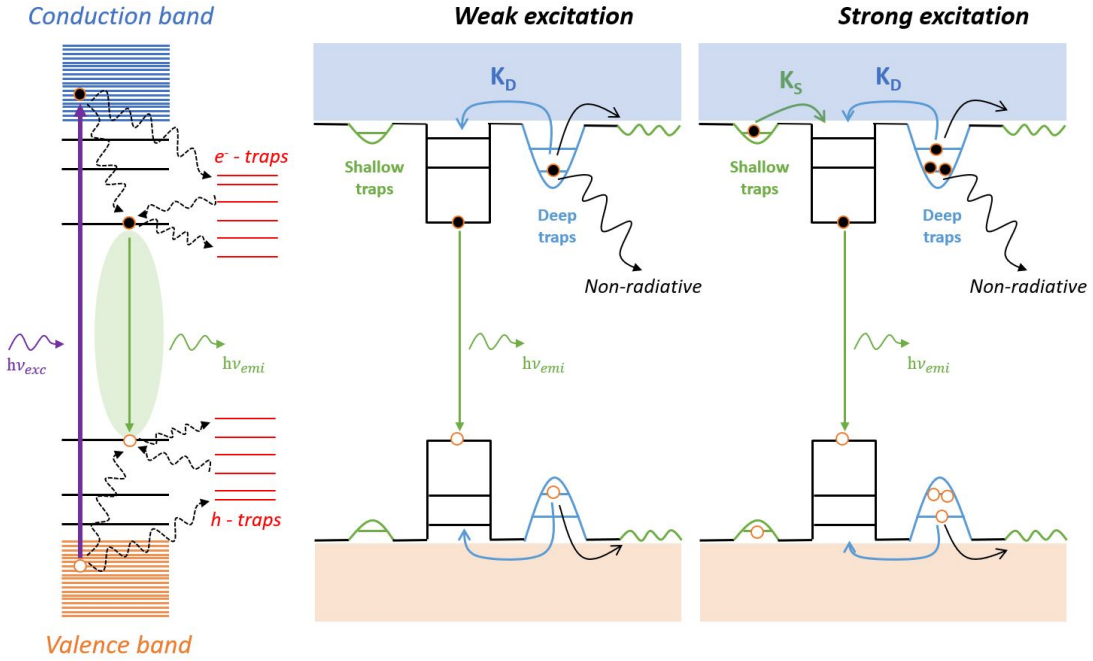

Figure 4.40: Scheme showing feeding of QD energy states with carriers in deep and shallow trap states.

of trapped states or feed the QD. In some cases, one can expect a continuum of trap levels whose populations are equilibrated by the thermal energy. At very high excitation, more traps are filled with excitons, more traps feed the QD with a faster average feeding rate. And therefore, we see an increase in the I_l^* of the long time contribution.

From NW S10a_1 to S10c_2 to S7_3 we have seen that the long time contribution for both low and high powers for both exciton and bi-exciton have decreased. In fact, sample S10a was the least optimized sample with the shell growth at 300 °C and as we have seen in chapter 3, shell growth at this temperature results in defects. Defects give rise to trap states. For sample S7, the shell was grown at 320 °C with much less defects and we have seen that the effect of long decay time is minimum for NW S7_3 from this sample.

4.14 Summary of Part B

In Part B, we saw that a short decay time and a long decay time exist for our QD-NWs. The short decay time is less than 1 ns for both exciton and bi-exciton states and is attributed to the radiative lifetimes. The long decay time is observed for both exciton and bi-exciton. For long decay time higher than the pulsed laser repetition time, the anti-bunching experiment under pulsed excitation behaves like performed under continuous wave excitation. With anti-bunching experiments it is confirmed that the origins of the long decay time is not due to the dark-exciton but to the feeding of the QD from an external source- traps.

For the NW from the most optimized growth sample S7, the effect of long decay time seems negligible and anti-bunching with $g^2(0)$ values of about 0.02 is obtained at 5 K under pulsed excitation.

Part C: Single photon emission at room temperature

This section is dedicated to the single-photon emission capabilities of our QD-NWs at room temperature (without vacuum), at which all the experiments and results reported in this section were performed.

Resolving exciton and bi-exciton peaks at room temprature is important to not pollute the single photon emission of X with bi-exciton and vice-versa. For this high bi-exciton binding energy (B_{XX}) is needed. Only for sample S7, high B_{XX} of $\sim$ 20 meV was observed for all three NWs reported. Therefore, for measurements at room temperatures we focused only on sample S7.

4.15 Exciton and bi-exciton at room temperature

Single-photon detection from a single-photon emitter directly at room-temperatures is difficult as emission peaks broaden and therefore intermix, so that it becomes difficult or impossible to resolve them. Therefore, after X, XX and other multi-X emission peaks are identified at cryogenic temperatures, usually temperature is then progressively increased to keep track of their positions.

The need to go to cryogenic temperatures is eliminated if excitonic emission peaks can be identified and resolved directly at room temperatures. Key to resolving two peaks close to each other is that their linewidths should be of the order or greater than their peak separation. On NWs in sample S7, we performed power dependent measurements directly at room temperature.

4.15.1 Power dependence measurement

Power dependent measurements at room temperatures could not be performed on any of the three NWs in sample S7 presented before, because they bleached in intensity (discussed later in section 4.17). Power dependent measurements at 297 K performed on other NWs from the as-grown sample S7 (NW S7_4 and S7_5) are reported in this section.

In Fig 4.41 (a) are shown μ-PL spectra of NW S7_4 for powers varying from 100 nW to 8 μW, at 297 K, under pulsed excitation. A low spectrometer grating of 600 lines/mm was used, which provides an optical resolution of 0.04 meV (0.09 nm). At all powers above 0.4 μW, a main peak around 2.200 eV (565 nm) with a bump on the high energy side is clearly visible. At very high powers (6.6 and 8 μW), the peak intensity of the main emission peak are similar (5400 and 5200 counts/s respectively).

In Fig 4.41 (b), an extended view at low powers is shown. At 100 nW, a main peak at 2.208 eV with a shoulder on the low energy side can be seen. At 200 nW, the shoulder peak intensity on the low energy side has increased but the high energy peak is still dominant. At 300 nW, the low energy peak has increased in intensity and is similar to high energy peak. At 400 nW, the low energy peak is dominant in intensity.

For comparison, in Fig 4.41 (c), spectra at low power of 100 nW and high power of 8 μW is shown with two vertical scales. For both spectra, a main peak is observed, with a shoulder peak on the low energy side for 100 nW, whereas for the 8 μW spectrum, the shoulder is observed on the high energy side. There is an energy difference of about 20 meV between the maximum intensity of the main peaks of the two spectra.

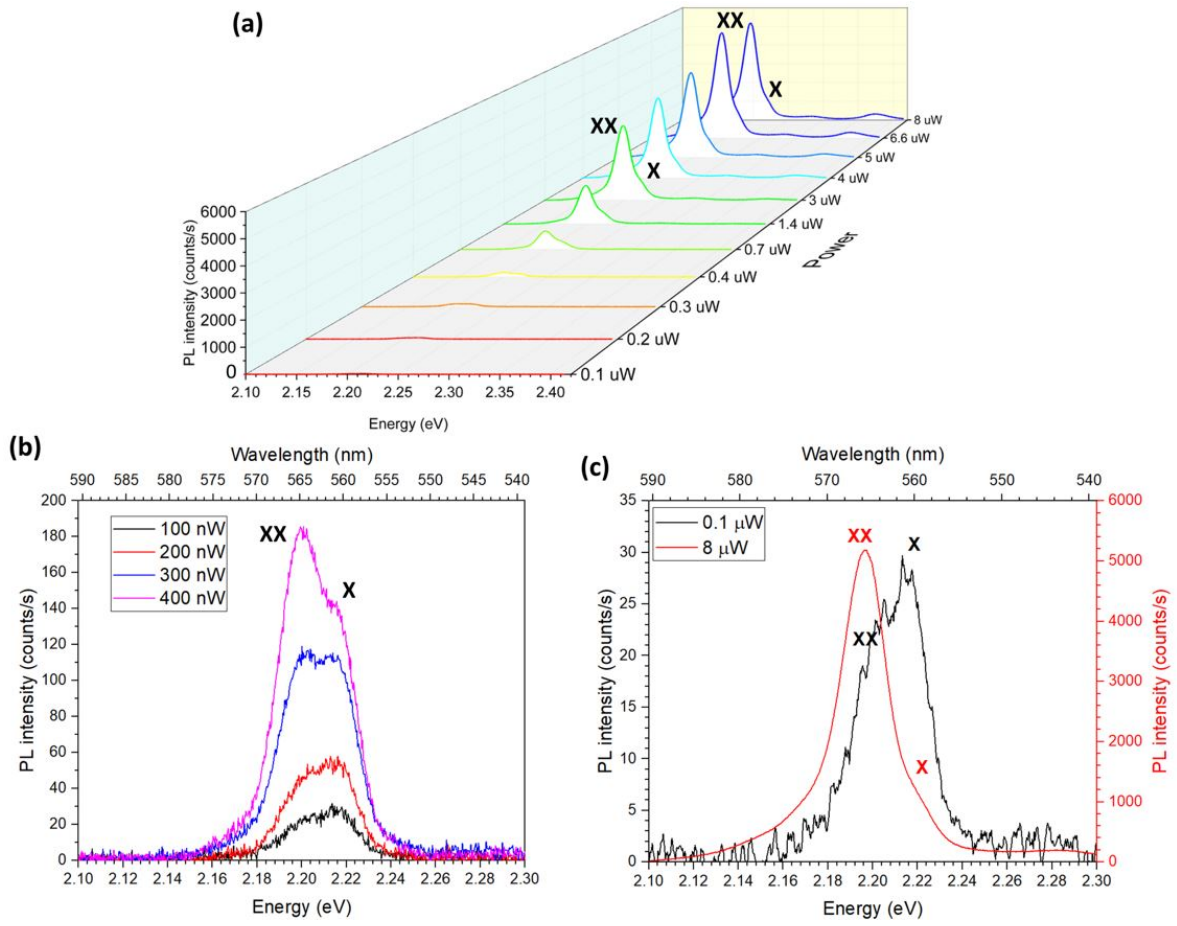

Figure 4.41: Power-dependent μ-PL measurements on NW S7_4 at 297 K for (a) 0.1 to 8 μW, for (b) low powers and for (c) lowest (0.1 μW) and highest (8 μW) excitation power with two different y-axis.

The emission peaks at all powers are then fitted with symmetric Voigt peaks, see Fig 4.42. In black is represented the experimental spectrum. At 100 nW, the emission peak is made of an X and XX peak at 2.2158 eV (blue) and 2.1967 eV (magenta) respectively. The X peak is higher in intensity. The linewidth for both peaks is same at 22.2 meV, which is similar to X linewidth of NW S10a_1 at 300 k (24 meV) observed in section 4.5.3.

For all higher powers, 400 nW and above, at least a third MX peak and MX1 peak of same shape had to be included in the fit at 2.1806 eV (green) and 2.1598 eV (orange) respectively. These peaks belong to the multi-X states as they appear only at high powers.

The integrated intensity of the X and XX peaks plotted as a function of increasing power is shown in Fig 4.44 (a). The integrated intensity of the X increases linearly at low powers before saturating at high powers. The intensity of the XX increases quadratically at low powers before saturating at high powers (around 6.6 μW). The saturation intensity of the XX is higher than the X. This behavior is similar to what is typically observed for X and XX states under pulsed excitation and was also observed for the X and XX peaks in NW S10c_2 at 5 K in section 4.10.

The B_{XX} for this is 19.0 meV, similar to observed for three NWs from the same sample characterized

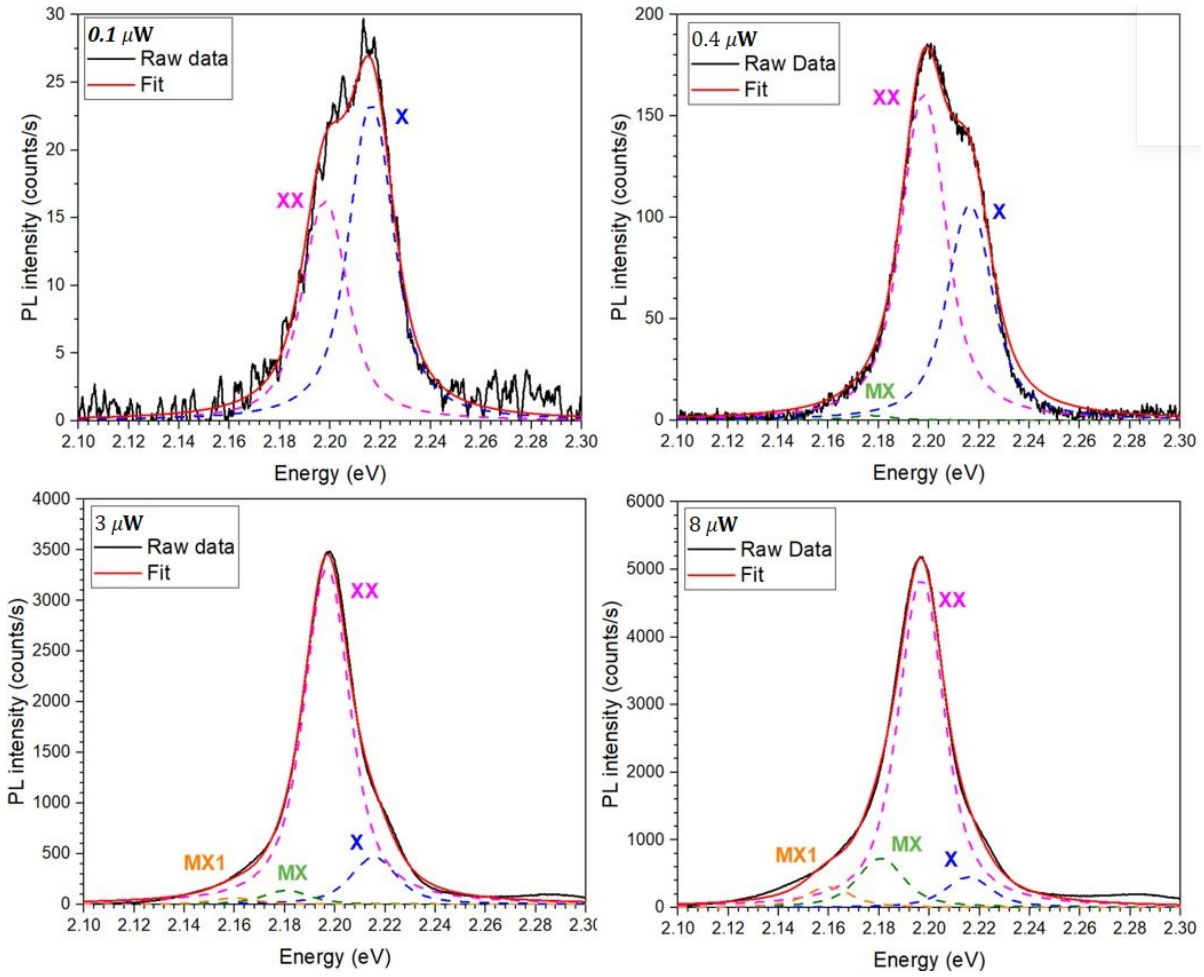

Figure 4.42: Fits for the PL emission peak in NW S7_4 for (a) 0.1 μW, (b) 0.4 μW, (c) 3 μW and (d) 8 μW. Fits are obtained using X (blue), XX (magenta), MX(green) and MX1 (orange) Voigt peaks. In black is the experimental data and in red is the fit.

at 5 K and reported in section 4.6. The B_{XX} is similar to the linewidth of the X and XX peaks (22.1 meV), this enables to resolve the X and XX at room temperatures.

It is clear from Fig 4.42 that the X intensity at higher powers is considerably lower than XX. In Fig 4.44 (b) is plotted the ratio of the integrated intensity of X (I_X) and of XX (I_{XX}). Also is plotted the ratio I_{XX}/I_X. At powers above 1 μW, the I_{XX} is considerably higher than I_X and at very high powers (8 μW), I_{XX} is more than 9.3 times the I_X. Such extreme values are not reached at cryogenic temperatures. For NW S10c_2, at high power when pulsed excited at 5 K, the I_{XX} is just 1.3 times the I_X (Fig 4.28 (b)). This decrease in X intensity at high temperatures is due to the non-radiative channels of the X state: through traps states and through dark-X (explained in section 4.5.4).

Another NW on which power dependence measurements were performed at 297 K is NW S7_5, see Fig 4.44 (a). In Fig 4.44 (b) for comparison μ-PL spectra are shown at very low power of 500 nW and very high power of 20 μW. The spectra are similar to NW S7_4. There is an energy difference of 20.1 meV between the peaks of the two spectra.

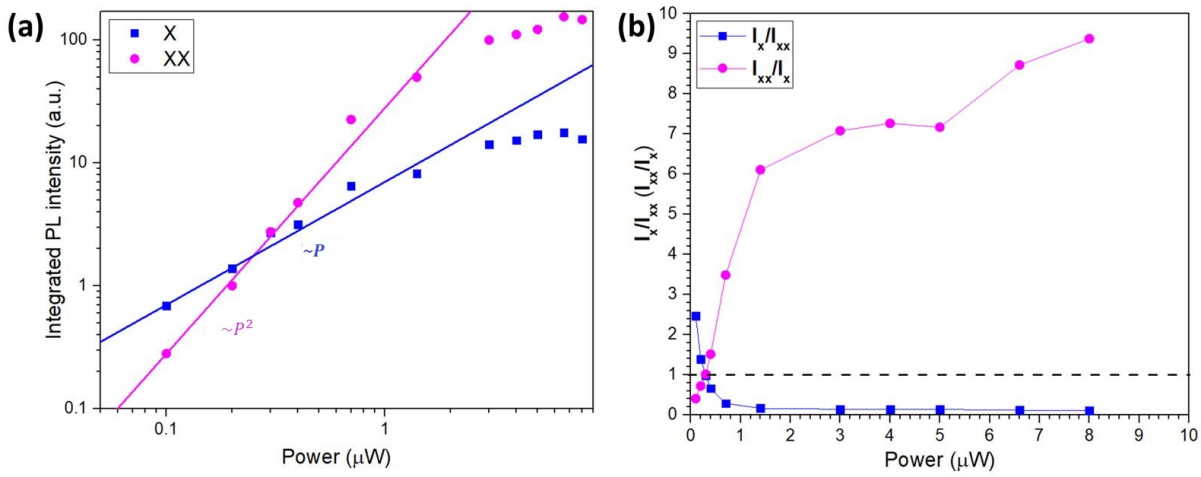

Figure 4.43: Integrated intensity plot as a function of power for NW S7_4 at 297 K. In blue and magenta are represented integrated intensity for the X and the XX fitting Voigt peaks respectively. Blue and magenta solid lines represent linear and quadratic increase of intensity. (b) Ratio of integrated intensity of X Voigt fitting peak (I_X) and that of XX Voigt fitting peak (I_{XX}). In blue is the ratio I_X/I_{XX} and in magenta is the ratio I_{XX}/I_X.

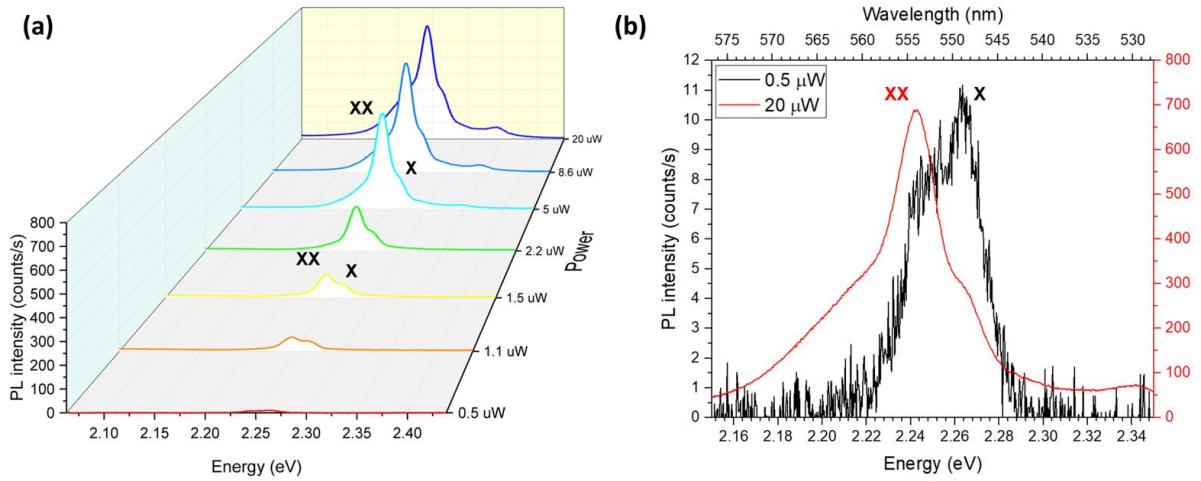

Figure 4.44: Power-dependent μ-PL measurements on NW S7_5 at 297 K for (a) 0.5 to 20 μW and for (b) lowest and highest excitation powers with two different y-axis.

Spectra for this NW were also fitted with X and XX at low powers and with an additional MX peak at high powers. In Fig 4.46 (a) is plotted the integrated intensity of the blue and magenta Voigt peaks as a function of increasing powers. Similar to NW S7_4, linewidth of the peaks is 21 meV and at high power I_{XX} is 3.5 times higher than I_X (Fig 4.46 (b)).

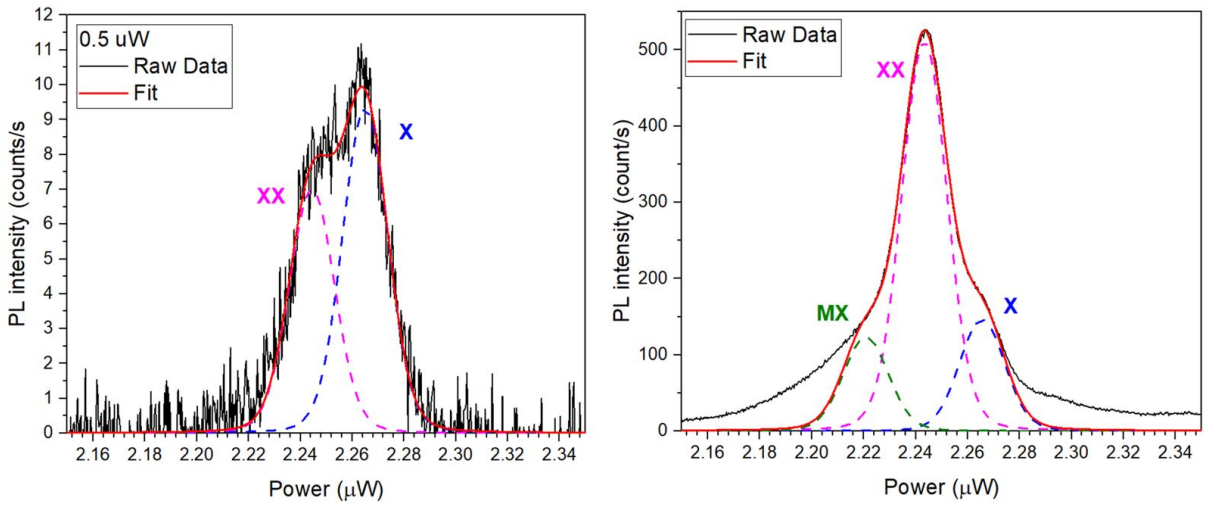

Figure 4.45: Fits for the PL emission peak in NW S7_5 for (a) 0.5 μW, (b) 5 μW. Fits are obtained using X (blue), XX (magenta), MX(green) Voigt peaks. In black is the experimental data and in red is the fit.

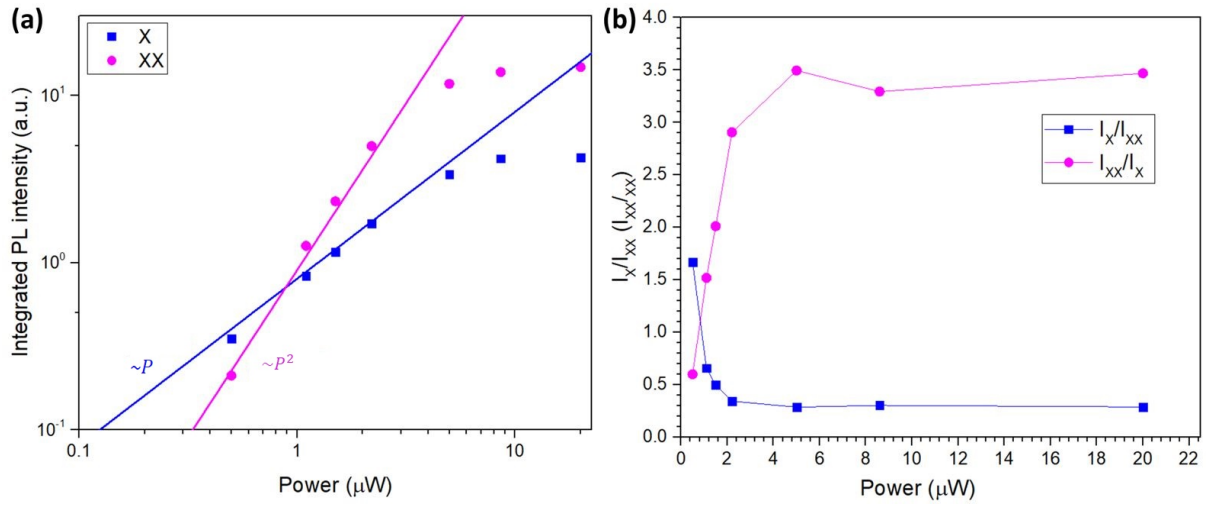

Figure 4.46: Integrated intensity plot as a function of power for NW S7_5 at 297 K. In blue and magenta are represented integrated intensity for the X and the XX fitting Voigt peaks respectively. Blue and magenta solid lines represents linear and quadratic increase of intensity. (b) Ratio of integrated intensity of X Voigt fitting peak (I_X) and that of XX Voigt fitting peak (I_{XX}). In blue is the ratio I_X/I_{XX} and in magenta is the ratio I_{XX}/I_X.

4.15.2 Lifetimes

At 5 K we observed a short and a long decay time for all NWs. We wanted to see how lifetimes are affected at room temperature.

Lifetime measurements were performed on NW S7_4. Lifetimes were measured at 565.5 nm (2.192 eV) and 561.5 nm (2.208 eV) for a spectral window of 0.7 nm, see Fig 4.47 (b). The two wavelengths

Energy	Power (μW)	τ_r (ns)	τ_s (ns)	τ_l (ns)	C	I_r	I_s	I_l	I_l^*	$I_l^*/(I_s + I_l^*)$
2.208 eV	6.6	0.1±0.05	0.49±0.05	2.52±0.2	51±5	-2000	7280	405	400	0.07
2.192 eV	6.6	0.13±0.05	0.43±0.05	2.34±0.2	56±5	-6500	16650	1070	1060	0.05

Table 4.10: Fitting parameters obtained after fitting of X and XX decay curves in Fig 4.47 (b) with eq. (4.17).

were chosen to measure the lifetime of XX and X, see Fig 4.47 (a). The lifetime spectra are shown after subtraction of background.

The decay curves are clearly not mono-exponentially decaying, and were fitted with one exponential rise and two decay functions using eq. (4.16). The fitting parameters are given in table 4.10.

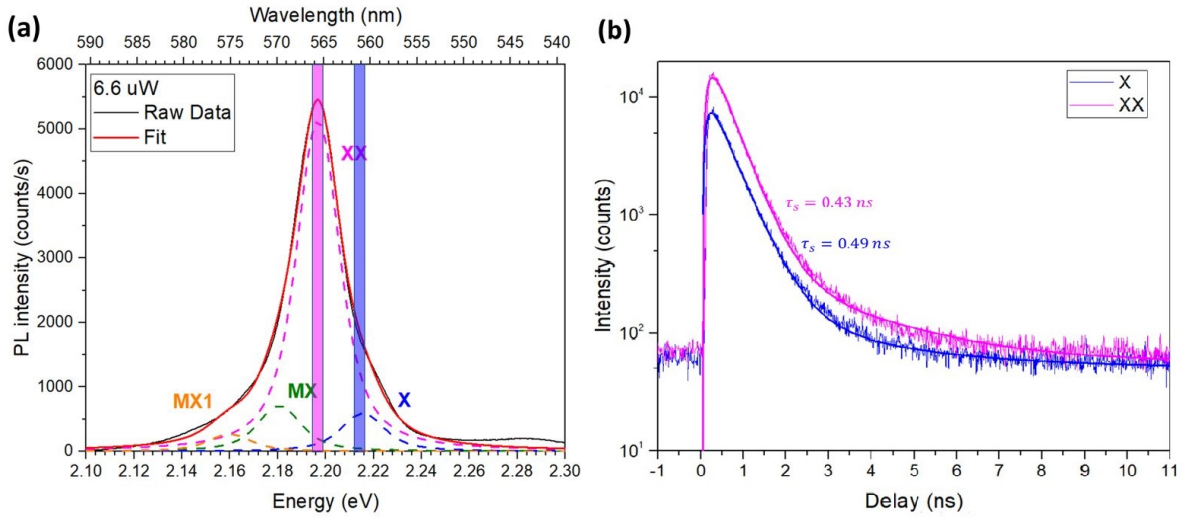

Figure 4.47: (a) μ-PL spectrum of NW S7_4 at 6.6 μW using a 440 nm pulsed laser with 13.1 ns repetition time at 297 K, along with the X, XX, MX and MX1 Voigt fits. In black is the experimental data and in red is the fit. (b) Decay curve obtained for the spectral region marked in (a) at same 6.6 μW pulsed excitation at 297 K. Decay curve in magenta is obtained from magenta shaded spectral region in (a).

After about 4 ns, both decay curves become constant around the same 50 counts offset (compared to 10^4 peak counts). Therefore, the 50 counts could be background. The short decay time (τ_s) for X and XX are similar at 0.43±0.05 and 0.49±0.05 ns. The τ_s values are similar to τ_s of XX (0.4 ns) of NW S7_3 at 5 K. The long time (τ_l) for X and XX are 2.32±0.2 and 2.52±0.2 ns respectively, and are shorter than observed at 5 K for 10 s QD NWs (NW S10a_1 and S10c_3). The long time contribution to the total decay (I_l^*) is negligible for both X and XX at 0.07 and 0.05 respectively.
From the fits it can be realized although that at 565.5 nm (magenta shaded region), the XX peak contributes the most, but at 561.5 nm, even though the X peak is at peak intensity, there is a substantial contribution from the XX peak (blue shaded region) of 70 % to the total signal. This means that even at 561.5 nm, we are still measuring the lifetimes of the XX, which explains the very similar decay curves.

We could lower the excitation power to favor the X emission intensity over the XX as we saw in Fig 4.44 (b) for NW S7_4 and in Fig 4.46 (b) for NW S7_5. But at very low powers, the PL intensity is very low to perform lifetime measurements.

4.16 Anti-bunching at room temperature

In this section are discussed results on anti-bunching measurements performed at room temperature on NW S7_4 and two other NWs (S7_6 and S7_7) under pulsed excitation. NW S7_5 bleached before anti-bunching measurements could be performed.

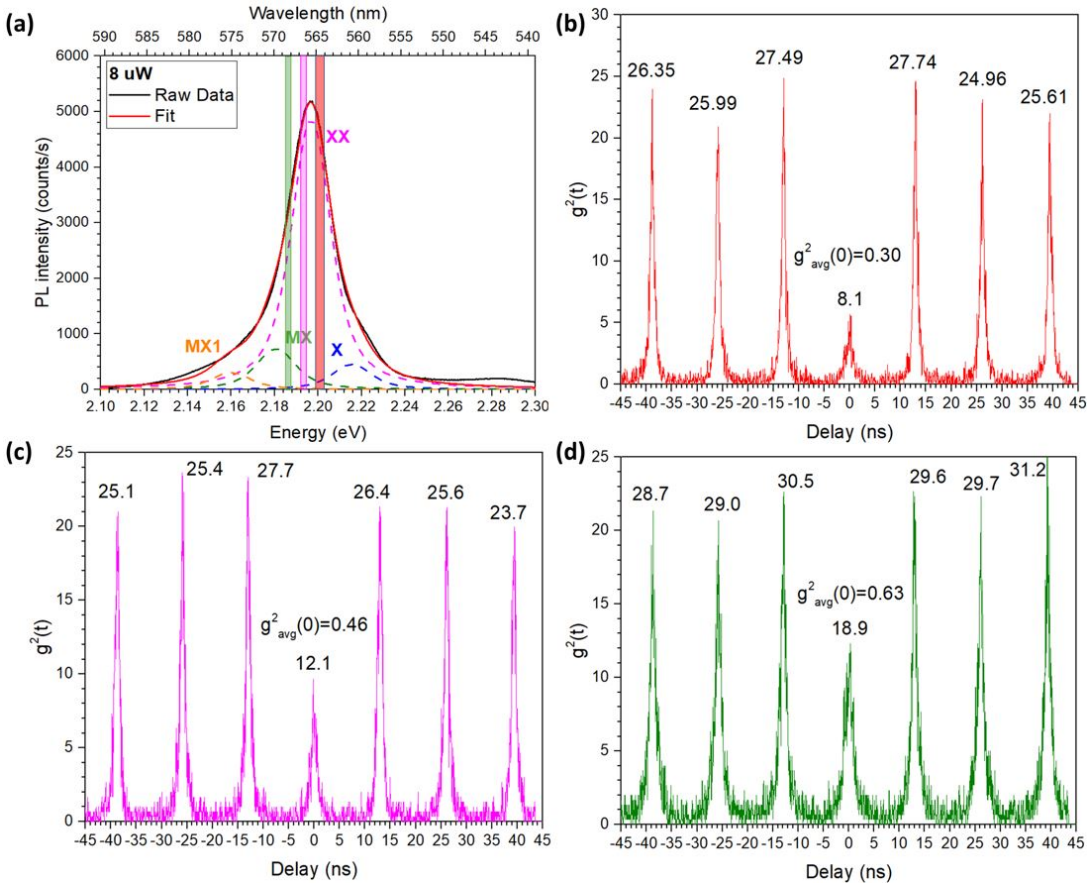

Figure 4.48: (a) μ-PL spectrum of NW S7_4 at 8 μW pulsed excitation at 297 K with X, XX, MX and MX1 Voigt fitting peaks. In black is the experimental data and in red is the fit. The shaded regions are spectral windows for which $g^2(t)$ curves were obtained in (b) for red shaded region, in (c) for pink and in (c) for green. For each peak in $g^2(t)$ curves, the intensity is also given integrated in a window of 3 ns. The $g^2_{avg}(0)$ takes into account all the non-zero delay peaks.

In Fig 4.48 (a) is shown μ-PL spectrum of NW S7_4 at 8 μW (saturation power) pulsed excitation and 297 K, along with the fits of the X, XX and MX peaks and also the shaded regions which corresponds to the spectral windows for which anti-bunching measurements were performed. In Fig 4.48 (b), (c) and (d) are shown $g^2(t)$ curves obtained for the red, pink and green shaded regions respectively. On every

peak is mentioned average correlation counts integrated within a spectral window of 5 nm. $g^2_{avg}(0)$ is the ratio of integrated correlation counts of zero delay peak and average of all high order peaks. The average counts/s on a single APD from this NW at 564.5 nm (red) were about 15000. The integration time was 80 min for (b) and 60 min for (c) and (d).

It can be seen that the signal decreases almost to zero in all the $g^2(t)$ curves, indicating that the influence of a long decay time is weak here. There is an increase in $g^2_{average}(0)$ values from the red region ($g^2_{average}(0) = 0.30$) to the pink region (0.46) to the green region (0.63).

In table 4.11, the contribution of the X, XX, MX and the MX1 fitting peaks in the total PL intensity are given for the red, pink and green shaded regions along with the $g^2_{average}$ obtained for each region. An increase in the XX contribution from 568.4nm to 564.5 nm explains the decrease in the obtained $g^2_{average}(0)$. At 564.5 nm, the PL intensity is mostly due to single peak (XX, 93.8 % from fit) and therefore the $g^2_{average}(0)$ is the lowest.

Shaded region	Contribution in spectra (%)				$g^2_{average}(0)$
	X	XX	MX	MX1	
568.4 nm	1.4	69.8	27.1	1.0	0.6
566.5 nm	1.6	90.1	7.8	0.3	0.4
564.5 nm	3.0	93.8	2.9	0.2	0.3

Table 4.11: Contribution of X, XX, MX and MX1 fitting Voigt peaks in the total PL intensity of NW S7_4 at 8 μW, shown in Fig 4.48 (a).

We performed anti-bunching measurements on two other random NWs (S7_6 and S7_7) on the sample S7 at 297 K. The μ-PL spectra of both NWs are shown in Fig 4.49 (a) and (c) respectively. Along with the X and XX peaks, for both NWs a third peak on the high energy side is visible. This peak belongs to the X_3 state. The maximum counts/s on a single APD were 4,000 and 25000 for NW S7_6 and S7_7 respectively. The $g^2(t)$ measurements were performed in the shaded regions with a spectral window of 0.7 nm. Their corresponding $g^2(t)$ are shown in Fig 4.49 (b) for NW S7_6 and in (d) for NW S7_7. Integration time was 40 min for both NWs.

Similar to NW S7_4, the signal decreases to zero for both NW's $g^2(t)$ curves. The $g^2_{average}(0)$ was 0.36 and 0.31 for NW S7_6 and S7_7 respectively.

These values are similar to NW S7_5. These experimental $g^2(0)$ values without any correction are better than reported for CdSe QD in ZnSe NW in our group in 2012 ($g^2(0) = 0.48$) [11]. And as far as we know, in the visible range, $g^2(0)$ values obtained with our optimized CdSe-ZnSe QD-NW system are better than SKQD or NW-QD system emitting in the visible at room temperature.

4.17 Bleaching of QD emission at room temperature

While we obtained good $g^2(0)$ values on several QD-NWs, we were unable to perform anti-bunching measurements on many NWs at room temperature. The NW's emission bleached at room temperatures. This is the reason why we could not perform anti-bunching measurements on the three NWs characterized at 5 K in part A and B, and also NW S7_5.

In fact the PL intensity of NWs on which we presented $g^2(0)$ measurements in the previous section also bleached during the measurements. For NW S7_6, the counts/s on a single APD went down from

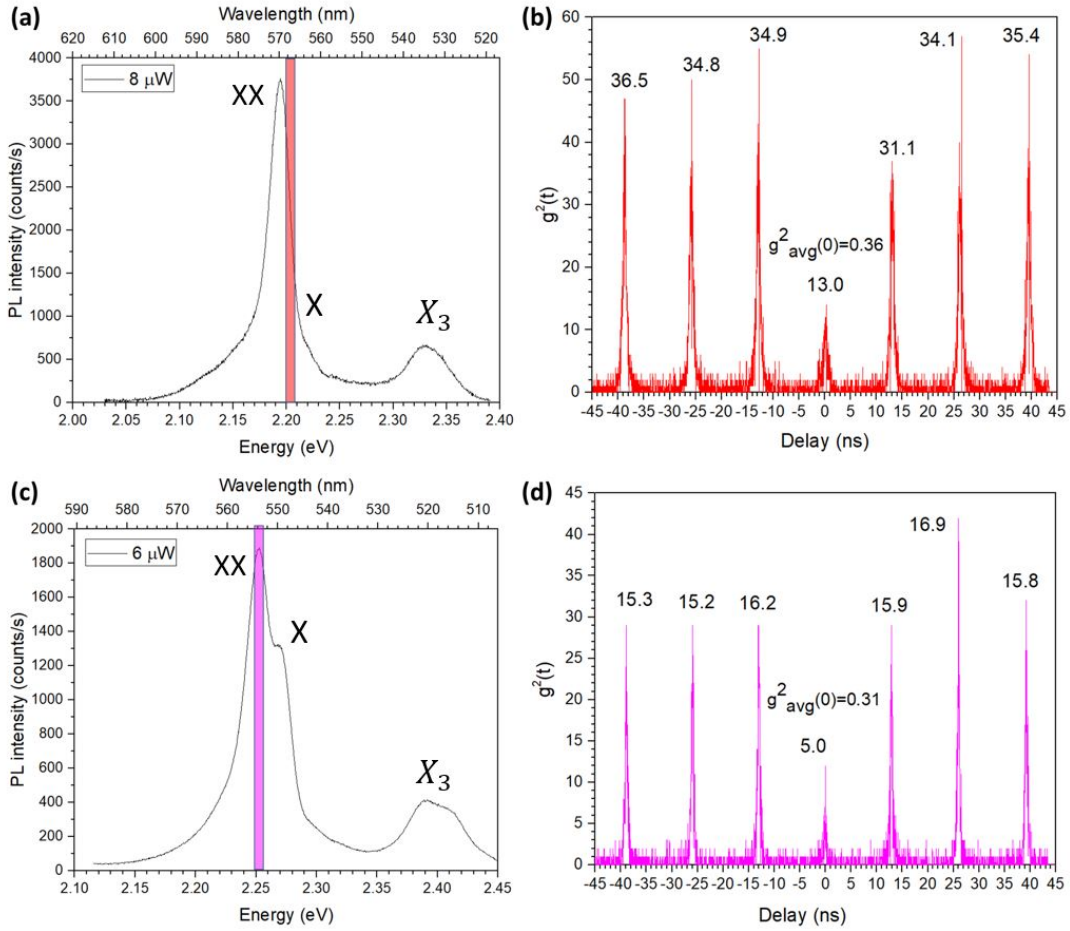

Figure 4.49: (a) μ-PL spectra of NW S7_6 in (a) at 8 μW pulsed excitation and for NW S7_7 in (c) at 6 μW pulsed excitation at 297 K. The shaded regions are spectral windows for which $g^2(t)$ curves were obtained in (b) for red shaded region of NW S7_6 and in (d) for pink shaded spectral window for NW S7_7. On every peak is mentioned average correlation counts integrated within a spectral window of 5 nm. $g^2_{avg}(0)$ is the ratio of integrated correlation counts of zero delay peak and average of all high order peaks.

40000 at the start of the $g^2(0)$ measurements to about 20000 counts/s in 40 mins towards the end of the measurement.

To measure the effect of excitation power on bleaching of NWs, we measured PL intensities over time of two NWs where one is excited with a high and other with a low excitation power. The NWs were exposed to laser continuously during the time period. In Fig 4.50 (a) is shown X and XX peak intensities of a random NW S7_8 as a function of time when excited with a low 2.2 μW pulsed excitation. In Fig 4.50 (b) is shown X and XX peak intensities of another NW S7_9 when excited at high 18 μW pulsed excitation. For both cases, X and XX PL intensity bleaches almost completely.

Bleaching and blinking of QDs emission at room temperatures is an on-going issue for practical applications. Bleaching of CdSe/ZnS core-shell nanoparticle QDs was reported to be linked with the presence of oxygen [121]. Photo-induced oxidation of the CdSe crystallites and oxygen-induced

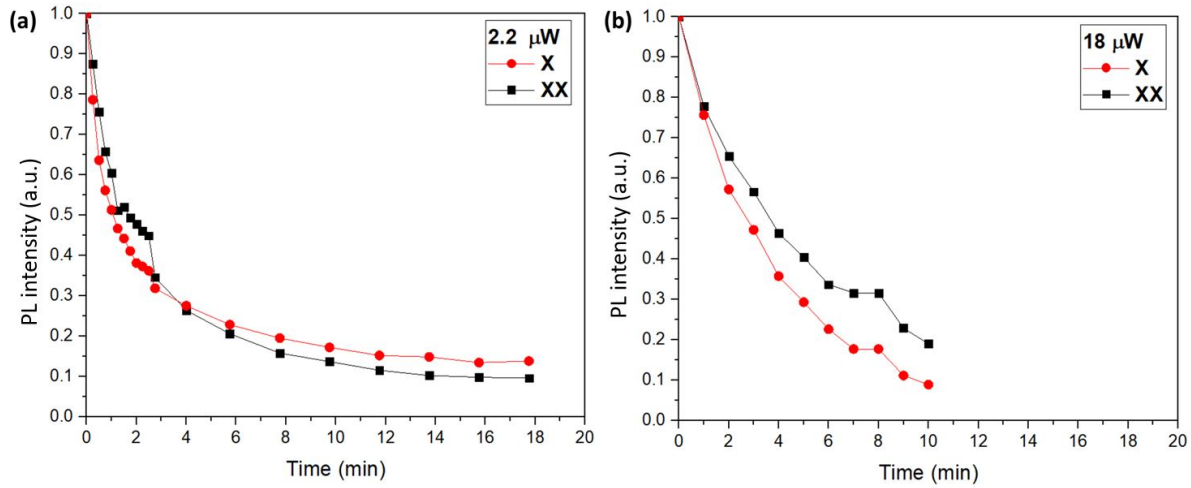

Figure 4.50: Room temperature variation of the PL intensity with time of (a) NW S7_8 when excited with a power of 2.2 μW and of (b) NW S7_9 excited with 18 μW power. The NWs were continuously exposed to the laser throughout the time period.

quenching of defect states was reported as one of the main reasons for QD emission bleaching.

PL measurements under vacuum

Therefore, we also measured PL intensities of another NW at 297 K at 6 μW pulsed excitation and exposed with laser continuously. But this time the NW was kept under vacuum. In Fig 4.51, are shown spectra of a NW at 0 min and at 30 min of continuous exposure. There is only 5 % decrease in the peak intensity at 2.23 eV after 30 mins of continuous exposure with laser. Bleaching of PL intensity may depend on the structural quality of the NW and it is also possible that for this NW, no-bleaching has more to do with the structural quality of this NW and less with the vacuum environment.

However, only one NW was checked for its emission in vacuum and more data is needed to conclude that a vacuum environment prevents oxygen-induced bleaching effects in our case.

4.18 Summary of Part C

In Part C, we saw that for the 7 s QD-NW sample S7 with an average bi-exciton binding energy of 20 meV, exciton and bi-exciton peaks could be resolved directly at room temperatures. The effect of power dependence measurements could be observed directly at room temperature and at atmospheric pressure. Even under pulsed excitation, at very high excitation powers the bi-exciton intensity was observed to be more than 3 times than the exciton intensity. A $g^2(0) = 0.3$ was observed for three NWs with average counts of 40000 on an APD. And as far as we know, these values are better than any known SKQD or NW-QD system at room temperatures.

Bleaching of NWs intensity was observed at room temperatures. The bleaching is stronger under high excitation. However, for one NW, bleaching effect was completely suppressed under vacuum. Therefore, bleaching could be as a result of oxygen-induced quenching of trap states at the surface of

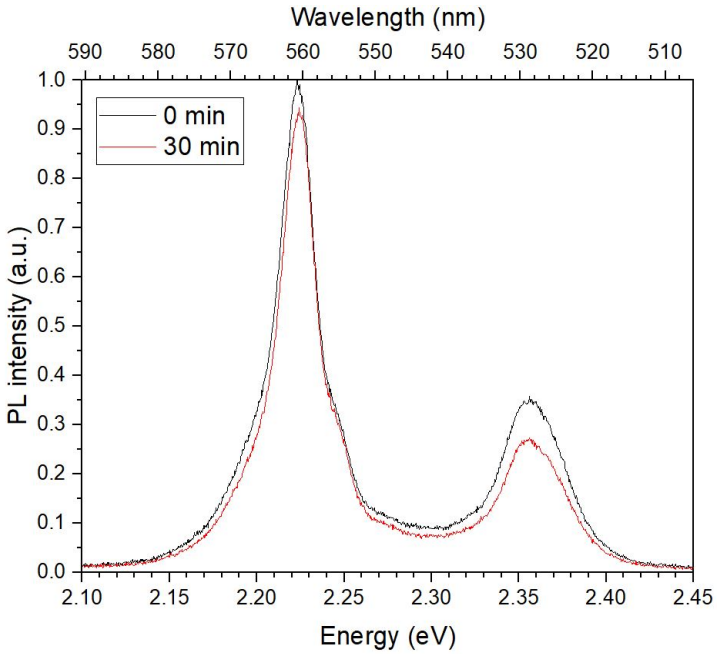

Figure 4.51: μ-PL spectra of a NW at 0 min and at 30 min of continuous exposure with a pulsed laser at 6 μW at room temperatures and in vacuum.

the NWs. These results are very encouraging and further studies are required.

4.19 Conclusion

This chapter presents:

- results on optical spectroscopy measured along the NW axis on as grown samples, with both CW and pulsed excitation, from cryogenic to room temperature, including auto-correlation data
- on 4 CdSe QD in ZnSe NW samples (S10a, S10b, S10c - all with a 10 s QD, and S7 with a 7 s QD); with improving structural quality, progressively optimized shell diameter.

No QD signal is observed from the sample S10b, due to too low shell thickness (important in the present case of excitation-detection along the NW axis, as opposed to transverse excitation-detection, as seen in previous studies with NWs dispersed on a foreign substrate).
The exciton, bi-exciton and more excited states were identified from the power dependence in CW and pulsed excitation, at low temperature but also at room temperature in the sample with the smaller (S7) QD size
Increase of the bi-exciton binding energy is observed, from 15 to 20 meV, when decreasing the QD size (from 10 s to 7 s insertion). However, this is to be confirmed with more statistical data on the current samples and on a future series of samples.
Precise study of the linewidth was performed and the following results were observed:

- at 5 K, record linewidth for the zero phonon line, 210 μeV; this is still slightly larger than in the best III-V QDs with non-resonant excitation.

– At room temperature, the zero phonon line is negligibly small and the linewidth is about 20 meV from the phonon sideband. A detailed study of the phonon sideband needs to be completed.

Auto-correlation studies were performed, with state of the art values of auto-correlation function $g^2(0)$ for a II-VI QD at low temperature, and with record values for an epitaxial semiconductor QD at room temperature.
Role of traps was particularly evidenced in pulsed spectroscopy at low temperature and specific contribution of traps to the auto-correlation was observed. The auto-correlation data allowed us to decide between dark-exciton and traps in the onset of slow components of time-resolved PL measurements. However, the traps were strongly suppressed and their effects greatly reduced in the last (most optimized) sample (S7) at low temperature and room temperature.

Finally, there were evidence of the absence of competition of neutral-exciton and charged-exciton for single photon emission. Anti-bunching was observed on (neutral) bi-exciton and charged-exciton together and it is deduced that the QD hops between neutral and charged state. However, to describe the results completely, rate equations are to be written and solved.

CHAPTER 5

Towards integrated photonics

Contents

Many quantum technologies based on single-photon source requires integration of the sources with photonic devices. For applications, such as, in quantum computation, complex photonic network between qubits is required on chip. And therefore efficient coupling of single-photon source's emission into waveguides becomes critical for practical ways to implement single photon based quantum technologies.

Integration of single-photon source with photonic devices on chip is critical for practical ways to implement single-photon based quantum technologies. For applications requiring complex circuitry such as for quantum computation applications, integrated sources are required.

In chapter 2 we discussed the design of a tapered QD-NW source for efficient collection of light in free space. In this chapter we are going to discuss the coupling of light from the QD-NW source with integrated photonic devices (waveguides). The choice of waveguide material is silicon nitride as it exhibits broadband transparency that extends to the visible spectrum and is CMOS-compatible.

This chapter is presented as a prospect for future studies for integration of light from our CdSe-ZnSe QD-NW with a tapered design into a waveguide. First, we will discuss the different strategies that are available in literature to couple light from self-assembled QDs or QD-NWs to waveguides in section 5.1. Then we will present the optimization of the dimensions of silicon nitride waveguide for guiding light of 550 nm (mean emission wavelength for our CdSe QDs) in section 5.2 . And finally, will be presented finite-difference time-domain numerical simulations for coupling light from our QD-NW source to waveguides in section 5.3.

5.1 Strategies to couple light from QD to waveguides

An optical waveguide guides electromagnetic waves in a preferred direction with minimal loss of energy. It consists of two dielectric materials where refractive index of one material is higher than the other. In the ray-optics picture, light is guided in the higher refractive index material due to total internal reflection. The higher refractive index material is called the core and the other is called the cladding as it surrounds the core material. Most waveguide offers confinement in two-dimensions while permitting

propagation in one direction. Several strategies have been implemented to couple a QD emission to a waveguide.

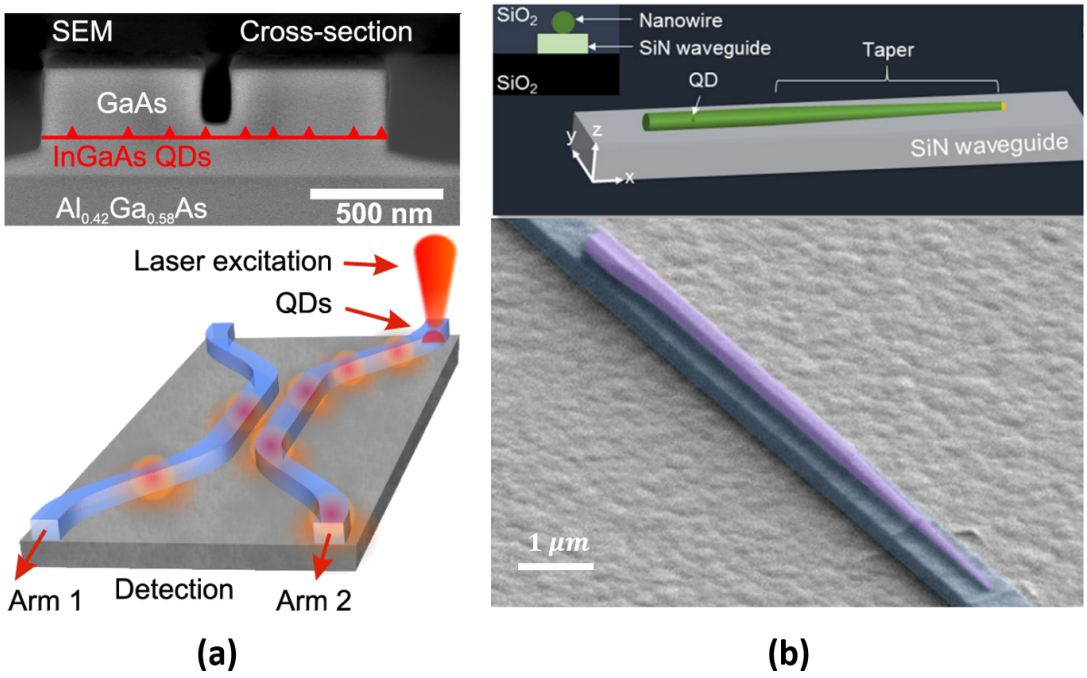

Figure 5.1: (a) Cross-section SEM image of InGaAs SKQDs embedded in GaAs waveguide. And below is the excitation scheme to excite the QD from the top and collect its emission in both output arms simultaneously. Taken from [122]. (b) Schematic for evanescently coupling the emission from an InP NW to a SiN waveguide. And SEM image (below) QD-NW with a taper length of 8 μm on a silicon nitride ridge waveguide. Taken from [10].

Previously, waveguides were defined through lithography techniques directly on the sample with self-assembled QDs [123, 124, 125, 122]. Mario Schwartz *et al.* [122] coupled InGaAs SKQDs emission to GaAs waveguides (Fig 5.1 (a)). First a InAsGa/GaAs SKQD sample was grown with MOCVD technique on top of $Al_0.42Ga_{0.58}$, as cladding layer. Waveguides were then defined using e-beam lithography. Due to the high density of SKQDs it is assumed that at least one QD is embedded in the waveguide. They were able to perform anti-bunching measurements with such a system directly on chip. Although such a system ensures direct coupling of the QD light to the waveguide, there are two inherent problems with it. First, there is always a high probability of embedding more than one QD in the waveguide and second, the waveguide material is restricted to the wetting layer material.

QD-NW design provides much higher flexibility with pick-and-place technique. QD-NW is picked from the growth substrate using micro/nano-manipulators and then placed on a substrate. Waveguides are then defined around this QD-NW. But such techniques require high precision and alignment during the fabrication of waveguides. Moreover, QD-NW cannot be replaced as they are embedded in the waveguide [126].

Very recently, evanescent coupling of emission from QD-NWs to waveguides was shown as an exciting option for self-contained, all fiber, plug-and-play solution to integration of SPS with waveguides. The idea is to place the QD-NW outside the waveguide and still couple its emission to the waveguide.

Khaled Mnaymneh *et al.* [10] coupled emission from tapered InAsP QDs embedded in tapered InP NWs to silicon nitride waveguides with evanescent coupling. The QD-NW was picked up from the growth substrate and placed on top of pre-fabricated silicon nitride waveguides (see Fig 5.1 (b)). A coupling efficiency less than 74% was experimentally observed. However, this efficiency takes into account waveguide propagation losses, waveguide-fiber coupling loses, spectrometer losses (fiber transmission and monochromator), leaky mode losses, *etc.* Same evanescent coupling approach is also discussed for our CdSe-ZnSe QD-NW in section 5.3. But before that we will define the dimensions of the silicon nitride waveguide that are necessary to guide light emitted by our CdSe QDs in the following section.

5.2 Optical confinement in silicon nitride waveguide

A waveguide supports only a finite number of modes, which are spatial solutions to the Maxwell´s equations. In integrated photonic platforms, the most common waveguides used are slab, rib and strip waveguides. For the slab waveguides, an analytical solution to the mode field can be easily formulated but the case of rib and strip waveguides (Fig 5.2) are complex and require numerical solutions. In strip waveguides, the core material is completely etched down to the cladding material, while in rib waveguides, the core material is partially etched. The horizontal confinement in strip waveguides is tighter than in rib waveguides. Moreover, the main source of losses in propagation in waveguides is due to surface roughness. And rib waveguides offer lower loses as they are only partially etched. Nevertheless, the silicon nitride waveguides we have studied in this thesis are strip waveguides.

The mode field of a waveguide can be numerically solved using the same finite element (FEM) solver used in chapter 2 to optimize the shape and size of ZnSe NWs. COMSOL multiphysics tool was used for this purpose. Using FEM solvers, the waveguide dimensions with a complex refractive index distribution can be calculated. These solvers outputs the eigenvectors and its eigenvalues which corresponds to the modes and propagation constants β of the modes. The β gives the phase delay when light travels a certain unit length along the direction of propagation. The effective index can then be calculated from the propagation constant as:

$$n_{eff} = \frac{\beta}{k_0} \tag{5.1}$$

where k_0 is the wavenumber in vacuum given as: $k_0 = 2\pi/\lambda_0$. The λ_0 is the wavelength in vacuum. The effective index n_{eff} is a weighted average of core and cladding refractive indices with the mode field distribution acting as the weight. Therefore, modes are more confined in the core for higher values of n_{eff}.

For rectangular waveguides, both TE and TEM modes exists. For the TE mode, the electric field is polarized along the width (X axis) of the waveguide. And for the TM mode, the electric field is polarized along the height (Y axis) of the waveguide. For rectangular waveguides, TE mode is the fundamental mode. The degree of confinement of the mode can be quantitatively evaluated using the effective mode area A_{eff} which is the area that the mode of a waveguide effectively covers in the transverse direction and can be expressed as:

$$A_{eff} = \frac{\left(\iint |E(x,y)|^2 dxdy\right)^2}{\iint |E(x,y)|^4 dxdy} = \frac{\left(\iint I\ dxdy\right)^2}{\iint I^2\ dxdy} \tag{5.2}$$

where E is the electric field and I is the optical density. The integral is taken over the entire X-Y plane of the core and cladding. The A_{eff} of a waveguide is modified by changing the X or Y dimensions of

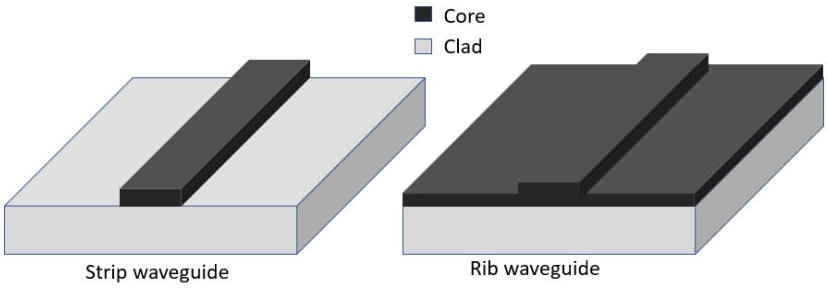

Figure 5.2: Schematic of a (a) strip and (b) rib optical waveguide.

the waveguide. A consequence of a small mode area is that the optical intensities for a given power level are high. Moreover, small mode areas are usually a result of strong guiding, where bend losses and other effects are weak. For a Gaussian beam with radius r, the effective mode area is πr^2.

In Fig 5.3 (a) is shown an example of the TE mode field simulated for a silicon nitride (Si_3N_4 core and SiO_2 cladding) waveguide of 200 nm width and 300 nm height on top of a 500 nm SiO_2 layer. This wavelength is chosen because our CdSe QD emit around this wavelength. In Fig 5.3 (b) is shown the A_{eff} for waveguide height from 150-400 nm for a fixed width of 200 nm at wavelength of 550 nm. The A_{eff} is the least for a height around 300 nm at 0.074 μm^2 and corresponds to maximum confinement. The A_{eff} increases slightly when the height is increased beyond 300 nm and drastically increases when height decreases below 300 nm indicating that the confinement weakens quickly.

While a small A_{eff} is beneficial for compact integration, a waveguide with large A_{eff} is widely used to match the mode field between the waveguide and an optical fiber. This is done to reduce coupling loses. For the following discussion we will consider a Si_3N_4 waveguide of 200 nm width and 300 nm height dimensions.

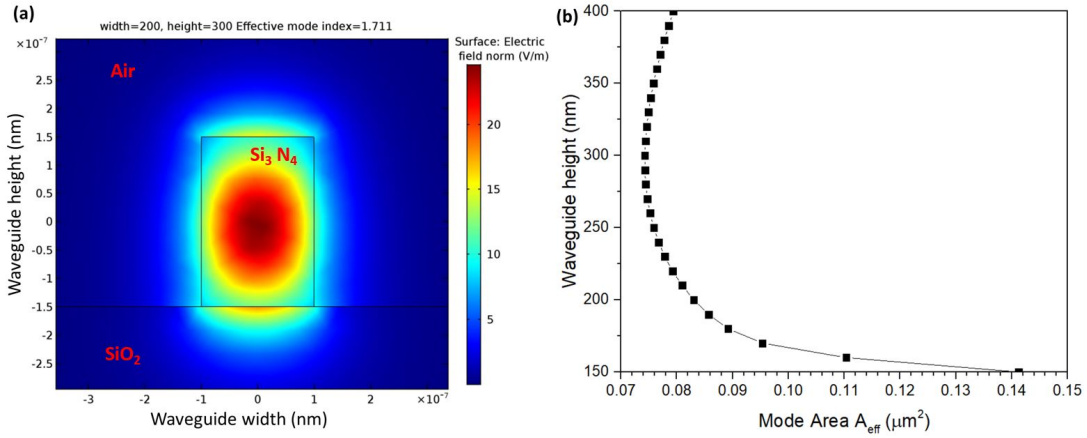

Figure 5.3: (a) Mode profile of the electric field for the fundamental TE for a Si_3N_4 strip waveguide with height 300 nm and width 200 nm at 500 nm wavelength. (b) Waveguide height as a function of effective mode area (A_{eff} of fundamental quasi-TE mode for a fixed width of 200 nm at 550 nm wavelength.

5.3 Evanescent Coupling of QD-NW emission to waveguides

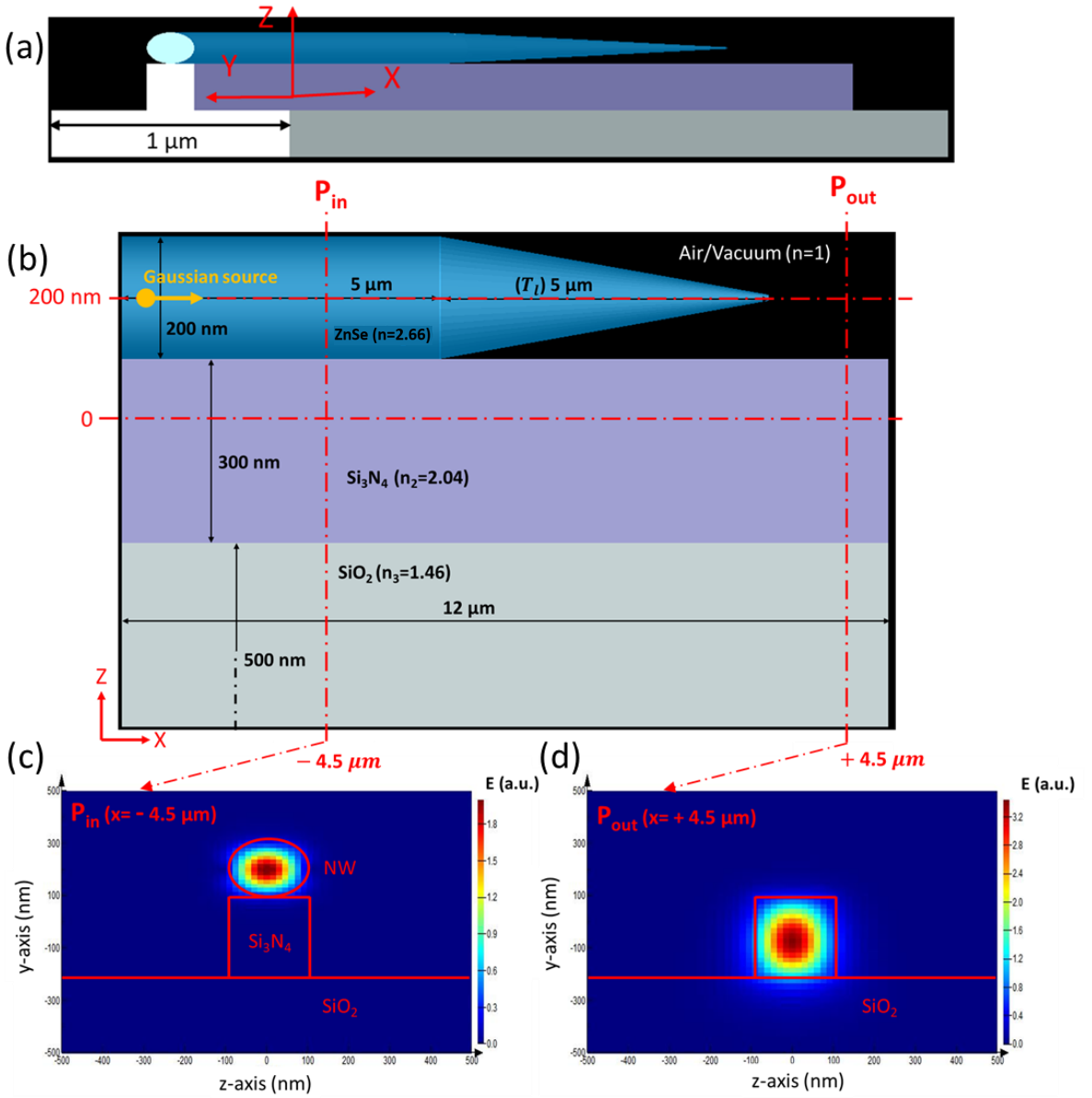

Figure 5.4: Schematic for the evanescent coupling of the emission from a ZnSe tapered NW into a silicon nitride waveguide in (a) 3D and in (b) 2D along the long axis. A Gaussian sources is placed at the center of the NW. The NW is placed on top of a silicon nitride waveguide of 300 nm height and 200 nm width, which is on top of the 500 nm silicon oxide layer. The electric field mode profile at the cross-section of the model in Y-Z plane is shown in (c) before the tapering of the NW starts at position P_{in}. And the same is shown after the tapering of the NW at position P_{out} in (d).

Evanescent coupling approach allows pre-fabrication of ultra low loss silico-nitride waveguides prior to nanowire transfer. With SKQDs or QD-NWs embedded in waveguides approach, the silicon nitride

has to be deposited at lower temperatures (using e.g., plasma-enhanced CVD (PECVD)) due to decomposition or inter- diffusion of most QDs or NWs at high temperatures for e.g., InP is limited to about 350° C. Also our CdSe QD and ZnSe NWs growth is done at 300-400° C. Nitride films deposited using PECVD are shown to have high losses then compared to films grown using low-pressure-high-temperature CVD (LPCVD). With evanescent coupling approach, low loss silicon nitride waveguides with complex circuitry can be pre-fabricated and QD-NWs can be placed in the vicinity of the waveguides with simple nano-manipulator techniques without the need of alignment marks.

Our NWs with optimal radius (80-100 nm) guides the light from the QD in the HE_{11} mode. To couple this HE_{11} mode to the fundamental TE mode of the waveguide, once again the tapered section of the our NWs will be useful to adiabatically expands the HE_{11} mode. The key parameter here will then be the taper length. To visualize the evanescent coupling between a NW and a waveguide and to see the effect of the tapering length, we used finite-difference time-domain (FDTD) or Yee´s method numerical analysis [127]. Although FEM technique can also be used, for this purpose we used FDTD techniques as its physically more intuitive to visualize the propagation of light along the photonic structure. We used Lumerical simulation tool to perform FDTD simulations.

In Fig 5.4 (a) is shown a 3D model of the structure which was simulated in Lumerical. In (b) is shown a 2D view along the X-Z plane. On top of the waveguide is the ZnSe NW ($n_1 = 2.6$) of 100 nm bottom radius and 5 nm top radius. The empty space has an index $n = 1$. The NW radius was chosen to be optimal for the HE_{11} mode guiding. The NW has a cylindrical section and a tapered section. The long cylindrical section of 5 μm length is kept to observe propagation of light first in the cylindrical section and then in the tapered section of length T_l. On the Z-axis the center of the NW is at 200 nm and the center of the waveguide is at -50 nm. Perfectly matched layer boundary conditions are used at all edges of the structure.

A Gaussian source, with dipole oscillating along the Y-axis, and with light propagating towards the positive X-direction is placed at the center and base of the NW. The Gaussian source is chosen to mimic the CdSe QD emitting at 550 nm. At first, we used a T_l of 5 μm, which gives a tapering half-angle ($\theta/2$) of about 1°. We have seen in chapter 2 that at this angle the adiabatic expansion of the HE_{11} mode is high to collect maximum light in a numerical aperture NA of 0.6. The mode profile in Y-Z plane is calculated for two X-axis positions. One at $X = -4.5$ μm (P_{in}) before the tapering of the NW starts and the other at $X = +4.5$ μm (P_{out}) after the tapering of the NW.

In Fig 5.4 (c) is shown the electric field mode profile in the Y-Z plane at P_{in}. The mode is confined just in the center of the NW with no leaking in the waveguide. This is before the tapering of the NW starts. In (d) is shown the mode at P_{out} where just the Si_3N_4 waveguide exists. Here the mode is perfectly confined in the Si_3N_4 region.

In Fig 5.5 (a) is shown the electric field along the X-Z plane for the above described NW same as before. The solid red line is to indicate the NW and the dotted red line is to indicate the waveguide. Before the tapering length starts, the HE_{11} mode is confined in the NW with no leaking in the waveguide. From $X = -2$ μm, the tapering starts and the HE_{11} mode starts to couple with the TE mode of the waveguide. But the coupling is not smooth and also weak.

To calculated the coupling efficiency, the power is integrated over the cross-sections (Y-Z plane) at two positions along the X-axis. One, just at the cross-section of the NW before the tapering of the NW starts in the cylindrical section i.e at P_{in} ($X = -4$ μm). And the other just st the cross-section of the waveguide after the NW tapering i.e at P_{out} ($X = +4$ μm), see Fig 5.5. The evanescent coupling efficiency *i.e.* the fraction of HE_{11} mode of the NW that evanescently couples to the TE mode of the waveguide is then given as P_{out}/P_{in}. For a T_l of 5 μm, P_{in}/P_{out} is 71 %.

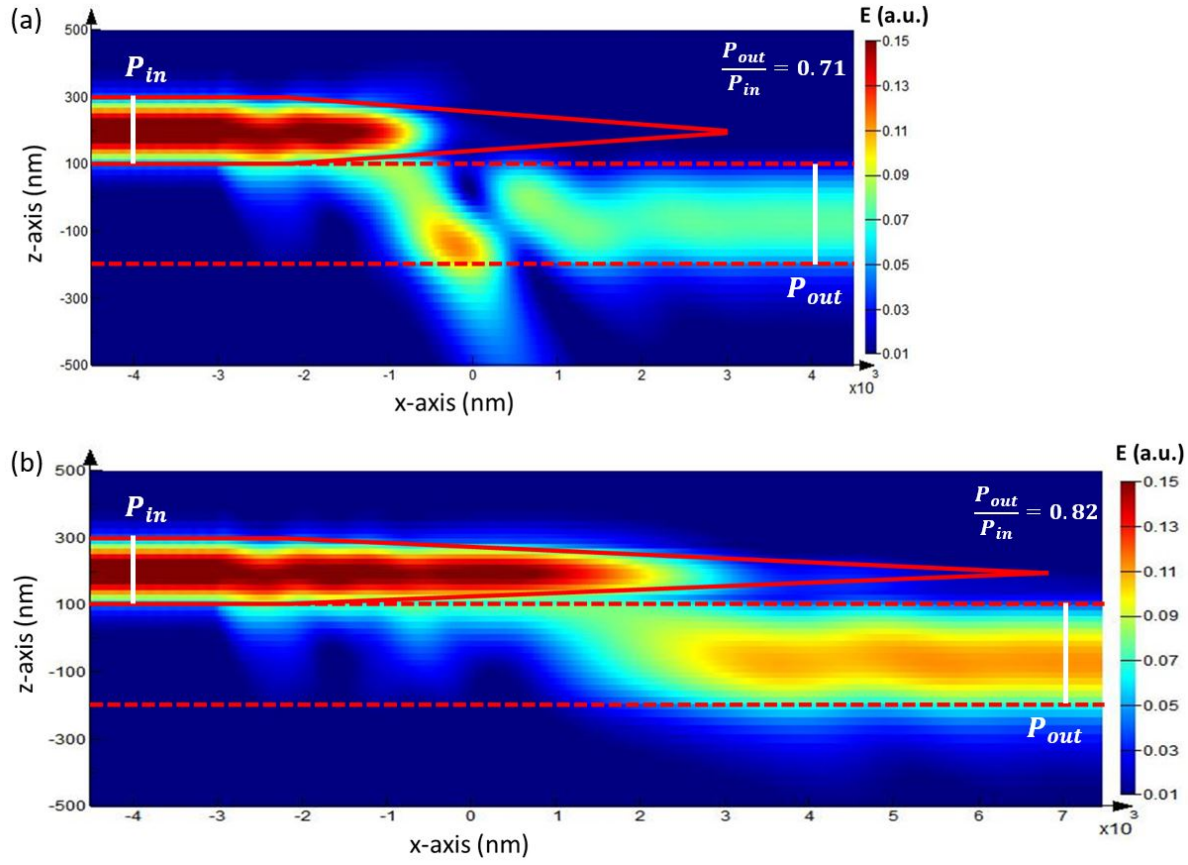

Figure 5.5: (a) Electric field profile in the X-Z plane showing coupling of light from NW to the silicon nitride waveguide for a NW with a tapering length of 5 μm. (b) The same is shown for a NW with a tapering length of 9 μm. In white is marked the cross-sections where P_{in} and P_{out} were calculated. The value of P_{in}/P_{out} is given for each configuration.

We also checked the effect of a long T_l value. In Fig 5.5 (b) is shown the electric field along the X-Z plane for T_l of 9 μm. In this case, the coupling of the HE_{11} mode to the TE mode of waveguide is very smooth and strong. Here, the power at P_{out} is calculated for $X = +7$ μm, after the tapering of the NW in the cross-section of the waveguide. The integrated P_{in}/P_{out} is about 82 % indicating strong coupling of NW emission to the waveguide.

It should be noted that in the model, there is gap between the tip of the NW and the waveguide layer. In reality the NW is bent and the complete surface of the NW is in contact with the 2D surface on which it is placed. This may be expected as a result of the Van der Waals forces between the NW and the 2D surface. Therefore, we also simulated a structure where the complete NW is in contact with the Si_3N_4 waveguide and a 2D view in the X-Z plane is shown in Fig 5.6 (a) for a NW with T_l of 9 μm. The electric field for this structure is shown in Fig 5.6 (b) along the X-Z plane. The coupling in this case is even smoother all along the tapered length of the NW. The coupling (integrated P_{in}/P_{out}) between the HE_{11} mode and the TE mode of waveguide is even stronger in this case at 90 %.

Mode coupling efficiency of 90 % with a 9 μm tapered length of ZnSe NW was obtained. This is similar to numerically calculated for InP NW on silicon nitride waveguide for a NW tapered length of

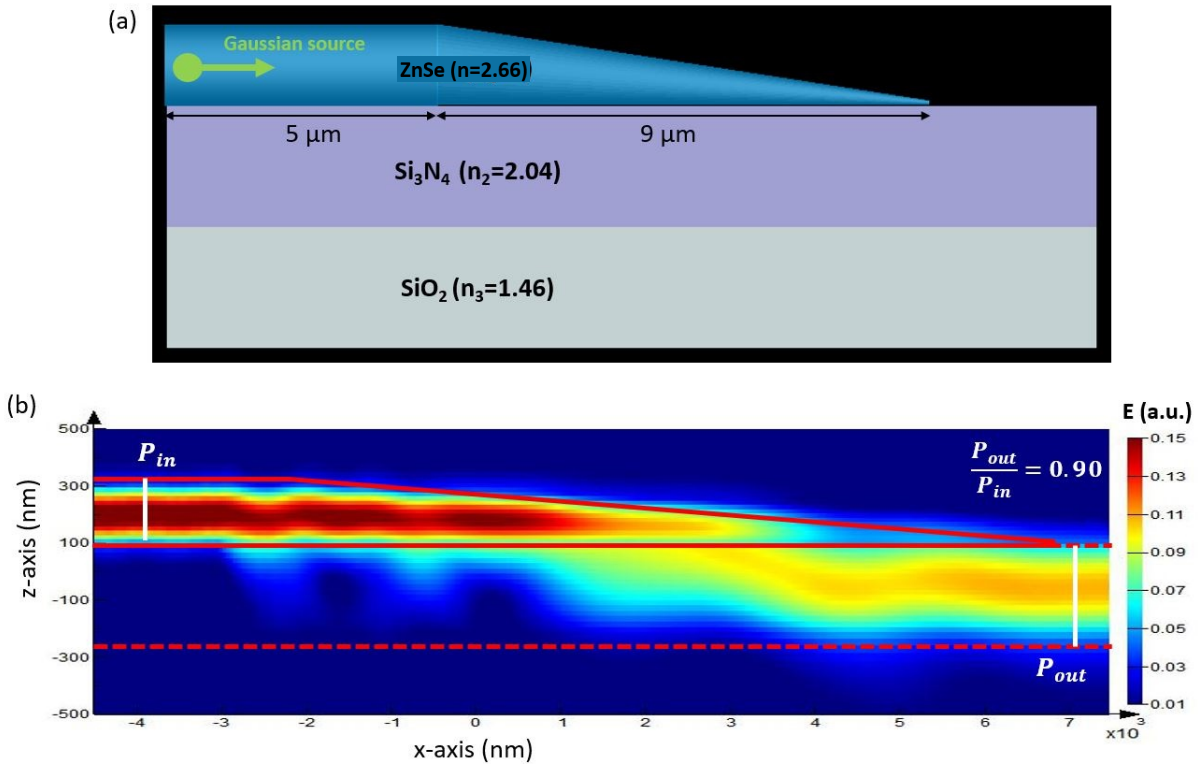

Figure 5.6: (a) Schematic for evanescent coupling of a NW where the tapered length is stuck to the waveguide surface due to Van Der Waals forces. (b) Electric field profile in the X-Z plane. In white is marked the cross-sections where P_{in} and P_{out} were calculated. The value of P_{out}/P_{in} is also given.

above 10 μm [10].

5.4 Integrated photonic chip

To explore single-photon based integrated photonics, we have started to fabricate a photonic chip with simple components, designed by CEA-Leti. In Fig 5.7 is shown a schematic of the basic idea behind integrating NWs with waveguides. The QD-NW placed on top of the waveguide, can be excited directly by shining a laser on it. The light emitted by the QD-NW will be evanescently coupled in the waveguide. The light is then divided equally into two paths through a multi-mode interferometer structure (acting as a beam-splitter). The two light paths in the waveguide can then be outcoupled by the grating couplers to free space, which can then be collected by a microscope or an optical fiber at a certain angle with respect to the normal to the gratings. With this simple photonic design, single-photon anti-bunching measurements can be demonstrated on an integrated photonic chip.

The design of the photonic chip including the dimensions of the grating couplers, the size of the multi-mode interferometer, the grating to waveguide tapered section length, etc were all optimized and designed by the CEA-Leti. In Fig 5.8 is shown the final design of the photonic chip. The length of waveguide is 4.4 mm. At the end of each waveguide, a grating is provided 10x10 μm^2 big, with a period of 175 nm. The grating are coupled to the waveguide of 200 nm in width and height through a 500

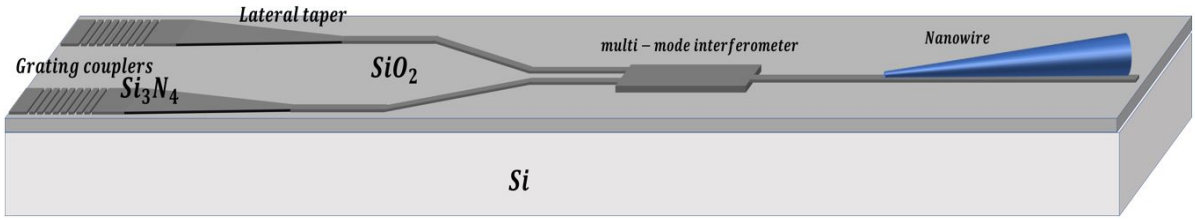

Figure 5.7: Schematic of a simple design to perform anti-bunching measurements on-chip. The silicon nitride (on 500 nm SiO_2) chip design consists of grating couplers to couple light from free-space to the waveguide or vice-versa, a multi-mode interferometer to split/combine light in/from two paths. In blue is the NW on top of the waveguide. NW can be excited directly from top or through the waveguide. Light emitted from the NW is evanescently coupled to the waveguide.

μm long tapered section for adiabatic coupling. Few waveguides are extended with curved paths to test the optical losses in the waveguides with each turn. The waveguides were then fabricated using e-beam lithography discussed in the following section.

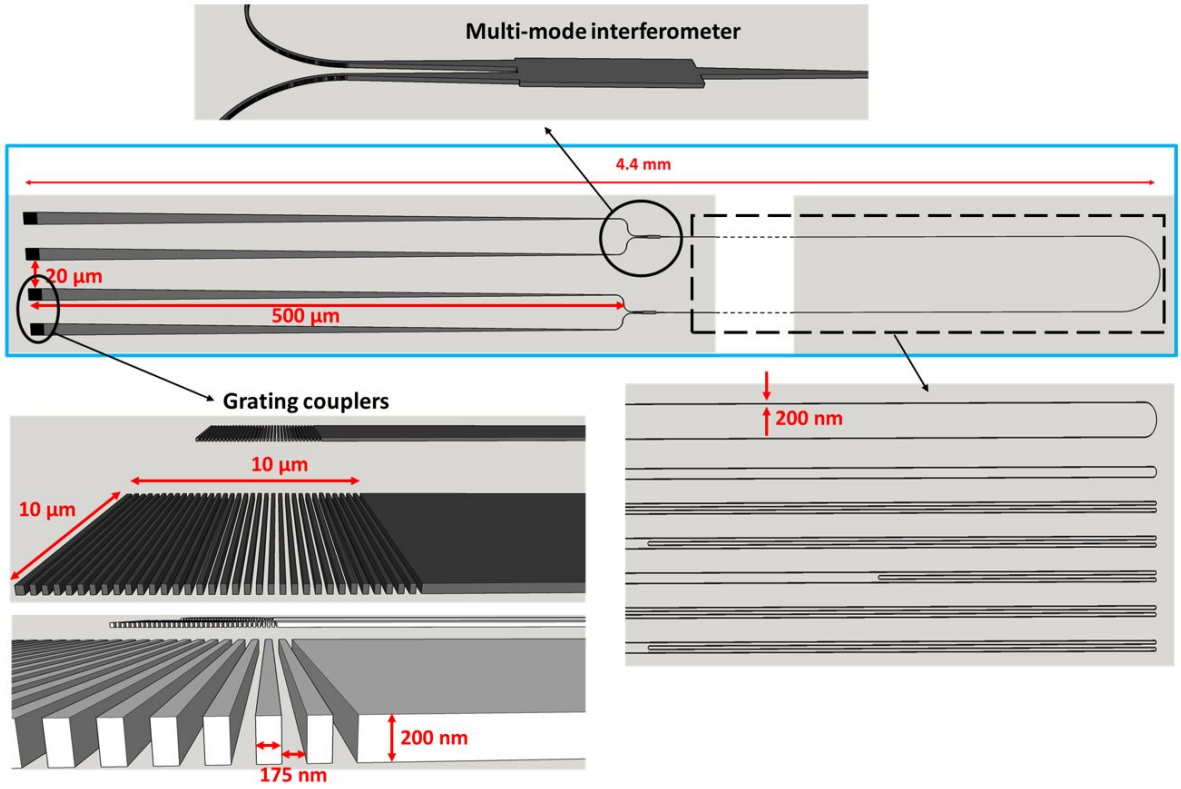

Figure 5.8: 3D waveguide design that was calculated and fabricated using silicon nitride. The design consists of grating couplers, multi-mode interferometer and a thin waveguide section of 200 nm in height and width coupling of NW emission to waveguides.

5.5 Fabrication of silicon nitride photonic chip

Silicon substrates with a 500 μm thick SiO_2 and then a 200 nm thick silicon nitride on top were provided by CEA-leti. The Si_3N_4 was deposited using PECVD. The Si_3N_4 layer is etched to realize Si_3N_4 waveguides. It should be noted that the height of the waveguides is fixed to 200 nm for these substrates and from FEM simulation, the optimum waveguide thickness is 300 nm in height (Fig 5.3). However, these substrates were used for testing the fabrication process.

The waveguide fabrication steps are as follows: first, a 1 cm^2 silicon nitride substrate is cleaned with acetone and kept in an ultrasonic bath for 5 minutes to remove any organic/oil residue. The residues left by acetone are cleaned by Isopropyl alcohol (IPA).

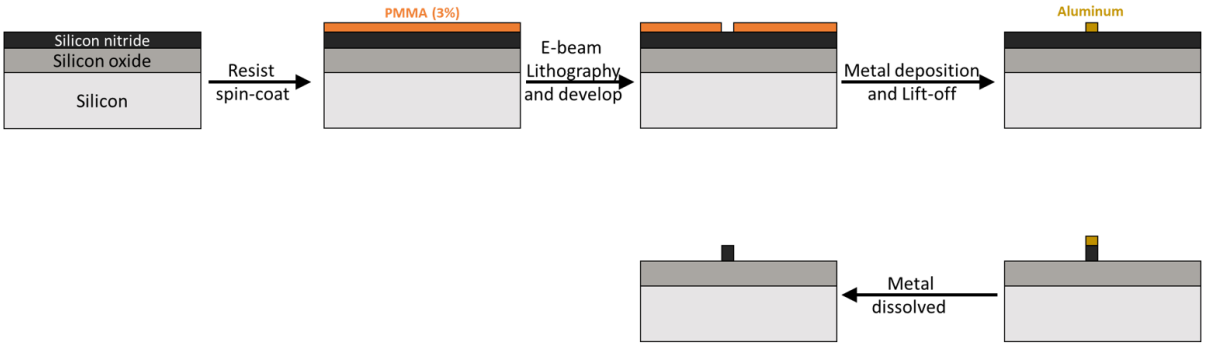

Figure 5.9: Silicon nitride fabrication steps with e-beam lithography. Aluminum thin film is used a mask to etch silicon nitride.

Then, the silicon nitride is etched to realize waveguides (Fig 5.9). For the aluminum mask, a 170-180 nm 3% PMMA resist is spin coated on the chip at a speed of 6000 rpm with an acceleration of 4000 rpm/s for 30 s followed by baking at 180° C. Then using e-beam lithography, electron beam is exposed to areas where waveguides are defined. The beam current between 9-11 nA was used. The substrate is then exposed to iso-propanol alcohol solution for 60 s to develop/remove the PMMA from areas exposed with electron beam. This is followed by deposition of 20-50 nm thick Aluminum in an e-beam evaporator and a lift-off process where the PMMA is dissolved in aceton for 60 min. What remains is aluminum on Si_3N_4 layer at areas where the waveguides are to be defined.

The 200 nm Si_3N_4 layer is then completely etched using a fluorine based gas CHF_3. The Si_3N_4 layer is protected at areas where Aluminum is deposited and therefore waveguides are defined. The aluminum is then dissolved in N-Methyl-2-Pyrrolidone solution for 60 min.

In Fig 5.10 are shown low magnification SEM images of the fabricated waveguides, The grating couplers, multi-mode interferometer and the 200 nm thick waveguides are well defined. In Fig 5.11 are shown two high magnification SEM images of the grating couplers with 9 nA and 11 nA beam current for e-beam lithography. With 11 nA the beam exposure is high and the vicinity of the waveguides are also exposed, with high surface roughness. With 9 nA the beam exposure is controlled and surface roughness has visibly improved.

Although, we have shown that the fabrication of Si_3N_4 waveguides with e-beam lithography is possible, the fabrication process requires modification and optimization as the surface roughness is still high. Any surface roughness reduces loses in waveguides due to scattering of light. Further optimization of e-beam current and thickness of the Aluminum mask is required to see the effect on surface roughness.

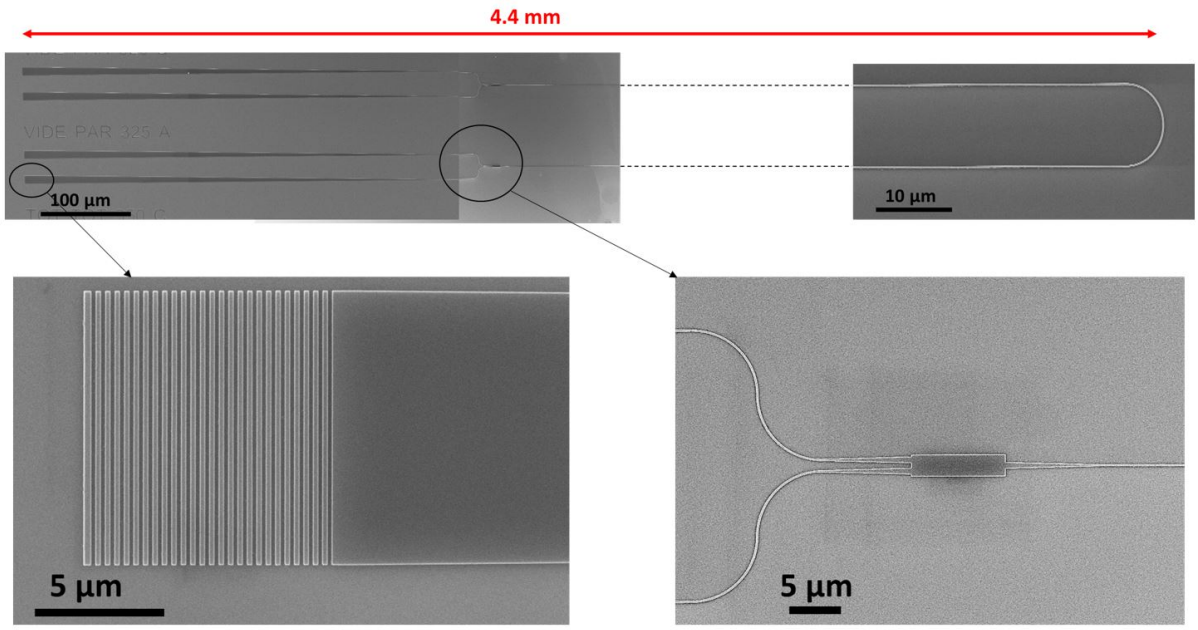

Figure 5.10: SEM images (top view) of the fabricated silicon nitride waveguides shown in Fig 5.8 using e-beam lithography.

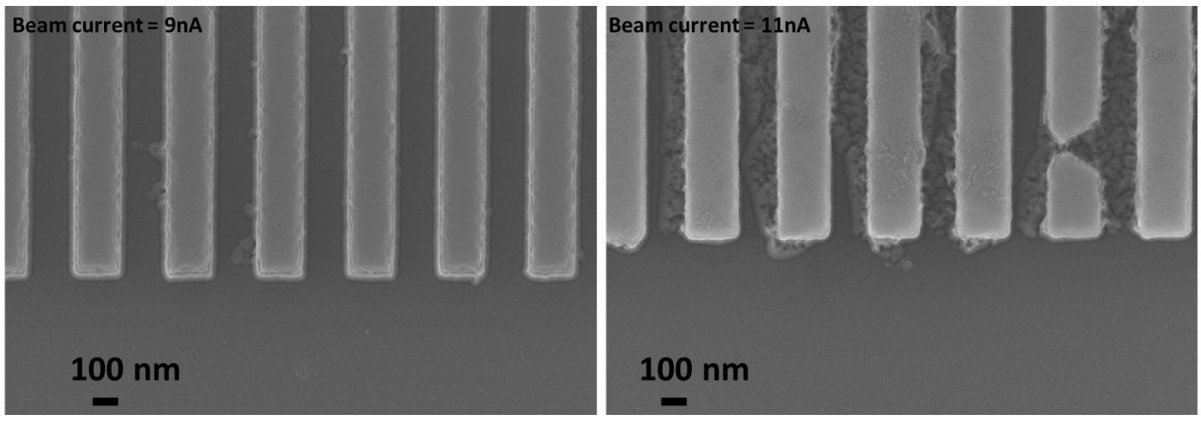

Figure 5.11: SEM images (top view) of the grating couplers in the waveguides when a beam current of 9 nA is used (a) and when 11 nA is used (b).

5.6 Conclusion

This chapter was introduced in the context of future prospective to address the integration of our QD-NW with silicon based photonics. The studies are incomplete but provide a few important results.

FDTD 3D numerical calculation shows that 90 % coupling efficiency of HE_{11} mode of the NW to the TE mode of the waveguide can be achieved with a NW having a long 9 μm tapered section. This coupling is achieved evanescently where a tapered section of the NW is required. However, this length

is too large to realize experimentally. More numerical calculations need to be performed to optimization the tapered length to a length that can be achieved experimentally with molecular beam epitaxy growth, without significant loss in efficiency.

The Si_3N_4 strip waveguide size on SiO_2 was numerically optimized at 200 nm in width and 300 nm in height to confine the principle TE mode. Based on the expertise of CEA-Leti, a photonic chip is designed with simple photonic components such as grating couplers and multi-mode interferometer to couple light to/from free space to the waveguide. The photonic chip is designed to demonstrate anti-bunching measurements on a QD-NW on chip. Finally, first test for fabrication of Si_3N_4 waveguides with e-beam lithography was achieved. Different e-beam current and metal (aluminum) mask thickness were explored to improve the surface roughness of the waveguides, however, the waveguide surface is still rough and further optimization is needed.

With this, we provide a direction for future studies to be performed to fully integrate our QD-NW with photonic devices.

Conclusions and Prospects

The goal of this thesis was to realize a "practical" single-photon emitter in the visible range and upto room temperature using a CdSe QD in a ZnSe NW. The main challenge for this thesis was to grow a thick and tapered epitaxial shell on vertically aligned thin ZnSe core, which guides the light from the QD (inserted in the core) in a given mode and enables efficient extraction and collection of the maximum of light in free space along the NW-axis. And then integrate this QD-NW single-photon source with photonic devices (waveguides).

Keeping this in mind, we started this thesis work with the designing of the NW shape. It was appreciated in *chapter 2* that the radius and tapering of the NW, along with a QD behaving like a radial dipole, plays main role in maximizing the extraction of light along the NW axis. And for this purpose, finite-element method numerical simulations were performed to optimize the radius to 80-100 nm, and the tapering half-angle to less than 3°.

Next, molecular beam epitaxy (MBE) growth of ZnSe NWs of this optimized NW shape was targeted (*chapter 3*). A core-shell growth approach for the NWs was followed, where core controls the radius of the QD. The NWs were grown with Au-NP (about 4 nm in radius) as catalyst under vapor-solid-solid growth mechanism. The effect of Zn and Se flux ratio, evolution of NWs with increasing Zinc amounts, effect of growth temperature and sample tilt was studied.

In general, low radial growth and not considerably enhanced axial growth of NWs, with high 2D growth of substrate was observed. The NWs were vertically oriented, thin with minimal radial growth (base radius ~10 nm, length ~0.5 to 1 μm), and with a cylindrical section at the top of the NWs of radius similar to Au-NP. A vertical NW is required for the control of the QD insertion and of the shell growth.

To grow a thick (80-100 nm in radius) and tapered Zn(Mg)Se shell on thin ZnSe NWs, we had to find the conditions to increase the radial growth.. One possible solution we found was to lower the growth temperatures. However, too low growth temperature (~300 °C) resulted in defects all along the NW. Also, shell growth induced increased 2D growth, and under "standard" growth conditions the NW-core (and therefore, the QD) was buried in the 2D layers. The challenge was to find growth configuration where we can keep (or increase) the radial growth of the NWs but reduce the 2D growth of the substrate. The solution to this problem was found by "tilting" the sample for shell growth. With a 10° sample "tilt", the flux onto the sides of the NW with respect to the substrate surface was increased by a factor of 1.14. With sample "tilt", the 2D growth rates were decreased, while the radial growth of NWs remain unchanged. We also decreased the temperature for the shell growth to 320 °C , a temperature high enough to keep good NW crystal quality.

Finally, vertically oriented, low density (much less than 1 NW/μm^2), thick (~90 nm radius) and tapered ZnSe/Zn(Mg)Se core/shell NWs (4-5 μm visible length) of good crystal quality were realized, with a core length of more than 500 nm above the 2D layer. Thus, with a QD inserted close to the tip of the core, these NWs ensured that the QD is not buried in the 2D-layers.

During the course of this thesis work, four as-grown QD-NW samples were grown, with improving structural quality and a shell radius of optimum values only for the last two samples. First three samples had a 10 s QD insertion and the fourth sample had a 7 s QD. *Characterization of a 10 s QD sample with energy-dispersive X-ray spectroscopy revealed a QD size of 3 nm in radius and 4 nm in height.* Optical characterizations were performed on the four QD-NW samples with CW and pulsed excitation, from cryogenic to room temperature (*chapter 4*). The excitation of NWs and detection of their emission was

done along the NW axis on as-grown samples.

For the QD-NW sample with a thin shell, no QD emission could be detected when excited along the NW-axis. This was probably due to the dielectric screening effect, because the exciting electric field is perpendicular to the NW axis. This effect is absent when excitation/detection is done in transverse directions for NWs dispersed on a foreign substrate, as in previous studies in our group. Then we observed that the surrounding of the QD affects the linewidth of emission lines. *For the QD-NW with a thick radius (~90 nm), a record linewidth of 210 μeV was observed with non-resonant excitation.* It was shown that at room temperature, the zero-phonon line is negligibly small and the experimentally observed linewidth is given by the phonon sideband. The effect of QD size on emission energy and on bi-exciton binding energy (B_{XX}) was also observed. A blue shift of the emission lines of about 50 nm was observed from 10s-QD to 7s-QD sample. The B_{XX} was higher for the sample with a 7 s QD insertion (about 20 meV) as compared to 10 s QD samples, and is similar to values reported for CdSe SKQDs.

Auto-correlation measurements were performed at 5 K under continuous excitation and pulsed excitation. Under continuous excitation, anti-bunching was demonstrated using not only the exciton and multi-exciton single emission lines, but also on two emission (the bi-exciton + charged-exciton) lines together, where it was deduced that the QD can hop between the neutral and the charged state.

A short (less than 1 ns) and a long (2-60 ns) decay time for both the exciton and the bi-exciton was observed for all QD-NWs studied. The short decay time was attributed to the radiative lifetimes of excitonic states. The long time was attributed to the presence of trap states in the vicinity of the QD. This was deduced from the temperature dependence and the power dependence of the long time, along with auto-correlation studies in pulsed excitation mode. For NWs, where the long decay time was much higher than the pulse laser repetition time, the anti-bunching experiment behaved like an anti-bunching experiment under continuous wave excitation. It was shown that even when single-photon emission is confirmed with anti-bunching measurements under continuous excitation, it does not confirm that the emitter can emit single-photons on-demand under pulsed excitation.

However, for the fourth/final QD-NW sample with a 7 s QD (with improved NW structural quality), the contribution of the traps was strongly suppressed and almost not visible at both low temperatures and high temperatures.

In the last part of *chapter 4*, single-photon emission was demonstrated at room temperature under pulsed excitation. For the fourth sample, *an average B_{XX} of 20 meV* was observed. This allowed resolving of the exciton and the bi-exciton peaks directly at room temperature, as evidenced by the power dependence study of exciton and bi-exciton intensities at room temperature. *Anti-bunching was observed at 300 K with a record $g^2(0) = 0.3$ on average for several NWs with average 40000 counts/s on one APD*. And as far as we know, these values are better than any known SKQD or NW-QD system at room temperatures. A short lifetime of less than 1 ns was observed at room temperature, allowing potentially GHz repetition rates.

Finally, coupling of light from our QD-NWs to waveguides was discussed in *chapter 5*. It was shown that tapering of the NW length is not only important for extracting light to free-space but also to couple light to waveguides. The light from the QD-NW can be evanescently coupled to a waveguide. *And with finite-difference time-domain numerical simulations it was shown that an evanescent coupling efficiency as high as 90 % of the HE_{11} mode of the tapered NW to the TE mode of a silicon nitride waveguide can be achieved.* At the end, a silicon nitride photonic chip is nanofabricated with simple photonic components such as grating couplers and multi-mode interferometer to couple light to/from free space to the waveguide. The photonic chip is designed to demonstrate in the future anti-bunching

measurements on a QD-NW on chip. With this, we provide a direction for future studies to be performed to fully integrate our QD-NW with photonic devices.

Future prospects

From the MBE growth of ZnSe NWs point of view, there are a few directions which require further attention. For *e.g.*, more TEM characterization are required to study the quality and crystal phase of the QD and the NWs. From the most optimized sample (S7), only six NWs at low temperatures and 4 NWs at room temperature were checked for their emission, as this sample was realized during the very end of this thesis work. Characterization on more NWs from this sample are required for a complete study to gather statistical information on the properties of this sample, such as on emission energy, bi-exciton binding energy (B_{XX}), linewidth and $g^2(0)$ values.

A phonon sideband was observed for all emission peaks at low temperature. A detailed study and model (in progress) is required. In future, a detailed study on the effect of QD height on the B_{XX} can be performed with a series of QD-NW samples with different QD heights, to see if B_{XX} can be further increased.

Till now, we have relied on dust particles and cracks to identify NWs on the as-grown sample so that multiple measurements can be performed on the same NW. And because of this we were limited in identifying NWs and many times could not come back to the same NW. With patterned substrates it will be easier to identify NWs, and this is mandatory if we want to select NWs suitable for the coupling to a waveguide. Towards the end of this thesis, NW growth on patterned substrate was performed. However, the patterned substrate surface is rough. Optimization of lithography process is required to obtain patterned substrate with smooth surfaces. Moreover, till now NWs grow randomly on the growth substrate. An attempt was also made to localize single NW growth using e-beam lithography. However, this direction requires further studies to be performed or a completely different approach.

To integrate QD-NWs with photonic devices, a complete study is required to optimize the length of the tapered section to the lowest length possible for efficient evanescent coupling to waveguides. The nanofabrication process requires further attention to improve the roughness of the waveguides. And finally, experiments needs to be designed for exciting a NW on waveguide and collecting light from the waveguides.

Bibliography

[1] Fulvio Flamini, Nicolo Spagnolo, and Fabio Sciarrino. Photonic quantum information processing: a review. *Reports on Progress in Physics*, 82(1):016001, 2018. (Cited on page ix.)

[2] Jeremy L O'brien. Optical quantum computing. *Science*, 318(5856):1567–1570, 2007. (Cited on page ix.)

[3] Han-Sen Zhong, Hui Wang, Yu-Hao Deng, Ming-Cheng Chen, Li-Chao Peng, Yi-Han Luo, Jian Qin, Dian Wu, Xing Ding, Yi Hu, et al. Quantum computational advantage using photons. *Science*, 370(6523):1460–1463, 2020. (Cited on pages ix and 2.)

[4] Vittorio Giovannetti, Seth Lloyd, and Lorenzo Maccone. Quantum metrology. *Physical Review Letters*, 96(1):010401, 2006. (Cited on page ix.)

[5] Alessandro Fedrizzi, Rupert Ursin, Thomas Herbst, Matteo Nespoli, Robert Prevedel, Thomas Scheidl, Felix Tiefenbacher, Thomas Jennewein, and Anton Zeilinger. High-fidelity transmission of entanglement over a high-loss free-space channel. *Nature Physics*, 5(6):389–392, 2009. (Cited on pages ix and 2.)

[6] Chao Zhang, Yun-Feng Huang, Bi-Heng Liu, Chuan-Feng Li, and Guang-Can Guo. Spontaneous parametric down-conversion sources for multiphoton experiments. *Advanced Quantum Technologies*, 4(5):2000132, 2021. (Cited on pages ix and 2.)

[7] H. J. Kimble, M. Dagenais, and L. Mandel. Photon antibunching in resonance fluorescence. *Physical Review Letters*, 39:691–695, Sep 1977. (Cited on pages ix and 3.)

[8] Christian Kurtsiefer, Sonja Mayer, Patrick Zarda, and Harald Weinfurter. Stable solid-state source of single photons. *Physical Review Letters*, 85:290–293, Jul 2000. (Cited on pages ix and 4.)

[9] F Sledz, S Piccolomo, AM Flatae, S Lagomarsino, R Rechenberg, MF Becker, S Sciortino, N Gelli, IA Khramtsov, D Yu Fedyanin, et al. Photoluminescence of nitrogen-vacancy and silicon-vacancy color centers in phosphorus-doped diamond at room and higher temperatures. *arXiv preprint arXiv:2101.05904*, 2021. (Cited on pages ix and 4.)

[10] Khaled Mnaymneh, Dan Dalacu, Joseph McKee, Jean Lapointe, Sofiane Haffouz, John F Weber, David B Northeast, Philip J Poole, Geof C Aers, and Robin L Williams. On-chip integration of single photon sources via evanescent coupling of tapered nanowires to sin waveguides. *Advanced Quantum Technologies*, 3(2):1900021, 2020. (Cited on pages ix, 93, 152, 153 and 158.)

[11] Samir Bounouar, Miryam Elouneg-Jamroz, M den Hertog, C Morchutt, E Bellet-Amalric, Régis André, Catherine Bougerol, Yann Genuist, J-Ph Poizat, Serge Tatarenko, et al. Ultrafast room temperature single-photon source from nanowire-quantum dots. *Nano Letters*, 12(6):2977–2981, 2012. (Cited on pages ix, 6, 7, 13, 14, 92, 93, 103, 125 and 146.)

[12] Mathieu Jeannin, Thibault Cremel, Teppo Häyrynen, Niels Gregersen, Edith Bellet-Amalric, Gilles Nogues, and Kuntheak Kheng. Enhanced photon extraction from a nanowire quantum dot using a bottom-up photonic shell. *Physical Review Applied*, 8(5):054022, 2017. (Cited on pages ix, 2, 9, 10, 13, 18, 33, 47, 59, 78, 79, 92, 93, 94 and 103.)

[13] Andreas Muller, Wei Fang, John Lawall, and Glenn S Solomon. Creating polarization-entangled photon pairs from a semiconductor quantum dot using the optical stark effect. *Physical Review Letters*, 103(21):217402, 2009. (Cited on page 2.)

[14] Charles H Bennett and Gilles Brassard. Quantum cryptography: Public key distribution and coin tossing. *arXiv preprint arXiv:2003.06557*, 2020. (Cited on page 2.)

[15] Francesco Basso Basset, Mauro Valeri, Emanuele Roccia, Valerio Muredda, Davide Poderini, Julia Neuwirth, Nicolo Spagnolo, Michele B Rota, Gonzalo Carvacho, Fabio Sciarrino, et al. Quantum key distribution with entangled photons generated on demand by a quantum dot. *Science Advances*, 7(12):eabe6379, 2021. (Cited on page 2.)

[16] Matthew D Eisaman, Jingyun Fan, Alan Migdall, and Sergey V Polyakov. Invited review article: Single-photon sources and detectors. *Review of Scientific Instruments*, 82(7):071101, 2011. (Cited on page 2.)

[17] Charles Santori, David Fattal, Jelena Vučković, Glenn S Solomon, and Yoshihisa Yamamoto. Indistinguishable photons from a single-photon device. *Nature*, 419(6907):594–597, 2002. (Cited on pages 2 and 95.)

[18] E. Dekel, D. V. Regelman, D. Gershoni, E. Ehrenfreund, W. V. Schoenfeld, and P. M. Petroff. Cascade evolution and radiative recombination of quantum dot multiexcitons studied by time-resolved spectroscopy. *Physical Review B*, 62(16):11038–11045, 2000. (Cited on page 3.)

[19] Samir Bounouar. *Photon correlations on a room temperature semi-conductor single photon emitter.* PhD thesis, Université de Grenoble, 2012. (Cited on pages 3, 92, 117, 125 and 129.)

[20] E Wu, J.R. Rabeau, F. Treussart, H. Zeng, P. Grangier, S. Prawer, and J.-F. Roch. Nonclassical photon statistics in a single nickel–nitrogen diamond color center photoluminescence at room temperature. *Journal of Modern Optics*, 55(17):2893–2901, 2008. (Cited on page 4.)

[21] JA Adams, JN Wang, PH Beton, and M Henini. Quantum dot fabrication by optical lithography and selective etching. In *Atomic and Nanometer-Scale Modification of Materials: Fundamentals and Applications*, pages 191–197. Springer, 1993. (Cited on page 5.)

[22] Arvind Baskaran and Peter Smereka. Mechanisms of stranski-krastanov growth. *Journal of Applied Physics*, 111(4):044321, 2012. (Cited on page 5.)

[23] Je-Hyung Kim, Tao Cai, Christopher JK Richardson, Richard P Leavitt, and Edo Waks. Two-photon interference from a bright single-photon source at telecom wavelengths. *Optica*, 3(6):577–584, 2016. (Cited on page 5.)

[24] Peter Michler, Alper Kiraz, Christoph Becher, WV Schoenfeld, PM Petroff, Lidong Zhang, Ella Hu, and A Imamoglu. A quantum dot single-photon turnstile device. *Science*, 290(5500):2282–2285, 2000. (Cited on page 5.)

[25] Lucas Schweickert, Klaus D Jöns, Katharina D Zeuner, Saimon Filipe Covre da Silva, Huiying Huang, Thomas Lettner, Marcus Reindl, Julien Zichi, Rinaldo Trotta, Armando Rastelli, et al. On-demand generation of background-free single photons from a solid-state source. *Applied Physics Letters*, 112(9):093106, 2018. (Cited on page 5.)

[26] Mark J Holmes, Satoshi Kako, Kihyun Choi, Munetaka Arita, and Yasuhiko Arakawa. Single photons from a hot solid-state emitter at 350 k. *ACS Photonics*, 3(4):543–546, 2016. (Cited on pages 5 and 6.)

[27] Yasuhiko Arakawa and Mark J Holmes. Progress in quantum-dot single photon sources for quantum information technologies: A broad spectrum overview. *Applied Physics Reviews*, 7(2):021309, 2020. (Cited on page 6.)

[28] Sebastian Tamariz, Gordon Callsen, Johann Stachurski, Kanako Shojiki, Raphaël Butté, and Nicolas Grandjean. Toward bright and pure single photon emitters at 300 k based on gan quantum dots on silicon. *ACS Photonics*, 7(6):1515–1522, 2020. (Cited on page 6.)

[29] Saniya Deshpande, Thomas Frost, Arnab Hazari, and Pallab Bhattacharya. Electrically pumped single-photon emission at room temperature from a single ingan/gan quantum dot. *Applied Physics Letters*, 105(14):141109, 2014. (Cited on pages 5 and 6.)

[30] T Wang, TJ Puchtler, Tongtong Zhu, JC Jarman, LP Nuttall, Rachel Angharad Oliver, and RA Taylor. Polarisation-controlled single photon emission at high temperatures from ingan quantum dots. *Nanoscale*, 9(27):9421–9427, 2017. (Cited on page 5.)

[31] MV Rakhlin, KG Belyaev, Sergei Valer'evich Sorokin, Irina Vladimirovna Sedova, Demid A Kirilenko, Aleksei Mikhailovich Mozharov, Ivan Sergeevich Mukhin, Marina Mikhailovna Kulagina, Yu M Zadiranov, Sergei Viktorovich Ivanov, et al. Single-photon emitter at 80 k based on a dielectric nanoantenna with a CdSe/ZnSe quantum dot. *JETP Letters*, 108(3):201–204, 2018. (Cited on pages 5, 93, 94, 103, 125 and 136.)

[32] K Sebald, P Michler, T Passow, D Hommel, G Bacher, and A Forchel. Single-photon emission of cdse quantum dots at temperatures up to 200 k. *Applied Physics Letters*, 81(16):2920–2922, 2002. (Cited on pages 5, 98, 107, 111 and 136.)

[33] O Fedorych, C Kruse, A Ruban, D Hommel, G Bacher, and T Kümmell. Room temperature single photon emission from an epitaxially grown quantum dot. *Applied Physics Letters*, 100(6):061114, 2012. (Cited on pages 5, 93, 94, 98, 103, 106, 111 and 136.)

[34] F Glas, C Guille, P Hénoc, and F Houzay. Tem study of the molecular beam epitaxy island growth of InAs on GaAs. In *Microscopy of Semiconducting Materials, 1987*, pages 71–76. CRC Press, 2021. (Cited on page 6.)

[35] D Leonard, M Krishnamurthy, CMv Reaves, Steven P DenBaars, and Pierre M Petroff. Direct formation of quantum-sized dots from uniform coherent islands of ingaas on gaas surfaces. *Applied Physics Letters*, 63(23):3203–3205, 1993. (Cited on page 6.)

[36] Manuel Gschrey, Alexander Thoma, Peter Schnauber, Mark Seifried, Ronny Schmidt, Benjamin Wohlfeil, Luzy Kruger, J-H Schulze, Tobias Heindel, Sven Burger, et al. Highly indistinguishable photons from deterministic quantum-dot microlenses utilizing three-dimensional in situ electron-beam lithography. *Nature Communications*, 6(1):1–8, 2015. (Cited on page 6.)

[37] Hai-Zhi Song, Mukhtar Hadi, Yanzhen Zheng, Bizhou Shen, Lei Zhang, Zhilei Ren, Ruoyao Gao, and Zhiming M Wang. InGaAsP/InP nanocavity for single-photon source at 1.55-μm telecommunication band. *Nanoscale Research Letters*, 12(1):1–7, 2017. (Cited on page 7.)

[38] Dan Dalacu, Khaled Mnaymneh, Jean Lapointe, Xiaohua Wu, Philip J Poole, Gabriele Bulgarini, Val Zwiller, and Michael E Reimer. Ultraclean emission from InAsP quantum dots in defect-free wurtzite InP nanowires. *Nano letters*, 12(11):5919–5923, 2012. (Cited on page 7.)

[39] V Zannier, Thibault Cremel, Alberto Artioli, David Ferrand, Kuntheak Kheng, V Grillo, and S Rubini. Optical properties of single wurtzite/zinc-blende ZnSe nanowires grown at low temperature. *Journal of Applied Physics*, 118(9):095702, 2015. (Cited on pages 8, 23 and 92.)

[40] Martien Den Hertog, Miryam Elouneg-Jamroz, Edith Bellet-Amalric, Samir Bounouar, Catherine Bougerol, Régis André, Yann Genuist, Jean-Philippe Poizat, Kuntheak Kheng, and Serge Tatarenko. Insertion of cdse quantum dots in ZnSe nanowires: Correlation of structural and chemical characterization with photoluminescence. *Journal of Applied Physics*, 110(3):034318, 2011. (Cited on page 8.)

[41] Lars Vegard. Die konstitution der mischkristalle und die raumfüllung der atome. *Zeitschrift fur Physik*, 5(1):17–26, 1921. (Cited on page 10.)

[42] H Benallali, K Hoummada, M Descoins, P Rueda-Fonseca, L Gerard, E Bellet-Amalric, S Tatarenko, K Kheng, and D Mangelinck. Nature of the ZnSe/GaAs interface investigated by atom probe tomography. *Scripta Materialia*, 69(7):505–508, 2013. (Cited on page 10.)

[43] M Tchernycheva, JC Harmand, G Patriarche, L Travers, and Ge E Cirlin. Temperature conditions for gaas nanowire formation by au-assisted molecular beam epitaxy. *Nanotechnology*, 17(16):4025, 2006. (Cited on page 10.)

[44] JC Harmand, G Patriarche, N Péré-Laperne, MN Merat-Combes, L Travers, and F Glas. Analysis of vapor-liquid-solid mechanism in au-assisted gaas nanowire growth. *Applied Physics Letters*, 87(20):203101, 2005. (Cited on page 10.)

[45] Eric Ngo, Weixi Wang, Pavel Bulkin, Ileana Florea, Martin Foldyna, Pere Roca i Cabarrocas, and Jean-Luc Maurice. Liquid-assisted vapor–solid–solid silicon nanowire growth mechanism revealed by in situ tem when using cu–sn bimetallic catalysts. *The Journal of Physical Chemistry C*, 2021. (Cited on page 11.)

[46] Frank Glas and Vladimir G Dubrovskii. Energetics and kinetics of monolayer formation in vapor-liquid-solid nanowire growth. *Physical Review Materials*, 4(8):083401, 2020. (Cited on page 11.)

[47] Hiroaki Okamoto, TB Massalski, et al. Binary alloy phase diagrams. *ASM International, Materials Park, OH, USA*, 1990. (Cited on page 12.)

[48] Ph Buffat and Jean Pierre Borel. Size effect on the melting temperature of gold particles. *Physical Review A*, 13(6):2287, 1976. (Cited on page 12.)

[49] XT Zhang, KM Ip, Z Liu, YP Leung, Quan Li, and SK Hark. Structure and photoluminescence of ZnSe nanoribbons grown by metal organic chemical vapor deposition. *Applied Physics Letters*, 84(14):2641–2643, 2004. (Cited on page 12.)

[50] JM DePuydt, H Cheng, JE Potts, TL Smith, and SK Mohapatra. Growth of undoped ZnSe on (100) GaAs by molecular-beam epitaxy: An investigation of the effects of growth temperature and beam pressure ratio. *Journal of Applied Physics*, 62(12):4756–4762, 1987. (Cited on page 12.)

[51] A Colli, S Hofmann, AC Ferrari, C Ducati, F Martelli, S Rubini, S Cabrini, Alfonso Franciosi, and J Robertson. Low-temperature synthesis of ZnSe nanowires and nanosaws by catalyst-assisted molecular-beam epitaxy. *Applied Physics Letters*, 86(15):153103, 2005. (Cited on page 12.)

[52] Yuan Cai, Siu Keung Chan, Iam Keong Sou, Yu Fai Chan, DANG SHENG Su, and Ning Wang. The size-dependent growth direction of ZnSe nanowires. *Advanced Materials*, 18(1):109–114, 2006. (Cited on page 12.)

[53] Yutaka Ohno, Takeo Shirahama, Seiji Takeda, Atsushi Ishizumi, and Yoshihiko Kanemitsu. Fe-catalytic growth of ZnSe nanowires on a ZnSe (001) surface at low temperatures by molecular-beam epitaxy. *Applied Physics Letters*, 87(4):043105, 2005. (Cited on page 12.)

[54] CH Hsiao, Shoou-Jinn Chang, SC Hung, YC Cheng, BR Huang, SB Wang, BW Lan, and SH Chih. ZnSe/ZnCdSe heterostructure nanowires. *Journal of Crystal Growth*, 312(10):1670–1675, 2010. (Cited on page 12.)

[55] Yejin Kim, Hyung Soon Im, Kidong Park, Jundong Kim, Jae-Pyoung Ahn, Seung Jo Yoo, Jin-Gyu Kim, and Jeunghee Park. Bent polytypic ZnSe and CdSe nanowires probed by photoluminescence. *Small*, 13(19):1603695, 2017. (Cited on page 12.)

[56] David Wisniewski, Kristopher Byrne, Christina F De Souza, Carlos Fernandes, and Harry E Ruda. Enhancement of transport properties in single ZnSe nanowire field-effect transistors. *Nanotechnology*, 30(5):054007, 2018. (Cited on page 12.)

[57] Thomas Aichele, Adrien Tribu, Gregory Sallen, Juanita Bocquel, Edith Bellet-Amalric, Catherine Bougerol, Jean-Philippe Poizat, Kuntheak Kheng, Régis André, Serge Tatarenko, et al. Cdse quantum dots in ZnSe nanowires as efficient source for single photons up to 220 k. *Journal of Crystal Growth*, 311(7):2123–2127, 2009. (Cited on pages 12 and 13.)

[58] Miryam Elouneg-Jamroz. *Croissance catalysée de nanofils de ZnSe avec boites quantiques de CdSe*. PhD thesis, Universite de Grenoble, 2013. (Cited on pages 13 and 48.)

[59] Mohamed Henini. *Molecular beam epitaxy: from research to mass production*. Newnes, 2012. (Cited on page 15.)

[60] Robin FC Farrow. *Molecular beam epitaxy: applications to key materials*. Elsevier, 1995. (Cited on page 15.)

[61] M Den Hertog. *Characterization of silicon nanowires by transmission electron microscopy*. PhD thesis, Universite Joseph-Fourier-Grenoble I, 2009. (Cited on pages 22 and 50.)

[62] M Abd Mutalib, MA Rahman, MHD Othman, AF Ismail, and J Jaafar. Scanning electron microscopy (sem) and energy-dispersive x-ray (edx) spectroscopy. In *Membrane characterization*, pages 161–179. Elsevier, 2017. (Cited on page 22.)

[63] Pamela Rueda-Fonseca. *Magnetic quantum dots in II-VI semiconductor nanowires*. PhD thesis, Universite Grenoble Alpes (ComUE), 2015. (Cited on pages 22, 48, 74 and 77.)

[64] Wolfgang Becker. *The bh TCSPC Technique: Principles and Applications*. Becker and Hickl GmbH, 2019. (Cited on page 23.)

[65] Becker and Hickl GmbH. *TCSPC Performance of the id100-50 detector*. Becker and Hickl GmbH, 2005. (Cited on page 25.)

[66] R Hanbury Brown and Richard Q Twiss. Correlation between photons in two coherent beams of light. *Nature*, 177(4497):27–29, 1956. (Cited on page 25.)

[67] Peter Grunwald. Effective second-order correlation function and single-photon detection. *New Journal of Physics*, 21(9):093003, 2019. (Cited on page 25.)

[68] Valery Zwiller and Gunnar Bjork. Improved light extraction from emitters in high refractive index materials using solid immersion lenses. *Journal of Applied Physics*, 92(2):660–665, 2002. (Cited on page 28.)

[69] Marc Sartison, Simone Luca Portalupi, Timo Gissibl, Michael Jetter, Harald Giessen, and Peter Michler. Combining in-situ lithography with 3d printed solid immersion lenses for single quantum dot spectroscopy. *Scientific Reports*, 7(1):1–7, 2017. (Cited on page 28.)

[70] Edward Mills Purcell. Spontaneous emission probabilities at radio frequencies. In *Confined Electrons and Photons*, pages 839–839. Springer, 1995. (Cited on page 29.)

[71] J. M. Gérard, B Sermage, B Gayral, B Legrand, E Costard, and V Thierry-Mieg. Enhanced spontaneous emission by quantum boxes in a monolithic optical microcavity. *Physical Review Letters*, 81(5):1110, 1998. (Cited on page 29.)

[72] Julien Claudon, Niels Gregersen, Philippe Lalanne, and Jean-Michel Gérard. Harnessing light with photonic nanowires: fundamentals and applications to quantum optics. *ChemPhysChem*, 14(11):2393–2402, 2013. (Cited on pages 30 and 39.)

[73] Daniel Y Chu and Seng-Tiong Ho. Spontaneous emission from excitons in cylindrical dielectric waveguides and the spontaneous-emission factor of microcavity ring lasers. *Journal of the Optical Society of America B*, 10(2):381–390, 1993. (Cited on page 30.)

[74] Matthew R Henderson, Shahraam Afshar, Andrew D Greentree, and Tanya M Monro. Dipole emitters in fiber: interface effects, collection efficiency and optimization. *Optics express*, 19(17):16182–16194, 2011. (Cited on pages 30, 40 and 43.)

[75] L Chen and E Towe. Nanowire lasers with distributed-bragg-reflector mirrors. *Applied Physics Letters*, 89(5):053125, 2006. (Cited on page 30.)

[76] Inbal Friedler, Christophe Sauvan, Jean-Paul Hugonin, Philippe Lalanne, Julien Claudon, and Jean-Michel Gérard. Solid-state single photon sources: the nanowire antenna. *Optics Express*, 17(4):2095–2110, 2009. (Cited on pages 30 and 44.)

[77] Kirk T McDonald. Radiation in the near zone of a hertzian dipole. *Joseph Henry Laboratories*, 2004. (Cited on page 33.)

[78] Nitin Singh Malik. *Les fils photoniques: une geometrie innovante pour la realisation de sources de lumiere quantique brillantes*. PhD thesis, Grenoble, 2011. (Cited on page 34.)

[79] Oktay Ural. *Finite Element Method: Basic Concepts and Applications*. Intext Educational Publishers, 1973. (Cited on page 35.)

[80] Bjorn Engquist and Andrew Majda. Absorbing boundary conditions for numerical simulation of waves. *Proceedings of the National Academy of Sciences*, 74(5):1765–1766, 1977. (Cited on page 37.)

[81] Jean-Pierre Berenger. A perfectly matched layer for the absorption of electromagnetic waves. *Journal of Computational Physics*, 114(2):185–200, 1994. (Cited on page 37.)

[82] Yeonjoon Park, Michael J Cich, Rian Zhao, Petra Specht, Eicke R Weber, Eric Stach, and Shinji Nozaki. Analysis of twin defects in gaas (111) b molecular beam epitaxy growth. *Journal of Vacuum Science & Technology B: Microelectronics and Nanometer Structures Processing, Measurement, and Phenomena*, 18(3):1566–1571, 2000. (Cited on page 48.)

[83] Robert W Meulenberg, Jonathan RI Lee, Abraham Wolcott, Jin Z Zhang, Louis J Terminello, and Tony Van Buuren. Determination of the exciton binding energy in cdse quantum dots. *ACS Nano*, 3(2):325–330, 2009. (Cited on page 48.)

[84] So-Yeong Joo, Da-Woon Jeong, Chan-Gi Lee, Bum-Sung Kim, Hyun-Su Park, and Woo-Byoung Kim. Room-temperature processing of cdse quantum dots with tunable sizes. *Journal of Applied Physics*, 121(22):223102, 2017. (Cited on pages 48 and 103.)

[85] Huibing Mao, Jing Chen, Jiqing Wang, Zhifeng Li, Ning Dai, and Ziqiang Zhu. Photoluminescence investigation of cdse quantum dots and the surface state effect. *Physica E: Low-dimensional Systems and Nanostructures*, 27(1-2):124–128, 2005. (Cited on page 48.)

[86] Pamela Rueda-Fonseca, Edith Bellet-Amalric, R Vigliaturo, Martien den Hertog, Yann Genuist, Régis André, Eric Robin, Alberto Artioli, Petr Stepanov, David Ferrand, et al. Structure and morphology in diffusion-driven growth of nanowires: the case of znte. *Nano Letters*, 14(4):1877–1883, 2014. (Cited on page 51.)

[87] VG Dubrovskii, NV Sibirev, GE Cirlin, IP Soshnikov, WH Chen, R Larde, E Cadel, P Pareige, T Xu, B Grandidier, et al. Gibbs-thomson and diffusion-induced contributions to the growth rate of si, inp, and gaas nanowires. *Physical Review B*, 79(20):205316, 2009. (Cited on page 74.)

[88] Vladimir G Dubrovskii, Alexey D Bolshakov, Benjamin L Williams, and Ken Durose. Growth modeling of CdTe nanowires. *Nanotechnology*, 23(48):485607, 2012. (Cited on page 74.)

[89] Pamela Rueda-Fonseca, Eric Robin, Edith Bellet-Amalric, Miguel Lopez-Haro, Martien Den Hertog, Yann Genuist, Régis Andre, Alberto Artioli, Serge Tatarenko, David Ferrand, et al. Quantitative reconstructions of 3d chemical nanostructures in nanowires. *Nano letters*, 16(3):1637–1642, 2016. (Cited on page 81.)

[90] Stefan Stufler, Patrick Ester, Artur Zrenner, and Max Bichler. Power broadening of the exciton linewidth in a single in ga as/ ga as quantum dot. *Applied Physics Letters*, 85(18):4202–4204, 2004. (Cited on page 92.)

[91] Michael E Reimer, Gabriele Bulgarini, A Fognini, Reinier W Heeres, Barbara J Witek, Marijn AM Versteegh, A Rubino, T Braun, M Kamp, S Höfling, et al. Overcoming power broadening of the quantum dot emission in a pure wurtzite nanowire. *Physical Review B*, 93(19):195316, 2016. (Cited on page 92.)

[92] DP Williams, AD Andreev, and EP O'Reilly. Self-consistent calculations of exciton, biexciton and charged exciton energies in InGaN/GaN quantum dots. *Superlattices and Microstructures*, 36(4-6):791–798, 2004. (Cited on pages 93 and 94.)

[93] D Simeonov, A Dussaigne, R Butté, and N Grandjean. Complex behavior of biexcitons in gan quantum dots due to a giant built-in polarization field. *Physical Review B*, 77(7):075306, 2008. (Cited on pages 93 and 94.)

[94] Supaluck Amloy, KH Yu, KF Karlsson, Rashid Farivar, TG Andersson, and Per-Olof Holtz. Size dependent biexciton binding energies in gan quantum dots. *Applied Physics Letters*, 99(25):251903, 2011. (Cited on pages 93 and 94.)

[95] Andreas V Kuhlmann, Jonathan H Prechtel, Julien Houel, Arne Ludwig, Dirk Reuter, Andreas D Wieck, and Richard J Warburton. Transform-limited single photons from a single quantum dot. *Nature Communications*, 6(1):1–6, 2015. (Cited on page 94.)

[96] CF Wang, A Badolato, I Wilson-Rae, PM Petroff, E Hu, J Urayama, and A Imamoğlu. Optical properties of single InAs quantum dots in close proximity to surfaces. *Applied Physics Letters*, 85(16):3423–3425, 2004. (Cited on page 94.)

[97] Arka Majumdar, Erik D Kim, and Jelena Vučković. Effect of photogenerated carriers on the spectral diffusion of a quantum dot coupled to a photonic crystal cavity. *Physical Review B*, 84(19):195304, 2011. (Cited on page 94.)

[98] SM Sze and KK Ng. Physics of semiconductor devices 3rd edn john wiley & sons. *Inc., New Jersey*, page 293, 2007. (Cited on page 94.)

[99] Jin Liu, Kumarasiri Konthasinghe, Marcelo Davanco, John Lawall, Vikas Anant, Varun Verma, Richard Mirin, Sae Woo Nam, Jin Dong Song, Ben Ma, et al. Direct observation of nanofabrication influence on the optical properties of single self-assembled InAs/GaAs quantum dots. *arXiv preprint arXiv:1710.09667*, 2017. (Cited on page 94.)

[100] Santanu Manna, Huiying Huang, Saimon Filipe Covre da Silva, Christian Schimpf, Michele B Rota, Barbara Lehner, Marcus Reindl, Rinaldo Trotta, and Armando Rastelli. Surface passivation and oxide encapsulation to improve optical properties of a single gaas quantum dot close to the surface. *Applied Surface Science*, 532:147360, 2020. (Cited on page 94.)

[101] Emmanuel Moreau. *Study of a single-mode solid source of single photons constituted by a semiconductor quantum dot in an optical microcavity*. PhD thesis, Universit 'e Pierre and Marie Curie-Paris VI, 2002. (Cited on page 96.)

[102] Jeppe Johansen, Brian Julsgaard, Søren Stobbe, Jørn M Hvam, and Peter Lodahl. Probing long-lived dark excitons in self-assembled quantum dots. *Physical Review B*, 81(8):081304, 2010. (Cited on page 97.)

[103] Katarzyna Roszak, Vollrath M Axt, Tilmann Kuhn, and Pawel Machnikowski. Exciton spin decay in quantum dots to bright and dark states. *Physical Review B*, 76(19):195324, 2007. (Cited on page 97.)

[104] Yatendra Pal Varshni. Temperature dependence of the energy gap in semiconductors. *Physica*, 34(1):149–154, 1967. (Cited on page 98.)

[105] W Shan, JJ Song, H Luo, and JK Furdyna. Determination of the fundamental and split-off band gaps in zinc-blende cdse by photomodulation spectroscopy. *Physical Review B*, 50(11):8012, 1994. (Cited on page 99.)

[106] O Madelung, U Rössler, and M Schulz. Springer materials—the landolt-börnstein database. *see http://www.springermaterials.com*, 2010. (Cited on page 99.)

[107] AB Novoselova and VB Lazarev. Physical and chemical properties of semiconductors. *Handbook, Moscow*, 1978. (Cited on page 99.)

[108] L Besombes, K Kheng, L Marsal, and H Mariette. Acoustic phonon broadening mechanism in single quantum dot emission. *Physical Review B*, 63(15):155307, 2001. (Cited on page 100.)

[109] Kuntheak Kheng, Sebatian Moehl, Ivan-Christophe Robin, Laurent Maingault, Régis André, and Henri Mariette. Temperature dependence of the exciton homogeneous linewidth in CdTe and cdse self-assembled quantum dots: Limit of single photon source operation. In *AIP Conference Proceedings*, volume 893, pages 917–918. American Institute of Physics, 2007. (Cited on page 102.)

[110] Gregory Sallen, Adrien Tribu, Thomas Aichele, Regis Andre, Lucien Besombes, Catherine Bougerol-Chaillout, Serge Tatarenko, Kuntheak Kheng, and Jean-Philippe Poizat. Dark exciton optical spectroscopy of a semiconducting quantum dot embedded in a nanowire. *arXiv preprint arXiv:0903.0497*, 2009. (Cited on pages 105 and 137.)

[111] DW Snoke, J Hubner, WW Ruhle, and M Zundel. Spin flip from dark to bright states in InP quantum dots. *Physical Review B*, 70(11):115329, 2004. (Cited on page 105.)

[112] Nicolas Chauvin, B Salem, G Bremond, G Guillot, C Bru-Chevallier, and M Gendry. Size and shape effects on excitons and biexcitons in single in as/ in p quantum dots. *Journal of Applied Physics*, 100(7):073702, 2006. (Cited on page 112.)

[113] GE Dialynas, N Chatzidimitriou, S Kalliakos, S Tsintzos, PG Savvidis, Z Hatzopoulos, and NT Pelekanos. Single dot spectroscopy on InAs/GaAs piezoelectric quantum dots. *Physica Status Solidi (a)*, 205(11):2566–2568, 2008. (Cited on page 112.)

[114] M Abbarchi, T Kuroda, C Mastrandrea, A Vinattieri, S Sanguinetti, T Mano, K Sakoda, and M Gurioli. Fine structure splitting of quantum dot excitons: Role of geometry and environment. *Physica E: Low-dimensional Systems and Nanostructures*, 42(4):881–883, 2010. (Cited on page 112.)

[115] Ali Jaffal, Philippe Regreny, Gilles Patriarche, Michel Gendry, and Nicolas Chauvin. Highly linear polarized emission at telecom bands in InAs/InP quantum dot-nanowires by geometry tailoring. *arXiv preprint arXiv:2106.08182*, 2021. (Cited on page 114.)

[116] M Shirane, Y Igarashi, Y Ota, M Nomura, N Kumagai, S Ohkouchi, A Kirihara, S Ishida, S Iwamoto, S Yorozu, et al. Charged and neutral biexciton–exciton cascade in a single quantum dot within a photonic bandgap. *Physica E: Low-dimensional Systems and Nanostructures*, 42(10):2563–2566, 2010. (Cited on page 120.)

[117] Alexios Beveratos, Izo Abram, Jean-Michel Gerard, and Isabelle Robert-Philip. Quantum optics with quantum dots. *The European Physical Journal D*, 68(12):1–14, 2014. (Cited on page 122.)

[118] T Flissikowski, A Hundt, M Lowisch, M Rabe, and F Henneberger. Photon beats from a single semiconductor quantum dot. *Physical Review Letters*, 86(14):3172, 2001. (Cited on page 125.)

[119] Olivier Labeau, Philippe Tamarat, and Brahim Lounis. Temperature dependence of single cdse/zns quantum dots luminescence lifetime. *Physical Review Letters*, 90:257404, 2003. (Cited on page 125.)

[120] Hamna F Haneef, Andrew M Zeidell, and Oana D Jurchescu. Charge carrier traps in organic semiconductors: a review on the underlying physics and impact on electronic devices. *Journal of Materials Chemistry C*, 8(3):759–787, 2020. (Cited on page 137.)

[121] WGJHM van Sark, PL Frederix, Ageeth A Bol, Hans C Gerritsen, and Andries Meijerink. Blueing, bleaching, and blinking of single cdse/zns quantum dots. *Journal of Physical Chemistry A*, 3:871–879, 2002. (Cited on page 147.)

[122] Mario Schwartz, Ulrich Rengstl, Thomas Herzog, Matthias Paul, Jan Kettler, Simone Luca Portalupi, Michael Jetter, and Peter Michler. Generation, guiding and splitting of triggered single photons from a resonantly excited quantum dot in a photonic circuit. *Optics Express*, 24(3):3089–3094, 2016. (Cited on page 152.)

[123] U Rengstl, M Schwartz, T Herzog, F Hargart, M Paul, SL Portalupi, M Jetter, and P Michler. On-chip beamsplitter operation on single photons from quasi-resonantly excited quantum dots embedded in gaas rib waveguides. *Applied Physics Letters*, 107(2):021101, 2015. (Cited on page 152.)

[124] Peter Schnauber, Johannes Schall, Samir Bounouar, Theresa Hohne, Suk-In Park, Geun-Hwan Ryu, Tobias Heindel, Sven Burger, Jin-Dong Song, Sven Rodt, et al. Deterministic integration of quantum dots into on-chip multimode interference beamsplitters using in situ electron beam lithography. *Nano Letters*, 18(4):2336–2342, 2018. (Cited on page 152.)

[125] Svetlana Khasminskaya, Felix Pyatkov, Karolina Slowik, Simone Ferrari, Oliver Kahl, Vadim Kovalyuk, Patrik Rath, Andreas Vetter, Frank Hennrich, Manfred M Kappes, et al. Fully integrated quantum photonic circuit with an electrically driven light source. *Nature Photonics*, 10(11):727–732, 2016. (Cited on page 152.)

[126] Iman Esmaeil Zadeh, Ali W Elshaari, Klaus D Jons, Andreas Fognini, Dan Dalacu, Philip J Poole, Michael E Reimer, and Val Zwiller. Deterministic integration of single photon sources in silicon based photonic circuits. *Nano Letters*, 16(4):2289–2294, 2016. (Cited on page 152.)

[127] K Alan Shore. Numerical methods in photonics, by andrei v. lavrinenko, jesper laegsgaard, niles gregersen, frank schmidt, and thomas sondergaard. scope: textbook, monograph. level: researchers, engineers, early career researchers, advanced undergraduates. *Contemporary Physics*, 57(2):262–262, 2016. (Cited on page 156.)